2012

ELEVATED TEMPERATURE LUBRICATED WEAR OF Al-Si ALLOYS

Sanjib Dey
University of Windsor

ELEVATED TEMPERATURE LUBRICATED WEAR OF Al-Si ALLOYS

SANJIB K. DEY

A Dissertation

Submitted to the Faculty of Graduate Studies

through Engineering Materials

in Partial Fulfillment of the Requirements for

the Degree of Doctor of Philosophy at the

University of Windsor

Windsor, Ontario, Canada

2011

Elevated Temperature Lubricated Wear of Al-Si Alloys

By

Sanjib K. Dey

APPROVED BY

Zoheir Farhat, External Examiner
Materials Engineering, Dalhousie University

Niharendu Biswas, Outside Program Reader
Civil and Environmental Engineering

William J. Altenhof, Program Reader
Mechanical, Automotive and Materials Engineering

Afsaneh Edrisy, Program Reader
Mechanical, Automotive and Materials Engineering

Ahmet T. Alpas, Advisor
Mechanical, Automotive and Materials Engineering

Behnam Shahrrava, Chair of Defense
Electrical and Computer Engineering

September 13, 2011

DECLARATION OF CO-AUTHORSHIP/PREVIOUS PUBLICATION

Co-authorship declaration

I hereby declare that this dissertation incorporates documentation of research work performed by the author under the supervision of Prof. A. T. Alpas. The numerical simulation work was performed under the guidance of Dr. W. J Altenhof and Prof. A. T. Alpas. The collection of electron images using transmission electron microscope was performed jointly by Dr. X. Meng-Burany, Michael P. Balogh and the author at General Motors Global Research and Development. The interpretation of these images was performed by the author. Dr. T.A. Perry and Dr. M. J. Lukitsch assisted with the provision of sample and brought an industrial perspective during the discussions of the results analysed by the author.

Declaration of previous publications

This dissertation includes material from two original peer reviewed journal articles that have already been published and one more journal article to be submitted for publication in peer reviewed journal.

Thesis Chapter	Publication title/ full citation	Publication Status
Chapter 4	Micromechanisms of low load wear in an Al-18.5% Si alloy	Published
Chapter 5	Ultra-mild wear mechanisms of Al–12.6 wt.% Si alloys at elevated temperature	Published
Chapter 7	Numerical Simulation of UMW mechanisms in Al-Si alloys	To be submitted

I certify that I have obtained a written permission from the copyright owner(s) to include the above published material(s) in my thesis. I certify that the above material describes work completed during my registration as graduate student at the University of Windsor.

I declare that, to the best of my knowledge, my dissertation does not infringe upon anyone's copyright nor violate any proprietary rights and that any ideas, techniques, quotations, or any other material from the work of other people included in my dissertation, published or otherwise, are fully acknowledged in accordance with the standard referencing practices. Furthermore, to the extent that I have included copyrighted material that surpasses the bounds of fair dealing within the meaning of the Canada Copyright Act, I certify that I have obtained a written permission from the copyright owner(s) to include such material(s) in my thesis.

I declare that this is a true copy of my dissertation, including any final revisions, as approved by my thesis committee and the Graduate Studies office, and that this thesis has not been submitted for a higher degree to any other University or Institution.

ABSTRACT

Cast hypereutectic Al-Si alloys made monolithic engine blocks is an outcome of the global drive towards lightweight vehicles. Eutectic alloys provide cost effective alternative to those expensive hypereutectic alloys. However, the tribological performances of the eutectic alloys needed rigorous evaluation and the objectives of this dissertation were to investigate the ultra-mild wear (UMW) mechanisms of eutectic Al-12.6%Si alloys, chemical and mechanical properties of tribolayers and their long term stability at elevated temperatures under boundary lubricated conditions.

Sliding experiments were conducted using 5W30 engine oil on three etched Al-Si alloys containing 12-25% silicon at temperatures between 25 °C and 160 °C for sliding cycles up to 6×10^6 revolutions. Statistical measurements based on optical profilometer were carried out to quantify UMW damage parameters and volumetric loss. A criterion to asses UMW damage was then developed. Numerical models containing single- and multi-particle were developed to conduct a parametric study investigating the effect of different matrix yield strength and strain hardening characteristics, and the tribofilm formation on UMW damage parameters.

UMW in Al-18.5%Si alloy lasted up to 10^4 cycles at 5.0 N load. In the eutectic alloy, three stages of UMW were identified at 25 and 100 °C at 2.0 N load, and UMW performance at 100 °C was found to be superior to that at 25 °C. At elevated temperatures, island-like tribofilm formation on silicon particles and the composition of oil-residue layer were the characteristic differences compared to 25 °C. The island like-tribofilm consisted of zinc sulphide and short chain zinc pyrophosphate, and the ORL was formed by mixing of tribofilm with aluminum matrix. The long term durability of ORL investigated for different Al-Si alloys at 100 °C elucidated

the effectiveness of it in maintaining UMW. Findings from the numerical study were in good agreement with experimental observations. The parametric study showed that higher yield strength and strain hardening exponent of the matrix, and presence of tribofilm on silicon were beneficial in prolonging UMW and delayed the transition of UMW-I to UMW-II stage. The experimental findings suggested that the eutectic alloy can be used as a cost effective replacement of the hypereutectic alloys.

To

my parents

ACKNOWLEDGMENTS

I would like to take this opportunity to express my sincere gratitude to my advisor Prof. Ahmet T. Alpas for accepting me as a student under his guidance and spending his valuable time and effort for steering me to conduct scientific research. I am very thankful for his encouragement, support and patience throughout my tenure as a graduate student at University of Windsor. I also would like to thank Dr. William J. Altenhof for his valuable time and effort in teaching me to conduct numerical simulations. I am grateful for the opportunity of studying and conducting research under their guidance.

I wish to thank my committee members: Dr. Afsaneh Edrisy and Prof. Niharendu Biswas for their time and invaluable suggestions. I acknowledge Dr. Xianying Meng-Burany for taking TEM images used in this dissertation. I would like to acknowledge Dr. Anil Sachdev, Dr. Michael J. Lukitsch and Dr. Thomas A. Perry from General Motors Global Research and Development for their support, guidance and many insightful discussions. I would also like to thank Nicholash Irish, Michael P. Balogh and Daad Haddad from General Motors Global Research and Development for their assistance in XPS, TEM and nanoindentation characterization. I would also like to thank Dr. S. Reyntjens of FEI for carrying out EDS maps and FIB milling.

I would like to thank Mr. P. Seguin, Mr. Robinson, Mr. Gang Li and the members of the technical support centre at the University of Windsor for their technical support during the course of the research work. I also want to thank Ms. B. Tattersall for her administrative assistance in numerous occasions during the past four years.

I wish to express thanks to all the past and current fellow researchers of the NSERC/General Motors of Canada Industrial Research Chair in Tribology of Lightweight Materials for their help and friendship.

I would like to acknowledge financial support from Natural Science and Engineering Council (NSERC) and General Motors of Canada through the Industrial Research Chair program at the University of Windsor. I am also thankful for the financial assistance from Ontario Government and University of Windsor through Ontario Graduate Scholarship in Science and Technology (OGSST) awards and In-Program Doctoral Tuition Scholarship awards.

I would also like to thank my parents, Mr. S. L. Dey and Mrs. G. Dey, my parents-in-law, Mr. S.C. Das, and R. Das for their love and affection. I am thankful to my brother, Santosh, my sister, Soma, my brother-in-law, Arindam and my sister-in-law, Gopa for taking care of many of my responsibilities which allowed me to concentrate on my study and research far away from home. Finally, there are no words to thank enough my dear wife Sarmistha for her love, encouragement and many sacrifices she made in the past years.

TABLE OF CONTENTS

LIST OF TABLES

LIST OF FIGURES

LIST OF APPENDICES

NOMENCLATURE

α	Viscosity constant of lubricating oil
η	Viscosity,
η_0	Viscosity constant of lubricating oil (related to α)
η_p	Energy dissipation coefficient
λ	Film thickness ratio
μ	Coefficient of friction
h_{min}	Lubrication film thickness, m
r^*	Composite surface roughness of two contacting bodies
E^*	Composite elastic modulus between two bodies
U	Sliding speed, m/s
W	Applied load, N
WT	Wear Track
BO	Bridging Oxygen
COF	Coefficient Of Friction
EDX	Energy Dispersive X-ray spectroscopy
HDF	Height Distribution Frequency
MW	Mild Wear
NBO	Non Bridging Oxygen
ORL	Oil-residue layer
POD	Pin-on-disc
SEM	Scanning Electron Microscope
SW	Severe Wear

TEM	Transmission Electron Microscope
UMW	Ultra-Mild Wear
XANES	X-ray Absorption Near Edge Structure
XPEEM	X-ray Photo-Emission Electron Microscopy
XPS	X-ray Photoemission Spectroscopy
ZDDP	Zinc DialkylDithioPhosphate

1. CHAPTER 1– INTRODUCTION

1.1 Overview

Use of Al- and Mg-based lightweight materials in automotive industries worldwide has become very important in the last decade to meet the demand of producing vehicles with higher fuel efficiency and cleaner exhaust to reduce the carbon footprint in the environment. To meet this demand, use of Al-based alloys in the automotive industries or in the transportation industry in general is on the rise [**1**]. The properties of Al-based alloys can be engineered precisely to the demands of specific applications of automotive industries through the choice of alloy composition, heat treatment, and fabrication process. The key characteristics of aluminum in automotive use are lightweight, high strength-to-weight ratio, resilience, corrosion resistance, forming and fabricating, joining, crashworthiness, cold resistance, recyclability, thermal conductivity, and reflectivity [**2**]. Use of Al-Si alloys in powertrain components such as engine block, pistons, piston rings, and cylinder bore to replace cast-iron and steel components is a result of this global drive for lightweight vehicles and improved emission.

The use of Al-Si alloys, more specifically 3xx.x series used in powertrain components, offer excellent castability, specific strength, and higher thermal conductivity and make these alloys a suitable alternative material to cast iron. Under normal running condition of an internal combustion engine, the estimated material removal rate should not exceed a few nanometers per running hour. The alternative materials must also meet these criteria. Therefore, tribological behaviour of the cast Al-Si alloys needs to be investigated for successful application of these alloys as engine block materials. Because the mechanical properties of these cast alloys vary

with microstructure and to facilitate the microstructure based design of engine block materials, the effect of the microstructure needed thorough evaluation in dry and lubricated sliding conditions.

The wear behaviour of Al-Si alloys with different silicon content and other alloying elements under dry sliding conditions have been studied for many years [**3-12**] in *mild wear* (MW) and *severe wear* (SW) regimes. These studies used various test configurations and various load and sliding speeds often reported the volumetric wear loss as being much higher than that observed in an internal combustion engine over its life time. Therefore these studies [**3-12**], pertaining to extreme loading conditions and without any lubrications, are relevant in understanding cold scuffing [**13**]. Apart from tribological understanding of this new class of materials for automotive application, the manufacturing cost of these components must be taken into consideration, for example, easy castability and machinability without significant tool wear, which ultimately provides cost effectiveness.

To cope with the demand, the automobile manufacturers and their suppliers developed engines with cast iron liners inserted in them [**14**]. This technology had a few disadvantages such as increased cost of production, reduction in weight savings, and lower thermal conductivity of the cast iron liner. Engines were also made of hypereutectic Al-Si (A390) alloys [**14**], but these alloys had machinability problems because of the presence of large and hard primary silicon particles. Likewise, many expensive commercial solutions were developed over the years whose applications were limited only to the premium vehicles. Thus, the development of hypoeutectic and eutectic Al-Si alloys allowed linerless engines to overcome the cost associated with the manufacture of engines made of hypereutectic Al-Si alloys. This created the need to understand the tribological behaviour of eutectic and hypoeutectic Al-Si alloys in lubricated sliding

conditions at low loads which mimic the microstructure evolution in normal engine running conditions.

Under normal operating condition of the automobile engine, lubricant is present between the cylinder bore and the piston ring, and the engine operates in different regimes of lubrication depending on the location within the bore. However, the harshest condition prevails in boundary lubrication regime. Therefore it is very important that the study of tribological performance of any new material for potential use in engine block must be conducted in boundary lubrication regime. Recently a study [**15**] on Al-Si alloys was conducted in boundary lubrication regime with the aim of understanding the UMW mechanisms at room temperature. The study revealed that UMW had three subregimes: in the first subregime (UMW-I), there is no wear of aluminum matrix. Silicon particle damage is limited to formation of abrasive scratch marks on the top surface. Particle sinking-in and fracture/fragmentation is also often observed depending on silicon particle morphology; in UMW-II, silicon particle sinking-in takes place causing pile-up of aluminum matrix surrounding the particles, and aluminum matrix wear starts to occur. In UMW-III, matrix wear decreases due to formation of an oil-residue layer. However, the authors did not quantify the pile-up formation, and the long term durability of the ORL to sustain the UMW-III was also not studied.

1.2 Objectives of this research

One objective of this dissertation was to study the UMW mechanisms of Al-Si alloys at an elevated temperature of 100 °C and to compare them with those at 25 °C. The formation of ORL layer was also studied at these two temperatures to characterize the mechanical and chemical properties of the ORL at 100 °C. The long-term durability of the ORL was investigated to understand the role of this layer in maintaining UMW. Another objective of this dissertation

was to develop a fine element model to simulate the silicon particle sinking-in and aluminum pile-up formation, thereby studying the effect of the mechanical properties of the matrix, such as yield strength and strain hardening on the aluminum pile-up formation in Al-Si alloys.

1.3 Organization of the dissertation

This dissertation is divided into eight chapters. The first chapter is a general introduction to this dissertation to emphasize the focus of the work carried out. The second chapter reviews previous work on relevant topics to this dissertation, such as a brief introduction to Al-Si alloys, the effect of some major alloying elements in 3xx series alloys, lubrication in engine oil and the additives in engine oil, dry and lubricated sliding behaviour of AL-Si alloys, and tribolayer/tribofilm formation. In the next chapter, materials used, experimental and data analysis techniques, and different characterization techniques used within the scope of this dissertation are detailed. In the fourth chapter, the results of lubricated sliding of a hypereutectic Al-Si alloy (Al-18.5% Si) are provided to elucidate the realm of UMW and transition from UMW to MW at 25 °C. In chapter five, experimental results of lubricated sliding of Al-12.6% Si alloy are presented to identify the UMW mechanisms at 100 °C and to compare them with those at 25 °C for the same alloy. The results of the characterization of a tribofilm and a tribolayer (ORL) formed at 100 °C are also described. In chapter six, the results of lubricated sliding experiments carried out on four different Al-Si alloys to investigate the durability of the ORL layer are presented. In the next chapter, the development of the finite element model to study the UMW mechanisms (sinking-in and pile-up of silicon particle) is introduced. The results of the numerical simulation to investigate the effect of aluminum matrix properties on the UMW mechanisms are also explained in this chapter. In the following chapter, Chapter eight, a general discussion on the experimental results and simulated results is presented. Finally in

chapter nine, this dissertation is summarized, and specific conclusions drawn from the experimental and numerical work and the significance of this research work are presented. Some suggestions for future work are also included in this chapter.

2. CHAPTER 2 – LITERATURE REVIEW

2.1 Introduction

In this chapter, previous work on dry sliding and lubricated sliding behaviour of Al-Si alloys used in automotive engine block were reviewed. The effects of silicon particle content and morphology on the tribological behaviour of Al-Si alloys were summarized. Specific attention was paid to discuss the formation of tribolayer or tribofilm in both dry and lubricated sliding. Finally, the literature concerning the UMW behaviour of Al-Si alloys in boundary lubricated region and the complementary engine dynamometer studies were also discussed.

2.1.1 Al-Si alloys as an engine block material

Aluminum-silicon (Al-Si) alloys have inherent advantages of lightweight, high specific strength, and good heat transfer ability, which make them possible alternatives to replace components made of ferrous alloys. The engine blocks made of hypoeutectic alloys such as A356 or A380 were under production [**16**], but these alloys showed modest wear resistance and had cast-in steel liners. But the production cost of die-cast Al-Si alloys with a cast iron liner was higher [**14**]. Furthermore, eliminating the liners by using linerless blocks made of Al-Si had the additional advantage of eliminating thermal expansion problems between aluminum and cast iron. Thus, the development of all aluminum engine block made of hypereutectic Al-Si alloys started. The Al-Si alloy, used as an engine block material in the linerless Chevrolet Vega 2300 engine, was a hypereutectic A390 alloy first introduced at the AFS Casting Congress [**17**]. After successful use in the Vega, 390 alloy was later used in Chevrolet Corvette ZL1, Porsche 928, Mercedes 3.8L V8, BMW, Audi, Volkswagen, Toyota, and other engines [**18**]. Thereafter, many commercial solutions, such as low pressure die cast AlSi17Cu4Mg (Alusil^{TM}), a metal matrix

composite produced by aluminum infiltration of the silicon preform to obtain 15% or 25% silicon at the bore surface (Lokasil^{TM}, and spray compacted hypereutectic $AlSi_{25}$ alloy (Silitec^{TM}) were developed [**19**], but their use has been limited to premium vehicles due to high production cost. Wear resistance in Al-Si alloys is primarily due to the presence of silicon in the aluminum matrix. Increasing the silicon content in Al-Si alloys not only increases the wear resistance of the alloy, but also the strength [**20**]. However, the improvement in strength and wear resistance comes at the cost of machinability and castability.

There are also other Al-Si alloys produced by either powder metallurgy technique [**21,22**] or spray forming techniques [**23,24**]. The driving force in these two alternate routes to produce Al-Si alloys is high silicon content with refined microstructure having uniform distribution of silicon particles. One of the spray cast Al-Si alloys under the trade name "Silitec" having a composition of Al-25%Si-4%Cu-Mg is produced by PEAK Werkstoff GmbH for Daimler-Benz automotive engines.

2.1.1.1 Microstructure and properties of cast 3xx series alloys

There are seven basic families of cast aluminum alloys [**14,25**]**:** Al-Cu (2xx), Al-Si-Cu (3xx), Al-Si (4xx), Al-Si-Mg (3xx), Al-Mg (5xx), Al-Zn-Mg (7xx), and Al-Sn (8xx). Thus, cast 3xx alloys have silicon as the principal alloying element, but other alloying elements such as copper and magnesium are specified. Among these, 3xx series alloys are extensively used for automotive components such as cylinder blocks, cylinder heads, and pistons [**14,16,25**]. The chemical composition of some of the commercial 3xxx series alloys is listed in **Table 2. 1** [**26**]. On the Al-Si binary phase diagram, shown in **Figure 2. 1** [**27**], these alloys are classified into eutectic (12.6 % Si), hypoeutectic, and hypereutectic alloys. Silicon has a low density, and it reduces the weight of Al-Si alloys. It also improves fluidity and feeding characteristics of molten aluminum, thus enhancing the overall castability. Both hypo- and hypereutectic Al-Si alloys have shown

promise as an engine block material due to their adequate wear resistance and higher strength-to-weight ratio **[3,4,9,28,29]**. Depending on percentage of silicon, casting parameters, and alloying additions (modifiers), Si in Al-Si alloys is present as either primary silicon or a eutectic phase. Typical physical and mechanical properties of some selected commercial 3xx series alloys are reproduced in **Table 2.2 [26]**.

2.1.1.2 Effect of alloying additions in Al-Si alloys

Alloying additions are made to binary Al-Si alloys to improve their desired properties, such as mechanical properties (ultimate tensile strength, yield strength, fatigue strength), corrosion resistance, and fabrication characteristics, such as castability, machinability, formability, and forgeability. In this section a small review will be presented to discuss the major alloying additions which are made to the binary Al-Si alloys for engine block application. The main alloying additions found in the Al-Si alloys used in engine block are copper (Cu), magnesium (Mg), nickel (Ni), iron (Fe), manganese (Mn), sodium (Na), and strontium (Sr).

Among these alloying elements, Cu and Mg are the two most important elements which are added to Al-Si alloys to improve their strength, occasionally accompanied by a decrease in ductility [**26,30-33**]. Addition of Cu improves the strength and hardness of the alloys in cast and heat treated conditions, and the maximum improvement in mechanical properties is observed with 4.0-5.5% copper [**26**]. Moustafa et al. [**30**] reported that addition of 3% copper in modified Al-11.5% Si alloys increased the yield strength by 57% with a loss of ductility by 33%. However, addition of Cu decreases corrosion resistance [**26**] and increases porosity [**34**].

Addition of Mg in Al-Si alloys provides the benefit of altering the mechanical properties by heat treatment. The β-phase (Mg_2Si) in Al-Si-Mg alloys displays the solubility limit corresponding to approximately 0.7% Mg [**26**]. Gustaffson et al. [**35**] reported that addition of

Mg in A319 alloys had increased the tensile strength and decreased the ductility. Moustafa et al. [**30**] also reported similar results for modified Al-11.5% Si alloys.

Ni addition in Al-Si alloys improves the elevated temperature mechanical properties and also reduces coefficient of thermal expansion [**26,31**]. Cho et al. [**31**] found that simultaneous increase in Cu and Ni in Al-12% Si alloys improved the elevated temperature mechanical properties. The authors reported that increasing Ni resulted in increase of $Al_3(Cu,Ni)_2$ and Al-(Ni,Fe) intermetallics, and increasing Cu and Ni simultaneously resulted in increase in $Al_3(Cu,Ni)_2$ phase. The authors showed that increase in mechanical properties at elevated temperature was due to the increased formation of $Al_3(Cu,Ni)_2$ phase and other intermetallic phases.

Fe and Mn are generally considered to be impurity elements in casting. Mn has very little solubility in aluminum and, as a result of this, it combines with Fe, Si, and Al to produce ($Al_{15}(Mn,Cr,Fe)_3Si$) intermetallic [**31,32**]. Iron reacts to form a number of insoluble intermetallic phases such as FeAl3, FeMnAl6, and α-AlFeSi, which are responsible for strength improvements at elevated temperature [**26**]. However with increasing Fe content due to these insoluble phases, feeding characteristics are adversely affected.

Na and Sr are used as eutectic modifiers in Al-Si alloys [**36-38**]. Sodium works well as a modifier in the absence of phosphorous (P) as it has a tendency to react with P [**26**]. Effective modification with Sr was achieved in slow solidification rates [**36,37**], whereas Na works as an effective modifier in all solidification conditions.

2.1.2 Dry sliding wear of Al-Si alloys

2.1.2.1 Tribological behaviour of Al-Si alloys in dry sliding

There have been many studies conducted on tribological behaviour of cast Al-Si alloys in the last four decades. In this section, the wear mechanisms of Al-Si alloys under dry sliding

condition and the influence of two most important parameters such as silicon content and their morphology on the wear mechanisms will be reviewed very briefly.

Antoniou and Subramanian [**39**], following the work of Lim and Ashby [**40**] on wear map for steel-on-steel, developed a wear mechanism map for aluminum alloys. The authors used data produced by the previous researchers using pin-on-disc (POD) apparatus and identified the mechanisms by direct observations of the topography and microstructure of the wear debris and the corresponding worn surfaces. **Figure 2. 2** [**39**] shows the wear mechanism map where Antoniou and Subramanian characterized five different regions. In Region a (formation of fine equiaxed particles), at low sliding velocities and applied pressures, the worn surface appeared smooth and interspersed with granular wear scars, which appeared as black due to the presence of iron. The debris generated in this region was a mixture of fine equiaxed particles of aluminum, silicon, and α-iron with diameter < 5 μm. In Region b (delamination of compacted equiaxed particles), with intermediate pressure and velocities, the debris particles were flake-like with a smoother upper surface and an irregular bottom surface. The composition of these flake-like debris were the same as that in Region a, and that debris formed by compaction of small equiaxed particles within the depression of the worn surface and later generated by delamination. In Region c (delamination of deformed aluminum alloy), at pressure and velocities higher than Region b, subsurface cracks were generated with increase in load or sliding speeds, which later separated from the alloy by delamination and transferred to the counterface. The worn surface appeared smooth and scarred, the latter of which was indicative of ductile shearing. In Region d (gross material transfer), at very high pressures and velocities, significant amount of materials transfer was observed until the counterface was almost covered by the aluminum alloy; thus the contacting asperities were mainly aluminum, and significant adhesion occurred. At very high pressure, seizure was more likely. In Region e, at very high applied loads

and independent of sliding velocities, the surface temperature exceeded the melting point of the material, which caused the removal of material by election or extrusion from the contact point; reduction in COF was also observed.

Liu et al. [**41**] proposed another wear mechanism map for aluminum alloys. The authors collated data from the literature and delineated the dominant wear mechanisms with reference to the models derived by Lim and Ashby [**40**]; four dominant mechanisms were reported as shown in **Figure 2. 3** [**41**]. At relatively low sliding velocities and applied pressure, oxidation dominated wear mechanisms were reported. Frictional heat generated at the asperities formed a thin oxide layer. The delamination wear or plasticity dominated wear involved the plastic shearing of metal in the sliding direction. The original theory was proposed by Suh [**42**], which considered the nucleation of cracks and then propagation of those cracks to the surface, generating particle-like wear debris.

Later, Zhang and Alpas [**43**] and Wilson and Alpas [**44**] constructed a wear mechanism map for 6061 Al alloy and A356 aluminum alloy, respectively, sliding against AISI 52100 steel in a block-on ring apparatus. **Figure 2. 4a and b** [**43,44**] show the wear mechanism map in these two alloys; the map provided some new insight into the wear mechanisms and the transition between them. Zhang and Alpas [**43**] revealed the presence of fine equiaxed particle debris and large plate-like debris in the MW regime. Based on microscopic evidence, the authors concluded that the MW was caused by the delamination of *mechanically mixed layer* (MML) allowing fresh metal to metal contact that prompted oxidation and iron transfer to occur simultaneously. In the SW region, thermal softening of the material resulted in massive plastic deformation. The transition from MW to SW occurred when the bulk surface temperature (T_f) exceeded a critical value, corresponding to about 0.4 of the melting temperature (T_m) of the aluminum alloy. Wilson and Alpas [**44**] showed similar findings for A356 alloy.

Thus, depending on the wear rate, worn surface characteristics, and the debris generated during sliding, the wear of Al-Si alloys can be categorized as MW or *oxidative wear* and SW or *metallic wear*. Later, MW was further subdivided into MW-I and MW-II subregimes by Elmadgli and Alpas [**10**]. Also, seizure was reported by Somi Reddy et al. [**7,45**] for Al-Si alloys with 7-17% silicon, and ultra-mild wear (UMW) was reported by Zhang and Alpas [**5**] for 6061 Al with 20 vol.% A12O3 and Elmadagli [**46**] for Al-18.5% Si alloys in two specific testing conditions.

2.1.2.2 Effects of silicon content on dry sliding of Al-Si alloys

The effect of silicon content is the most general parameter which many researchers [**3,6,47-51**] studied on wear behaviour of Al-Si alloys. Based on the silicon content, the Al-Si alloys are classified into eutectic, hypoeutectic, and hypereutectic alloys, and the silicon content can only be changed during casting process or later by surface modification techniques. There are contradicting findings in the literature on the effect of silicon. Shivanath et al. [**47**] studied the wear behaviour of binary Al-Si alloys with silicon varying from 4 to 20% using a pin-on disc wear tester against steel disc. The authors conducted the tests at a constant speed of 1 m/s up to a load of 24 kg and found that the amount of silicon had a pronounced effect on the transition load from MW to SW with the exception of Al-11% Si alloy, which showed a discontinuity in the linear relation between transition load and the silicon content. The authors also showed that within the mild wear or oxidative wear region, the wear rates were independent of the silicon content or the particle size of the silicon. Clarke and Sarkar [**3**] and Sarkar and Clarke [**48**] also conducted similar wear studies using a pin-on-bush wear tester on binary Al-Si alloys with silicon content varying from 2 to 22% Si against a hard EN31 steel disc. **Figure 2. 5** [**3**] shows the wear rate as a function of silicon content from this study which revealed that the beneficial effects of silicon on wear resistance increased up to 11% Si, after which the wear rate decreased and the higher silicon content had no beneficial effect. In fact,

the silicon particles in hypereutectic alloys caused wear on the steel counterface. The authors also showed that the only benefit in hypereutectic alloys was that the seizure load in those alloys was higher compared to the hypoeutectic alloys.

Andrews et al. [**49**] studied the effect of silicon content on the wear behaviour of hypereutectic alloys alone containing 17, 20, 23, and 26% silicon using pin-on-disk wear tester against M2 tool steel disk. The alloys had other alloying elements such as 4.5%-3.2% Cu, 0.5%-0.3% Mn, 0.1% Zn, 0.2% Ti, 0.05% P, and 0.4% Fe. The authors in this study reported that an increase in silicon content resulted in a reduction in wear rates and an increase in the transitional load from MW to SW. Later Pramila Bai and Biswas [**50**] studied the wear behaviour of binary Al-Si alloys with silicon content varying from 4%-24% in a POD wear tester against EN 24 steel disc. Using variance analysis, the authors showed that the silicon content had no significant effect on the wear rates and the coefficient of friction of the alloys studied in the range of 4%-24%. However, the wear rate of these alloys was much lower compared to commercial purity aluminum. Torabian et al. [**6**] also did similar studies to examine the effect of silicon content on the wear behaviour of binary Al-Si alloys with Silicon content varying from 2 to 20% and found that the wear rate decreases with increase in silicon content. However the decrease in wear rate was not significant after 15% silicon content. The transitional load from MW to SW was also decreased with increasing silicon content, and the wear process changed with alloy composition and the experimental conditions; wear debris was generated by cracking and spalling of oxides and particles and/or by delamination of surface layers.

Wang et al. [**51**] also investigated the effect of silicon content on the dry sliding wear properties of spray deposited Al-Si alloys with 12, 20, and 25% silicon using a POD machine at four different normal loads. The counterface in this study was a quenched T8 tool steel. This study showed that at low load of 8.9 N, the wear rate decreased with increasing silicon content,

but at a high load of 35.6 N, the alloy with 20% silicon content showed better wear resistance than the other two alloys. The dominant wear mechanism at low load was mainly oxidative wear, whereas at high loads it was delamination and third body abrasive wear.

2.1.2.3 Effects of silicon particle morphology

Once the silicon content is fixed in an Al-Si alloy, the silicon particle morphology can be varied either by adding modifiers during the casting process [**37,38**], or by altering the casting parameters (solidification rate, application of injection pressure, and so on), or later by heat treatment [**37,38,52,53**], or by using a combination of both or by a combination of all three. Although many authors studied the effect of silicon particles on wear behaviour, very little work was done to discover the effects of silicon particle morphology (shape, size, and distribution) on the dry sliding wear behaviour of Al-Si alloys. Riahi et al. [**54**] studied the effect of silicon particle morphology on the onset of scuffing in two different Al-Si alloys with different silicon particles and other second phase particle morphology. The number of hard phases per unit area with aspect ratio greater than 10 in those two alloys was 45±14 and 980±18 mm^{-2}. The authors conducted a dry sliding test using a POD wear tester and detected the onset of scuffing based on the electrical resistance between the pin and the disc (Al-Si alloy samples). The onset of scuffing was associated with a large drop in electrical resistance from 20-40 Ω to 0.2-0.7 Ω. In this study, the authors reported that the onset of scuffing was observed earlier in the alloy, which had a significantly larger number of hard phase particles per unit area.

Later, Elmadagli et al. [**12**] did a comprehensive investigation to find the relationship between microstructure and wear resistance in Al-Si alloys. In this study, the authors conducted dry sliding tests using block-on-ring tests in Al-9.5% Si, Al-18.5% Si, and Al-25% Si alloys over a wide range of normal loads and at a constant sliding velocity of 1 m/s. The silicon particle morphology in these three alloys was characterized by the aspect ratio and sphericity (defined

as: 4π×area/perimeter^2) of the alloys. Also the particle morphology in Al-9.5% Si alloy was modified using heat treatment. The authors reported two subregimes in MW (MW-I and MW-II) observed in all three alloys, and the applied normal load (L) dependency of wear rate (W) in both subregimes followed a power relation, $W = C \times L^n$, where C was the wear coefficient, and n was the wear exponent. **Figure 2. 6a-d** [**12**] shows the effect of silicon particle sphericity and aspect ratio on the wear coefficients, C_1 and C_2, in MW-I and MW-II, respectively, and the transition loads, L_1 and L_2, corresponding to the upper limit load of MW-I and the load above which MW-II occurred. The authors showed that changing the silicon particle sphericity from 3.75 to 1.98 in Al-9.5% Si alloy resulted in reduction of wear coefficients C_1 by 27% and C_2 by 31% and increased the transition loads L_1 and L_2 by 25% and 40%, respectively. Reduction in silicon particle aspect ratio had a similar effect on the wear coefficients and the transition loads. These results indicated that the particles with higher sphericity values, which were less prone to fracture, increased the wear resistance in dry sliding.

2.1.3 Tribo-layers in dry sliding of Al-Si alloys

The formation of tribo-layers has commonly been observed in dry sliding of Al-Si alloys or generally in most sliding surfaces, although they may not have been termed as tribo-layer. Shivanath et al. [**47**], in their study of dry sliding of Al-Si alloys against steel, had reported the formation of oxide layer which was harder than the matrix of the alloy and resulted in low wear rates. Razavizadeh and Eyre [**55,56**] conducted XPS of dark-coloured layers on Al-16% Si alloy surface slid against a steel disc and detected the formation of a patchy oxide layer. Heilmann et al. [**57**] investigated the chemical composition of transfer layer and the debris particles generated during sliding experiments using OM, SEM, EDX, TEM, and STEM. Based on their investigations they concluded that formation of transfer layer was common in both dry and lubricated sliding and that they formed much before the loose wear debris was generated. Also

the composition of transfer layer consisted of a mechanical mixing of materials that originated from the contacting asperities, and the loose debris generated later in sliding process had a similar composition to that of the transfer layers. Rice et al. [**58**], in their study of repetitive, impulsive, and continuous sliding contact of various metallic pairs, characterized the microstructure of surface and subsurface region based on the microscopic and spectroscopic evidence. **Figure 2. 7** [**58**] shows a schematic depicting a characteristic feature of the subsurface where three distinct zones were identified and the topmost zone was labelled as tribo-layer by various researchers. Antoniou and Borland [**4**], in their study of MW of binary Al-Si alloys, also reported mechanical alloying to explain the formation of the dark surface layers. Using XRD and TEM investigations of these dark layers, the authors concluded that they were an ultrafine mixture of aluminum, silicon, and α-iron particles less than 100 nm in size; the presence of α-Al_2O_3 was also noticed sometimes.

Riahi and Alpas [**8**] carried out a systematic investigation on the role of a tribo-layer in unlubricated sliding wear behaviour of two graphitic aluminum matrix (A356) composites containing 10% SiC and 5% Al_2O_3 against AISI 52100 steel in UMW, MW, and SW regime. The authors showed that the mechanically mixed tribo-layer, having hardness eight times the hardness of the unworn composite, consisted of fractured reinforcement (SiC/ Al_2O_3), Al_3Ni and silicon particles mixed with aluminum. **Figure 2. 8** [**8**] shows the comparison of MW-SW transition boundaries for the materials studied in a wear mechanism map. The formation of the tribo-layer resulted in transition from MW to SW in graphitic aluminum matrix composites at load and sliding speed combinations which were higher compared to those for the non-graphitic composite and the base A356 alloy. However, the tribo-layer was removed in SW region, and it also caused scuffing of the steel counterface beyond a critical sliding speed.

Elmadagli and Alpas [**10**], in their study of dry sliding wear behaviour of Al-18.5% Si alloy, investigated the growth mechanisms of tribo-layers and progression of materials-transfer events in the two subregimes of MW, namely MW-I and MW-II. The authors found that the tribo-layer formation in MW-II occurred at a faster rate compared to MW-I. **Figure 2. 9a-e** and **f-j** [**10**] show the elemental composition maps acquired by electron probe microanalyses (EPMA) of the tribo-layer in MW-I (sample tested at 10N) and MW-II (sample tested at 60N). Thin tribo-layer in MW-I formed at the beginning of the sliding process did not always cover the entire contact surface, and the morphologies and the compositions of that layer did not change in the rest of the sliding in MW-I. In MW-II the tribo-layer had a layered structure, and it was thicker than that of MW-I. A thin metallic aluminum layer with the tribo-layer in MW-II was observed.

Li et al. [**11**] studied the effect of test environment on the formation of tribo-layers and their effect on the sliding wear behaviour of aluminum A390 alloy. The authors conducted dry sliding wear tests in air and argon atmosphere and investigated the surface and subsurface microstructure using various microscopic techniques. The authors found that the tribo-layer formed in argon was more stable than that formed in air, and thus the wear behaviour of the alloy in argon atmosphere was better. The tribo-layer in air was hard and consisted of heavily oxidized iron and aluminum; thus they were severely fractured due to their brittleness. The tribo-layer in argon, on the other hand, was primarily composed of mechanical mixing of ultrafine grain aluminum and silicon particles.

2.1.4 Lubrication in automotive engines

2.1.4.1 Lubrication regimes

All surfaces are rough surfaces; only the asperity heights change with the scale of magnification. When two surfaces come in contact with each other in the presence of lubrication oil, the simple situation arises when the asperities from both surfaces are completely

separated by a thick film of oil. Such a situation can arise with high viscosity lubricants or at low loads, and the lubricant carries the applied load. This condition is known as hydrodynamic or full-film lubrication and is the most desirable situation in any contacting bodies because it provides low friction and high resistance to wear.

With the increase in load, when the thickness of the lubricating oil film reaches of the order of a few molecules thick, the roughness, composition, and melting point of the surfaces strongly influence the friction between them. The viscosity plays little or no part in controlling the frictional behaviour. This condition is known as boundary lubrication. Increasing load or sliding speed has little effect on the high frictional value observed in this condition.

Hydrodynamic or full-film lubrication and boundary lubrication are two extreme cases of lubrication; there exist two intermediate regions known as elastohydrodynamic lubrication and mixed-film lubrication. The former is also nominally full-film lubrication with surface separation, but the elastic deformation of the surfaces and the effect of pressure on lubricant viscosity are important in controlling frictional behaviour. The mixed-film lubrication is a mixture of elastohydrodynamic lubrication and boundary lubrication condition where some asperity contacts are made. Understanding of lubrication in these regimes is important because the contact between the piston ring and the cylinder bore takes place in these conditions. In one single stroke of the piston, the piston ring may experience boundary, mixed- and full-fluid film lubrication [**59**].

Thus, the lubrication is a function of lubricant viscosity, the applied load, sliding speed, temperature, surface roughness, and the nature of the surface film [**60**]. The relationship between coefficient of friction (COF, μ), and viscosity (η), load (W) and sliding speed (U) can be represented graphically by a Stribeck curve [**61**] where COF is plotted against the dimensionless parameter ($\eta U/W$). **Figure 2. 10** [**59,62**] shows a modified Stribeck curve which

plots COF against the film thickness ratio (λ) defined as the ratio between effective film thickness (h_{min}) to composite surface roughness (r^*).

2.1.4.2 Lubricants and additives

The lubricating system of an automotive engine performs several tasks: it holds an adequate supply of oil to cool, clean, lubricate, and seal the engine. The lubricant or the engine oil is delivered from a reservoir to where it is necessary. The lubricating system should also be capable of removing contaminants from the oil and delivering the oil to all required areas. Most of the contacting surface within an automotive engine comes into contact with the engine oil. Today's automotive engine oils are specially formulated and contain many additives to fulfill several purposes [**63**], such as: (i) friction and wear reduction, (ii) prevention of rust and corrosion, (iii) lubrication without foaming, (iv) cooling of the engine components it flows on, (v) keeping the components clean, (v) small particle suspension and carrying them to the oil filter.

Based on functions performed, lubricant additives can be grouped into three categories [**64**]: (i) surface protective additives, (ii) performance additives, and (iii) lubricant protective additives. Antiwear or extreme pressure modifier, anticorrosion and rust inhibitor, detergent and dispersant, and friction modifier are grouped under surface protective additives. Pourpoint depressant and viscosity index improvers are classified under performance additives. Antioxidant, antifoamant, and other additives are called lubricant protective additives. Among all these additives, zinc dialkyldithiophosphates (ZDDPs) are the most important additives, which act as antiwear or extreme pressure additive and anticorrosion and rust inhibitor additive. ZDDP is an organometallic compound having four sulphur atoms coordinated to one zinc atom, which is in a tetrahedral sp3 hybridized state. The molecular structure of ZDDP is shown in **Figure 2. 11** [**60**].

2.1.5 Lubricated sliding of Al-Si alloys

2.1.5.1 Tribological behaviour of Al-Si alloys in lubricated sliding

In the literature, although many studies were performed on dry sliding of Al-Si alloys, lubricated sliding investigations of Al-Si alloys is rather scarce considering their application in the engine block. In this subsection, lubricated sliding wear behaviour of Al-Si alloys in the presence of engine oil [**65-74**] and other organic liquids [**75-77**] will be briefly reviewed. Timmermans and Froyen [**65**] studied the wear behaviour of a forged hypereutectic Al-17Si-5Fe-3.5Cu-1.1Mg-0.6Zr P/M alloy to be used as a connecting rod against hardened steel in the presence of SAE 15W50 engine oil. The authors conducted pin-on disc tests under boundary lubrication condition at 150 °C and also at room temperature with no lubrication for comparison. The authors showed that in the presence of the lubricating oil, a stable wear condition was reached after an initial running-in period where the friction was higher than the stabilized region. Characterization of the worn surface showed the presence of ingredients of the lubricating oil in isolated dark region of the worn counterface and rarely on the Al-Si samples; however based on the increase in contact resistance, the authors claimed that a surface layer was formed due to a tribo-chemical reaction between the additives in the oil used and the substances of mainly the steel specimens and for a minor instance of the Al–Si specimens. Das and Biswas [**66**] have found similar improvement in wear behaviour of an Al-12.26% Si alloy when a drop of SAE 20W40 engine oil was added to the sliding contact without further replenishment. The authors said that the improvement in the wear behaviour was due to the formation of a surface layer or mechanically mixed layer adherent to the alloy surface which kept the sample and the counterface separated.

In another study, Das et al. [**67**] had shown the benefit of etching to expose silicon particles during lubricated sliding of a hypoeutectic Al-10% Si alloy. Pin-on disc tests were

conducted with the etched alloy surface against AISI 52100 steel ball in the presence of SAE 5W30 engine oil. The authors showed that upon etching to expose the silicon particles, surface hardening was achieved, and plastic deformation in the aluminum matrix was initiated at a much higher load than what was observed in unetched alloy. **Figure 2. 12a and b** [**67**] show the 3D optical profilometer image and a 2D cross sectional profile of the wear track in unetched alloy, and **Figure 2. 12c and d** [**67**] show the same in etched alloy, respectively at 5.0 N load and after 500 laps of sliding. It is observed from this figure that under identical conditions, the etched alloy showed less damage in the matrix. Using an analytical contact model, the authors showed that the normal load applied during sliding was distributed over a larger area in etched alloys than would be in unetched alloy. Das et al. [**68**] also conducted the unidirectional lubricated sliding wear tests of an unetched Al-13% Si alloy against a flat pin made of molybdenum containing high speed tool steel over a load range of 1-100 N using engine oil. The authors studied the transition in wear rates and found three different regimes: ultra-mild wear, mild wear, and severe wear. The authors reported that the wear rate in ultra-mild wear regime was close to the resolution of the profilometer with which the wear rate was measured, and that the wear rate was insensitive to increase in normal contact pressure (1- 10 MPa); in mild wear, the wear rate increased slowly with normal contact pressure (10-70 MPa), and in severe wear, the wear rate increased nonlinearly with the normal contact pressure (>70 MPa).

Some researchers [**69-71,73,74**] had studied the lubricating effect of zinc dialkyldithiophosphate (ZDDP) on the wear behaviour of Al-Si alloys. The results of such studies were contradictory and not conclusive. Wan et al. [**71**] investigated the effect of ZDDP concentration in the base oil on sliding of bearing steel against A2024 aluminum alloy using an oscillating friction and wear apparatus. The authors reported that ZDDP is not effective in reducing friction at any concentration, whereas the wear resistance is the same as that for the

base oil up to 1% concentration, and an increase in wear rate occurred at 5% ZDDP concentration. The authors concluded that at higher concentrations, wear rate increased due to the corrosive chemical reactions between the additives and aluminum. Later, Neville et al. [**74**] reported similar results for cast iron and Al-23% Si alloy tribosystems in a POD configuration.

Kawamura and Fujita [**69**] and many other researchers later [**70,72,73**] had found that addition of ZDDP to the base oil improved the performance of paraffinic base oil and also improved the wear resistance of the A390 (Al-18% Si) alloy compared to the performance of other phosphate and phosphide additives which were also studied. The authors [**69**] provided indirect evidence to suggest that under boundary lubricant conditions, the ZDDP molecules polymerize at the surface and therefore impart firm protection to the metal substrate. Konishi et al. [**70**] had studied the wear behaviour of A390 aluminum alloy against itself using a POD-type configuration under fully flooded condition. The authors used hydrocarbon-based fluids such as mineral oils or poly-α-olefins containing 2 wt.% ZDDP and polar base fluids such as polyol esters or polyalkylene glycols as lubricants. The study showed that mineral oils exhibited better wear-protecting property and higher load-carrying capacity than polar base fluids.

Hu et al. [**75**] studied the tribological behaviour of Al-12% Si alloy against itself in the presence of four different lubricants such as ethyleneglycol, ethanolamine, ethylenediamine, and triethylenetetramine to investigate the antiwear function of organic groups such as $–NH_2$, –OH, and the combination of $–NH_2$ and –OH. The authors used FT-IR, XPS, and thermal gravimetric (TG) analysis to characterize the wear surface and found that the triethylenetetramine had the best antiwear performance, and among the other three, ethanolamine and ethylenediamine exhibited better performance than ethyleneglycol. Qu et al. [**76**] synthesized two categories of ionic liquids with imidazolium and ammonium cations and tested them with Al6061-AISI52100 tribosystem using a reciprocating ball-on-disc apparatus and

benchmarked against two conventional hydrocarbon oils, mineral oil, and 15W40 diesel engine oil. Out of eight imidazolium-based and five ammonium-based liquids, the best performance was observed in $[C_8H_{17}]_3NH{\cdot}Tf_2N$, which provided significant friction reduction in the entire lubrication regime, from elastohydrodynamic to boundary lubrication, compared to the fully-formulated 15W40 engine oil; no adhesion of aluminum to the counterface was observed. The authors also found that a mixture of mineral oil with 10% ionic liquid in volume produced lower wear than either the base oil or the neat ionic liquid. Later in another study, Qu et al. [**77**] studied the performance of the same ammonium-based ionic liquid [C8H17]3NH·Tf2N for three different aluminum alloys (aluminum 1100, 6061, and 319 alloys) against steel. The wear tests performed using the reciprocating ball-on-disc wear tester showed that in the presence of the ammonium-based ionic liquid, up to 35% reduction in friction and up to 55% reduction in wear were achieved compared to the 15W40 engine oil.

2.1.5.2 Tribolayer formation and characterization in lubricated sliding

As reviewed earlier, tribo-layer formation was observed and reported in almost all studies concerning dry sliding behaviour of Al-Si alloys in MW and UMW region. In this section, a review will be presented to understand the tribo-layer or tribofilm formation in lubricated sliding of Al-Si alloys against steel counterface using engine oil or its main additive, ZDDP, as a lubricant.

The characterization of the tribofilms formed on Al-Si alloy surface was carried out using XPS and X-ray absorption near-edge structure (XANES). Fuller et al. [**72**] first characterized the formation of a tribofilm formed on 6061Al alloy and A390 aluminum alloy in the presence of 1.2 wt.% ZDDP containing MCT-10 base oil. The wear tests were conducted on a Cameron-Plint high frequency wear tester with the same counterface as that of the alloy. The authors used a comparative study of P L-edge and S L-edge XANES of the tribofilms generated on the samples,

and pure ZDDP and zinc metaphosphate to find the molecular nature of the tribofilm and also of a thermal film formed on A390 alloy by decomposing ZDDP at high temperatures. Based on the study, the authors concluded that the tribofilm consisting of a zinc polyphosphate and zinc sulphide was identical to those formed on hardened steel. Similar findings were observed by Nicholls et al. [**78**] in their study to investigate the tribofilm formation in two different Al-Si alloys (6061 Al and A319) against either a steel counterface or with the same counterface under boundary lubrication using mineral base oil with 1.2 wt.% ZDDP additive. Using the P L-edge and P K-edge spectra obtained from XANES experiments, the authors showed that the tribofilm contained a zinc polyphosphate glass, phosphide, linkage isomer, and the unreacted ZDDP. It was also shown that the amount of polyphosphate increased with increase in sliding time in the case of A319/AISI 52100 steel couple, and the amount of linkage isomer species and the unreacted ZDDP decreased. In 6061/AISI52100 couple, the amount of phosphide was much higher than the amount of phosphate. The high wear in both alloys during the running-in period was associated with an increase in phosphide formation and the authors suggested that the nascent aluminum exposed during the sliding process was responsible for the formation of phosphide.

Nicholls et al. [**79**] also carried out another study on A390 alloys running against steel using a reciprocating cylinder-on-block tribometer (Cameron-Plint) at boundary lubricated region using 1.2 wt.% ZDDP containing MCT-10 base oil. The authors used, in addition to XANES, X-ray photoelectron emission microscopy (X-PEEM) and the nanoindentation techniques to characterize the tribofilms formed on A390 alloy surface and then compared the tribofilm formed under similar conditions on a steel surface. The authors concluded that the tribofilm formed on A90 alloy was bilayer structured with longer-chain polyphosphates at the surface and shorter-chain phosphates in the bulk closer to the Si-tribofilm interface. X-PEEM analysis

showed that the tribofilm formed on both aluminum and silicon surfaces, and the films on both surfaces consisted of zinc polyphosphate. However, authors suggested that the antiwear pads were formed mainly on silicon, and the silicon carried the load but not the matrix. Nanoindentation measurements of the antiwear pads formed on silicon suggested that the indentation modulus ($E_S^* = \frac{E_S}{(1-\nu_S^2)} = 50 - 65\ \mathrm{GPa}$) was lower compared to that formed on steel (110±8 GPa).

Later, Pereira et al. [**80,81**] also studied the tribofilm formation in chemically etched Al-25% Si alloy [80] and unetched Al-10.5% Si (A383) alloy [**81**]. The tribofilm was generated by conducting wear tests on reciprocating cylinder-on-block tribometer at boundary lubricated region using 1.2 wt.% ZDDP containing MCT-10 base oil. The authors varied difference experimental parameters, such as the etching time of sample surface to expose silicon particles, sliding time, test temperature, applied loads, and ZDDP concentration in the base oil and used similar characterization techniques used by Fuller et al. [**72,73**] and Nichollas et al. [**78,79**] to identify the composition of the tribofilm. **Figure 2. 13** [**80**] shows the P L-edge XANES spectra of three different tribofilms generated under different conditions: 30 min. sliding time (tribofilm A), 200 °C (tribofilm B) and 700 min. sliding time (tribofilm D). In this study the authors deconvoluted the P K- and L-edge XANES spectra to find the polyphosphate chain length and found that tribofilm formed after longer sliding time consisted of longer chain polyphosphates, whereas that formed at higher temperatures consisted of shorter chain polyphosphates. Also at higher temperatures, the tribofilm had sulphates along with other minor sulphur containing compounds. Using X-PEEM coupled with EDX mapping, the authors also showed that the longer chain polyphosphates were formed on silicon surfaces, and shorter chain polyphosphates mixed with unreacted ZDDP were found on the aluminum surfaces. The

study using unetched Al-10.5% Si (A383) [**81**] alloys generated similar findings on tribofilm composition.

Xia et al. [**82**] and Jiménez et al. [**83**] studied the formation of tribofilm on Al-16-18% Si alloy slid against cast iron (BS EN1452 CI) and AISI 52100 steel plate under boundary lubrication in the presence of ZDDP containing oil and ZDDP, and ZDDP and molybdenum dithiocarbamate (MoDTC) mixture containing oil. The authors found that the presence of MoDTC reduced friction and wear of the Al-Si samples and formed a continuous tribofilm on the worn surface, consisting of Al, Si, Zn, P, S, O, and C species due to the interaction of additives with Al–Si alloys. Based on SIMS and XPS analysis, Jiménez et al. [**83**] reported the absence of Al in the top layers of the tribofilm; in the presence of 0.8% ZDDP, this top layer was mainly composed of Fe from the steel pin, and Zn, as well as a mixture of sulphides and phosphates. Adding MoDTC in the lubricating oil, the composition of this top layer was found to be a mixture of phosphates and MoS2.

Recently, Mahato et al. [**84**] studied the lubricated sliding of an etched Al-Si alloy against steel using POD instrument. The authors conducted XPS studies within the wear track and found formation of various polyphosphates within the wear track. The authors suggested that the nascent steel chips formed by abrasion of the counterface by silicon particles assisted the decomposition of ZDDP to yield friction modifying chemical products.

2.1.5.3 Mechanisms of tribofilm formation in presence of ZDDP

Research work to understand the mechanism of tribofilm formation in the presence of ZDDP containing oil began in the 1950s after the lubrication industry realized its potential as an antiwear additive [**85**]. Unfortunately even today no unified mechanism has been established in the literature. The main function of ZDDP is to reduce wear and oxidation. In his literature review article, Spikes [**85**] summarized from the literature different stages of ZDDP behaviour as shown in **Figure 2. 14**. Accordingly ZDDP, when in solution, can exhibit three different types of

chemical reaction on steel surfaces: ligand exchange, antioxidant activity, and thermal degradation.

Spikes [**85**] showed that in the ligand exchange process, due to the labile nature of dithiophosphate ligands, the zinc cation was exchanged by another metal cation such as Fe or Cu to form metal dialkyldithiophosphates (MDDP) according to the following reaction:

$$((RO)_2PSS)_2Zn + M^{2+} \rightarrow ((RO)_2PSS)_2M + Zn^{2+}$$

The above reaction could take place in the solution or at metal oxide surfaces. Dithiophosphates acted as metal extraction agents and the relative order of extraction for various cations were established as follows [**86**]:

$$Pd^{2+} > Au^{3+} > Ag^{+} > Cu^{2+} > Fe^{3+} > Pb^{2+} > Ni^{2+} > Zn^{2+}$$

so that cations to the left would displace the cations to the right from MDDP. Thus the ligand exchange plays a very important role in the antiwear property of ZDDP.

Kennerly and Patterson [**87**] and Colclough and Cunneen [**88**] reported that ZDDPs acted as anitoxidants because of their ability to decompose hydroperoxides and peroxy-radicals. According to Al-Malaika et al. [**89**], when ZDDPs reacted with these hydroperoxides and peroxy-radicals, they generated effective oxidation inhibitors – the source of antioxidizing property of ZDDP. However, when ZDDPs decomposed to peroxide, the generated compounds from those reactions were not able to form effective zinc phosphate antiwear films. Furthermore, ZDDPs are very effective metal deactivators, and they prevent releasing of pro-oxidant metal ions into the oil. The pro-oxidant metal ions usually catalyze redox reactions, but the zinc cations are relatively harmless and can stay in the liquid phase [**85**]. Thus it is better to replace the pro-oxidant metal ions by zinc cations in the oil.

Thermal degradation mechanisms of ZDDP were established by Jones and Coy [**90**]. The essence of the thermal degradation was the exchange between O and S in ZDDP molecules with

the alkyl groups, which were initially bonded to O atoms in ZDDP being transferred to the S atoms. The reactions of this thermal degradation effectively aimed at replacing P-S, P=S, and C-O bonds by C-S bonds, P-O, and P-O bonds; the final product being a polyphosphate. The thermal degradation occurs in the absence of hydroperoxides and peroxy-radicals in the temperature range between 130 and 230 °C.

From this survey, it is emphasized that the exact nature of tribofilm formation in the presence of ZDDP is very complex, and all studies to understand the mechanisms of tribofilm formation were conducted on steel surfaces. There is no direct evidence that these mechanisms would still be valid for Al-Si surface.

2.1.6 Ultra-mild wear (UMW)

The wear of engine block must be a very slow process. Over the typical life of the engine of 1.5×10^5 km with average vehicle speed of 50 km/h, the acceptable limit of increase in the cylinder bore diameter is less than 50 μm. Accordingly, the material removal rate is calculated to be few nm/hr, and Al-Si alloys to be used as alternative engine block materials to cast iron in the automotive industry should also satisfy this condition. To simulate such wear rate and the operating mechanisms under lubricated sliding condition, the new terminology *ultra-mild wear* was coined [**91**], although the first use of this term was found in dry sliding of Al-Si alloy based composite by Wilson and Alpas [**44**]. The authors studied the sliding wear behaviour of a silicon carbide (SiC) reinforced A356 aluminum alloy under dry sliding conditions, and the wear rate in the UMW regime was of the order of $\approx 10^{-5}$ mm^3/m. Study of UMW in Al-Si alloys under lubricated sliding condition has been a fairly new area of research. In the literature, two complementary types of studies were reported to understand the origin of wear resistance of Al–Si alloys used for automotive engine blocks. Some researchers conducted laboratory wear tests [**67,92-94**] using different contact configuration in lubricated condition at different

temperatures. Other studies [**95-99**], aimed at the post-mortem approach where the cylinder wall surface from an engine ran in engine dynamometer, were characterized thoroughly using various techniques.

2.1.6.1 Laboratory studies

The literature on laboratory studies on UMW of Al-Si alloys is very limited. Chen et al. [**92-94**] studied the mechanics and mechanisms of UMW for five different Al-Si alloys at room temperature using a POD configuration under boundary lubrication. In their first study, Chen et al. [92] investigated the role of matrix hardness in maintaining the UMW for eutectic and near eutectic AL-Si alloys. In this study Al-11% Si and Al-12% Si alloy having matrix hardness of 68.0±12.5 HV10 and 40.0±8.3 HV10, respectively, was tested against the AISI 52100 steel at 0.5 N normal load. The alloys had comparable particle size and morphology. **Figure 2. 15a** [**92**] shows the change in silicon particle height with sliding distance, and **Figure 2. 15b** and **c** [**92**] show the optical profilometer images of the wear track after 5×10^4 sliding cycles for Al-11% Si and Al-12% Si alloys. The authors showed in this study [**92**] that in Al-12% Si alloy with lower matrix hardness, scratch marks on the aluminum matrix were seen after 5×10^3 sliding cycles, and silicon particles were embedded in the matrix completely after 5×10^4 sliding cycles. However, in Al–11% Si alloy with higher matrix hardness, early fracture of silicon particles were seen after 104 sliding cycles, and then embedding of silicon particles were observed. The estimation of contact pressure showed that the Al–12% Si alloy, with matrix hardness 0.60 times the maximum contact pressure, had a larger degree of particle sinking-in than Al–11% Si, where the matrix hardness was 1.03 times the maximum contact pressure.

In another study, Chen et al. [**93**] studied the UMW of a hypereutectic Al-18.5% Si alloy containing large block-like primary silicon particles and compared the behaviour with Al-12% Si alloy. Lubricated sliding wear tests were performed at 0.5 N load for up to 6×10^5 sliding cycles. It

was shown that the surface damage in Al-18.5% Si alloy was limited to formation of a few scratch marks on the top surface of the large silicon particles even after 6×10^5 sliding cycles. But in Al-12%Si alloy, extensive damage consisting of particle sinking-in, aluminum pile-up formation, as well as particle fragmentation was observed. **Figure 2. 16a** and **b** [**93**] show the change in particle height with sliding cycles in Al-18.5% Si and Al-12% Si alloys and surface damage in Al-18.5% Si alloy after 6×10^5 sliding cycles. The particle height in Al-18.5% Si alloy remained unchanged throughout the sliding process without damaging the aluminum matrix. Estimating the real contact pressure applied, adapting Greenwood Tripp multi-asperity model [**100**], it was rationalized that silicon particles carried the applied load because the applied contact pressure (834 MPa) was lower than the matrix hardness (715 MPa). From this study [**93**] it was inferred that the microstructure of Al–18.5% Si was more effective in maintaining the original microstructure in UMW region with the minimum amount of damage on the contacting surface.

Chen et al. [**94**] also studied the mechanics and micromechanisms of UMW in Al-25% Si alloy with the matrix hardness of 108±20 HV10 and compared them with those of an Al-11% Si alloy having comparable particle size and morphology but with much lower matrix hardness. The two alloys had small, well distributed silicon particles with aspect ratios of 1.60±0.20 and 1.70±0.15, respectively. The authors conducted lubricated sliding wear tests in the presence of 5W30 engine oil at 3 different loads of 0.5, 1.0, and 2.0 N for different sliding cycles up to 6×10^5 sliding cycles. The authors in this study evaluated the damage to silicon particles, measured the wear in aluminum matrix by profilometry, and explored the role of an oil-residue layer formation. This study showed that the ORL, which was supported by the sliding deformation induced ultra-fine grain aluminum matrix, stabilized the wear rates in both alloys after prolonged sliding despite the different initial matrix hardness and silicon percentage. **Figure 2.**

17a and **b** [**94**] shows a cross sectional image showing ORL on the surface and formation of UFG aluminum in the subsurface region, and volumetric wear loss with sliding cycles in Al-11% Si in comparison with Al-25% Si showing stabilization of wear loss in both alloys, respectively. The ORL consisted of amorphous carbon mixed with aluminum oxide and degraded lubricating oil additives.

In their analytical model, Chen et al. [**92-94**] have adopted the Greenwood-Tripp [**100**] multi-asperity model to estimate the contact pressure applied on silicon particles under lubricated sliding conditions. In this approach, chemically etched silicon particles were assumed as contacting asperities embedded in elasto-plastic aluminum matrix. The maximum contact pressure, P_r at the centre of the contact is expressed as:

$$P_r = \left(\frac{4}{3\pi}\right) E^* \left(\frac{\sigma}{R_p}\right) \frac{F_{3/2}(h)}{F_1(h)}\Bigg|_{r=0} \tag{2.1}$$

where E^* is the reduced elastic modulus, R_p is the particle length, σ is the standard deviation of the particle height, $F_{3/2}(h)$ and $F_1(h)$ are the parabolic cylinder functions; the general solution for such functions for Gaussian distribution can be given as:

$$F_m(h) = \left[\frac{1}{(2\pi)^{1/2}}\right] \int_h^\infty (s-h)^m \exp\left(-\frac{s^2}{2}\right) ds \tag{2.2}$$

The authors postulated the silicon sinking-in during sliding analogous to the plain strain deformation of aluminum by silicon particle considered as a rigid punch. To initiate plastic deformation in this process, the upper-bound solution to this problem according to slip line filed theory requires an indentation pressure of P=2.89Y (Y is the yield strength of the matrix in tension) – approximately the Vickers hardness of the matrix. First calculating the contact pressure using Greenwood-Tripp [**100**] model (solving **equations 2.1 and 2.2** numerically), the authors then showed that whenever the applied contact pressure, which is dependent on a composite modulus between the asperities in contact, asperity distribution and height of the

sample surface, and a parabolic cylinder function, is more than the matrices of Vickers hardness, the plastic deformation of aluminum surrounding the particles in the form of pile-up would take place.

2.1.6.2 Engine dynamometer studies

Scherge et al. [**101**] applied radionuclide technique (RNT) to measure wear continuously in combustion engine. This technique is very adaptive for measuring low wear rates as low as 0.1 nm/h or 1 µg/h. In this technique, two different continuous wear measurement methods, the concentration method and the difference method are used. In the former method, wear is measured by detecting the radiation emitted by the wear particles carried away from the worn area by a medium such as lubrication oil in the case of a combustion engine; thus, the wear is reported by the wear particle per volume of the medium. The latter method is used when no medium can be used to carry away the wear particles, and the wear is studied by measuring the decrease in residual activity of the irradiated machine part. Using RNT, the authors [**101**] measured the wear in a water-cooled four-cylinder diesel engine using different oils for a range of cylinder wall temperatures under hot test operations (maximum speed at full load). It was reported that at temperatures below 150 °C, the wear rate of the cylinder liner measured around the top dead center position for the top piston ring was measured to be below 500 µg/h.

Dienwiebel et al. [**95**] studied the wear of an AlSi17Cu4Mg alloy made engine bore surface which had been operated in a fired engine dynamometer test for 250 h over full speed and torque range of the engine using 5W30 fully formulated engine oil. The wear rate during the test was monitored using radionuclide-technique (RNT) [**101**], and the authors reported that the wear rate for all operating conditions was below 20 nm/h, and at partial load the wear rate was below 10 nm/h. In this study the authors reported that during running-in, a surface layer consisting of wear particles from different sources mixed into aluminum matrix was formed

which provided the wear resistance. The authors did not report any tribofilm comprising breakdown products of anti-wear additives.

Yu [**96**] performed a tribological failure analysis of a scuffed linerless Al-11% Si alloy made engine cylinder bore subjected to engine dynamometer test. Metallographic analysis of the worn surface and the subsurface damage were performed using optical and electron microscopes. The author [**96**] reported five different types of wear damage: virgin area, normal wear, burnishing wear, comet area, and severe wear, as shown in **Figure 2.18** [**96**].

Slattery et al. [**97**] had conducted a similar engine dynamometer study on a linerless eutectic Al-Si alloy made engine subjected to 300 h of high load, high speed, and high temperature running-in. The alloy had 11-12% Si along with other alloying elements like Cu, Ni, Mg, and Fe, and the bore surface was prepared mechanically without chemical etching. The authors in this study concluded that during running-in, a stable surface was developed by the combined action of polishing by the piston ring and re-deposition of polishing debris into aluminum matrix, and the bore surface wear of ≈13 nm/hr was achieved. In another study, Slattery et al. [**98**] investigated the surface and subsurface microstructure of an engine made of a similar alloy as in [**97**] subjected to an engine dynamometer test of 300 h. The alloy was chemically etched after the honing process, and the test was done with 5W30 engine oil. The study concluded that the wear resistance of linerless eutectic Al–Si engine is a synergetic effect of silicon particle exposure, oil deposits formed on matrix, and reduced grain structure in the subsurface region. In another recent study, Meng-Burany et al. [**99**] investigated the subsurface microstructure in a linerless V8 engine surface made of Al-11% Si alloy subjected to 33 h of dynamometer testing. In this study the authors also observed the formation of an oil-residue layer on the surface and ultra-fine grain in the aluminum matrix of the subsurface region after dynamometer tests.

Tomastik et al. [**102**] investigated the surfaces of Al-Si cylinder liner from an internal combustion engine using nanoindentation and XPS and also compared the results with a worn surface generated using a reciprocated wear tester at 120 °C in the presence of a diesel and engine oil mixture. The XPS study showed that the engine surface had carbon soot on the surface in addition to the elements from the Al-Si engine surface (Al, Si, Cu, and Mg) and the lubricant additives (Zn, P, S, and Ca). On the other hand, the worn surface generated using the tribometer did not have any soot.

2.1.7 Summary of UMW in Al-Si alloys at room temperature

From the literature survey presented in **Sections 2.1.5** and **2.1.6** the following summary on UMW of Al-Si alloys can be made:

1. The Al-Si alloys derived their wear resistance from hard silicon phase and a tribolayer or ORL generated during sliding. The ORL at room temperature was composed of amorphous carbon mixed with aluminum oxide and other degraded oil additives supported by ultra-fine grain aluminum layer.

2. The UMW mechanisms of Al-Si alloys at room temperature are fairly well understood. The sequence of damage events were categorized into three stages. In the first stage (UMW-I), there was no wear of aluminum, and silicon particles in this stage sunk-in in the matrix. In the second stage (UMW-II), the wear of piled-up aluminum started to wear, and the volume loss could be detected. In stage-III, an ORL protected the aluminum surface, and decrease in wear loss was observed.

3. The laboratory studies and dynamometer studies showed that the eutectic Al-Si alloys can be a potential replacement of the expensive hypereutectic Al-Si alloys and cast iron liners.

However, some outstanding issues needed further investigation:

1. The effectiveness of the ORL at longer sliding cycles and at elevated temperature, in other words, the durability of this layer in maintaining UMW was not reported.

2. All studies pertaining to UMW region have been conducted at room temperature. The UME mechanisms of Al-Si alloys at elevated temperatures were not studied and require investigation.

3. The composition and mechanical properties of the ORL at elevated temperature need further attention.

TABLES – CHAPTER 2

Table 2. 1: Typical chemical composition in (wt.%) of selected commercial Al-SI alloys [26].

Alloy	% Si	% Cu	%Fe	%Mg	%Mn	%Ni	%Ti	%Zn
319	5.5-6.5	3-4	1.0	0.1	0.5	0.35	0.25	1.0
A356	6.5-7.5	0.2	0.2	0.25-0.45	0.1	-	0.2	0.1
A380	7.5-9.5	3-4	1.3	0.1	0.5	0.5	-	3
383	9.5-11.5	2-3	1.3	0.1	0.5	0.3	-	3
332	11-13	1.5-3.0	1.2	0.5-1.5	0.5-1.5	0.5-1.5	0.25	1.0
A390	16-18	4-5	0.5	0.45-0.65	0.1	-	0.1	0.2

Table 2. 2: Typical mechanical and physical properties of selected commercial Al-Si alloys [26].

Alloy	Mechanical properties				Physical properties	
	UTS, MPa	Yield strength, MPa	% Elongation	Hardness, Brinell	CTE, µm/mK	Thermal Conductivity, W/mK
319	186	124	2	70	21.6	0.27
A356	159	83	6	-	21.4	0.36
A380	324	159	4	75	21.1	0.26
A390	179	179	<1	85	18.5	0.32

FIGURES – CHAPTER 2

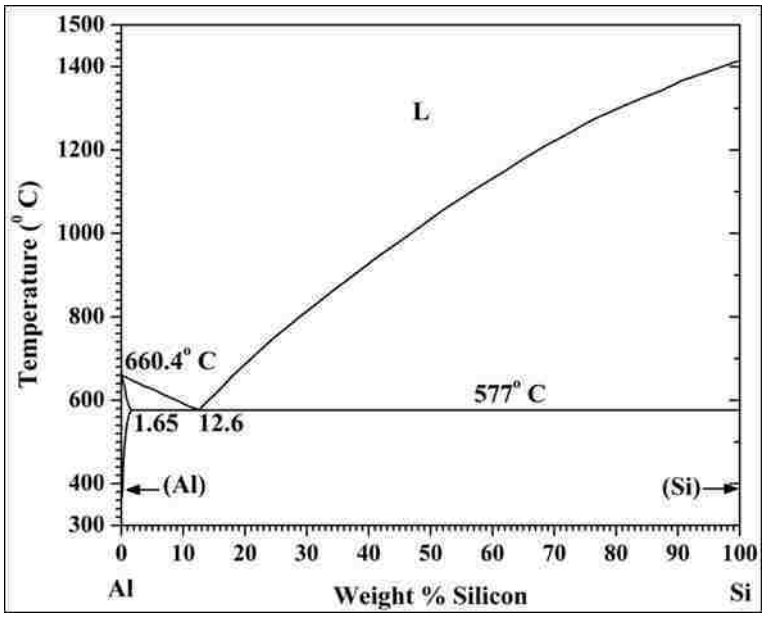

Figure 2. 1: Aluminum-Silicon binary phase diagram [27].

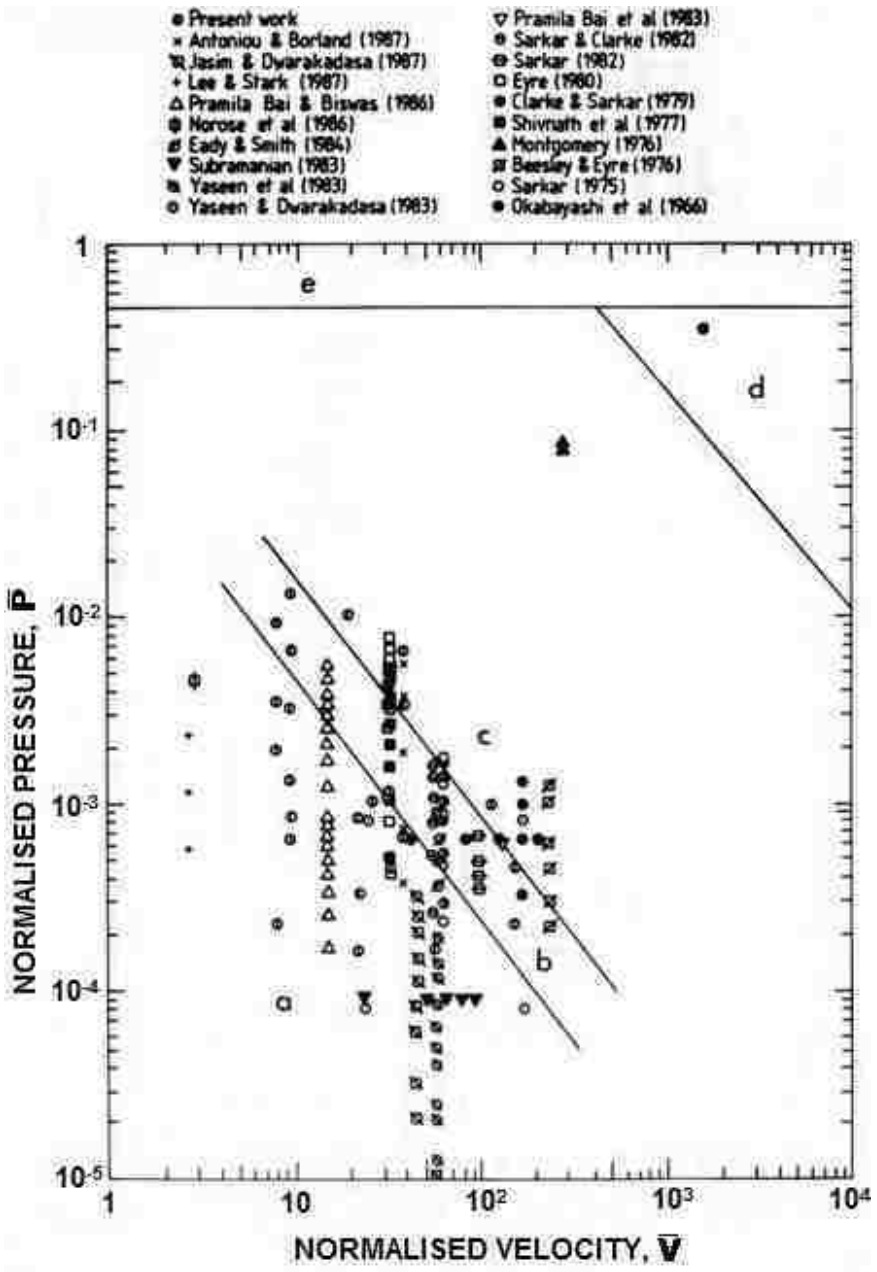

Figure 2. 2: Wear mechanism map for aluminium alloys [39].

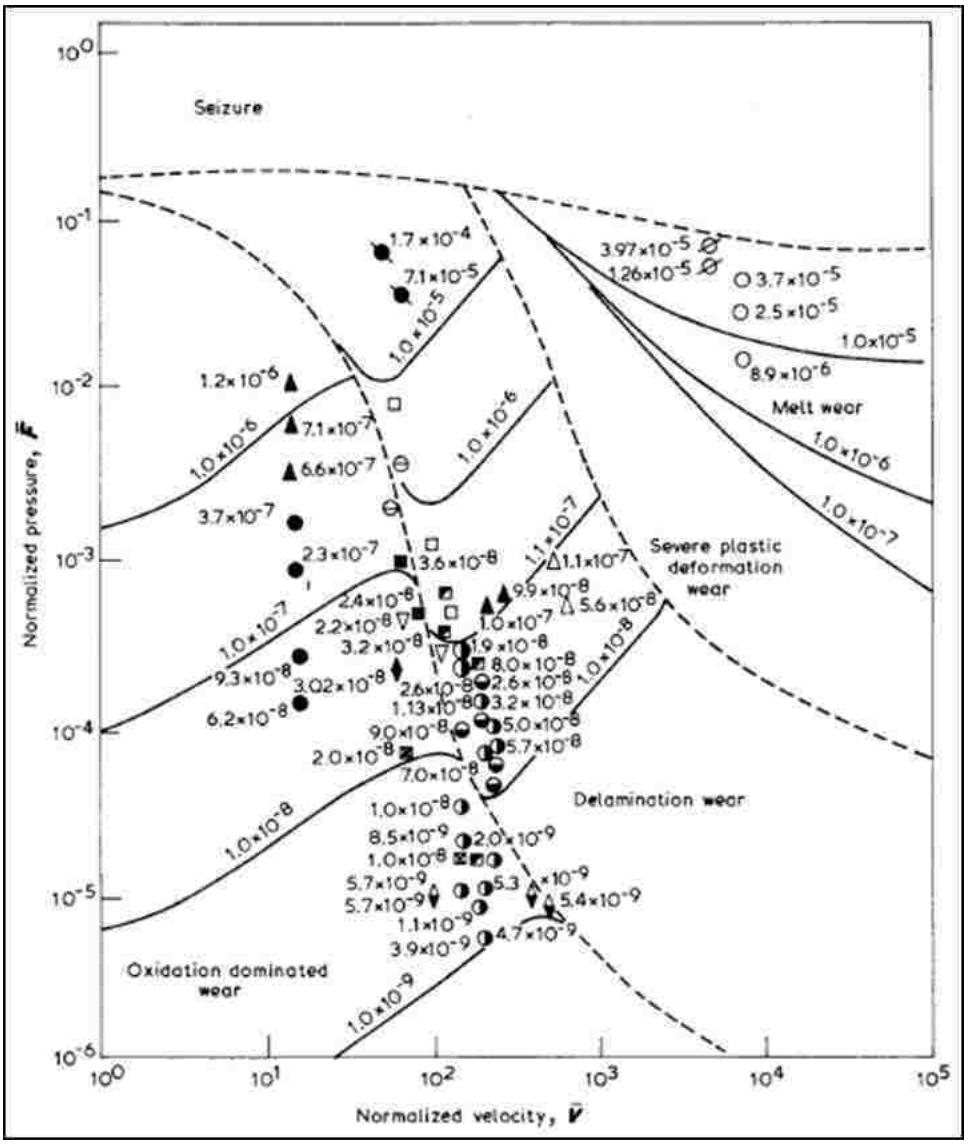

Figure 2. 3: A map for wear mechanisms in aluminium alloys. The numbers in the figure represent normalized wear rate, $\overline{W} = W/A_n$, where W is the wear rate in m^3m^{-1} and $A_n(m^2)$ is the nominal area of contact [41].

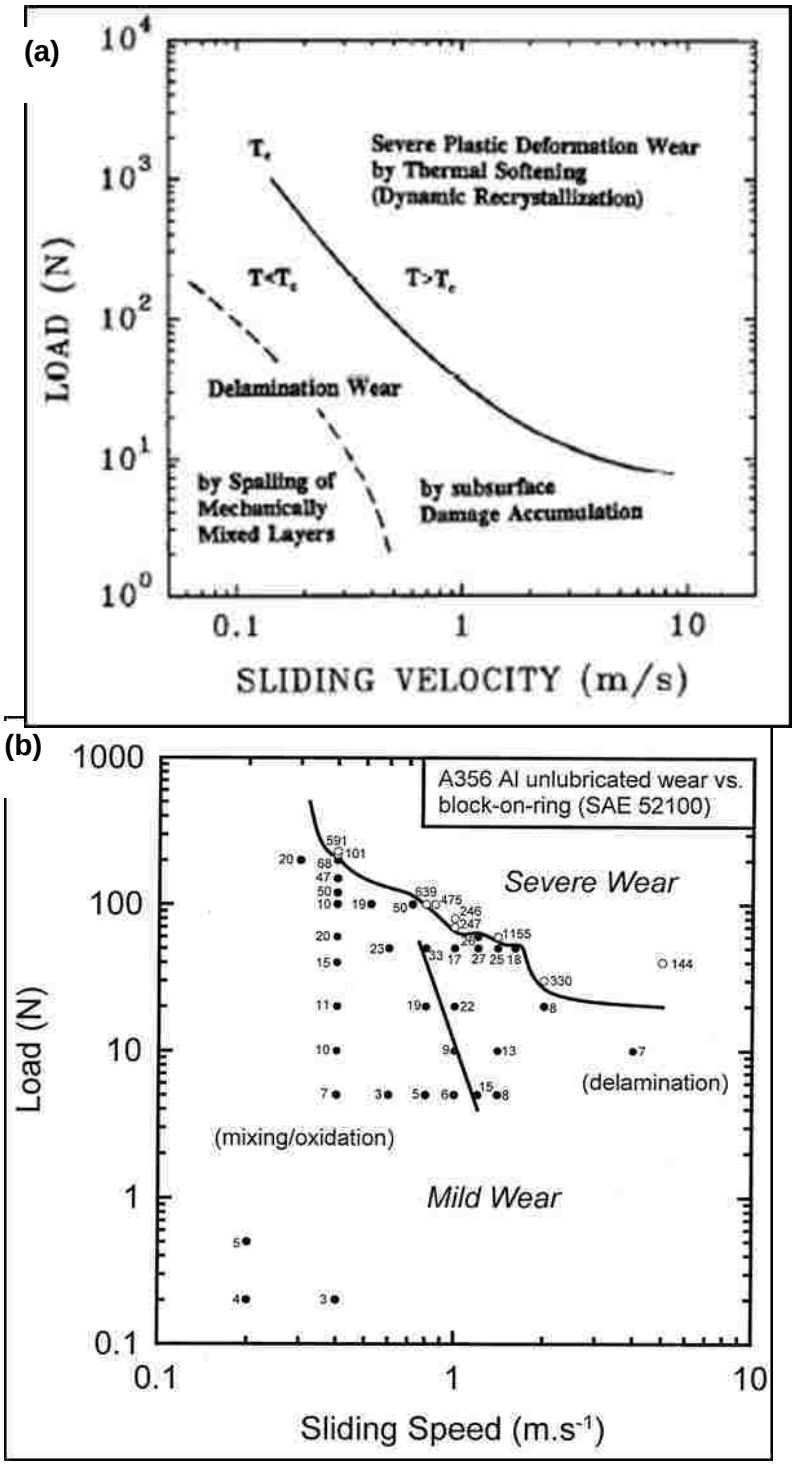

Figure 2. 4: (a) Wear mechanism map for aluminium alloys. The dotted line between the two mechanisms in the mild wear delineates load and velocity conditions where the wear debris consists of 50% plate-like and 50% mechanically mixed particles [43]; (b) Wear rate map for A356 Al worn against SAE 52100 steel counterfaces. The wear rates shown on the diagram have been multiplied by 10^4 mm^3 m^{-1} [44].

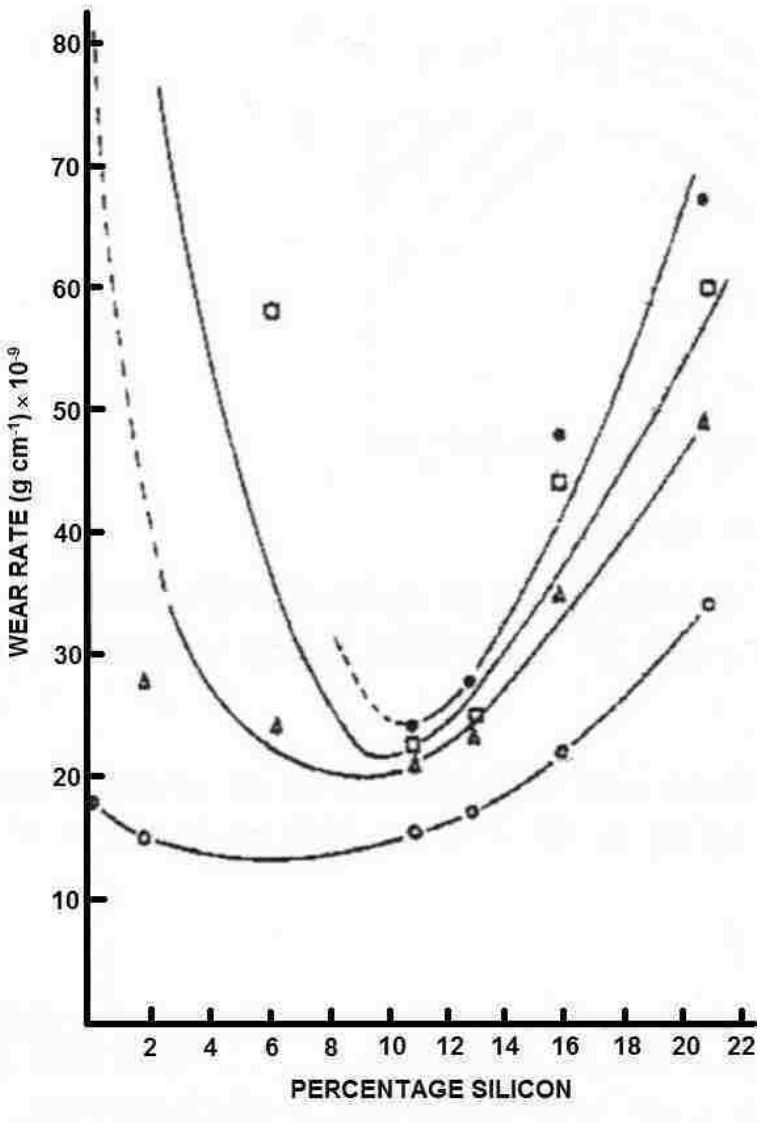

Figure 2. 5: Variation of wear rates of aluminium alloys sliding against a hard steel bush with silicon content. Loads: o, 1 kg; Δ, 1.5 kg; □, 2 kg; •, 2.5 kg [3].

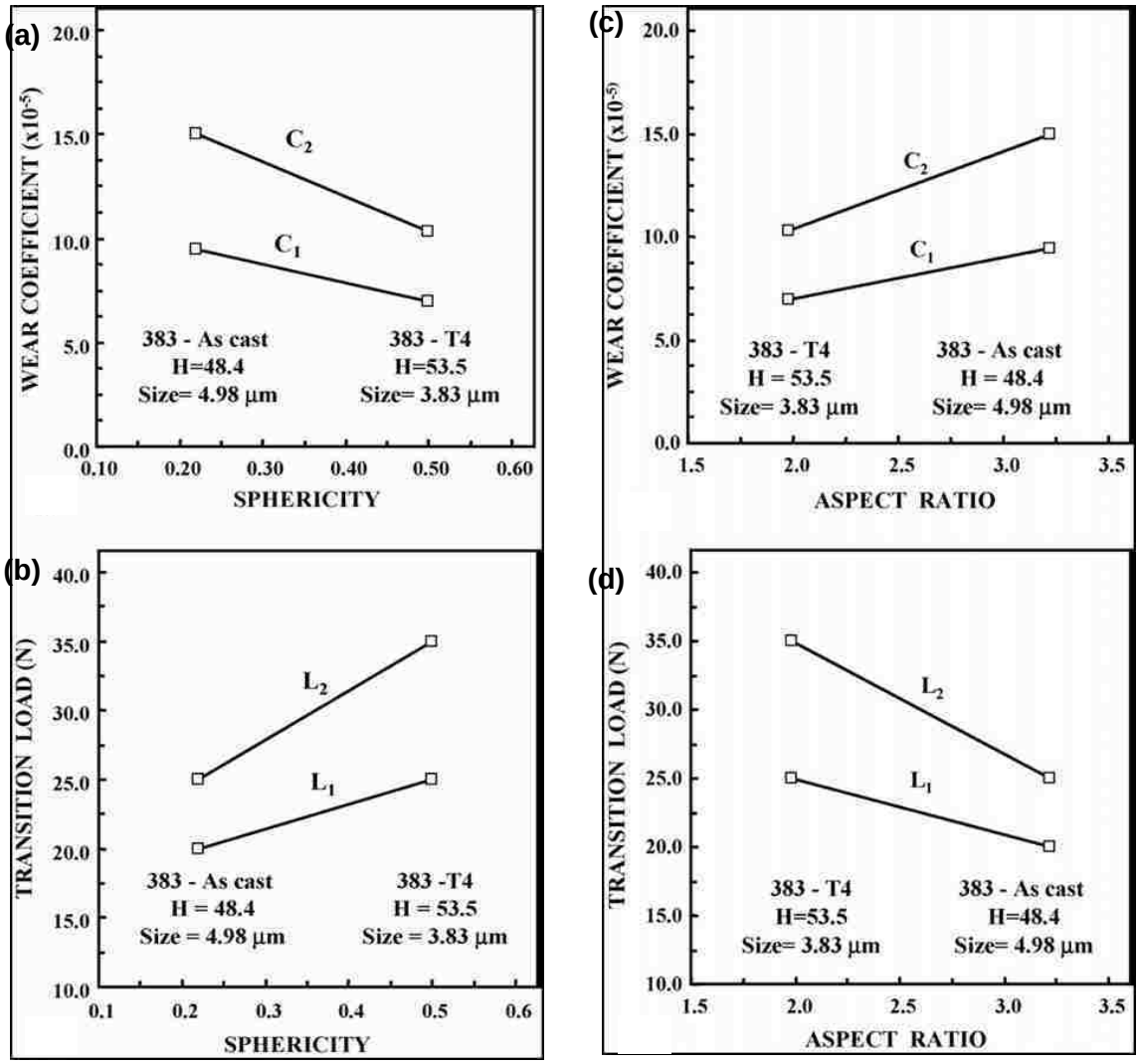

Figure 2. 6 Effect of Si particle shape (sphericity) on (a) wear coefficients, and (b) transition loads (383-as-cast vs. 383-T4); and Effect of Si particle shape (aspect ratio) on (c) wear coefficients, and (d) transition loads (as-cast of 383 vs. 383-T4) [12].

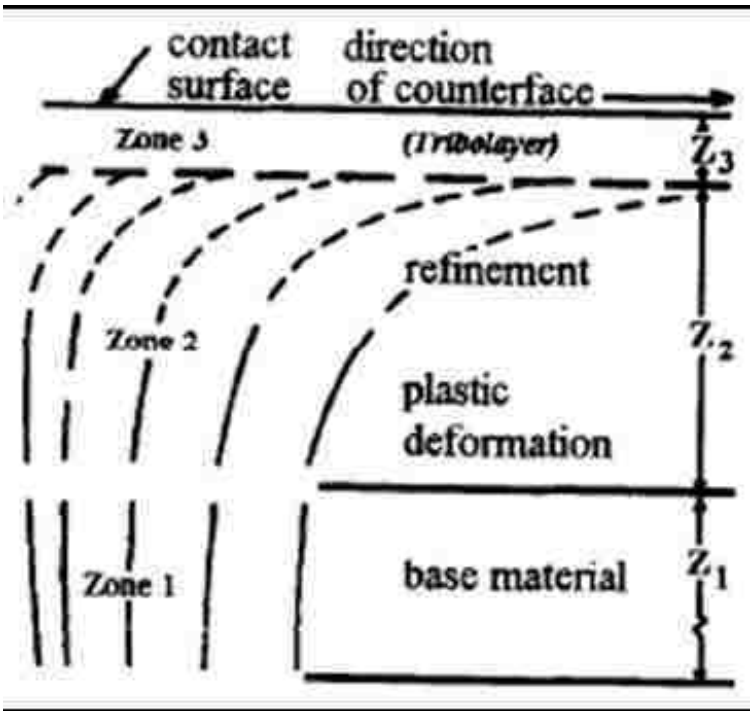

Figure 2. 7: Schematic diagram of subsurface zones found beneath wearing surfaces, modified from Rice et al. [58] by Deuis et al. [Deuis 1997]

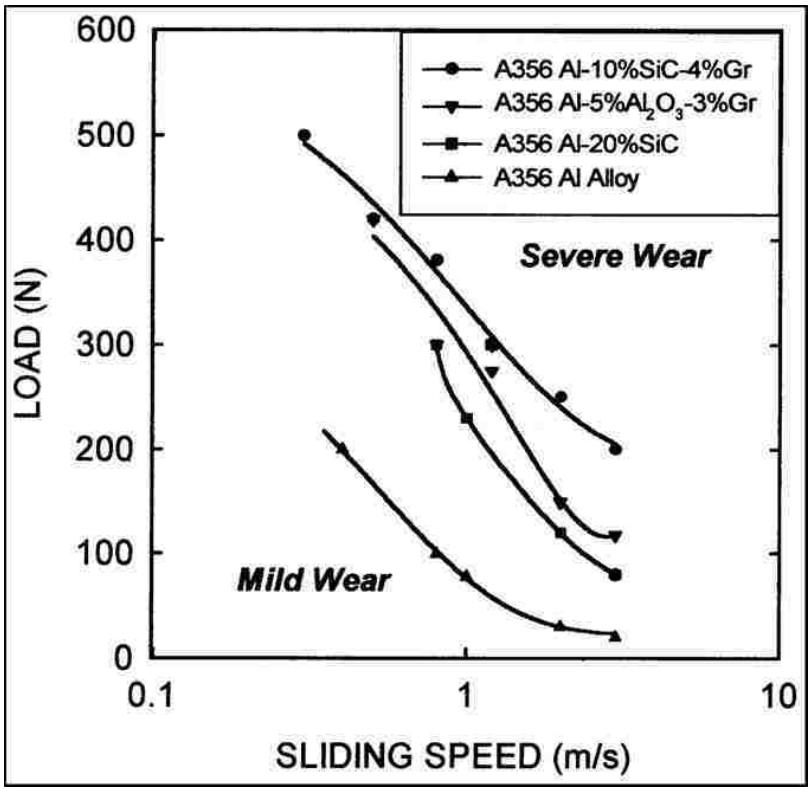

Figure 2. 8: Comparison of the mild-to-severe wear transition boundaries of the graphitic A356 Al–10% SiC–4% Gr and A356 Al–5% Al_2O_3–3% Gr composites with those of the non-graphitic composite A356 Al–20% SiC and the unreinforced matrix A356 Al alloy [8].

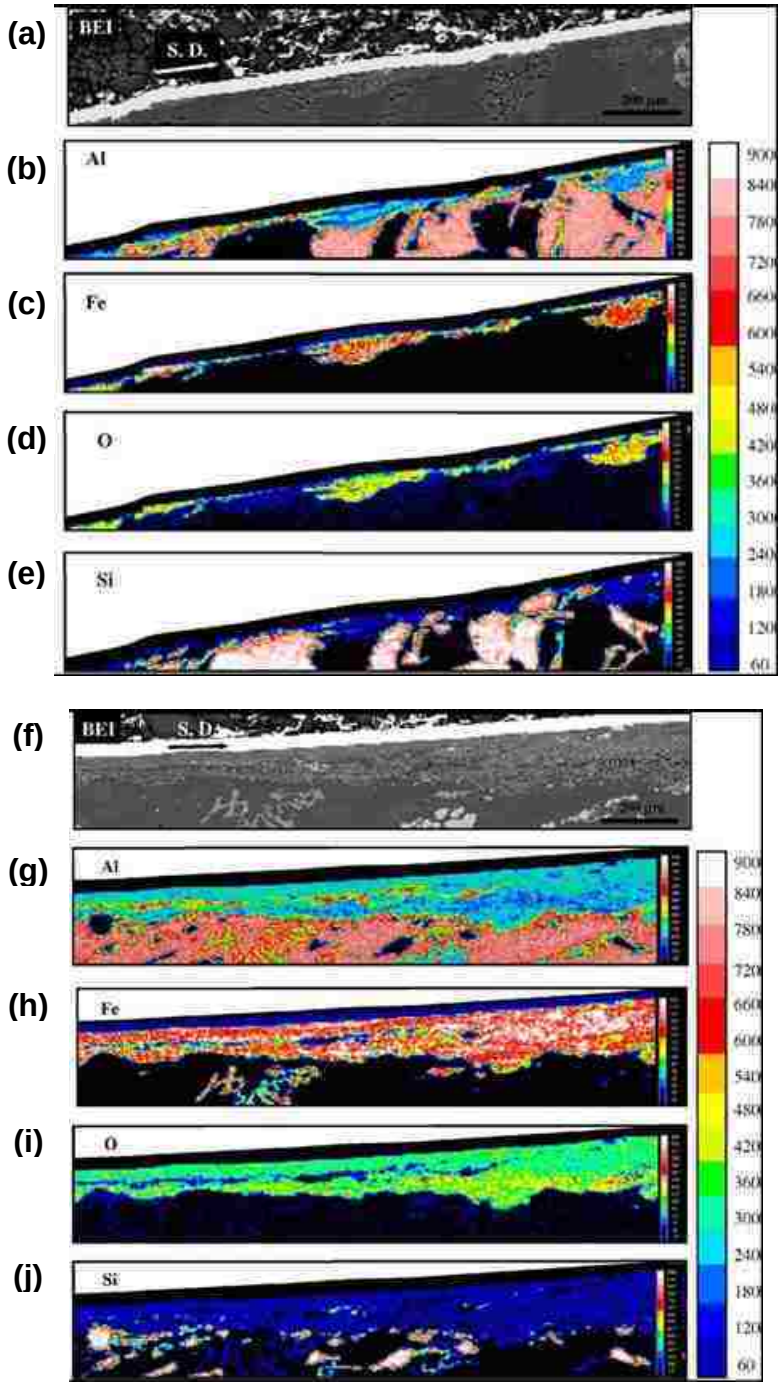

Figure 2. 9: EPMA maps of the cross-sections below the worn surfaces at 10 N - (a) back-scattered SEM image of the area mapped, (b) Al, (c) Fe, (d) O, and (e) Si; and at 60 N - (f) back-scattered SEM image of the area mapped, (g) Al, (h) Fe, (i) O, and (j) Si [10]. Figures a-e show the tribo-layer at MW-I and f-j show the tribo-layer at MW-II regimes.

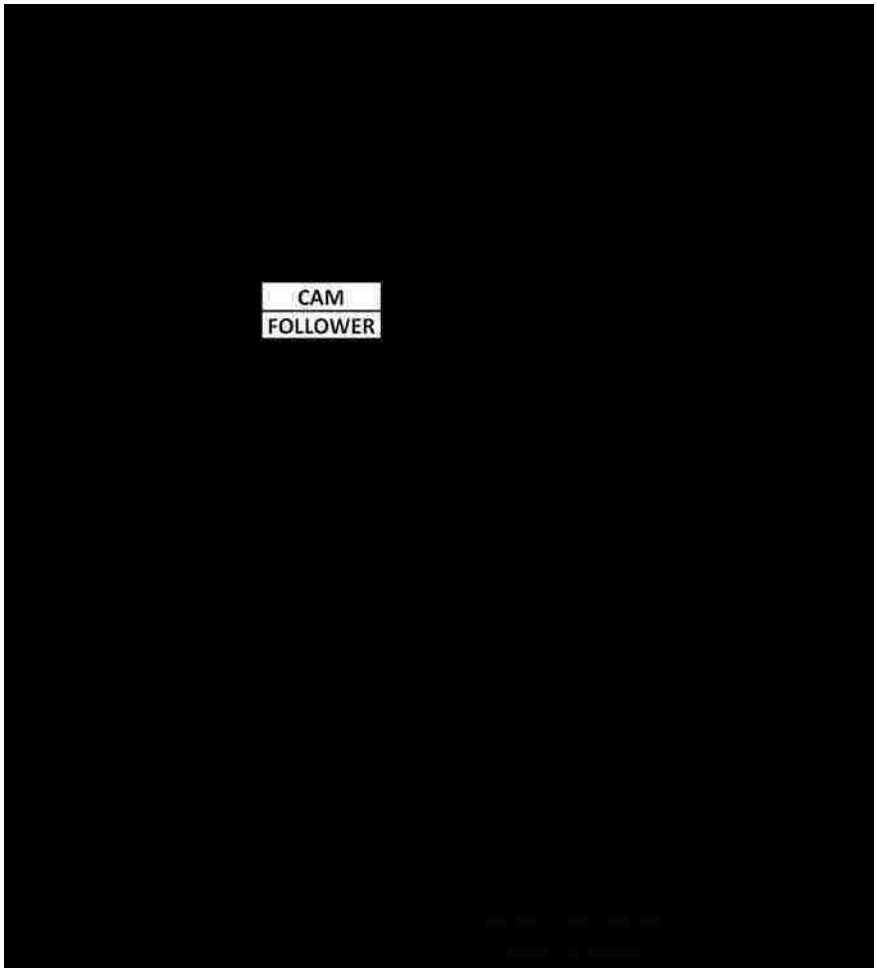

Figure 2. 10: The modified Stribeck diagram [59,62]. The x-axis is changed to film thickness ratio instead of dimensionless parameter ($\eta U/W$)

Figure 2. 11: Structure of ZDDP [60].

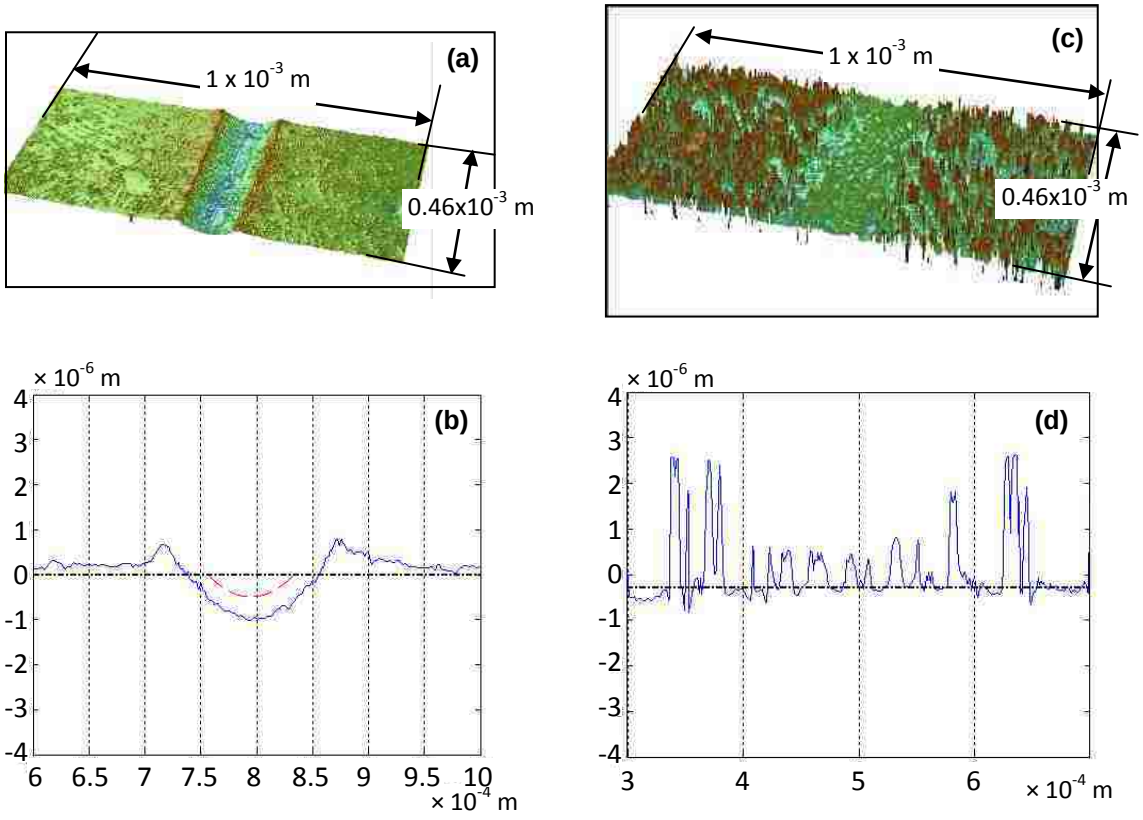

Figure 2. 12: 3D profilometric rendering of the lubricated slid surface of (a) polished and unetched (roughness=0.04 µm, RMS) aluminium–silicon alloy; (b) 2D profile of the cross section normal to the sliding direction seen in (a). 3D profilometric rendering of the lubricated surface of (c) etched (roughness=1 µm, RMS); (d) 2D profile of the cross-section normal to the sliding directions of grooves seen in (c) At load = 2.0 N and after 500 laps of sliding cycles [67].

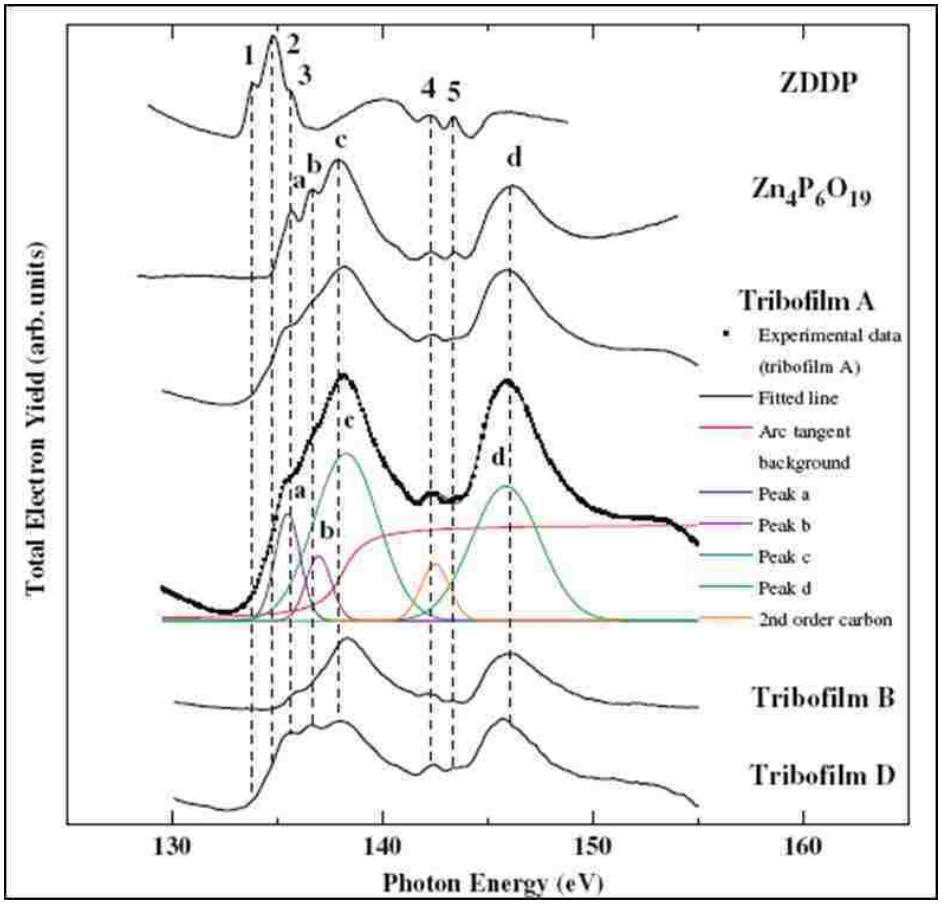

Figure 2. 13: Phosphorous L-edge XANES spectra of unreacted ZDDP, model compound Zn4P6O19, and three tribofilms. An example of peak fitting for tribofilm A performed on the P L-edge data to determine the relative peak heights pf peaks a, b, and c is included. Tribofilm B was made at 200 °C and tribofilm D was rubbed for 720 min [80].

Figure 2. 14: Main stages of ZDDP behaviour [85].

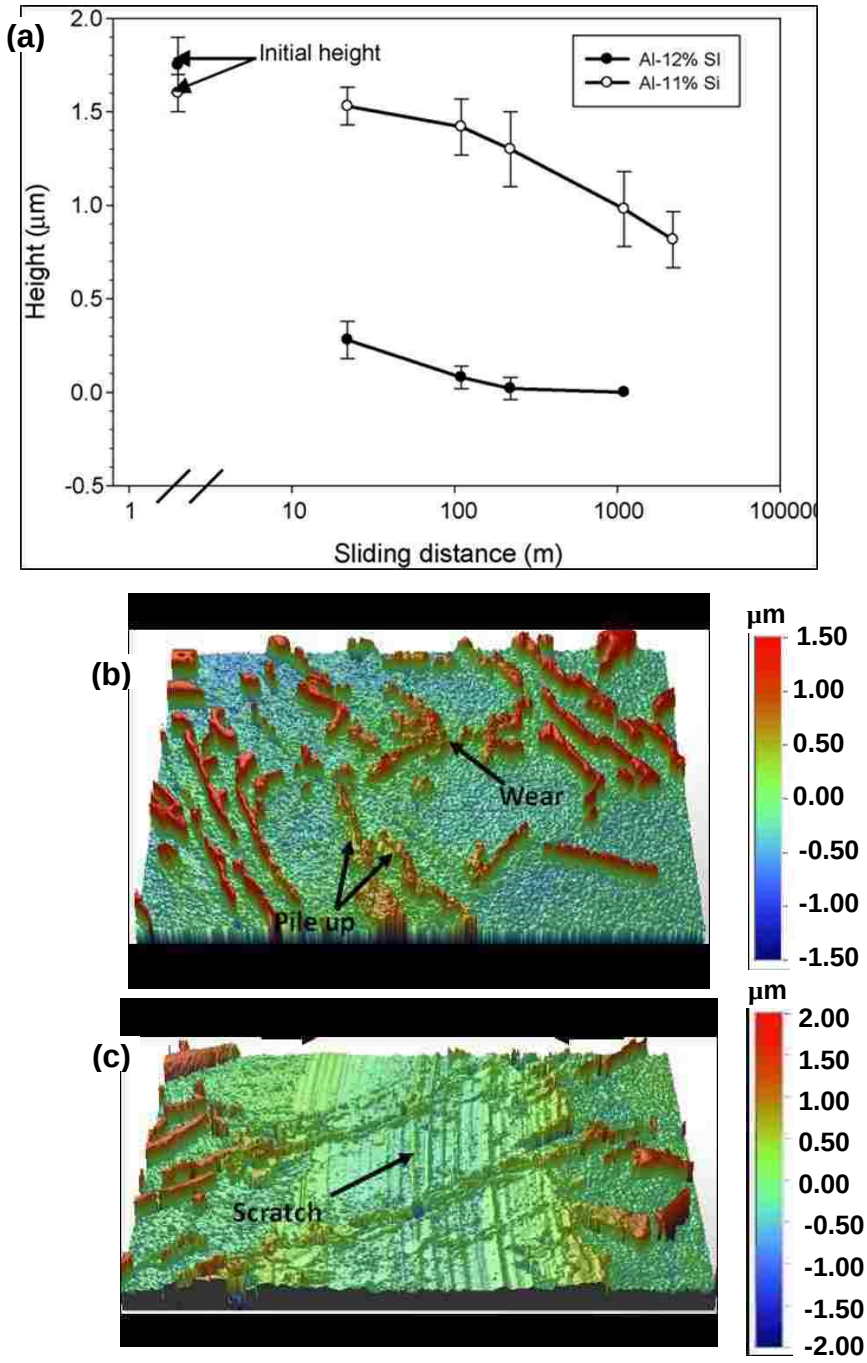

Figure 2. 15: (a) Change in the silicon particle height projected above the aluminum matrix with the sliding; 3D surface profile image showing the surface damage in (b) Al–11% Si alloy; (c) Al–12% Si alloy, after sliding to 1.1×10^3 m [92].

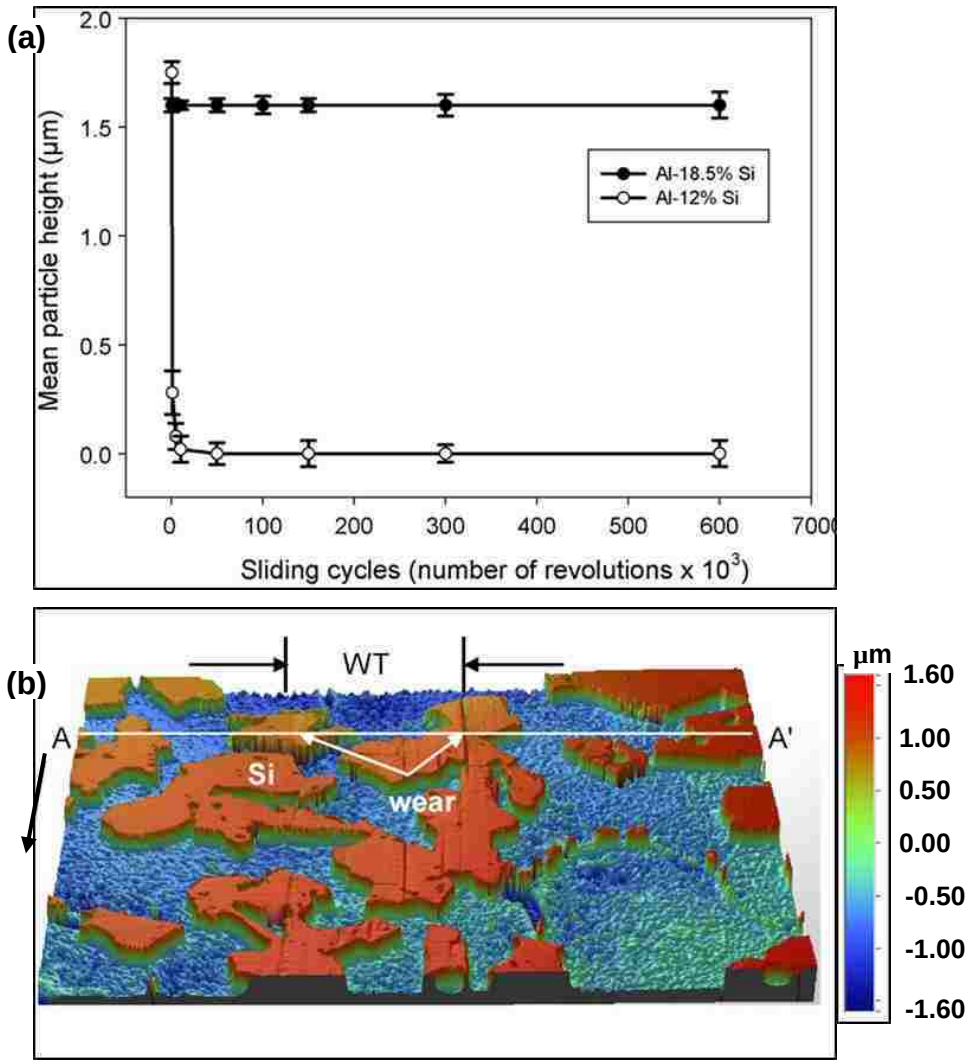

Figure 2. 16: (a) Variation of the mean silicon particle height with sliding cycles. Silicon particle elevation does not change with sliding distance in Al–18.5% Si (full circles), but an abrupt decrease after sliding to 103 cycles was observed in Al–12% Si (open circles); (b) 3-D optical surface profile image of Surface damage in Al–18.5% Si after sliding to 6×10^5 cycles [93].

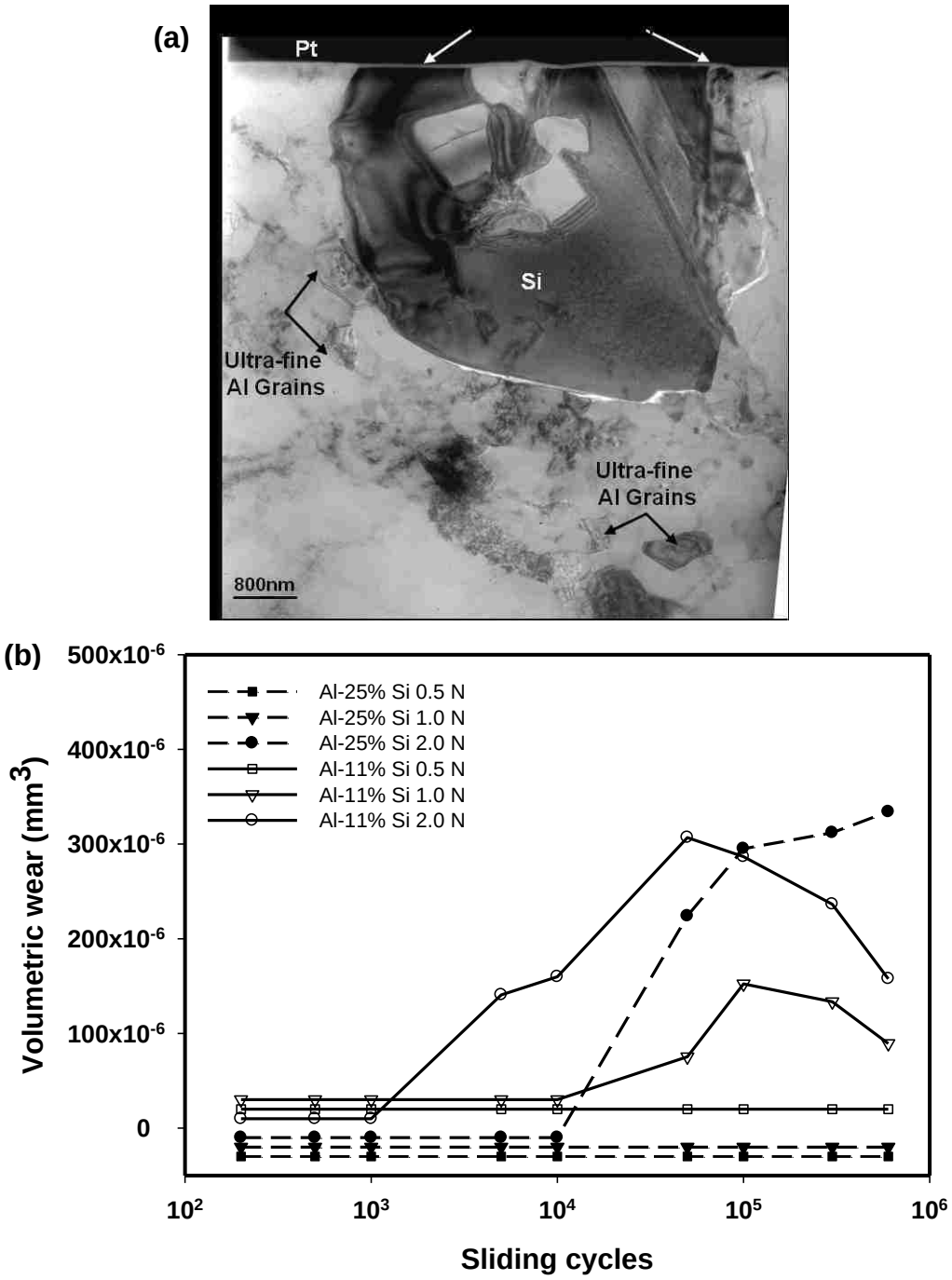

Figure 2. 17: Cross-sectional TEM image of the microstructure of the material under the wear track showing ultra-fine aluminum grains around the silicon particle and the oil residue layer in Al-25% Si alloy; (b) Variation of volumetric wear with sliding cycles in Al–11% Si in comparison with Al–25% Si. (All plots with zero volumetric loss were shifted vertically for clarity) [94].

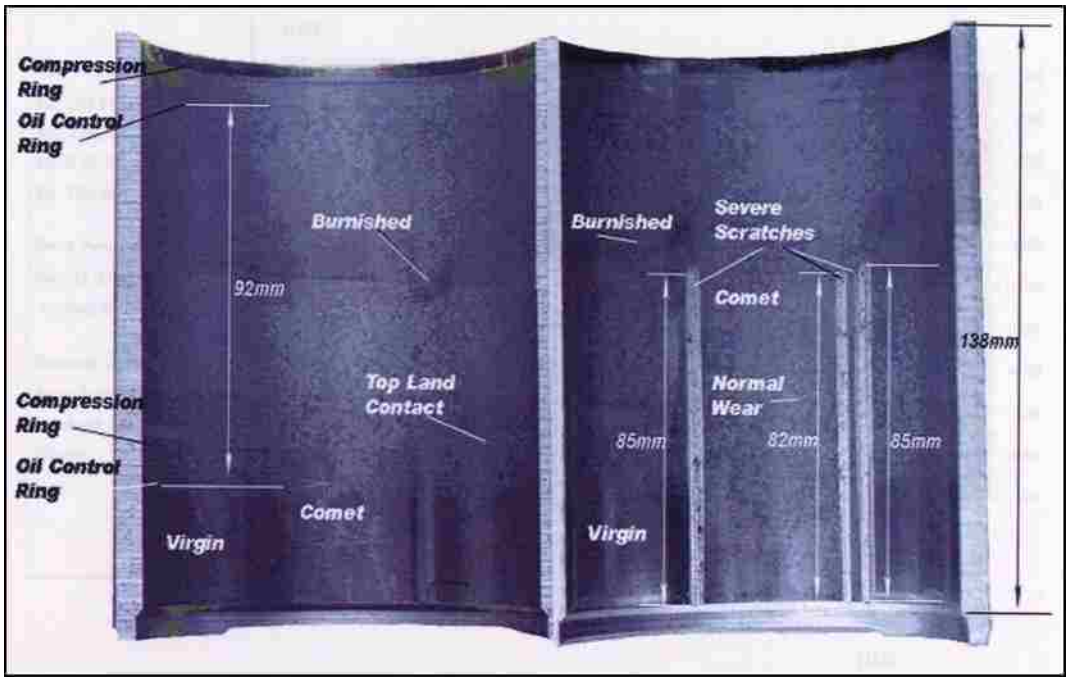

Figure 2. 18: Stereographic photos of the two major and minor surfaces with the indications of different wear types [96].

3. CHAPTER 3 – MATERIALS AND EXPERIMENTAL METHODS

3.1 Introduction

In this chapter, microstructure, hardness (matrix and particle) of the Al-Si alloys used will be reported. The details on surface preparation techniques prior to wear tests, wear testing technique, profilometer data analysis technique to measure the particle height before and after wear tests and to measure aluminum pile-up height after wear tests will be described. The worn surfaces were also characterised by nanoindentation technique and various x-ray and electron based spectroscopic techniques such as XPS, EDX and XANES. FIB ion milling was used to prepare cross sections and longitudinal sections of the wear track and subsurface microstructure was observed both in SEM (within the focused ion beam (FIB) workstation) and TEM. The details of these sample preparation and observation techniques will also be described in this chapter.

3.2 Al-Si alloys used in the study

Three different Al-Si alloys were used in this study. These alloys compositions are listed in **Table 3. 1**. The Alloys were received from General Motors Research and Development, Warren, MI, USA and were used as received. Al-12.6% Si alloy was a eutectic sand cast alloy in T7 heat treat condition. Al-18.5% Si alloy (A390) was a sand cast hypereutectic alloy and Al-25% Si alloy was a spray cast alloy .The silicon amount is always expressed in weight percentage.

3.2.1 Sample preparation to observe and quantify the microstructure

The alloys as received microstructure was prepared by the metallographic technique employing emery grinding with 180, 240, 400, 600, 1200 and 2400 grit silicon carbide emery

papers followed by cloth polishing using diamond suspension of 3.0 µm, 1.0 µm and 0.1 µm. The microstructure was then observed using a high resolution and high depth of field digital optical microscope (Keyence VHX 600) attached with image analysis software. The silicon particles aspect ratio was then calculated by measuring the length and the width of particles from randomly chosen field of view. In this measurements the longest dimension of the particles were considered their length and the dimension perpendicular to its length was considered their width. The aspect ratio of the particles was defined by the ratio of the length to the width of the particles.

3.2.1.1 Microstructure of Al-12.6% Si alloy

The microstructure of Al-12.6% Si alloy is shown in **Figure 3. 1a.** From this figure it is observed that this alloy had long and acicular silicon particles with various intermetallic phases, such as $Al_{15}(FeMn)_3Si$ and Ni_3Al. The silicon particles length and width was measured from approximately 500 particles and **Figure 3. 1b and c** shows the histogram of the particle length and width, respectively. The average length and width of the silicon particles in this alloy was 46.8±24.5 µm and 5.9±2.6 µm, respectively. Thus the aspect ratio of these particles was calculated to be 7.8.

3.2.1.2 Microstructure of Al-18.5% Si alloy

The microstructure of Al-18.5% Si alloy is shown in **Figure 3. 2a**, wherein the various phases of the alloy are identified. Primary silicon particles are block-like polygon shaped while the eutectic silicon phase is elongated needle shaped. Among the other phases observed were $CuAl_2$, $Al_{15}(Fe,Mn)_3Si_2$ and $Al_5Mg_8Cu_2Si_6$.

Silicon particle size (length, width and aspect ratio) analysis was done for both primary and eutectic silicon particles together. **Figure 3. 2b and c** shows the histograms of the length

and width of the silicon particles measured. The length and width was measured in a mutually perpendicular direction. The average length and width of the silicon particles were 41.7±27.0 μm and 19.7±14.8 μm, therefore, the average aspect ratio of the silicon particles was 3.2. In this measurement, 460 silicon particles were considered. The silicon particle area density was also measured at 500X magnification using the optical microscope. This was done with nine different measurement areas on the same sample. The average silicon particle area density was measured to be $7.6\times10^4\pm1.0\times10^4$ μm^2 out of the total area of 2.9×10^5 μm^2.

3.2.1.3 Microstructure of Al-25.0% Si alloy

Al-25.0% Si alloy samples were obtained from a liner of Mercedes engine block. The optical microstructure of Al-25% Si alloy is shown in **Figure 3. 3a**. This alloy had a uniform distribution of small silicon particles and other intermetallic phases. The average length and width of silicon particles in this alloy was 7.9±2.3 μm and 5.4±1.6 μm, respectively. The intermetallic phases in this alloy were $CuAl_2$ and $Al_5Mg_8Cu_2Si_6$. **Figure 3. 3b and c** shows the silicon particles length and width histogram of this alloy measured from approximately 500 silicon particles.

3.2.2 Hardness of the alloys

The Brinell hardness of the alloys were measured used a Brinell hardness tester with a 10 mm tungsten carbide indenter at 500 kg load and the Vickers hardness of the alloys' matrix were measure using a Vickers diamond pyramid indenter mounted in Buehler Micromet II® (Model 1600-9000) microhardness tester at 10 gf load. The Brinell and microhardness of the alloys tested are listed in **Table 3. 2**.

3.3 Lubricated wear testing method

Lubricated wear tests were performed to achieve UMW in Al-Si alloys under laboratory conditions. The choice of appropriate experimental conditions was based upon examination of the microstructure of the worn surface by SEM and TEM, rather than attempting to set external parameters. Conditions were selected to produce similar microstructure in previous tests **[95-99]** to that found in the relevant automobile engine surface. The sliding cycles were varied to produce the lowest detectable wear rate in the test lasting for a few hours to few days. In this section, details of lubricated sliding wear tests and other relevant information on surface preparation techniques, counterface materials and lubrication method will be provided.

3.3.1 Surface preparation of Al-Si alloys

All testing surface of the Al-Si alloys were polished using standard metallographic techniques employing emery grinding and then cloth polishing up to 0.1 μm diamond suspensions. The polished sample surfaces were then chemically etched by dipping the sample in the etchant to create a surface texture by protruding silicon particles out of the aluminum matrix. The etchant used was freshly prepared 10% NaOH (sodium hydroxide) solution by mass and the etching time was 120-180 s. The solution was continuously stirred during etching. Immediately after etching, the sample surfaces were neutralised by dipping the samples in a 50% nitric acid (by volume) solution for 10 s and then rinsing the sample thoroughly using water. The sample was then ultrasonically cleaned in acetone/hexane for 2 min. prior to testing to remove any loosely adhered particles and to achieve the best possible clean surface. Silicon particles height after etching was also measured using optical profilometry (see **Section 3.4.1.1)**.

Previous research work has shown the effect of etching the aluminum matrix on dry **[54]** and lubricated sliding **[67]** of Al-Si alloys. The general finding was that etching improved the

wear behaviour. However, over-etching may result in the easy detachment of particles from the matrix during sliding, thereby reduction of scuffing resistance as shown by Riahi et al. **[54]**. Care was taken during the surface preparation by adhering the etching procedure exactly such that over-etching could be completely avoided. The etching procedure was carried out for 180s which was established through various trials and each sample was inspected prior to the wear tests to confirm the silicon particles height was in between 1.6-1.7 µm.

3.3.2 Lubricated wear testing

The lubricated wear testing was carried out using a CSM Instruments Inc. made high temperature pin-on-disc (POD) wear tester equipped with friction transducer to measure COF continuously. The built-in heater and two ANSI type K thermocouples in the instrument were used to control the temperature of the heater and the sample during tests and a separate cooling circuit was used to cool the relevant areas of the tribometer. **Figure 3. 4** shows a 3D schematic of the testing configuration. The ball holder was connected to an elastic arm, which controlled the upward and downward motion of the ball holder through the software. A cylindrical holder, mounted on the rotating shaft which was connected to a motor controlling the rotational speed of the shaft was used to hold the sample. The sample was held in a fixed position by a top mounted ring with three screws. The holder was filled with sufficient quantity of the lubricant and then mounted with the sample on the top base of the shaft with a cylindrical ring fixed with screws. The wear testing parameters are listed in the **Table 3. 3**.

3.3.3 Static counterface material and surface preparation

The counterface in all wear tests was an AISI 52100 steel ball with 6 mm diameter. The composition of the steel in wt.% is as follows: 0.98-1.1 % C, 0.25-0.45 % Mn, 0.15- 0.30 % Si, 1.30-1.60 % Cr, <0.025% S, <0.025% P and the remainder is Fe. The hardness of the steel ball

measured using a vicker's indenter at 25 gf load to be 710±15 HV_{25}. These steel balls were commercially procured and cleaned in hexane to remove the rust protection oil. Then they were polished using 0.1 µm diamond suspension after mounting in the ball holder. During polishing the ball holder was held and rotated in such a way that the flattening of the ball was prevented.

3.3.4 Lubrication method and lubricant

The lubricant used was commercially procured Mobil1 5W-30 grade fully formulated synthetic engine oil. Approximately 8-10 ml of the oil was added to the holder for each test and thus the sample was fully immersed when the holder was stationary. Typical properties of the lubricant are given in **Table 3. 4**.

To evaluate the lubrication, the ratio (λ) of minimum lubrication thickness (h_{min}) over the composite r.m.s surface roughness (r^*) of the two contacting surfaces was calculated. The oil film thickness at the start of the experiment was estimated using [**103**] the following equation:

$$h_{min} = 1.79R^{0.47}\alpha^{0.49}\eta_0^{0.68}U^{0.68}(E^*)W^{-0.07} \tag{3.1}$$

where, R is the radius of the ball, U is the sliding speed, W is the normal load applied, and α and η_0 are viscosity constants of the lubricating oil. They are related to each other by the following relationship [**103**]:

$$\alpha \approx (0.6 + 0.965 \log_{10} \eta_0) \times 10^{-8} \tag{3.2}$$

E^* is the composite Young's modulus of the contact system calculated using the following equation:

$$\frac{1}{E^*} = \left[\frac{1-(\nu_{Al-Si})^2}{E_{Al-Si}} + \frac{1-(\nu_{Steel})^2}{E_{Steel}}\right] \tag{3.3}$$

where, E_{Al-Si}, Young's modulus of Al-Si, is calculated using $E_{Al-Si} = E_{Si}w_{si} + E_{Si}(1 - w_{si})$; w_{si} is the weight fraction of the silicon phase in the alloy and ν_{Al-Si} is Poisson's ratio of Al-Si alloy. The r.m.s surface roughness (r^*) of the two contacting surfaces was calculated using $r^* = \sqrt{r_{ball}^2 + r_{particle}^2}$; $r_{particle}$ and r_{ball} are the r.m.s roughness of the Si particle carrying the load and the steel ball. It should be noted here that since the silicon particles are the contacting asperities at the beginning of the wear tests, to calculate the composite roughness of the contact bodies r.m.s roughness is taken in the equation and not the surface roughness of the alloy itself. It may be noted that during the sliding process the alloy surface roughness decreased due to loss in initial texture, but the surface roughness of the counterface increased nullifying any significant change in r^*. Also the sliding velocity, load, and the viscosity parameters of the lubricating oil did not change during the test. The change in E^* can only reduce the h_{min} and the increase in effective radius of the counterface due to wear was not significant enough to change the value of minimum lubrication thickness (h_{min}) throughout the test. Thus the ratio, λ, was always less than 1.0 indicating that tests were conducted in boundary lubrication regime.

During the wear tests, the radius of the ball (R) and the sliding speed (U) was constant, but the test temperature, alloy properties and the normal load was varied. Accordingly the minimum oil thickness varied with the viscosity of the oil (**equation 3.1**), which is a function of temperature. The calculated film thickness (h_{min}), the surface roughness (r^*) and the film thickness ratio (λ) for various testing conditions are listed in **Table 3. 5**. Since the ratio (λ) was less than 1.0, it was concluded that the wear tests were conducted in boundary lubrication condition.

3.4 Surface and subsurface damage observation and characterisation

Various techniques were used to investigate and quantify the surface damage during wear testing. Three important surface damage parameters such as, silicon particle height, aluminum pile-up height and volumetric wear loss were measured using white light interferometer. The evolution of surface morphology and sequence of damage events were investigated using optical microscope, white light interferometer and scanning electron microscope (SEM). The worn surface and the subsurface microstructure were observed, and change in chemistry and nanomechanical properties were also measured using various techniques. In this section, details of all these techniques and the instruments used will be provided.

3.4.1 Optical methods based surface characterisation

The surface of the Al-Si samples after wear tests were observed using optical microscope (Keyence VHX 600) and white light interferometer (WYKO NT 1100) in vertical scanning interferometry (VSI) mode.

3.4.1.1 Optical microscopy

The worn surface of in Al-18.5% Si alloys was observed using the Keyence VHX 600 optical microscope. The fracture and fragmentation was observed and quantified. The change in silicon particles aspect ratio as a function of sliding cycles in first stage of (UMW-I) was calculated. In this method the aspect ratio was calculated in similar way as it was described earlier (see **Section 3.2.1**). The length and width measurements before fracture indicate the measurements carried on fractured particles by assuming that the particles were intact, that is the fracture did not occur. However, since the particles were fractured during the sliding

process, the direction of measurement of length and width of fractured particles was kept the same as that of before fracture.

3.4.1.2 White-light based interferometry

The white light based interferometry was used to measure the change in silicon particles height, Al-pile-up height and volumetric wear loss in the aluminum matrix. A Veeco (now Brucker) made 3D optical surface profilometer (NT 1100) was used to collect the surface profile data after etching and within the wear track after wear tests. The profilometer was equipped with software, WYKO Vision, which controlled the acquisition, analysis, storage and display of data collected with the interferometric microscope. The data was collected in VSI mode, wherein a white-light beam light passes through a microscope objective to the sample surface. A beam splitter reflects half of the incident beam to the reference surface and then the reflected beam from reference mirror combines with the light reflected from the sample surface to form interference fringes, where the best-contrast fringe occurs at best focus. The Vision software then demodulated the envelope of the fringe signal and vertical position corresponding to the peak of the interference signal was extracted for each point on the surface – thus generating the 3D map by collecting data from each point over a periodic array of points on the surface. The surface height distribution data was then exported and analysed to extract height information of silicon particles and the piled-up aluminum. The data analysis technique is described later (see **Section 3.5**).

3.4.2 Analytical electron and x-ray based surface characterisation

In the previous UMW studies at room temperature it was found that during the sliding process the lubricant additives break down and form an ORL after long sliding cycles. The emphasis was duly noted to understand and characterise the formation of similar ORL at

elevated temperature. Therefore, the surface damage events and the surface chemistry were also investigated using SEM, EDS, XPS and XANES.

3.4.2.1 Scanning electron microscopy and energy dispersive x-ray spectroscopy

The worn surfaces after wear tests were cleaned thoroughly by dipping them in hexane overnight to remove the lubricant oil from the surface. The surfaces were then observed using either JEOL 6400 or FEI Quanta 200 field emission gun microscope. Both these microscopes were equipped with EDS detector. Since the surface features were of interest, the wear surfaces were observed at a relatively lower voltage, 7.0 keV. The surfaces were observed both under secondary electron and back scattered electron imaging mode.

Surface chemistry identification and then elemental distribution were carried out using EDAX EDS x-ray detector. The EDS elemental analysis was also carried out at 7.0 keV to achieve minimum penetration to the surface and obtain elemental information within the area of interest.

3.4.2.2 X-ray photoelectron spectroscopy

The maximum thickness of the tribofilm and ORL was less than 200nm. At this length scale XPS is a very good technique to obtain elemental composition where the information is obtained from first few nm of the surface. Site specific x-ray photoelectron spectroscopy was carried out using PHI Quantera Scanning X-ray microprobe (Ulvac-PHI, Inc) to identify the chemical nature of the worn surfaces. Both survey scans and high resolution scan was conducted. The high resolution scans were obtained for Zn, S, P and S. From the high resolution scans, the background was subtracted using Shirley background [**104**]. The P peaks were then deconvoluted to identify the contributions from electron transitions corresponding to 2p 1/2 and 2p 3/2. And the O peak was deconvoluted in three different peaks corresponding to oxide,

bridging oxygen (BO) and non bridging oxygen (NBO). The results were then analysed to find out the composition of the ORL.

3.4.2.3 X-ray absorption near edge structure spectroscopy

To identify the molecular nature of the tribofilm, XANES was used at Canadian light Source Inc. (CLS), located at University of Saskatchewan, Saskatoon, SK, Canada. XANES spectroscopy using synchrotron light is element specific and can provide non-destructive chemical and structural information from the surface and the bulk of materials. In XANES spectroscopy technique the absorption characteristics of a particular core level electron are measured. Since the resulting spectrum is a function of the local environment around the element of interest, fine structure observed in the XANES spectra are very sensitive to the formal oxidation state of an element, thus reflect differences in local geometry between species with the same formal oxidation state.

The XANES spectra were collected using total electron yield (TEY) technique. In the TEY technique, the current from the sample generated by the ejection of photo, Auger and secondary electrons is directly measured. Due to the shallow escape depth of secondary electrons, this technique gives spectra from species in the first few nanometers of material. In this study O 1s, (K-edge) along with S, P and Zn 2p (L-edges), due to a dipole transition which is proportional to the unoccupied density of states (K-edge XANES probes states with p-type character and L-edge XANES probes states with s- or d-type characters), were studied; the spherical grating monochromator (SGM) beamline at the CLS was used for O K-edges and Zn L-edge studies and PGM beamline for S and P L-edges studies. A minimum of two scans on each of two different spots have been performed to obtain the spectra. Along with the data for the tribofilm sample, XANES spectra of a few standards compounds with known structures were

collected to serve as a “fingerprint” to aid in the identification of chemical species in the worn surface.

3.4.3 Subsurface microstructure observation and characterisation

During the sliding process the subsurface was also damaged – sliding induced fine grain aluminum was formed, formation of cracks within the silicon particles and at the Al-Si interface was also observed. Subsurface microstructure beneath the wear track was observed by making cross sections using FIB and TEM. The change in microstructure was limited to 500 nm to 2 µm from the surface. The thickness of ORL and the tribofilm was also measured from the cross section images. Detail on such sample preparation using FIB and TEM will be provided in this section.

3.4.3.1 Focused ion-beam milling

Site specific cross-sectional samples were also prepared using focused ion beam (FIB) milling technique to observe the sub-surface microstructure and damage induced during sliding process. Prior to milling a thin layer of platinum on the wear surface followed by a carbon layer of 2 µm thick was deposited on the platinum layer to prevent direct damage by the ion beam. Ion milling was performed with Ga^+ ion beam generated from Ga-based liquid metal ion-source at 30.0 kV accelerating voltage. During rough milling beam current was varied between 13 nA to 700 pA and the final milling prior to taking image was carried out at 80 pA to reduce beam induced damage to the microstructure. The cross-sectional microstructure was then observed at 5.0 kV using Zeiss NVISION 40 dual beam (secondary electron beam/ ion beam).

3.4.3.2 Transmission electron microscopy

Transmission electron microscopy (TEM) samples were prepared using a focused ion beam workstation. Two different techniques such as H-bar method and lift-out at FIB

workstation were used to prepare TEM samples. The FIB lift-out technique is shown in **Figure 3. 5**. TEM cross-sectional microstructures were obtained using a JEOL JEM-2100F field emission electron microscopes operated at 200 kV. In this method, the area of interest was first identified in the FIB workstation in secondary electron imaging mode. Then a thick C deposit was made on the surface (**Figure 3. 5a**). After that a trench was milled on either side perpendicular to the longest dimension of the area of interest (**Figure 3. 5b**) and the thin section (TEM sample) was partially freed from the bulk by milling the bottom side and part of the two opposite sides (**Figure 3. 5c**). At this point the TEM sample was connected to the bulk at two points as shown in **Figure 3. 5c**. During milling similar beam currents were used as that during cross sectional microstructure observation explained earlier (see **Section 3.4.3.1**). In the next step a tungsten manipulator was brought close to the TEM sample and then using carbon deposit the TEM sample was attached to the manipulator and finally the TEM sample was completely freed from the bulk (**Figure 3. 5d**). Then the TEM sample was lifted out of the trench and joined with a copper grid using carbon deposit (**Figure 3. 5e**). Finally the manipulator was removed from the TEM sample and final thinning to make the sample electron transparent was carried out with 80 pA beam current.

3.5 Quantification of surface damage parameters

The average silicon particle height before wear tests and the change in particle height after the wear tests was measured using 3D white light optical interferometer in VSI mode. In the previous UMW studies **[92-94]** with etched Al–Si alloys, it was shown that silicon particles sinking-in in the aluminum matrix took place soon after sliding contact began, which was followed by the wear of piled-up aluminum around the embedded particles. The process of silicon sinking-in can be thought of as plain strain deformation of aluminum matrix by pressing a

rigid punch (in this case by silicon particles). According to slip line field theory, application of an indentation pressure of 2.89 times the yield strength of the aluminum matrix is necessary to initiate yielding of the matrix. It was shown **[92-94]** that within the load range used in the current experiments the contact pressure exerted on silicon satisfied this condition, thus causing yielding of aluminum matrix. The displacement of plastically deformed aluminum adjacent to a sinking silicon particle was then formed the aluminum pile-up observed. The pile-up height was, however, not quantified in those **[92-94]** studies. In the present study, measurement of aluminum pile-up height was carried out using the optical interferometer.

3.5.1 Statistical measure of silicon particle height after etching

Using optical interferometer the surface elevation of the chemically etched surface was measured. To measure the average silicon particle height and average pile-up height, a reference was needed and the average surface elevation of etched aluminum matrix was used as the reference. A statistical analysis was done by fitting the surface elevation data to two Gaussian peaks, which corresponded to aluminum and silicon height distributions, and then the etched aluminum matrix peak (reference) was fixed at zero.

3.5.1.1 Particle height in Al-12.6% Si alloys

A typical 3D interferometer image of etched Al-12.6% Si alloy surface prior to UMW testing appears in **Figure 3. 6a**. **Figure 3. 6b** shows the fitting of the histogram data for **Figure 3. 6a** with two Gaussian peaks. The separation distance between these two peaks represented silicon particle exposure height after etching (**Figure 3. 6b**). Accordingly, the silicon exposure height prior to wear tests in Al-12.6% Si alloy was 1.66±0.05 µm.

3.5.1.2 Particle height in Al-18.5% Si alloys

Figure 3. 6c shows an optical profilometer image of a representative surface of the alloy after etching and in **Figure 3. 6d**, the black curve represents the histogram of surface elevations from the representative surface shown in **Figure 3. 6c**. The histograms of aluminum and silicon elevations from six different areas were plotted and fitted with two Gaussian profiles. The height of silicon particles, averaged from six different areas, was determined as 1.77±0.09 µm.

3.5.1.3 Particle height in Al-25.0%Si alloys

Figure 3. 6e shows a typical optical interferometer image of Al-25.0%Si alloy surface after etching. Similar data fitting was performed on the histogram data obtained from the six different figures similar to **Figure 3. 6e**. **Figure 3. 6f** shows a typical data and the data fitting for the histogram plotted from **Figure 3. 6e**. Accordingly, silicon particle height in this alloy after etching was 1.69±0.06 µm.

3.5.2 Silicon particle and aluminum pile-up height measurement after wear test

During UMW, silicon particle sinking-in is accompanied by the plastic deformation of aluminum matrix surrounding the silicon particles, resulting in aluminum pile-up formation. The silicon particle height change after the wear tests was measured in similar way as explained previously (see **Section 3.5.1**), but the data fitting procedure needed to be modified whenever aluminum pile-up formation was observed; e.g. in Al-12.6% silicon alloys. **Figure 3. 7a** shows a representative optical profilometer image of wear surface after 10^3 sliding cycles at 100 °C. **Figure 3. 7b** shows the corresponding line profile along AA´ from **Figure 3. 7a**. The pile-up of aluminum matrix surrounding silicon particles are marked in the 2D profiles. This pile-up formation results in a positive skewness in the aluminum height distribution.

Figure 3. 8a, c and e show the typical surface profile of the wear track in Al-12.6% Si alloy after 10^3 cycles, 5×10^3cycles and 5×10^4 cycles, respectively and **Figure 3. 8b, d and f** shows the corresponding histogram and data fitting with three separate Gaussian curves. The aluminum height distribution peak after the wear tests (**Figure 3. 8b, d and f**) was positively skewed due to the contribution from piled-up aluminum, which was a characteristic feature of UMW in Al–Si alloys. Hence, the surface elevation data corresponding to the aluminum matrix was resolved further into two Gaussian distribution. Thus, the complete histogram of the surface elevation after wear tests in **Figure 3. 8b, d and f** was fitted using three Gaussian curves – one representing aluminum matrix (dotted curve), second one for the piled-up aluminum (solid curve with the arrow) and the last one for Si particles (dashed curve with the arrow). **Figure 3. 8b, d and f** shows representative diagrams illustrating the change in surface elevation with the sliding and the fitting procedure to measure the silicon particle height decrease and aluminum pile-up height after wear tests.

3.5.3 Aluminum matrix wear loss measurement

The volume of material removed from the alloy surface was measured using profilometry data. **Figure 3. 9** shows an optical image of the wear track in Al-18.5% Si alloy at 2.0 N load after 2×10^6 sliding cycles at 25 °C. The surface profile of each circular wear track was measured at eight different areas (A_i) by taking three 2D cross sectional profile $\left(A_j, j = 1 - 3 \text{ for each } i\right)$ from each area. **Figure 3. 10a** shows a typical 2D cross section profile of Al-12.6% Si alloy and **Figure 3. 10b** shows a 2D profile along AA' from **Figure 3. 10a,** where the area below the initial etched aluminum is marked. These individual areas along each of the 2D profiles were summed. The average cross sectional area $\left(A_j\right)$ below the initial aluminum surface elevation corresponded to the material removed from the each area (A_i) was measured. The average cross sectional area of the wear track (A_{WT}) multiplied by the circumference of the wear track

determined the volumetric wear loss (V). The calculation method can be expressed numerically as shown below:

$$\left.\begin{aligned} A_{WT} &= \frac{1}{l}\sum_{i=1}^{l} A_i \quad , l = 8 \\ A_i &= \frac{1}{m}\sum_{j=1}^{m} A_j \quad , m = 3 \end{aligned}\right\} \tag{3.4}$$

$$V = 2\pi r_{WT} \times A_{WT} \tag{3.5}$$

3.6 Numerical Model Development

In this section the details regarding the finite element model to investigate the effect of matrix properties on the UMW mechanisms are given. Two different models, one containing a silicon particle with ideal geometry embedded in aluminum matrix and another containing multi-particle embedded in aluminum matrix was developed. The single particle model represented an idealised microstructure, whereas, the multi-particle model generated from actual images of a microstructure within a finite three dimensional volume was an actual representation of microstructure in an Al-12.6% Si alloy.

3.6.1 Geometry of silicon particle(s) and aluminum matrix

3.6.1.1 Single-particle model

In single-particle model, discretization of the silicon particle and the aluminum matrix was completed using TrueGrid **[105]**. In this numerical study, the geometry of silicon particle was considered to be of regular shape as an approximation having circular cross section and with one end having a spherical shape which was buried in the aluminum matrix. Due to symmetric geometry of the silicon particle considered in the model, 1/24th of the model was discretized for the numerical analysis. The silicon particle and the aluminum matrix were discretized using three dimensional solid elements. An axisymmetric element formulation could

not be incorporated in this model due to limitations associated with the contact for modeling of the silicon-aluminum interface. The differences between the two models will be detailed in **Chapter 7** and **8**.

3.6.1.1.1 Modeling of the silicon particle

The linear dimensions of the silicon particle were selected as follows: length of 7.6 μm, cylinder diameter of 3 μm and sphere radius of 3 μm. The FE discretization of the silicon particle was comprised of 79312 solid hexahedral elements. The characteristics length of the elements, defined by the ratio of volume of any particular element to the area of the largest face of that particular element, within the silicon particle varied from 0.004 to 0.053 μm and the aspect ratio varied from 1.216 to 22.28 with less than 1% element along the symmetry edge were larger than 10. The linear dimension of the elements varied from 33 nm to 142 nm along the particle-matrix interface. Although experimental observations indicated fracture of irregular shaped particles, particles with diameter less than 10 μm having a planar aspect ratio close to unity seldom exhibited fracture. Also, the hardness of silicon particle is much higher compared to aluminum matrix. Accordingly, fracture of the silicon particle was not modeled in the present study and the particle was modeled as an elastic entity. The elastic modulus, density and Poisson's ratio of the silicon particle were assigned to be 107 GPa, 2.33 Mg/m^3 and 0.28, respectively.

3.6.1.1.2 Modeling of the aluminum matrix

The length and depth of the aluminum matrix were 15 μm and 12 μm. The discretization of the aluminum matrix was completed using 134532 hexahedral solid elements. The aspect ratio of the solid elements varied between 1.216 to 13.92 and 7.7% of total elements within the matrix exceeded aspect ratio 10.0. The elements with aspect ratio larger than 10 were far away

from the interface region and were closer to the bottom surface. The characteristic length of the elements in the matrix varied from 0.002 µm to 0.24 µm and all the elements within 1.0 µm from the interface had characteristic length less than 0.05 µm. The mesh sensitivity study was also carried out to represent the top surface curvature after sinking-in without any irregularities at the vicinity (500 nm from the interface) of the interface. The discretization of the silicon particle and the matrix along the Al-Si interface was finer such that the linear dimension of the elements varied from 33 nm to 142 nm, respectively. The nodes and element faces along the either side of the matrix-particle interface was aligned to each other perfectly. A solid element with selectively reduced integration was assigned to the solid elements of the aluminum matrix. The material model discussed in **Section 3.6.3** was assigned to the aluminum matrix. **Figure 3. 11a** and **b** illustrates the FE discretization of the silicon particle and the aluminum matrix. Note the finer discretization density in the vicinity of the interface

3.6.1.2 Multi-particle model

During the actual sliding process multiple particles comes in contact with the counterface and sinks-in simultaneously. The purpose of the multi-particle model was to investigate the effect of multiple particles sinking-in simultaneously on the plastic deformation of the matrix surrounding the particles, i.e. the formation of pile-up. In the multi-particle model, image based discretization was carried out starting with cross sectional images obtained from SEM using a commercially available automated mesh generation software, ScanIP version 4.3 **[106]**. The software converts 3D images or a series of parallel images representing any volume of interest (VOI) in to a computer-aided design (CAD) or finite element models. Volume images or 3D images can be considered as 3D tables, containing a value for a particular position in space. In 3D images, those sampling points are positioned on a rigid 3D grid and a 3D pixel is called voxel. A typical workflow within the ScanIP software is given in **Figure 3. 12**. The

advantage of this mesh generation technique is that any complicated microstructure can be reproduced to a 3D model which in conventional mesh generation techniques is not possible. The discretization of both aluminum matrix and the silicon particles were carried out simultaneously. The mesh generation process for the Al-12.6% Si alloy microstructure is detailed below.

3.6.1.2.1 Acquiring 2D parallel images

The VOI chosen from the Al-12.6% Si alloy is shown in **Figure 3. 13a**. Within this VOI parallel sectioning was carried out in a Quanta 3D FEG FIB workstation. A total of 330 sections with 100 nm spacing between them were made with a beam current of 65 nA and images were recorded. Upon close observation of the parallel sections it was found that the change in topology of the silicon particles within the matrix was not significant within 100 nm. Thus, to reduce the amount of dataset and to increase the computing time to process the image data, only 82 alternate images with 200 nm (i.e. the volume of material enclosed by the 164 images with 100 nm spacing) spacing between them was considered for further analysis and image processing. Out of the 82 images, 14 images are shown in the **Appendix A1**.

3.6.1.2.2 Image processing

These 82 images were then cropped from all four sides to a dimension of 28.8×10.3 μm^2. **Figure 3. 13b** shows the SEM micrograph of the first section from **Figure 3. 13a** and another nine images are shown in **Appendix A1**. These 82 images were then imported in to the software to do necessary image processing which included the 'background separation' and 'segmentation'.

Background data is the original greyscale data from the SEM images. The segmentation of background data then generated one or more volume called masks, which defined how an

object filled the space. These masks represented any given object or part (for a multi-part model) or a phase (in multi-phase material). In the present scenario, two masks representing Si and Al phase were created. Using the threshold values of the two different phases from greyscale data (SEM image) segmentation was completed. Some additional pixels belonging to aluminum matrix were artificially added to generate the final depth of 12.6 µm and to avoid the fixed boundary conditions on the odes belonging to silicon particles. **Figure 3. 13c** shows three principal views of a typical image of one of the section shown in **Figure 3. 13b** after segmentation. Thus, the total volume of the material was 28.8×12.6×15.75 μm^3.

3.6.1.2.3 Generation of surface and volume mesh

In this step first a surface comprising the total volume of the geometry was generated from the segmented data and then the volume discretization was completed. **Figure 3. 13d** shows a voxel mesh of the VOI. Note the irregularities (sharp transitions) in the VOXEL mesh around the curved surfaces. The voxel mesh was then further discretized in to a smoothed mesh (**Figure 3. 13e**) using the +FE free **[106]** algorithm of the ScanIP software. This algorithm allowed the conformity between the aluminum and silicon segments and the nodes at the interface were aligned perfectly. Various parameters during this volume mesh generation such as, adaptive remeshing, densification (to add more elements in thinner sections), characteristic lengths of the elements, surface and internal change rate (to specify how fast the mesh size could change) were altered suitably to optimise the quality of the tetrahedral elements. Also, mesh refining at selected locations within the volume to generate finer mesh along the Al-Si interfaces were performed.

3.6.1.2.4 Discretized microstructure of the multi-particle model

The model was exported in to the finite element model as LS Dyna keyword format and the final model setup to define boundary conditions, contact and the control of the simulation

was completed in LS Prepost version 2.4 **[107]**. **Figure 3. 13e** shows the 3D model generated using ScanIP from the 2D parallel images as shown in **Figure 3. 13a**. Note the finer discretization (**Figure 3. 13f**) on both matrix and particles along the Al-Si interface compared to that elsewhere in the model. Thus the final mesh was comprised of 253312 four noded tetrahedral elements out of which 198422 elements were used to discretize the aluminum matrix and the balance for silicon. The mean and maximum edge-length aspect ratio was 1.62 and 5.49, respectively. A solid element with one point integration was assigned to the tetrahedral solid elements of the multi-particle model. Several attempts were made to simulate the model with four noded tetrahedral elements with rotational degree of freedom, but due to nonlinearity of the problem all attempts resulted in early termination. The material model discussed in **Section 3.6.3** was assigned to the aluminum matrix and same materials properties for silicon as detailed in **Section 3.6.1.1.1** were used.

3.6.2 Pile-up and sink-in simulation procedure

3.6.2.1 Single-particle model

The bottom section of the aluminum matrix (**Figure 3. 11a**) was fully constrained, whereas, the two geometrical faces symmetric about a plane perpendicular to the radial direction and the face connecting those two faces were constrained for the symmetry conditions. The silicon particle was constrained to move only in the vertical direction (normal to the bottom face of aluminum matrix). Displacement was prescribed to the silicon particle in the negative z-direction (in to the aluminum matrix) to simulate the "sinking-in" process. Experimentally it was observed that during lubricated sliding wear the exposed silicon particles were embedded in to the matrix. Accordingly, the total displacement (sinking-in) prescribed to the silicon particle was 1.6 µm. In the loading cycle (**Figure 3. 14**), prescribed displacement to the silicon particle increased linearly up to the maximum displacement (1.6 µm) and during the

unloading cycle, the prescribed displacement to the particle was removed and movement of the particle was a result of the elastic response from the matrix. Numerical simulations were simulated statically, with 19 implicit time steps, using the double precision version of LS-DYNA 971, revision 4.2 [**108**].

The interface between the aluminum and silicon particle was modeled using a penalty based algorithm incorporating the potential for a tiebreak within the contacting surface. Kinematic conditions for mating segments at the interface are conserved for contacting surfaces until the defined failure criterion according to **equation 3.6** is satisfied. The penalty formulation used in this simulation also incorporated an additional segment based treatment option (SOFT=1) which improved numerical contact behaviour. This contact algorithm also takes in to consideration the values for normal failure stress (NFLS) and the shear failure stress (SFLS) of the contact interface to evaluate the failure criteria. The Al-Si interface failure criterion incorporated in this contact definition was expressed in **equation 3.6** and was similar to the quadratic delamination criterion (QDC) used for simulating interface failure in composite material by various researchers [**109,110**]. A quadratic failure surface in both normal and shear stress state space existed. In **equation 3.6**, σ_n and σ_n were the normal and shear stresses at the interface. NFLS and SFLS represented the normal and shear strength of the interface, respectively.

$$\left(\frac{|\sigma_n|}{NFLS}\right)^2 + \left(\frac{|\sigma_s|}{SFLS}\right)^2 \geq 1 \qquad (3.6)$$

In addition, once failure occurred tensile coupling was deactivated in this algorithm. According to previous studies using molecular dynamics simulations by Noreyan et al. [**111**], Al(111) and Si(111) has the lowest shear strength and Al(100) and Si(100) has the highest shear strength. Hence, the normal (NFLS) and shear strength (SFLS) values of the weakest interface (Al(111)-Si(111)) were considered in **equation 3.6**. From **equation 3.6** it may be noted that the failure of the interface is governed by the shear strength, as it is always an order of magnitude

lower than the normal strength of the interface. In addition, a parametric study was conducted during model development to investigate the effect of different strengths of the interface. It was observed that the effect of the interface strength on the amount of pile-up was insignificant. That is why the normal and shear strength value for Al(111)-Si(111) interface were prescribed as 7.2 GPa and 0.318 GPa [**111-113**]. The values for the static and dynamic COF in all simulations were assigned to be 0.2 and 0.1, consistent with experimental values (shown in **Figure 3. 15**), to simulate friction between the silicon particle and the aluminum matrix. Nodal z-axis displacements of the aluminum matrix top surface along the edge were measured at the end of the loading and the unloading cycles as a function of distance from the Al-Si interface. A sample input file is given in **Appendix A2**.

3.6.2.2 Multi-particle model

Similar boundary conditions as prescribed in single-particle model were used in the multi-particle model. The nodes at the bottom face were fixed for all degrees of freedom and the symmetrical boundary conditions were prescribed for the nodes at the four vertical faces. The contact between the matrix and the particles were modeled identically to that in the single-particle model. Numerical simulations were simulated using an explicit time integration method for 10^{-4} s using the double precision version of LS-DYNA 971, revision 5.0 [**108**]. The choice of the different time integration method for the multi-particle model is explained in **Section 3.6.2.3**.

The particle sinking-in multi-particle model was performed with a rigid AISI 52100 steel counterface. The counterface was assumed to be a flat surface considering the width of the model (28.8μm) over which the contact was being made. It was discretized with 16000 eight noded hexahedral solid elements with one point integration. The density of the counterface material (AISI 52100) was considered to be 7.81 Mg/m^3, and the Young's modulus and the Poisson's ratio were considered to be 210 GPa and 0.33. The displacement was then prescribed

to the counterface in the negative z-direction to simulate particle sinking in as shown in **Figure 3. 16**. The loading and unloading rate was same as shown in **Figure 3. 16**.

3.6.2.3 Choice of integration method

The single particle model was solved using implicit time integration method to perform a static solution. However, the multi-particle model was solved using explicit time integration method. Several attempts were made to solve the multi-particle model using implicit time integration method. However, because of the non-linearity of the solution arising from materials behaviour, contact between the mating surfaces and geometry of the particles, it was not possible to obtain the complete solution and all those attempts resulted in undesired termination of the solution.

3.6.3 Material and material model for the aluminum matrix

To appropriately incorporate the elastic/plastic behaviour of the aluminum alloy within the numerical model, tensile and compressive testing was completed in accordance with the ASTM E8 and E9 standards, respectively [**115,116**]. Standardized tensile testing was completed on four rectangular cross-section specimens with gauge length of 25.4 mm. The tensile tests were completed at the rate of 0.5 mm/min. A total of three tests were performed and material's mechanical responses were observed to be consistent. Standardized compressive testing was also completed on four cylindrical shaped specimens at a rate of 0.5 mm/min and testing observations from the experimental compressive tests was again found to be consistent. **Figure 3. 17a** and **b** illustrates the true stress versus effective plastic strain data for the Al-12% Si alloy obtained from the uniaxial tensile and compressive tests, respectively. The alloy was very ductile in the compressive mode but was brittle in tensile mode as evident from **Figure 3. 17a** and **b**. Presence of the silicon particles make the Al-Si alloys very brittle in the tensile mode.

An isotropic elastic-plastic material model that incorporates different yield stress versus effective plastic strain responses for tension and compression was selected to model the material behaviour of the aluminum matrix. Values for the density, Young's modulus, and Poisson's ratio were 2.72 Mg/m^3, 70.7 GPa, and 0.3, respectively. The yield strength (σ_y) of the aluminum alloy was observed to be 172.6 MPa and was consistent for both tensile and compressive loading conditions. The stress versus effective plastic strain relationships from the tensile and compressive tests (**Figure 3. 17a** and **b**) were utilized in the material model of the aluminum matrix.

3.6.4 Material Model Validation

To validate and obtain the complete generality of the material model used for the aluminum matrix in the particle sinking-in simulations, the tensile and compressive tests were simulated quasi-statically using the double precision executable of LS-DYNA version 971 revision 4.2 [**108**].

3.6.4.1 Tensile Testing

The experimental tensile test was simulated quasi-statically without taking the time dependant viscous and inertial effects into account using the implicit time integration method. The top most nodes of the specimen were fully constrained and a displacement was prescribed to the bottom most nodes at the rate of 0.5 mm/min. Three numerical tensile testing simulations were completed with different discretization densities for the purpose of a mesh sensitivity analysis. The element lengths in the three models were 0.4375 mm, 0.382 mm and 0.245 mm and the width of the elements were 0.596 mm, 0.3725 mm and 0.298 mm. The elements thickness was 0.2 mm in all three models. A selectively reduced solid element formulation was specified for the solid elements. **Figure 3. 18a** illustrates the stress versus

effective plastic strain obtained from the three numerical simulations. The difference between stress versus effective plastic strain response obtained from the three different mesh densities and experimental results (**Figure 3. 17a**) was less than 1%.

3.6.4.2 Compression Testing

The experimental compressive testing was also simulated quasi-statically for the purpose of material model validation. Due to symmetry, only a quarter of the model was considered in these simulations. A mesh sensitivity analysis was also carried out for the compressive tests. The linear dimensions of the elements were consistent with the tensile specimens as mentioned in the previous section. A penalty based contact algorithm was used to simulate the contact between the compression specimen and the rigid plates. The experimental values of coefficient of friction (COF) observed during lubricated wear testing using pin-on-disk experiments between Al-12.6% Si alloy and a 52100 steel counterface were 0.2 and 0.1 for the static COF (μ_s) and dynamic COF (μ_d), respectively. **Figure 3. 18b** exhibits the stress versus strain behaviour of simulated compression test which was observed to be identical with experimental data.

3.6.5 Energy balance

During the simulation, the energy must be conserved and the energy balance was monitored as a check for the solution accuracy. The total energy comprising the kinetic energy, internal energy (which includes the elastic strain energy and work done in plastic deformation), sliding interface energy, and the energy ratio were used as a check to the correctness of the numerical solution. In all the simulation the energy ratio, defined as the ratio of total energy at any point during simulation to the sum of total initial energy and the external work, was always close to 1 and the variation was within ±0.6%.

3.6.6 Assumptions in finite element simulation

While developing the finite element model to simulate the UMW mechanisms, various assumptions were taken. The first assumption was that the silicon particles were elastic entity and no failure criteria for the silicon particles were taken in to account. The primary reason for this assumption was that the models were developed to estimate the amount of aluminum pile-up and corroborate those data with experimental measurements. In addition the elastic modulus of silicon was almost twice that of aluminum matrix. Secondly, the macroscopic materials behaviour measured using uniaxial tensile and compressive behaviour were used to model the microscopic phenomena such as sinking-in and piling-up. However, the material models use von Mises criterion to relate the uniaxial stress data to any complex stress state. The third assumption was that particle sinking-in occurred only due to application of normal load. Since the total displacement of silicon was known from the experiments, displacement was prescribed to the particles to simulate silicon sinking-in. However in actual sliding tests there exists tangential loading of the particles which may aggravate the particle sinking-in and interface failure.

TABLES – CHAPTER 3

Table 3. 1: Typical chemical composition (in wt. %) of the Al-SI alloys used in the study.

Alloys	Si	Cu	Ni	Fe	Mn	Mg	Ti	Zn	Other	Balance
Al-12.6% Si	12.6	0.87	1.0	0.37	0.79	0.26	0.11	-	0.02 Sr	Al
Al-18.5% Si	18.4	4.0	0.02	0.23	0.07	0.57	0.05	0.1	<0.01Pb and Sn; < 0.002 Sr	Al
Al-25.0% Si	25	4.0	< 0.01	0.21	< 0.01	1.12	0.01	< 0.01	<0.002 Sr	Al

Table 3. 2: Brinell hardness (bulk hardness) of the alloys and Vicker's hardness of the matrix of the alloys used in this study. The standard deviation represents the variation from atleast six measurements for Brinell and nine measurements for Vickers hardness, respectively.

Alloys	Brinell hardness at 500 Kg load	Vicker's hardness at 10 gf
Al-12.6% Si	93.0±1.0	69.1±1.0
Al-18.5% Si	97.2±6.8	85.0±8.3
Al-25.0% Si	101.3±5.9	110±8.3

Table 3. 3: Sliding wear testing parameters.

Test parameters	Value
Load (W), N	2.0 N
Sliding speed (U), m s^{-1}	0.05
Sliding cycles, revolutions	between 10^3 and 6×10^6
Test temperature (°C)	100, 25
Counterface rad. (R), m	3×10^{-3}
Lubricating Oil	Mobil 1

Table 3. 4: Typical properties of lubricating oil used in wear tests.

Parameters	Value
SAE grade	5W-30
Viscosity, ASTM D 445	cSt @ 40 °C 64.8 cSt @ 100 °C 11.3
Viscosity index, ASTM D 2270	169
Sulfated ash, wt%, ASTM D 874	1.0
HTHS Viscosity, mPa·s @ 150 °C ASTM D 4683	3.09
Pour point, °C, ASTM D 5949	48
Flash point, °C, ASTM D 92	230
Density @15 °C kg/l, ASTM D 4052	0.80

Table 3. 5: Parameters required calculating minimum lubrication thickness (h_{min}), composite surface roughness (r^*) and the film thickness ratio (λ) according to equations 3.1 – 3.3.

Alloy	R (µm)	U (m/s)	E_{al} (GPa)	E_{si} (GPa)	E_{steel} (GPa)	r_{Si} (nm)	R_{ball} (nm)	W (N)	Temp. (°C)	h_{min} (µm)	λ
Al-12.6% Si	0.003	0.05	70	107	210	792	150	2.0	25	0.018	0.022
									100	0.004	0.006
Al-18.5% Si	0.003	0.05	70	107	210	100	52	2.0	25	0.018	0.156
									100	0.004	0.039
								5.0	25	0.017	0.146
Al-25.0% Si	0.003	0.05	70	107	210	95	78	2.0	100	0.004	0.036

FIGURES – CHAPTER 3

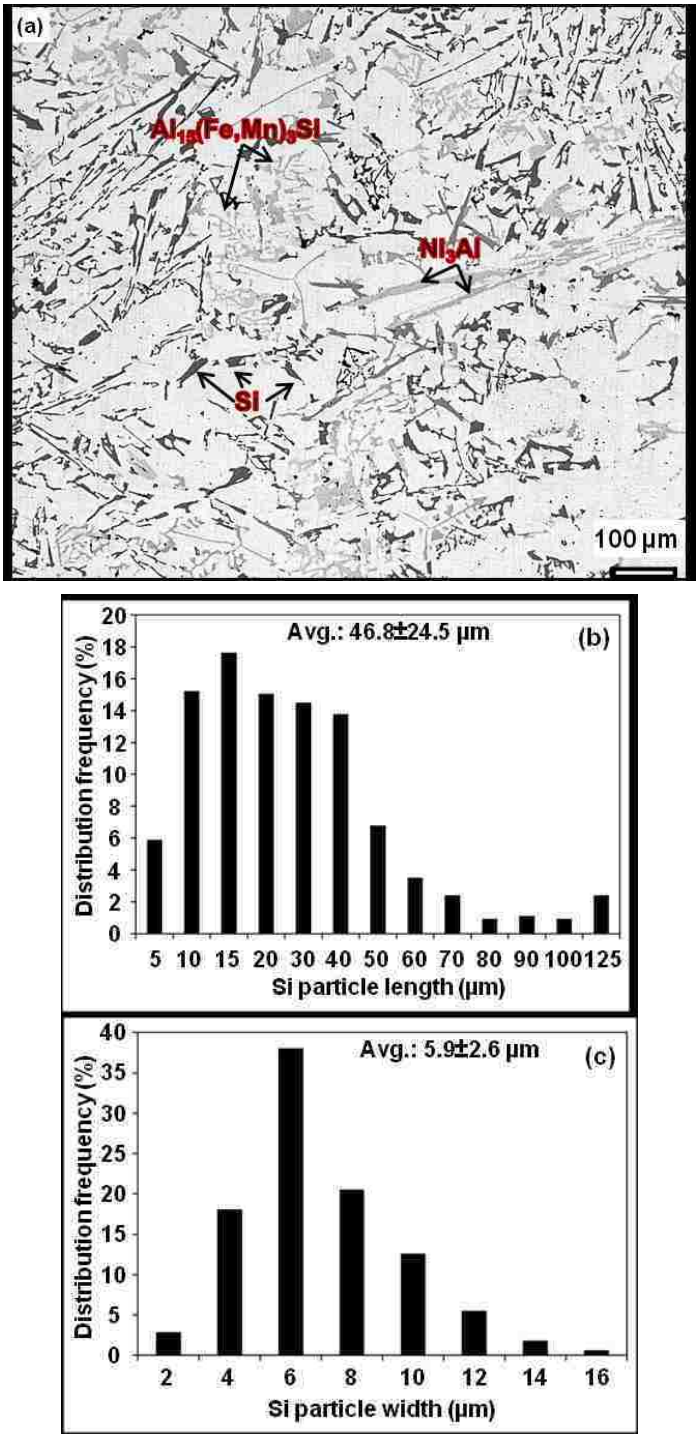

Figure 3. 1: (a) Typical optical microstructure of Al-12.6wt.% Si alloy showing distribution of silicon particles and intermetallic phases; (b) and (c) histogram of silicon particles length and width, respectively.

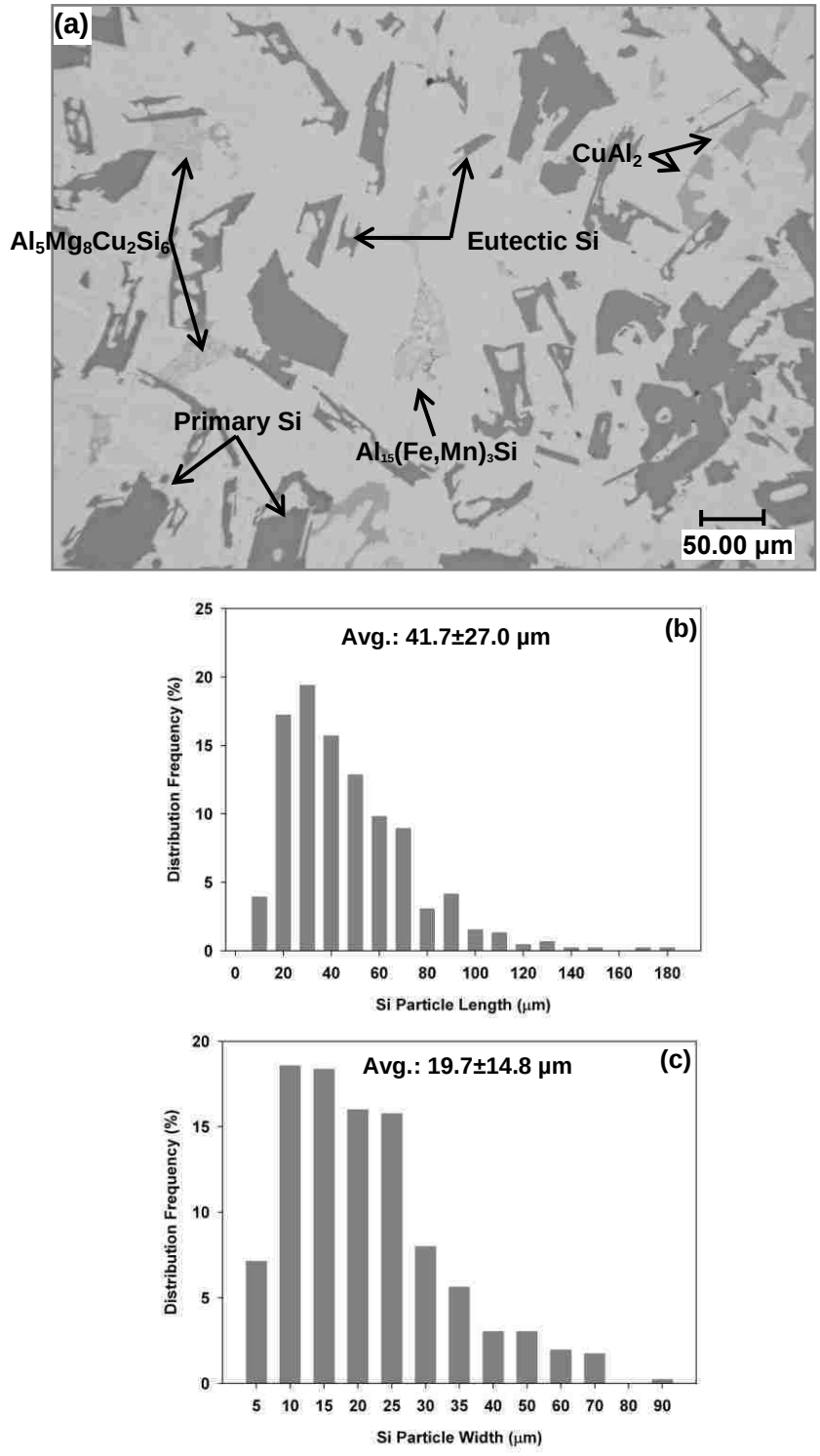

Figure 3. 2: (a) Typical optical microstructure of the Al-18.5% Si alloy showing various phases present; histogram shows the (b) length and (c) width of Si particles present in the alloy.

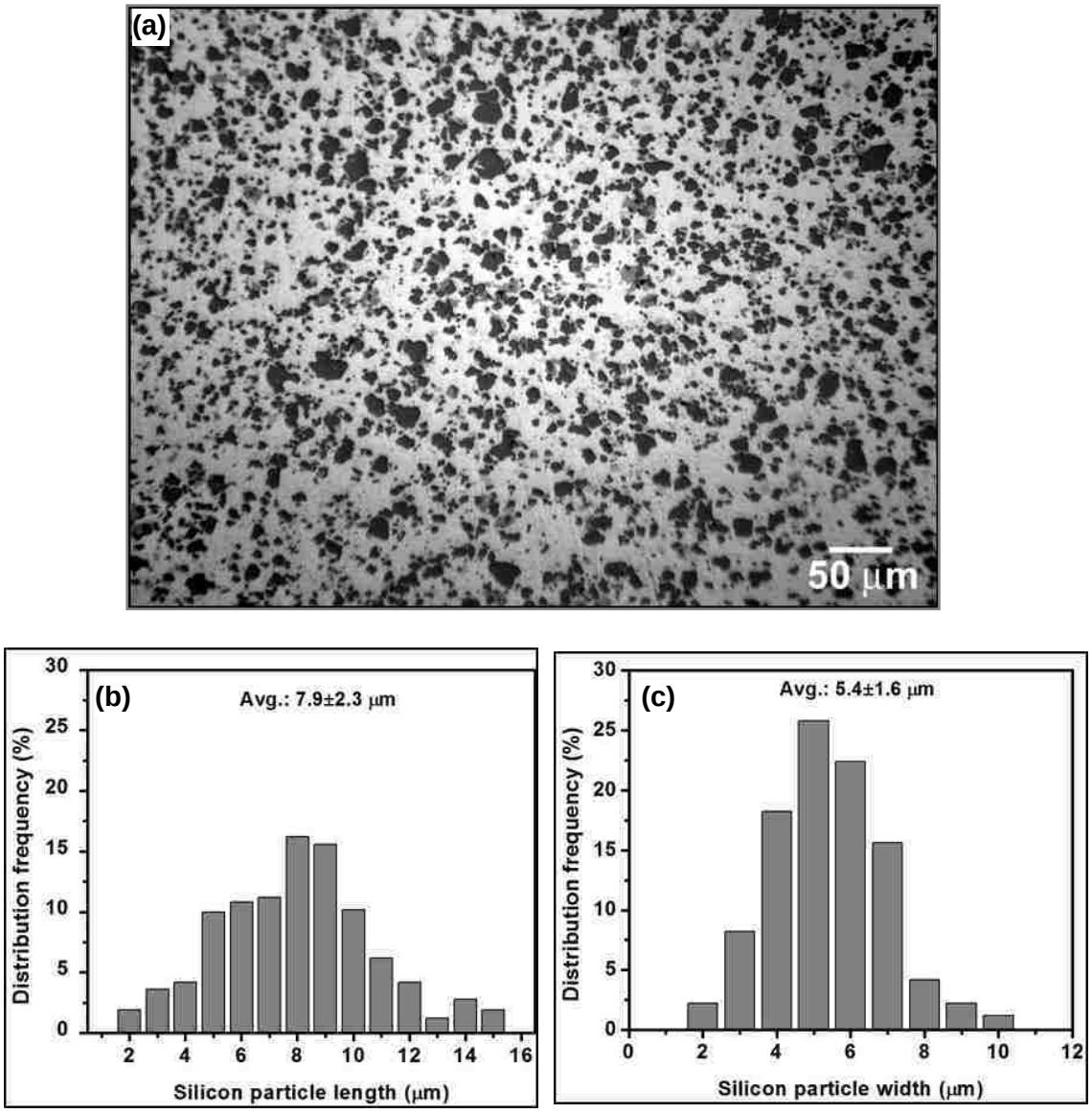

Figure 3. 3: (a) Typical optical microstructure of the Al-25.0% Si alloy showing various phases present; histogram shows the (b) length and (c) width of Si particles present in the alloy.

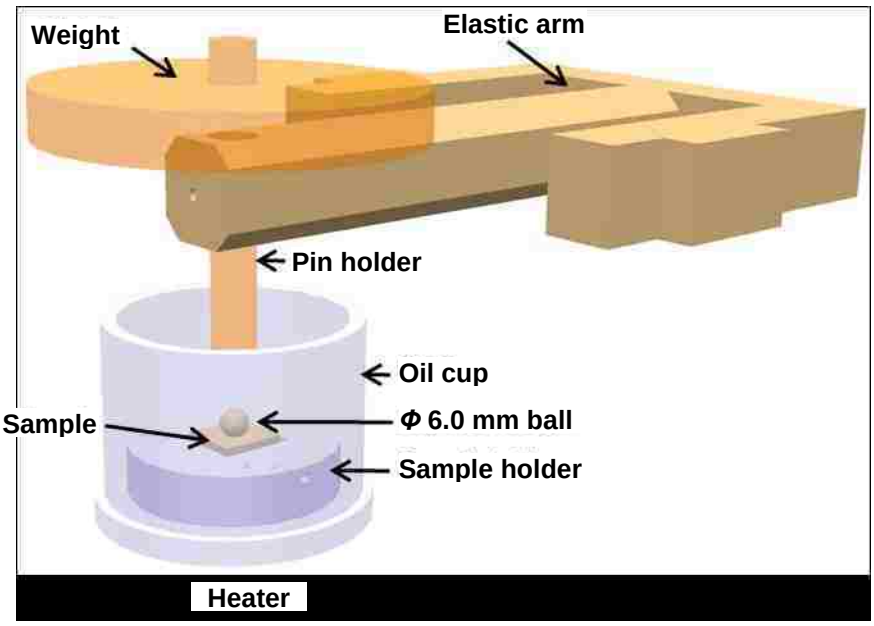

Figure 3. 4: Three dimensional (3D) schematic of the lubricated wear testing set-up in CSM High temperature POD wear tester, CSM Instruments Inc. The same wear tester was used to do the wear testing at 25 °C by keeping the heater turned off.

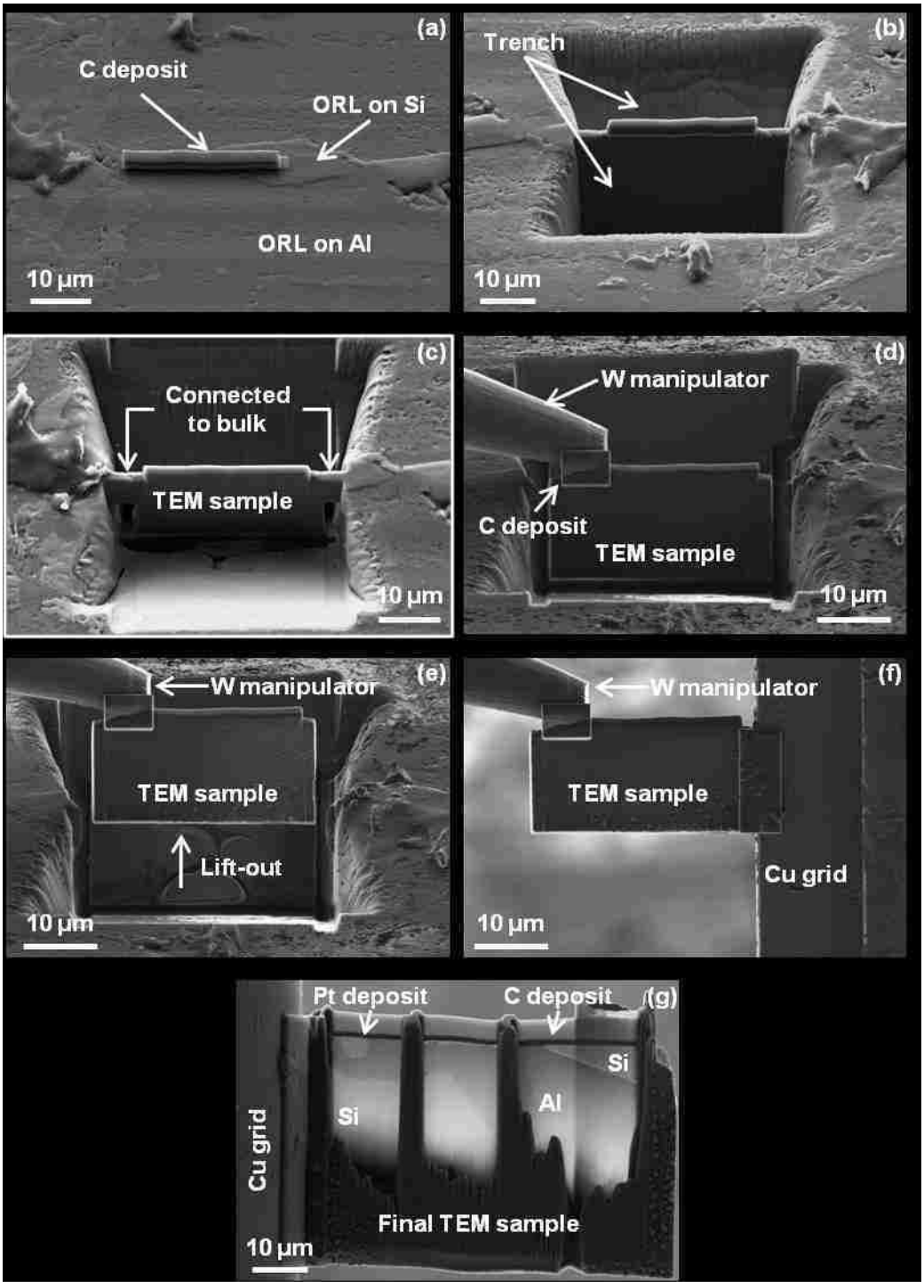

Figure 3. 5: TEM sample preparation stages in FIB Lift-out technique. (a) carbon deposition on the area of interest; (b) preparation of the trench on either side of the area of interest to make the preliminary TEM sample; (c) partial freeing of the sample from the bulk; (d) attaching the TEM sample with the W manipulator and complete freeing of the sample; (e) lift out of the sample from the trench; (f) mount the sample on Cu-grid; and (f) final thinning of the sample to make electron transparent.

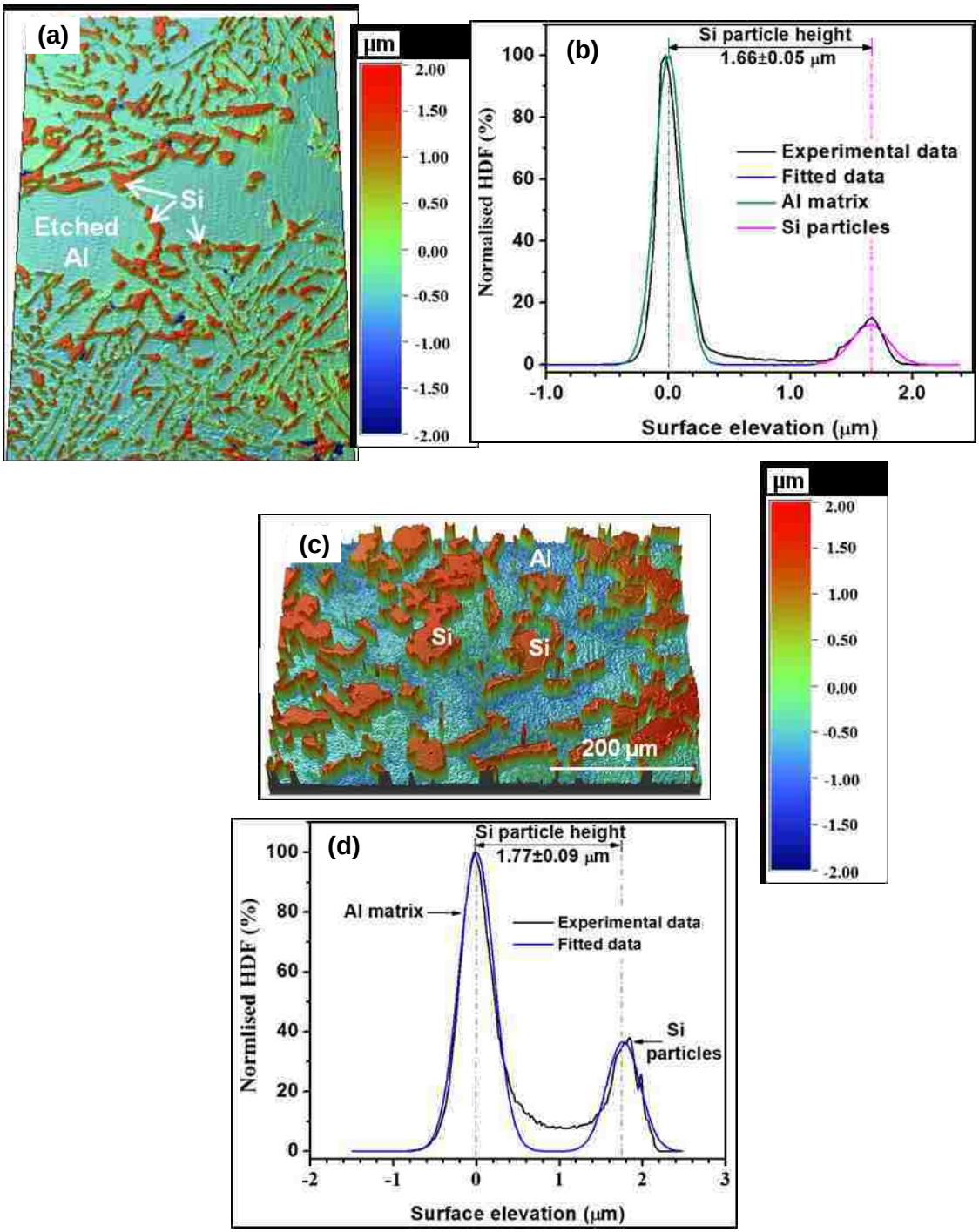

Figure 3. 6: 3D optical interferometer image of a typical surface and histogram profile of the height distribution of the surface elevation after chemical etching in (a)-(b) Al-12.6% Si alloy; (c)-(d) Al-18.5% Si alloy and (e)-(f) Al-25.0%Si alloy. The height distribution frequency (HDF) was normalised with the maximum frequency. Peak at zero corresponds to the etched aluminum matrix and the peak right of that corresponds to silicon particles. The separation distance between the two Gaussian profiles fitted to the experimental data is considered as silicon particle height after etching.

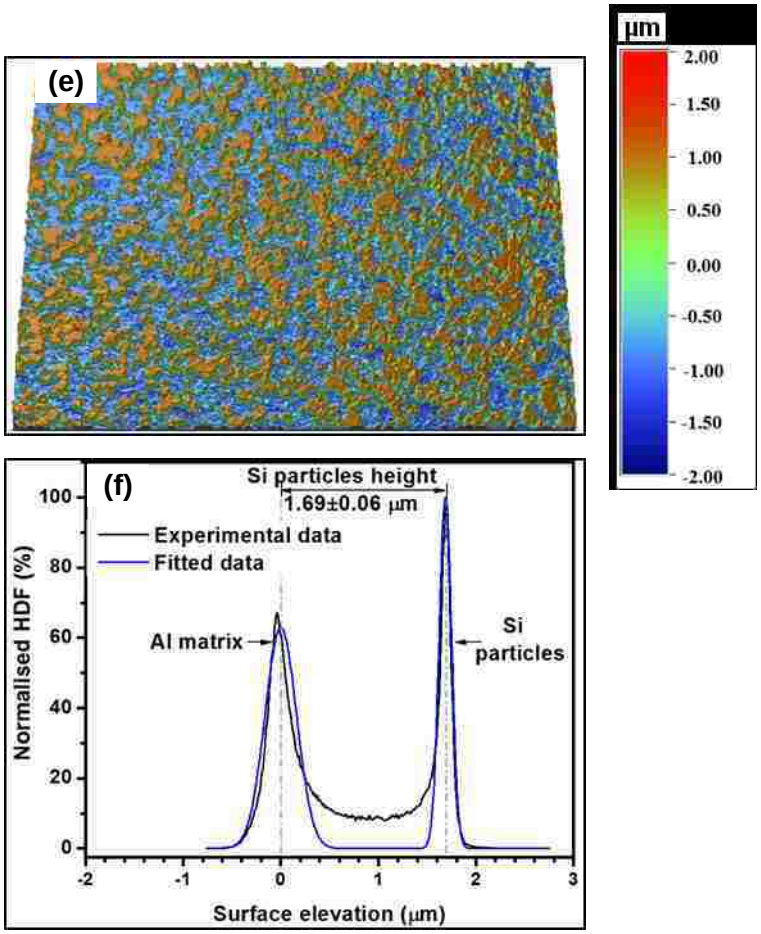

Figure 3. : Continued

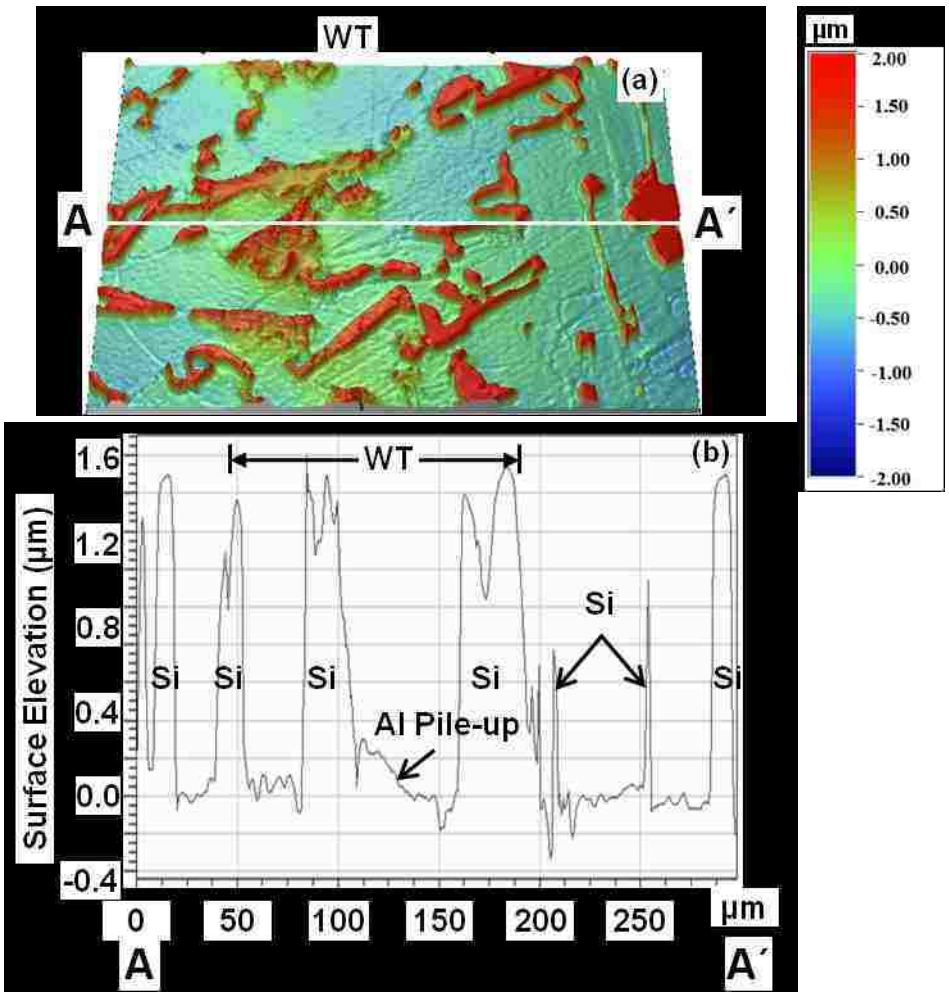

Figure 3. 7: (a) 3D optical interferometer image of a typical WT in Al-12.6% Si alloy showing the surface morphology of the WT; and (b) 2D cross sectional profile along AA´ in (a) showing the aluminum pile-up around silicon particle within the WT.

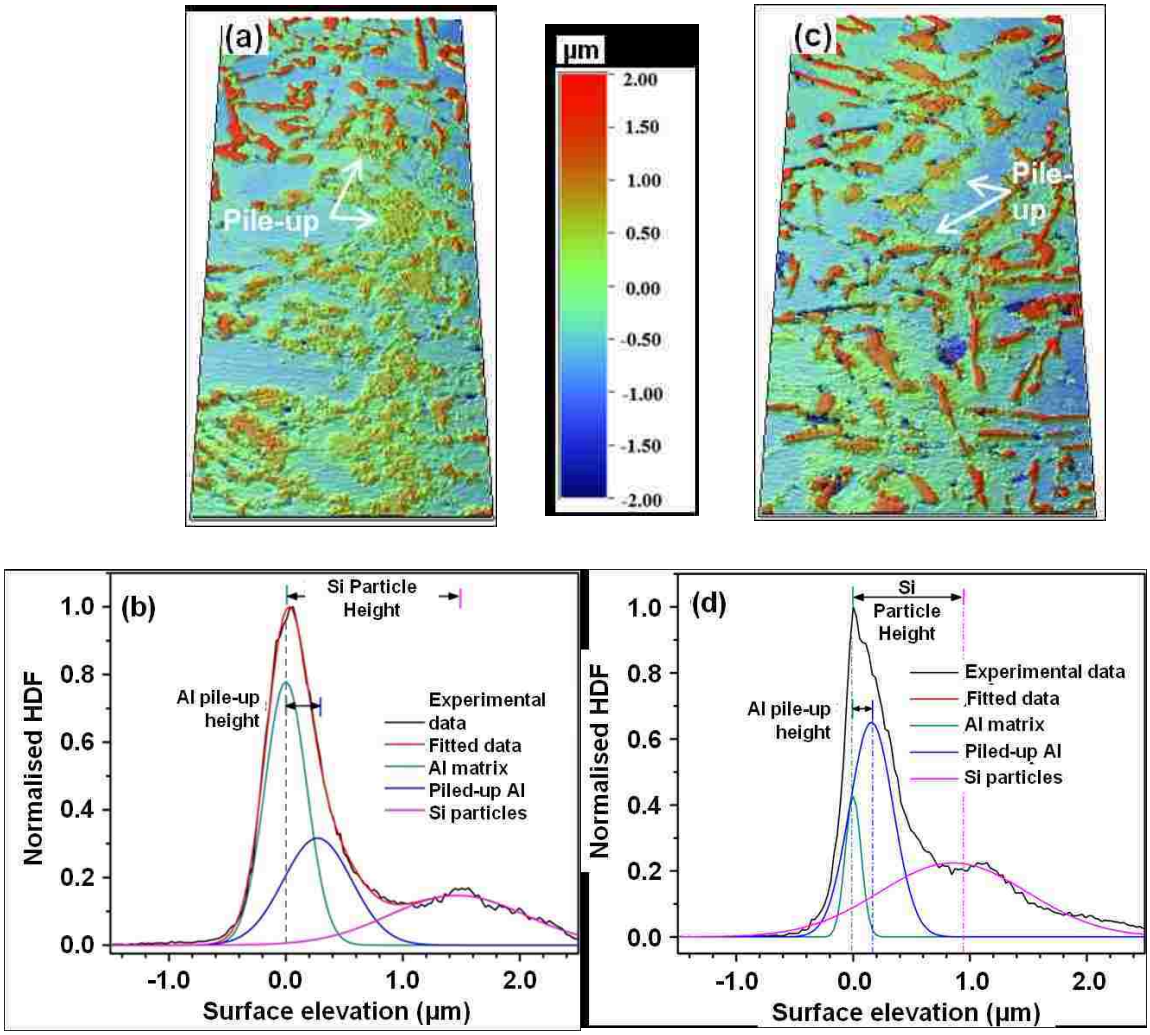

Figure 3. 8: Typical 3D optical interferometer images and corresponding histograms of theAl-12.6% Si alloy after (a)-(b) 10^3 cycles; (c)-(d) 5×10^3 cycles and (e)-(f) 5×10^4 cycles. The separation distance between aluminum matrix and piled-up aluminum peak is the pile-up height and the same between aluminum matrix and silicon peak is the silicon particle height after wear tests.

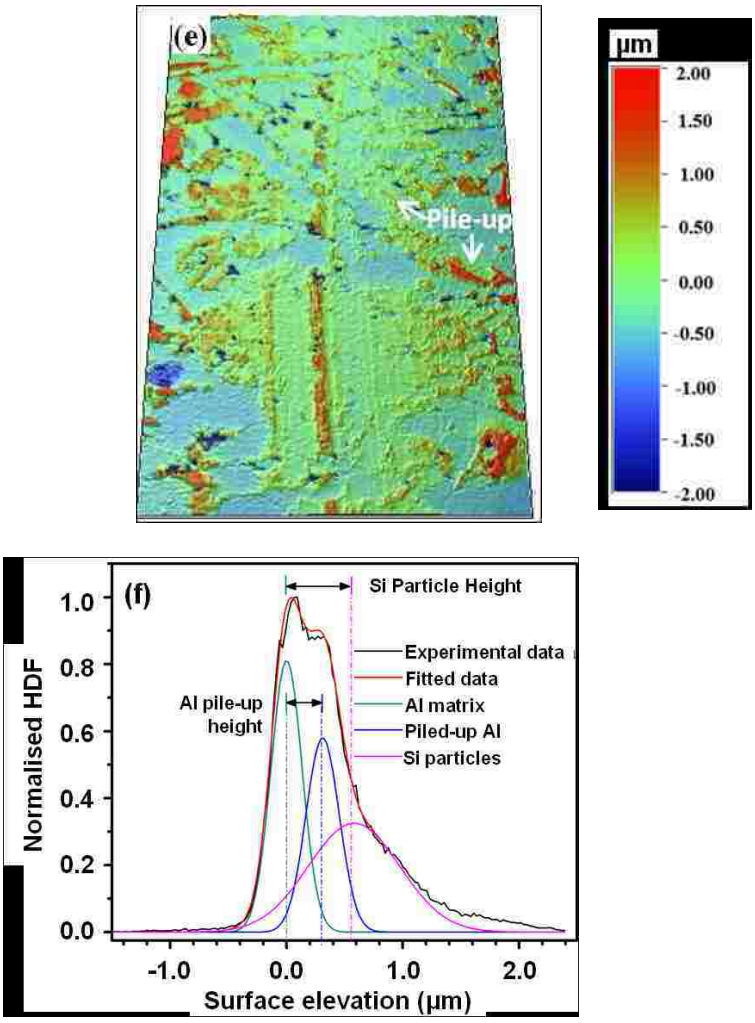

Figure 3.8: Continued

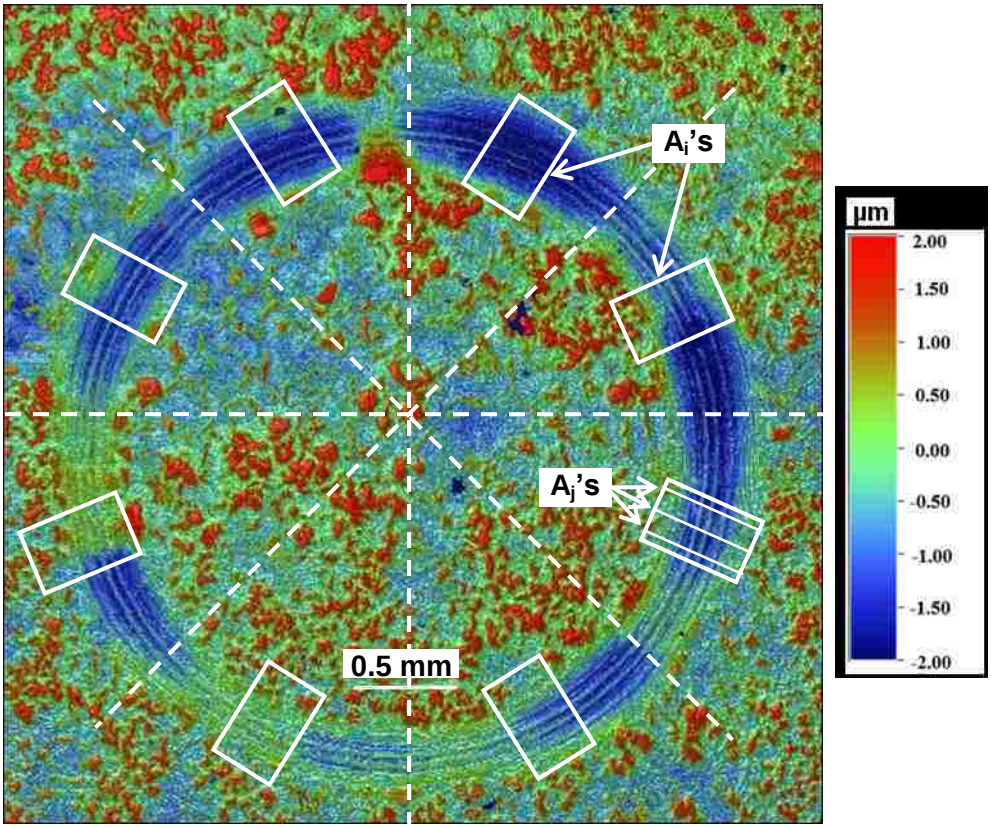

Figure 3. 9: A typical optical interferometer image of complete wear track showing the locations of eight different areas from the wear track which were considered to calculate the average volume loss. Within each region as identified by the rectangular box, three 2D cross sectional profile was chosen; thus a total of 24 numbers 2D profiles were considered to calculate the average cross section of the WT.

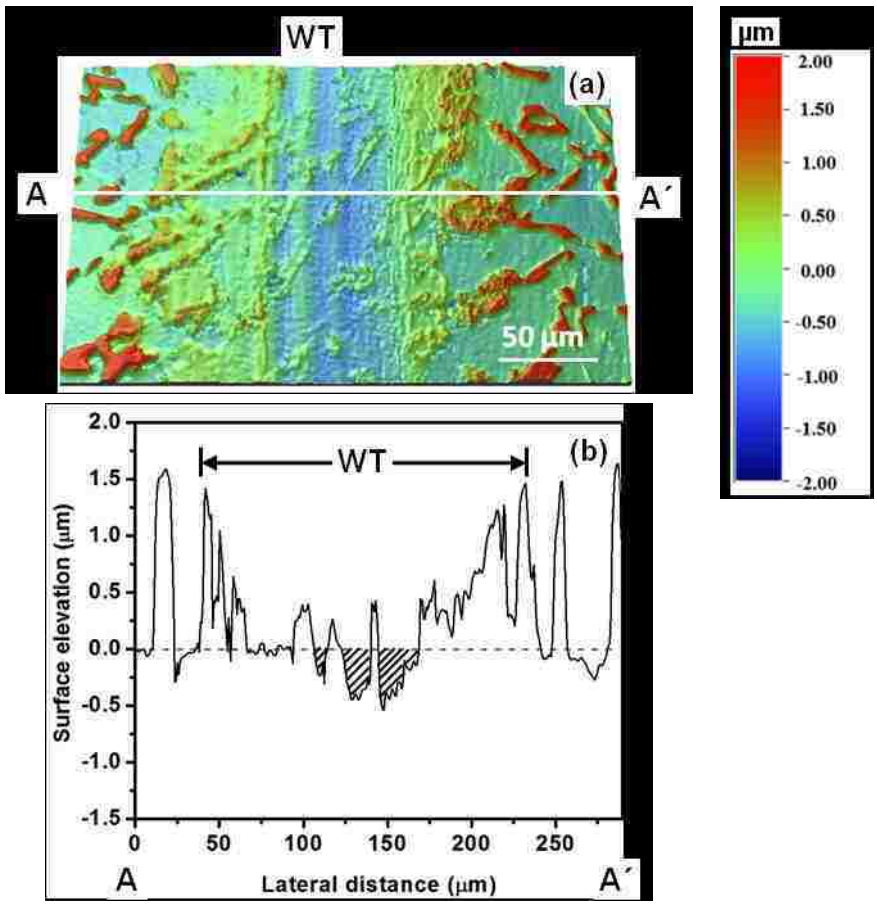

Figure 3. 10: (a) optical profilometer of the wear track in Al-12.6% Si alloy after 6×10^5 sliding cycles and (b) the cross section profile of AA′. The area hatched in the 2D profile is the cross sectional area of worn aluminum matrix (A_j). From each of eight images as shown in (a), three cross sectional profile was taken to calculate the wear loss.

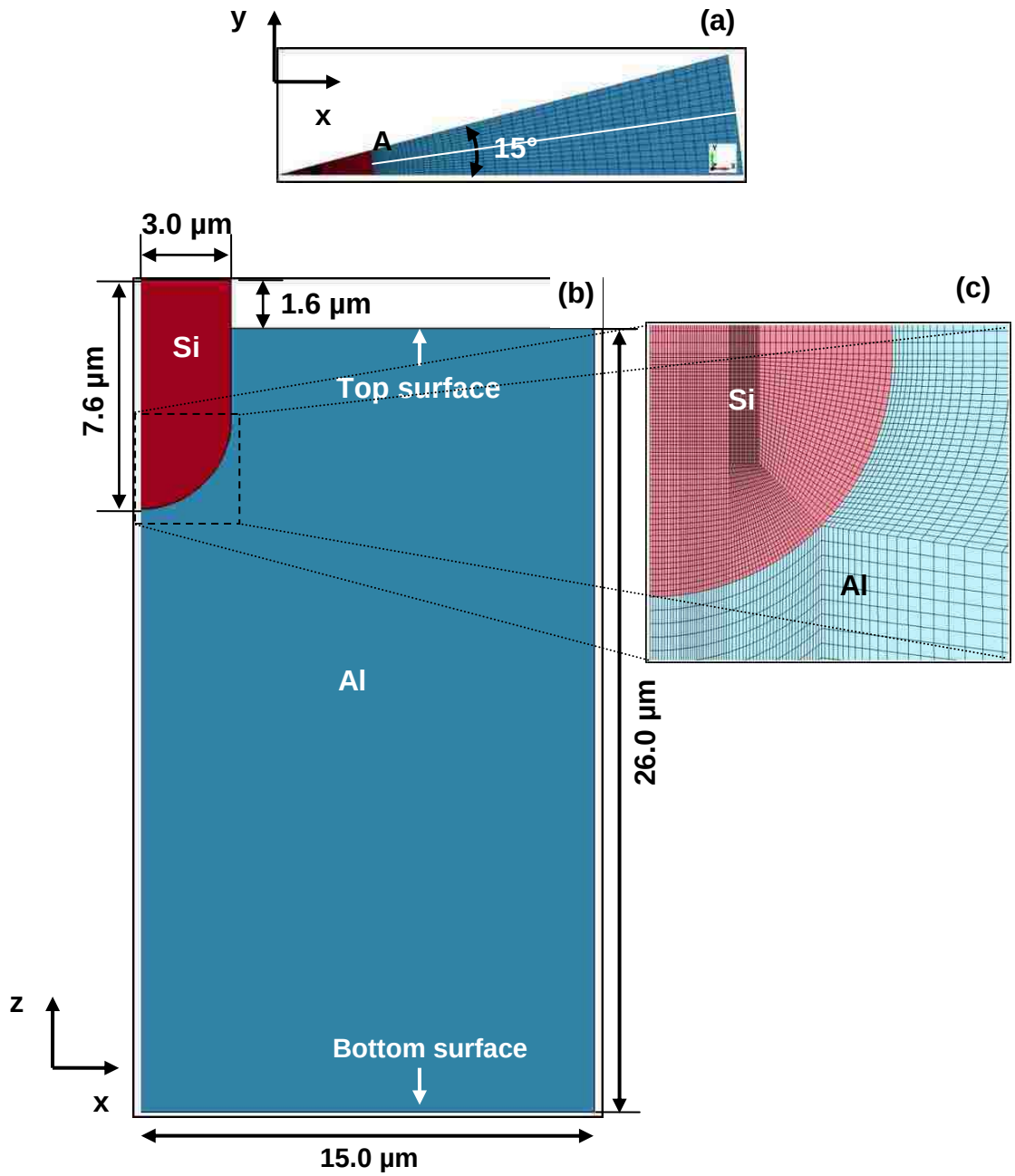

Figure 3. 11: Discretization of 3D model of a silicon particle embedded in aluminum matrix – (a) top view and (b) left side view – the discretization density in the vicinity of the Al-Si interface is shown. The mesh density near the interface indicated by the dotted square is shown in (c).

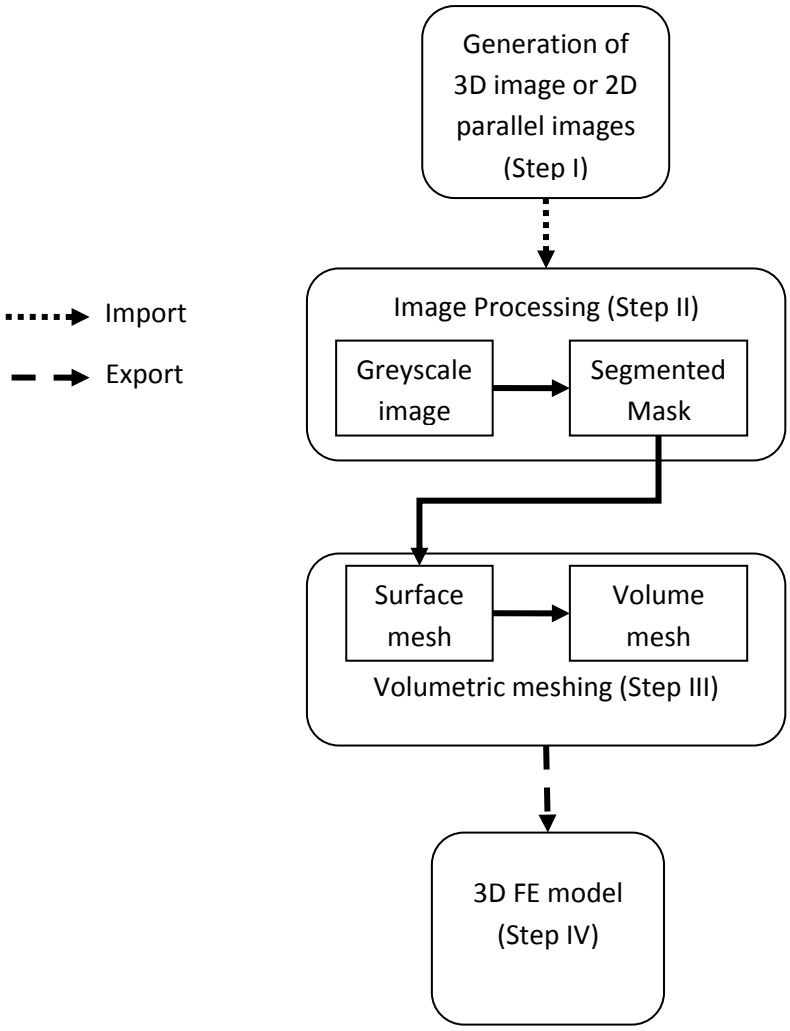

Figure 3. 12: A typical work flow to convert 3D image to 3D FE model using ScanIP. Segmented mask represents the process of identifying different regions within volume of interest. In the multi-particle model the two segments are the aluminum matrix and the silicon particles.

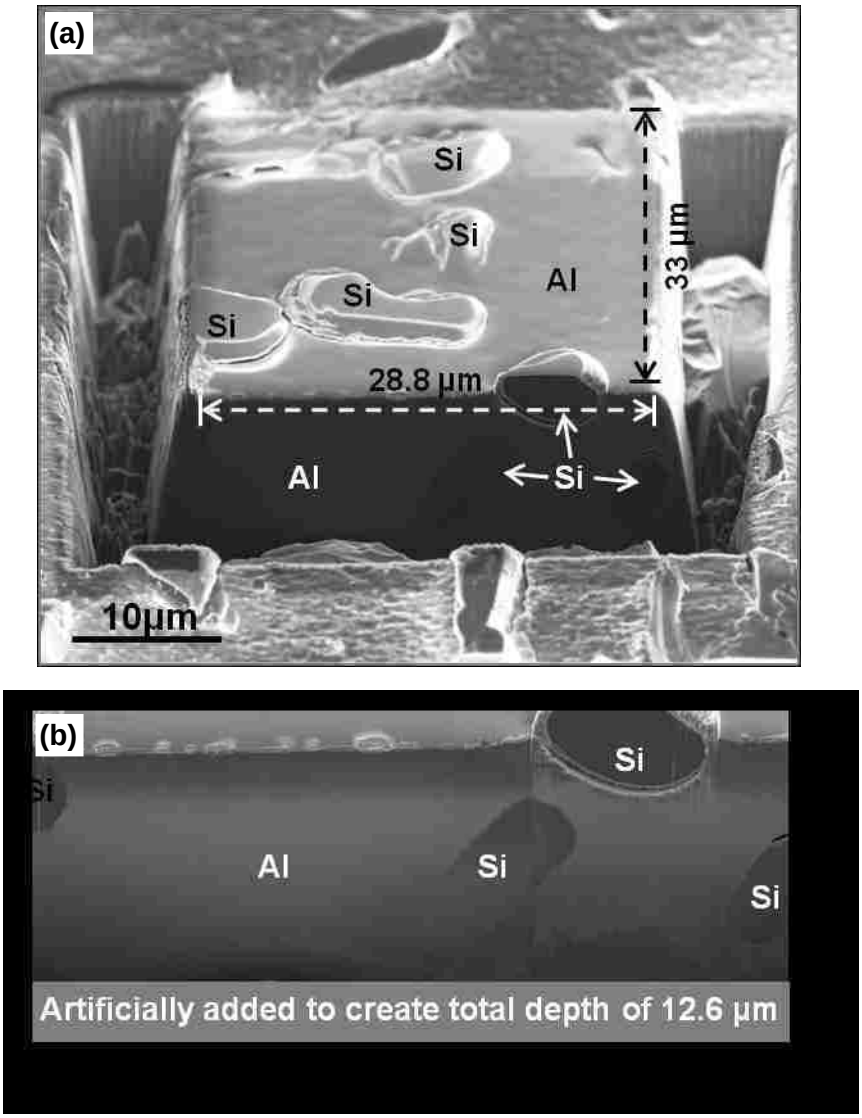

Figure 3. 13: (a) SEM image of the volume of interest (VOI) in Al-12.6% Si alloy from where 2D parallel images spaced between 100 nm were sectioned using FIB; (b) the first section from the VOI showing silicon particles and the aluminum matrix; (c) three principal views of the section from b showing the segmentation of aluminum matrix and silicon particles; (d) volumetric voxel mesh (mesh lines are not shown) and the mesh refinement regions; (e) and (f) final model of the microstructure from Figure 3. 13a with and without the mesh lines, respectively. Silicon particles are numbered with subscripts in (c) and (d) for easy identification of them.

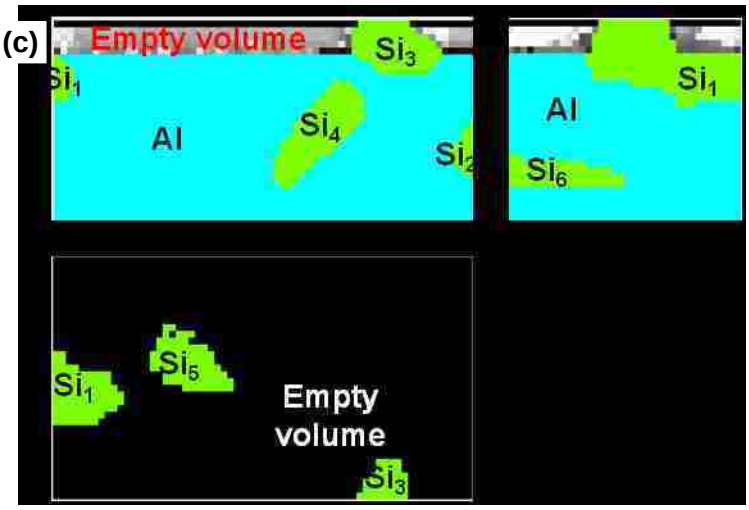

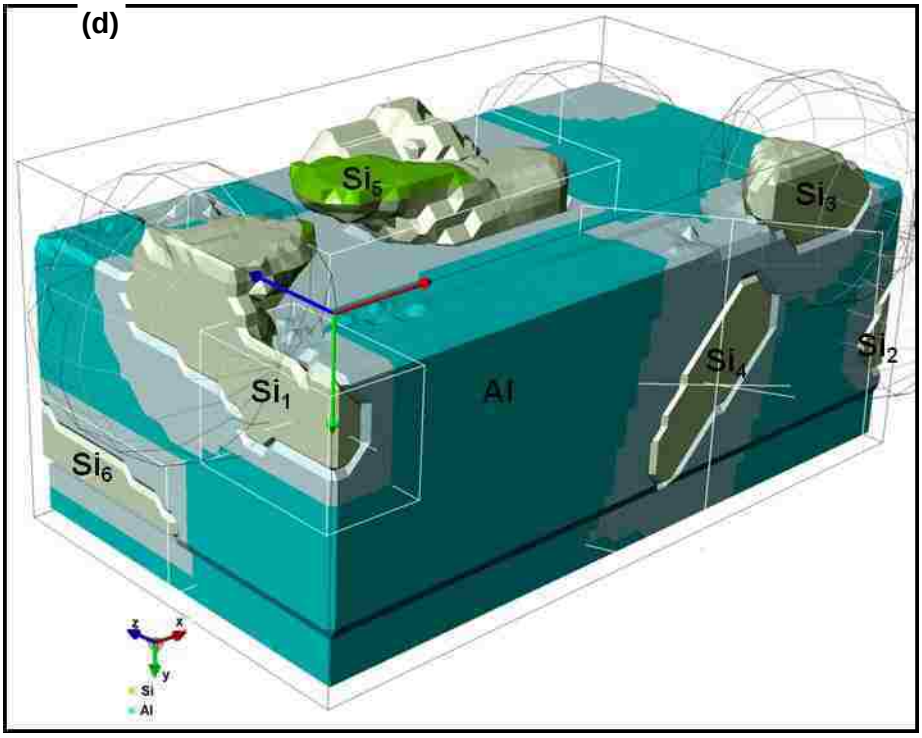

Figure 3. 13: continued

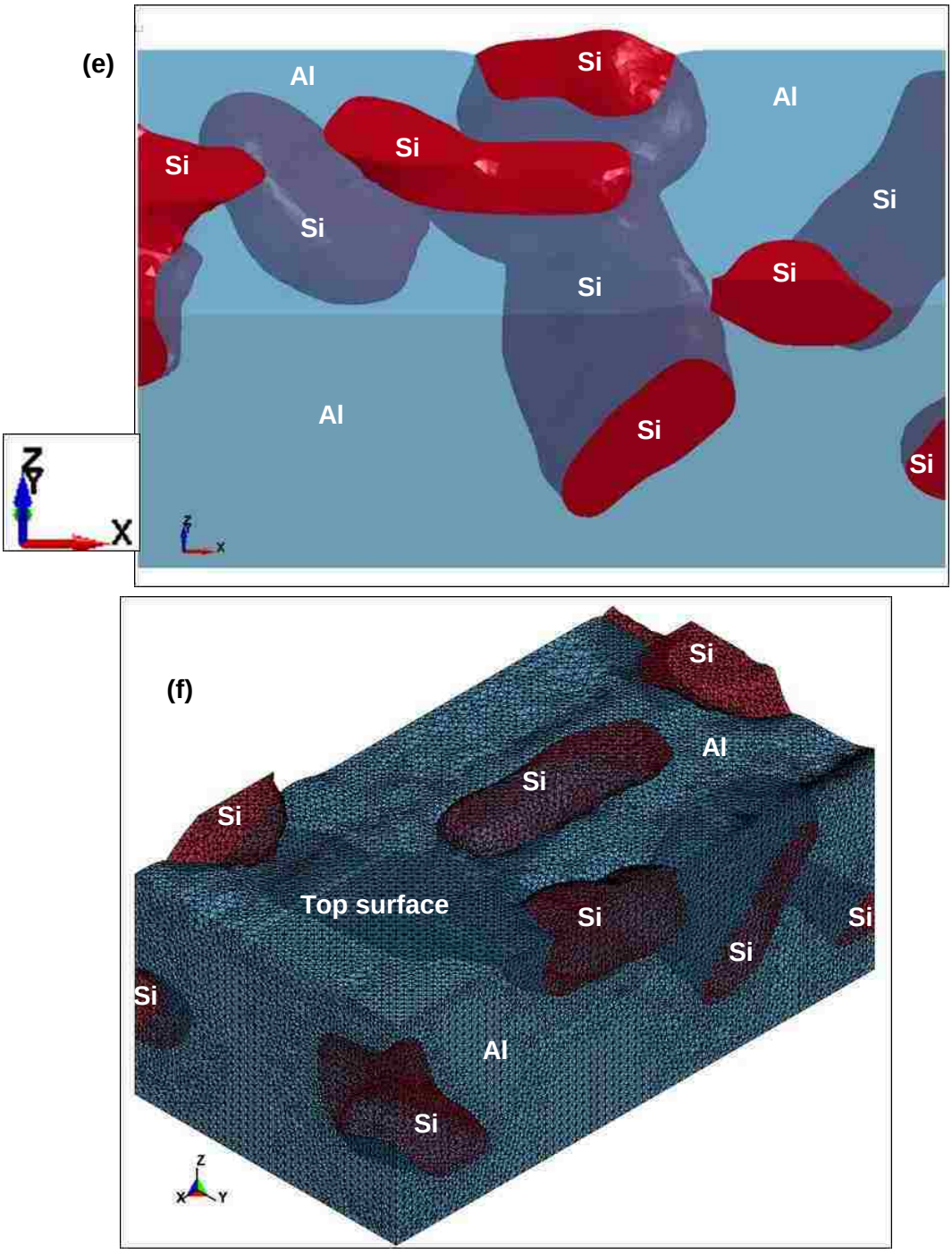

Figure 3. 13: Continued

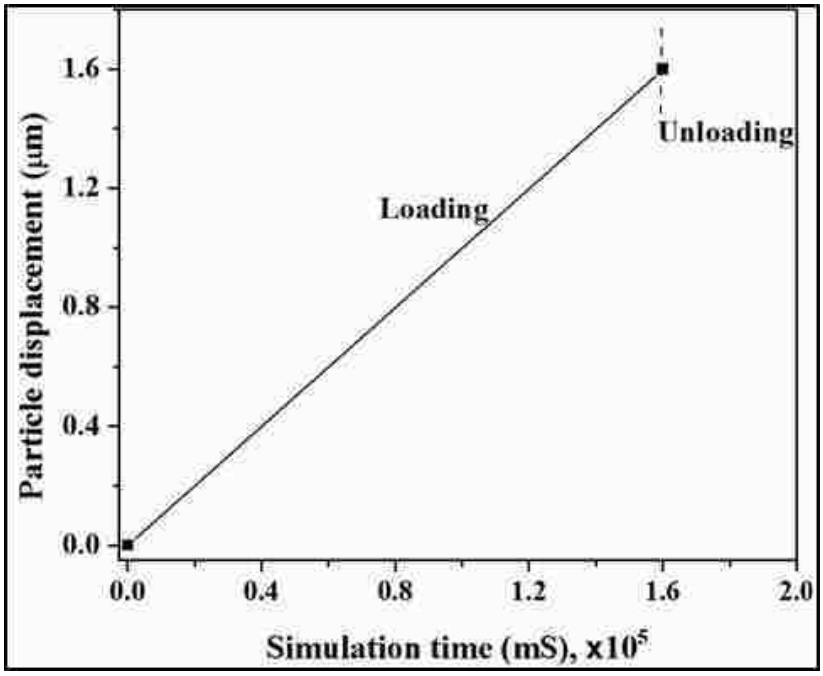

Figure 3. 14: The silicon particle loading-unloading cycle to simulate sinking-in in single-particle model.

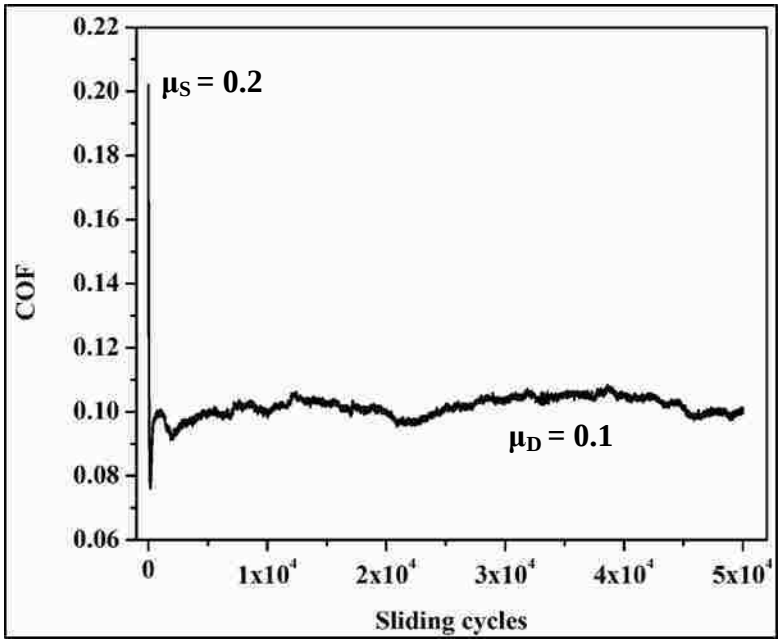

Figure 3. 15: Variation in COF during a lubricated pin-on-disk test using Al-12.6% Si alloys at 2.0 N load; static COF, μ_S=0.2 and average dynamic COF, μ_D=0.1 were used in the simulation.

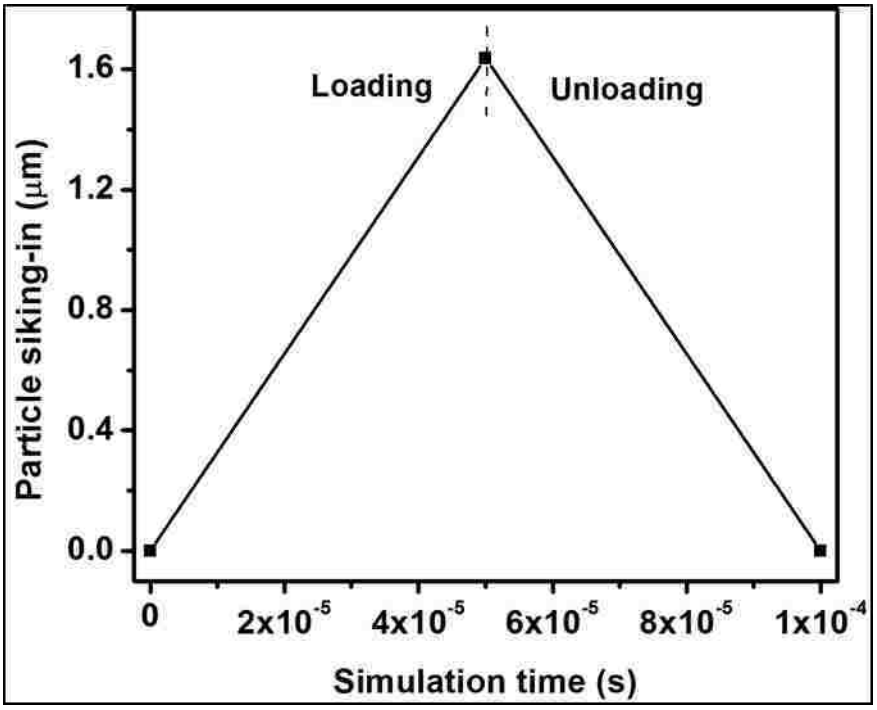

Figure 3. 16: The loading-unloading cycle for the particle sinking-in in multi-particle model. This curve was used to prescribe the displacement of the rigid counterface to simulate particle sinking-in.

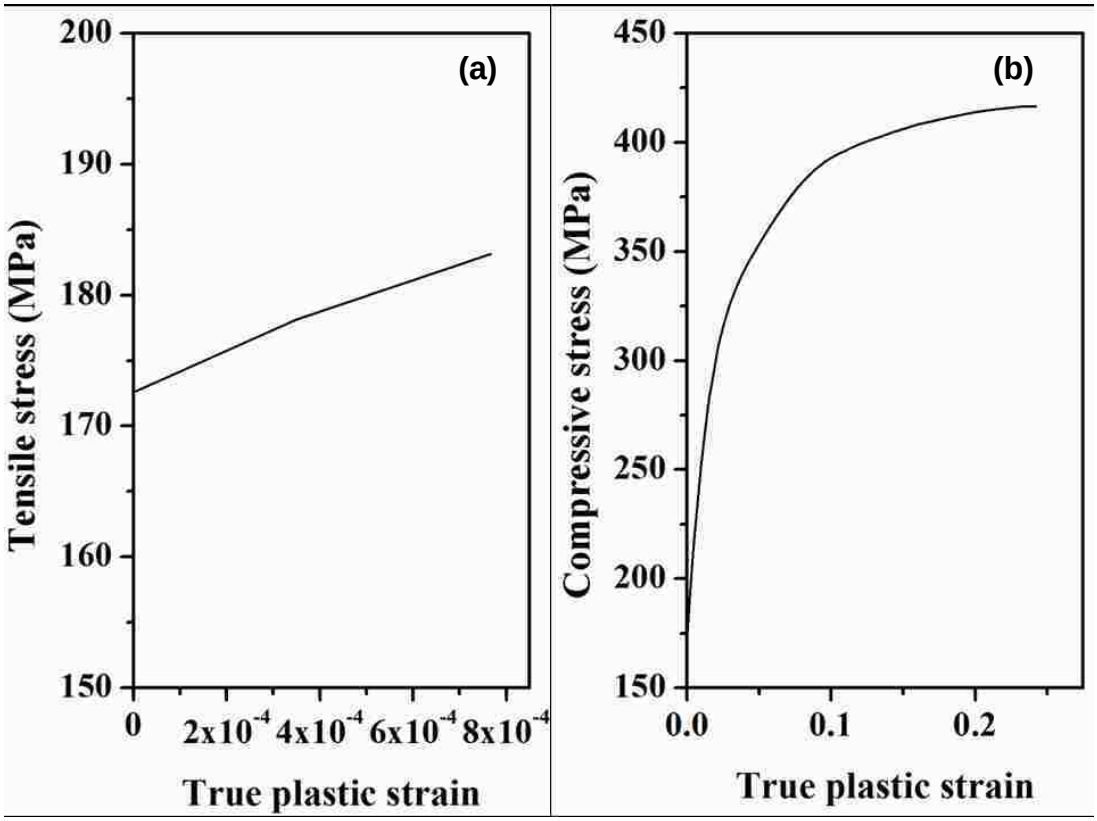

Figure 3. 17: Uniaxial (experimental) effective stress versus effective plastic strain diagram of Al-12.6% Si alloy in (a) compression and (b) tension. The true plastic stress and strain were calculated from the engineering stress and strain values measured from the uniaxial tests, respectively.

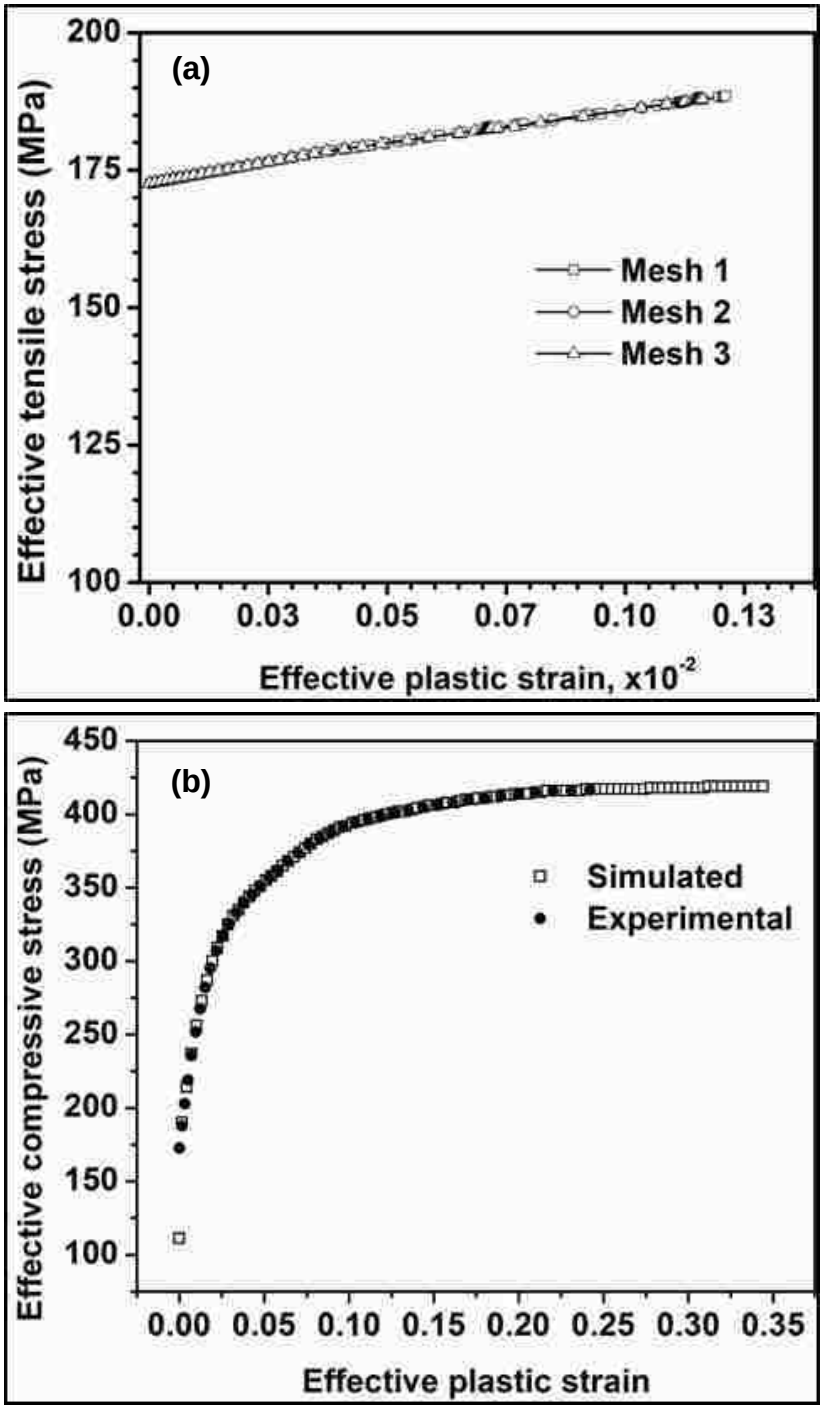

Figure 3. 18: (a) Simulated effective stress versus effective plastic strain diagram obtained from tensile testing. The three models were comprised of 2800, 5120 and 10000 elements. (b) Simulated effective stress versus effective plastic strain obtained from compression testing along the centre of the specimen and the experimental data from compression tests.

4. CHAPTER 4 – REALM OF UMW IN HYPEREUTECTIC Al-Si ALLOY

4.1 Introduction

The previous UMW study [**93**] on Al-18.5% Si alloy at room temperature was conducted at 0.5 N load. This study showed that in Al-18.5% Si alloy the UMW-I stage, a region of zero matrix wear, lasted for very long periods, up to 6×10^5 sliding cycles. Then it was necessary to investigate whether such UMW would last even at higher loads. Therefore in this chapter, the realm of applied load and sliding cycles in UMW in Al-18.5% Si alloy is presented. The UMW wear mechanisms and a UMW to MW transition of Al-18.5% Si alloy at normal load of 5.0 N, which was a magnitude higher than the previous study [**93**], are discussed.

4.2 UMW and MW characteristics – surface damage

At 5.0 N load the wear behaviour was different than that observed in previous studies at low loads (0.5 N). Two different wear regimes, namely UMW and MW, were observed. The UMW was observed to last for a very short period, and the particle fracture and particle sinking-in were observed during this period. With increase in sliding, matrix damage occurred, and a transition to MW was observed. In this section, quantification of key characteristics of surface damage pertaining to the UMW regime and the microstructural evolution will be presented.

4.2.1 Silicon particle height decrease

Figure 4. 1 shows one region of WT after 10^3 sliding cycles at 5.0 N load. The wear track area, as marked by WT in **Figure 4. 1**, was considered for silicon particle height measurement. From each of such regions, the histogram of the surface elevations was plotted and fitted with

two Gaussian peaks in a similar way, as shown in **Section 3.4.1.1**. **Figure 4. 1b** shows the histogram of the surface elevation of the region marked by WT from **Figure 4. 1a** and the fitting of the experimental data with two Gaussian peaks. The silicon particle height as a function of number of sliding cycles is shown in **Figure 4. 2**. It is important to note that after 4×10^5 sliding cycles, silicon particle heights were reduced to zero. In fact, it was not possible to differentiate silicon particle height from the aluminum matrix elevation inside the wear track region for 3×10^5, 6×10^5, and 2×10^6 cycles (see **Figure 4. 6**) because the particles were either pushed into the matrix or abraded by the fragmented particles and the counterface during the early sliding process. Initially at low sliding cycles, the large particles fractured first (see **Figure 4. 3a-c**) and then sank-in. At the same time, plastic deformation of particles also started at the very beginning of the sliding process. The height decrease of silicon particles is the result of the cumulative effects of abrasion (see **Figure 4. 1**), and then fracture and fragmentation followed by sinking-in in the aluminum matrix.

4.2.2 Fracture and fragmentation of silicon particles

Figure 4. 3a-d shows the wear surface morphology after 10^3, 5×10^3, 10^4, and 5×10^4 sliding cycles. Fracture of silicon particles was observed at the beginning, after 10^3 sliding cycles (**Figure 4. 3a**). Silicon particles continued to fracture and fragment into small pieces with an increasing number of cycles (**Figure 4. 3b** and **c**), and some particles were pushed into the aluminum matrix after fracture (**Figure 4. 3d**). The fragmented particles and/or the counterface appeared to abrade by cutting longitudinal marks on silicon particles (see **Section 4.3** for the counterface damage). Thereby the wear of silicon particles accelerated. The abrasion of silicon particles caused the formation of multiple longitudinal trenches on the surface of the particles. As the small particles were pushed into the matrix, the aluminum matrix around the particles was elevated, resulting in pile-up formation (**Figure 4. 3d**). This piled-up aluminum came into

contact with the counterface, and thus the damage to the aluminum matrix initiated as shown in **Figure 4. 3d**. With an increase in the number of sliding cycles, the wear of silicon particles continued; after 5×10^4 sliding cycles, the damage to the aluminum surface became apparent. However, the damage was limited to the raised surface of the pile-ups of aluminum around silicon particles where grooves parallel to each other were formed.

Thus, up to 5×10^4 sliding cycles, the damage was limited to silicon, but their effectiveness in protecting the aluminum matrix from wear decreased as the number of cycles increased. To determine the fractured particle dimensions, silicon particle fracture was quantified by measuring the length and width of the particles before and after fracture as explained in **Section 3.1.1**. At least 100 silicon particles were considered within the wear track, and particles which were partially exposed within the wear track were not taken into the analysis. In addition, a few particles that fractured into small pieces (less than 5μ) were not considered in this measurement. In the regions examined, the average particle length and aspect ratio before fracture and after 10^3, 5×10^3, and 10^4 sliding cycles are listed in **Table 4. 1**. The histogram of silicon particle length before fracture is shown in **Figure 4. 4a,** and the histograms of the fractured Si particle length are shown in **Figure 4. 4b-d**. The histograms indicate the decrease in particle size. A total of 66%, 69%, and 76% of Si particles within the wear track were fractured after 10^3, $5\times10^{3,}$ and 10^4 cycles. It is easier to embed smaller particles which reduce the effectiveness of the particles to withstand contact pressure, and consequently the wear of the Al matrix occurs. The aspect ratio of the silicon particles as they fractured was also measured and is shown in **Figure 4. 4e**. Particles after fracture showed to have a propensity to become more spherical. In **Figure 4. 4e**, the aspect ratio of particles which were not fractured is also shown. It can be observed that the aspect ratio of silicon particles with no fracture is

almost constant and independent of the sliding process. The aspect ratio of particles once fractured tends to reach a value closer to 1.5.

4.2.3 Microstructural evolution of worn surfaces

Fracture and abrasion of silicon particles initiated at low sliding cycles resulted in reduction of silicon particle height to zero beyond 4×10^5 cycles as shown earlier in **Figure 4. 2**. The damage on the aluminum and silicon surface after this sliding could no longer be considered as UMW. The volume loss from the surface was evident indicating that the wear was MW. In this section, results on the aluminum matrix wear and the related surface morphology will be presented.

The damage to the silicon particles was prominent even after 10^3 sliding cycles (see **Figure 4. 4**). The fractured particles acted as abrasive particles during the rest of the sliding contact. With further increase in sliding cycles, the fracture of particles and damage to the aluminum matrix continued to increase, and after 2×10^5 sliding cycles there were hardly any silicon particles standing out of the aluminum matrix in the wear track region (as shown in **Figure 4. 6**). **Figure 4. 5a**-**d** shows the SEM image of the wear surface after 10^3, 10^5, 6×10^5, and 2×10^6 sliding cycles, respectively. After 10^3 cycles (**Figure 4. 5a**), Si particles were still able to carry the load with some abrasive damage and fracture, whereas after 10^5 cycles the particles were embedded into the aluminum matrix, and a significant amount of contact between the aluminum matrix and the counterface was observed (**Figure 4. 5b**). The damage accumulation continued such that after 6×10^5 sliding cycles, the silicon particles were cut severely where the aluminum matrix became exposed and was similarly damaged. The material loss caused by this damage resulted in deepening and widening of the wear track, which will be shown later in this section. This corresponded to transition to MW regime. After 2×10^6 sliding cycles the wear surfaces appeared smoother and were covered by a tribolayer (**Figure 4. 5f**).

At 6×10^5 and 2×10^6 cycles (**Figure 4. 5c** and **e**, respectively), the wear of the alloy surface continued. However, there is one important morphological difference between the 6×10^5 and 2×10^6 cycle wear tests; small fragmented particles caused severe abrasive wear on the surface (**Figure 4. 5c and d**), and consequently after 6×10^5 sliding cycles, the wear track appears to be rough as it was worn by the formation of longitudinal grooves, whereas after 2×10^6 the wear surface is comparatively smooth. The abrasive action of particles on the surface is no longer present after 2×10^6 cycles. Sliding for long cycles made the surface smoother and reduced the rate of material loss. **Figure 4. 5f** shows the EDS spectra within the wear track after 2×10^6 cycles. EDS spectra show the presence of Na, P, S, and Ca whose primary source is the oil used for lubrication during the test. This indicates that during this rubbing process, the longitudinal grooves formed after 6×10^5 cycles were probably filled with the matrix material mixed with fragmented particles and additives from the oil and formed a protective layer on the surface.

Figure 4. 6a-c shows the optical profilometer images of the complete wear track after 3×10^5, 6×10^5, and 2×10^6 sliding cycles. These figures define MW damage in the alloy. Beyond testing for 2×10^5 sliding cycles, the height between silicon particles and aluminum matrix elevation disappeared as described in **Section 3.1** due to particle abrasion, fragmentation, and/or sinking-in. The aluminum matrix remained unprotected and was in contact with the counterface. This had lead to significant material loss. The damage in the wear track was not uniform. There were places along the wear track where the damage was more prominent as the indenting surface conformed to the surface profile of the counterface. The two-dimensional cross-sectional surface profile of the worn surface was obtained by applying a Fourier type filtering to the profilometer data (measured from the eight different areas within the wear track). **Figure 4. 7** shows the average cross-sectional surface profile of the wear tracks with increasing sliding cycles from 10^5 to 2×10^6 cycles. This figure shows the deepening of the

individual scratch marks within the wear track after 3×10^5 and 6×10^5 cycles and somewhat smoothening of the wear track after 2×10^6 sliding cycles in the MW regime. The smoothening of the wear track resulted in a reduction of the volume loss of the aluminum matrix.

4.2.4 Volumetric wear loss

Figure 4. 8 shows the volumetric wear loss against the number of sliding cycles. There was no measurable loss of material up to 10^4 sliding cycles, which corresponded to the UMW regime. When Si particles became embedded in the matrix, the volumetric wear loss increased, and thus the onset of MW became apparent for sliding up to 10^5 cycles. The damage beyond 2×10^5 cycles resulted in further increase in volumetric wear loss, which was considered as MW. A drop in volume loss was noted after sliding for 2×10^6 sliding cycles. However the volumetric wear loss after 2×10^6 sliding cycles was higher than that observed in UMW (typically of the order of 10^{-4} mm^3).

4.3 Counterface damage

The counterface damage was observed using optical profilometer. The volume loss of the counterface was calculated using spherical cap method according to ASTM G99-05 [**116**]. The volume loss for the lower sliding cycles tests (10^3, 5×10^3, and 10^4) were not calculated as there was no apparent change in the counterfaces. **Figure 4. 9a-d** shows the counterface surfaces after 5×10^3, 5×10^4, 6×10^5, and 2×10^6 sliding cycles, respectively. The counterface surface after 5×10^3 sliding cycles had only scratch marks with an average depth (peak to valley distance) of 0.58±0.10 μm formed in the direction of the sliding, whereas that after 5×10^4 sliding cycles had distinct change in the surface profile as observed by the formation of a depression shown in **Figure 4. 9b**. The average depth of the grooves on the counterface surface after 5×10^4 cycles was 0.71±0.15 μm. From the counterface surfaces it was evident that they also caused

abrasive action along with the small fragmented particles. **Figure 4. 9e** shows the calculated volume loss of the steel counterface versus the number of sliding cycles. The counterface after longer sliding cycles had similar surface morphology to that of the alloy surface after wear testing for a similar sliding period as shown in **Figure 4. 7** after 6×10^5 and 2×10^6 cycles, respectively. The surface after 6×10^5 cycles had deeper scratches (2.2±0.54 μm) than those observed on worn surfaces after 2×10^6 cycles (0.93±0.26 μm). The surface roughness of the counterface was also measured using the WYKO software, and **Figure 4. 9f** shows the average surface roughness of the counterface against the number of sliding cycles. The surface after 6×10^5 cycles was rougher (average roughness, R_a of 753 nm) than that after 2×10^6 cycles (R_a of 722 nm). Thus it is conceivable that the counterface initially made an abrasive action on the alloy surface. Later, after prolonged sliding (after 2×10^6 cycles) when a tribolayer formed on the surface, smoothening of the counterface by this tribolayer also contributed in generating less amount of wear on the alloy surface.

4.4 Discussion

4.4.1 Micromechanisms of wear

At 5.0 N load, the wear resistance of Al-18.5% Si alloy has reduced drastically relative to the prior lighter load experiments [**93**]. The characteristic features of the UMW mechanisms and the transition from UMW to MW are schematically summarized in **Figure 4. 10**. Four critical stages were identified for the complete sliding damage process, and each stage was correspondingly identified in the volumetric wear loss graph. Silicon damage started with abrasion accompanied by fracture and fragmentation. Consequently, the wear in the UMW regimes up to 10^4 cycles where there was no measureable volume loss of aluminum. In the second stage, small scale damage accumulated and the load-bearing capacity of silicon particles

reduced significantly as they wore out and fractured during the sliding process. The height of silicon particles and the aluminum elevation became the same (**Figure 4. 2**), and then the transition from UMW to MW regime was observed. Finally, formation of a hard surface and oil-residue layer reduced the MW.

When the wear studied by applying an order of magnitude lower load (0.5 N) [**93**], silicon particles were neither fractured nor sunk-in in the matrix; the damage was limited to abrasion on top of silicon particles in the form of longitudinal surface scratches parallel to the sliding direction. No sinking-in of particles was observed, and original silicon height was maintained. In Al-12% Si [**92,93**] with a lower matrix hardness of 392 MPa, particle sinking-in and aluminum pile-up formation subsequently were observed. The Al-18.5% Si alloy has higher hardness (834 MPa) in addition to high-volume fraction of large silicon particles. It seems that in this alloy, particle sinking-in does not occur immediately as the contact is made. The two possible reasons could be that the matrix has a higher hardness and/or the exerted contact pressure is not high enough to overcome the matrix hardness and deform the matrix plastically. At 0.5 N load, both conditions were met, that is, the matrix had a higher hardness and the contact pressure applied was not greater than the matrix hardness. At 5.0 N load, however, the scenario has changed and is discussed more critically with the help of contact pressure argument in **Section 4.4.2**.

4.4.2 Mechanics of wear: contact pressure applied to silicon particles

The estimation of contact pressure was carried out by adopting the Greenwood and Tripp model [**100,117**] as it was carried out by Chen et al. [**93**]. The maximum contact pressure, P_r, at the centre of the contact is expressed as:

$$P_r = \frac{dP}{dr} = \left(\frac{4}{3\pi}\right) E^* \left(\frac{\sigma}{R_p}\right)^{1/2} \frac{F_{3/2}(h)}{F_1(h)}\Big|_{r=0} \tag{4.1}$$

where E^* is the reduced Young's modulus, R_p is the particle length, σ is the standard deviation of the particle height, and $F_{3/2}(h)$ and $F_1(h)$ are the parabolic cylinder functions; the general solution for such functions for Gaussian distribution can be given as:

$$F_m(h) = \frac{1}{\sqrt{2\pi}} \int_h^\infty (s-h)^m exp\left(-\frac{s^2}{2}\right) \quad (4.2)$$

From **equation 4.2** it can be seen that the real contact pressure depends on E^*, R_p, σ, and $F_{3/2}(h)$, and $F_1(h)$. Once the particles fractured and R_p reduced, the real contact pressure increased. The parameters required to calculate the contact pressure are given in **Table 4. 2**. According to **Figure 4. 11a**, the highest contact pressure occurred at the centre of the contact and was 1079.4 MPa. The maximum contact pressure was 1.3 times higher than the matrix hardness (H=834 MPa). Assuming that particle sinking-in occurs when the contact pressure is greater than or equal to an indentation pressure, P, which in turn is equal to 2.89Y (Y, the yield stress of the material in tension) or the matrix hardness [**118**], it is expected that sinking-in would occur as the contact is made. However, the sinking-in was not observed immediately at the beginning of the sliding process. It seemed that relatively higher matrix hardness (834 MPa) and the higher contact pressure resulted in fracture of silicon particles first. But, if the matrix hardness had been lower as in the case of Al-12% Si [**92,93**], sinking-in would have been possible right away at the beginning of the sliding process. In other words, embedding of silicon particles was resisted by high matrix hardness, and the energy spent in applying the load was released by the formation of cracks in silicon particles and their ultimately fracture.

Fracture of the silicon particles worsens the mechanics of the contact between particles and the counterface. The particle size became smaller (**Figure 4. 4b-d**), and this had an adverse effect on the wear resistance in this particular alloy. The change in contact pressure as a function of particle size is plotted in **Figure 4. 11b** for Al-18.5% Si alloy at 5.0 N load. This figure indicates that the maximum contact pressure exerted on the silicon particles at 5.0 N could be

as high as 2.72 GPa at a particle length of 5 µm. So, as the contact pressure increased, more particles fractured, and then some particles did sink in even with higher matrix hardness resulting in aluminum pile-up formation (**Figure 4. 3d**). The damage to the aluminum matrix thus began, and the process continued with damage occurring in both matrix and particles to the point where there was no protection to the aluminum matrix. Thus, the alloy wear entered into MW regime. In the MW regime, the fragmented particles cut the aluminum matrix severely (**Figure 4. 5c** and **d**). Another factor which affected the aluminum wear in MW regime was the interparticle distance in this particular alloy. Because of the presence of large particles, there were areas where the interparticle distance was high enough such that large sections of aluminum became exposed without any protection from silicon. In the MW regime, once aluminum became exposed completely, the contact pressure argument did not hold true because of change in contact asperities, as the silicon particles no longer could be counted as contacting asperities. At this point in time, a high strain, shear induced deformation controlled the wear mechanisms and damage to the alloy. The previous study on an $AlSi_{17}Cu_4Mg$ alloy by Dienwiebel et al. [**95**] showed that a new surface layer was formed during running-in consisting of wear particles from different sources and from the aluminum matrix. This layer provided the wear resistance of the cylinder bore. In an earlier study by Pereira et al. [**80**], formation of antiwear films on top of silicon particles in a near hypereutectic Al-Si alloy was observed which helps in improving wear resistance. In the recent past, Chen et al. [**94**] had studied the formation of an oil-residue layer in Al-11% Si and Al-25% Si alloys. The study [**94**] showed that once the oil-residue layer formed, there was no evident difference between the wear rates of the two alloys. This was due to the formation of an ultra-fine aluminum grain substructure with high hardness beneath the thin oil-residue layer, which together enhanced the resistance of both alloys against sliding deformations. In the present study, with the evidence of the presence

of elements (see **Figure 4. 11a**) on the wear surface whose primary source is the lubricating oil, it is plausible that a similar protective oil-residue layer forms onto the wear surface after prolonged sliding up to 2×10^6 which stabilizes the MW.

It is also possible that the contact pressure at longer sliding surfaces was lowered due to increase in contact area. Therefore, the Hertzian pressure was calculated by measuring the radius of curvature of the wear track and the counterface using optical interferometer. The effective curvature was calculated to be 4.05×10^{-3} m and the composite modulus was calculated to be 62.2 GPa. **Figure 4. 11c** shows the Hertzian pressure distribution after 2×10^6 cycles and the drop in maximum contact pressures and increase in the contact area is apparent from **Figure 4.11c**. Thus increase in contact area after long sliding process in MW region also reduced the applied contact pressure which contributed to the stabilisation of volumetric wear loss.

4.4.3 Chapter summary

In this chapter, results of boundary lubricated POD tests on an Al-18.5% Si alloy were presented. The results showed that this hypereutectic alloy, used in the linerless automobile engine block, also had its limitation at higher contact pressures. The previous experiments [**93**] using this alloys at lower load (0.5 N) indicated that the UMW could be maintained in this alloy for a very long time. However, an increase in the applied load by an order of magnitude to 5.0 N resulted in UMW-MW transition after a short sliding duration. At lower load the silicon particles were able to withstand the contact pressure during sliding contact and maintain UMW regime for a very long period. Also, there was no change in particle morphology due to fracture during sliding, contact pressure virtually remained unchanged, and the large block-like primary silicon particles were able to protect the matrix from permanent damage. Thus, it seemed that the alloy was a perfect choice for UMW applications. However, extrapolation of such information must be done with caution as increase in applied pressure during sliding contact can worsen the

situation. The increase in applied load caused a corresponding increase in maximum applied contact pressure from 740.55 MPa at 0.5 N to 1079.4 MPa at 5.0 N at the centre of the contact. Thus it can be said that the UMW in this hypereutectic alloy was dependent on the applied load or the contact pressure during sliding contact; care must be taken during the design and manufacture of engine block using these alloys to consider overloading in actual engine running conditions and possible remedies which may be applied to prevent early engine failure. The pressure dependency of UMW is probably true for all Al-Si alloys, but more experiments may be needed to verify that information.

The following specific summary was made from the results presented in this chapter:

- UMW in Al–18.5% Si alloys occurred due to abrasive action on top of exposed Si particles and fracture of larger particles. The UMW lasted for very short sliding cycles (up to 10^4 cycles). Early fracture of silicon particles dominated the wear mechanism. Silicon sinking-in, common in Al–Si alloys with low matrix hardness, was not observed until the particles were fractured into smaller size.
- The onset of MW coincided with complete wearing out of exposed silicon particles. In MW, the matrix, no longer protected by silicon particles, was subjected to high wear rate by abrasive action of the counterface and/or fragmented silicon particles.
- The MW damage stabilized after prolonged sliding. The MW damage was stabilized possibly due to formation of a protective Tribolayer and increase in apparent contact area.

TABLES – CHAPTER 4

Table 4. 1: Average length and the aspect ratio of silicon particles within WT of Al-18.5% Si alloy before fracture and after 10^3, 5×10^3 and 10^4 sliding cycles.

Sliding cycles	Particles with fracture		Particles without fracture	
	Length (μm)	Aspect ratio	Length (μm)	Aspect ratio
0 (Initial)	41.7±27.0	3.2±0.6	-	-
10^3	30.9±23.3	2.0±0.7	19.4±14.7	1.5±0.9
5×10^3	25.6±12.4	1.5±0.7	18.1±15.1	1.6±0.8
10^4	23.3±14.0	1.6±0.9	19.9±18.3	1.6±0.7

Table 4. 2: Parameters required calculating the contact pressure distribution and maximum contact pressure variation with particle size in Figure 4. a and b.

Composite modulus, E^*, (GPa)	Particle length, R_p (μm)	Standard deviation of particle height, (μm)	Area density of particles
62.2	41.69	0.064	0.19

FIGURES – CHAPTER 4

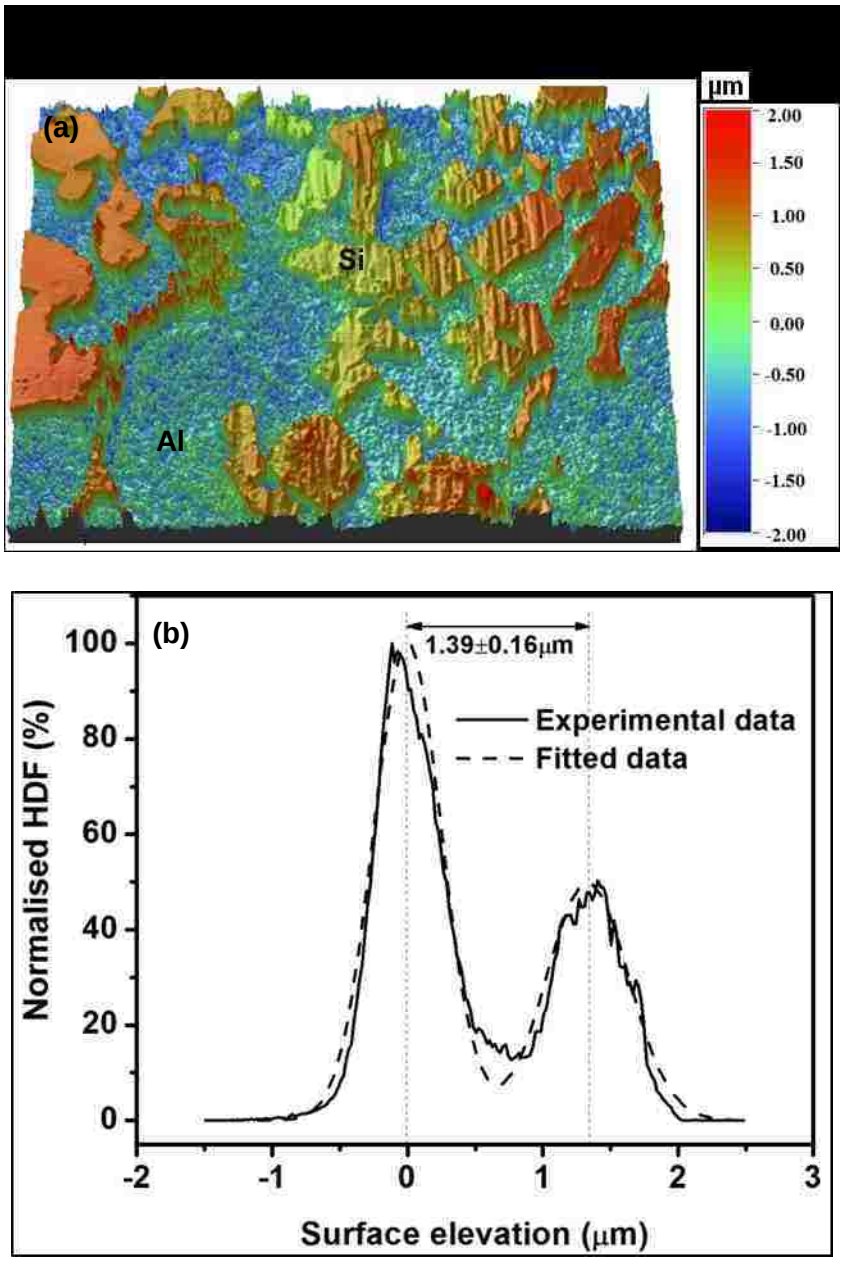

Figure 4. 1: (a) Optical interferometer image (296 µm × 225 µm) for Al-18.5% Si alloy, showing WT after 10^3 sliding cycles at 5.0 N load; (b) The histogram of the surface elevation within the region marked by WT in (a) and the fitted data to measure silicon particle height.

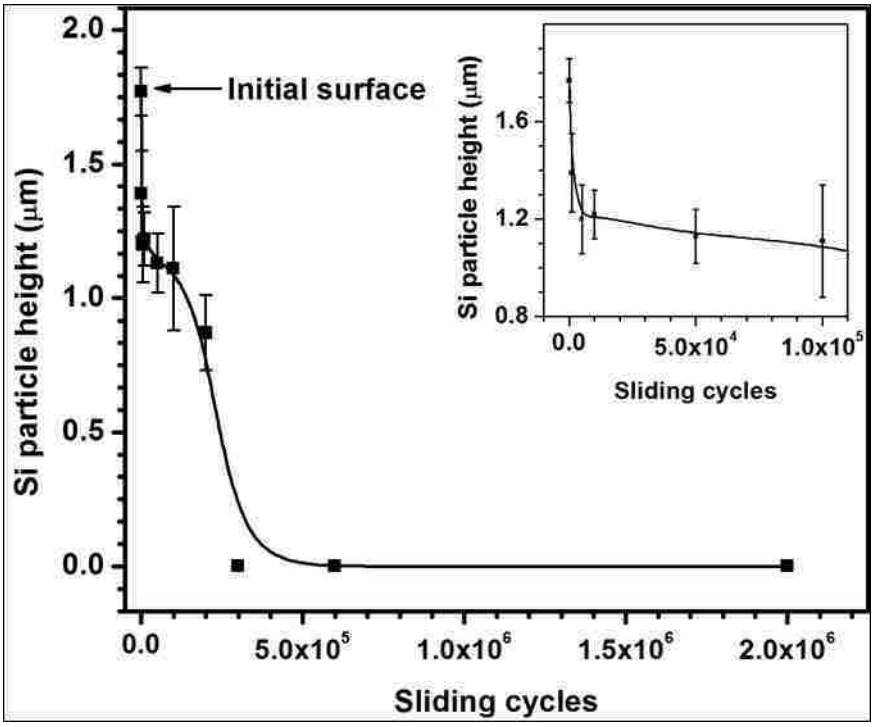

Figure 4. 2: Silicon particle height reduction in Al-18.5% Si alloy with increasing number of sliding cycles at 5.0 N normal load.

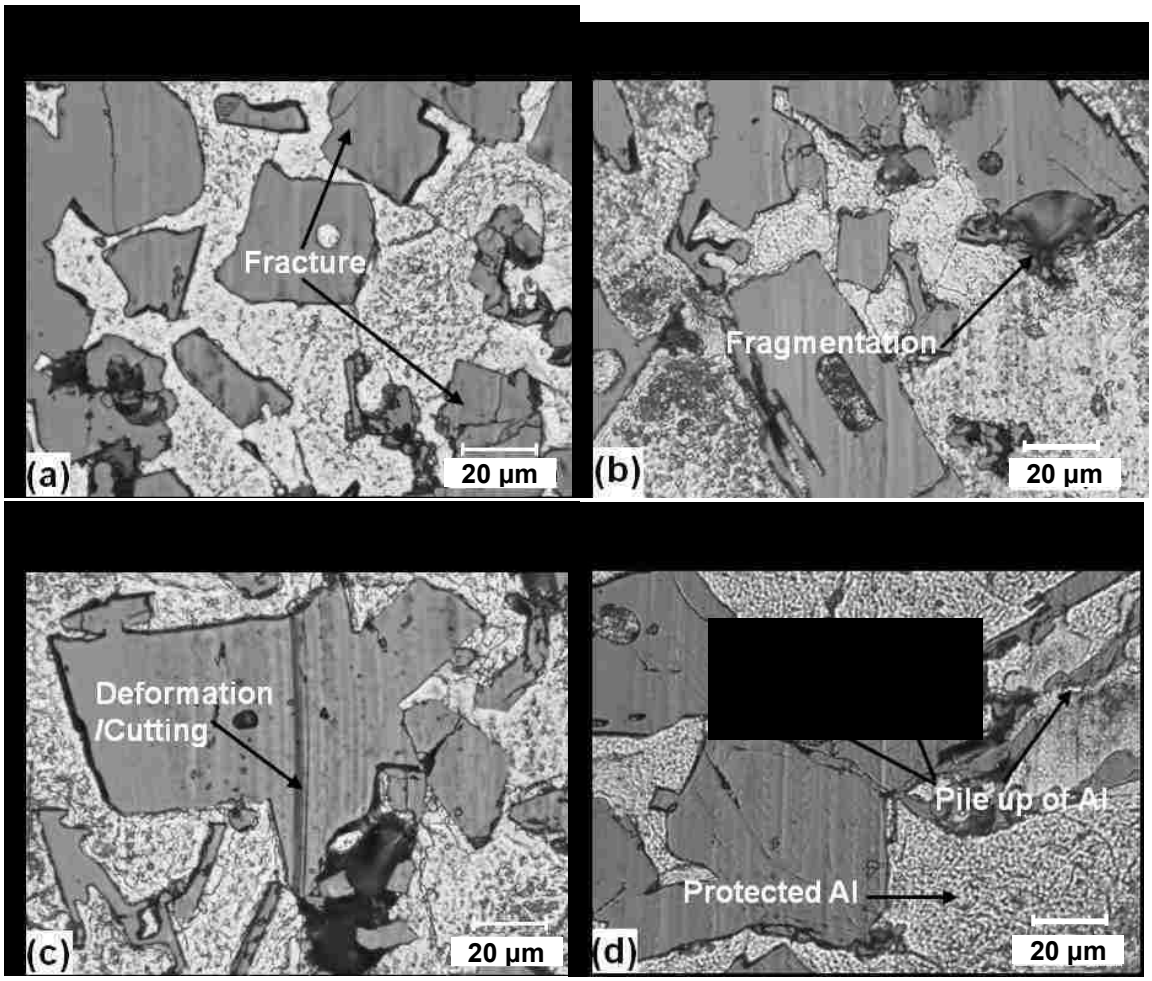

Figure 4. 3: Optical images of WT after (a) 10^3, (b) 5×10^3, (c) 10^4 and (d) 5×10^4 cycles at 5.0 N load. Initially the particles fracture and deform plastically; then small particle sink-in and aluminum pile-up takes place. The piled-up aluminum marked by dotted lines in (d) came in contact with counterface making them flat.

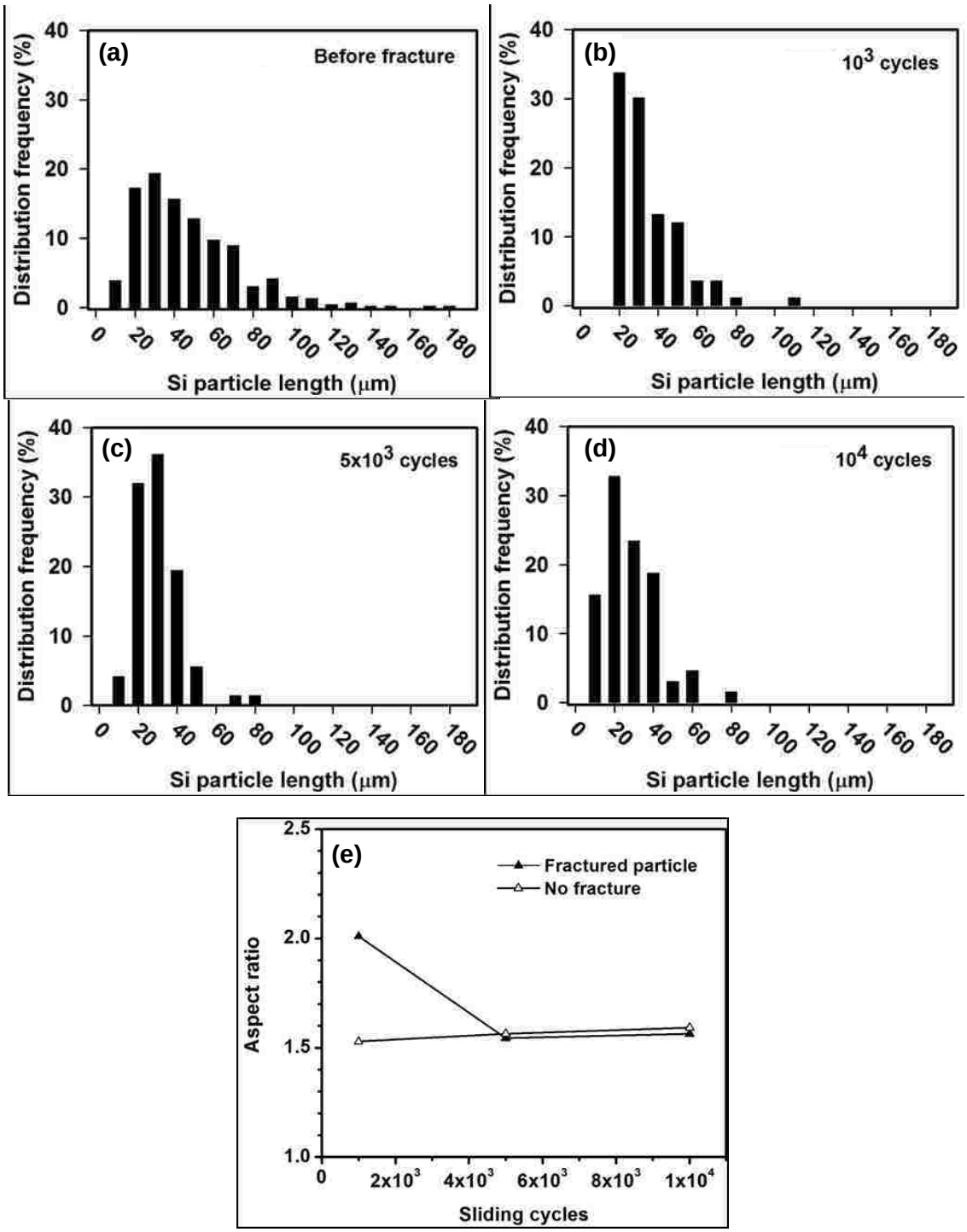

Figure 4. 4: (a) Histogram showing Si particle length distribution frequency within the wear track (a) before fracture, after (b) 10^3, (c) 5×10^3 and (d) 10^4 sliding cycles; (e) aspect ratio of Si particles after fracture (within the wear track) and particles with no fracture as a function of sliding cycles. The aspect ratio of the particles before fracture was 3.23.

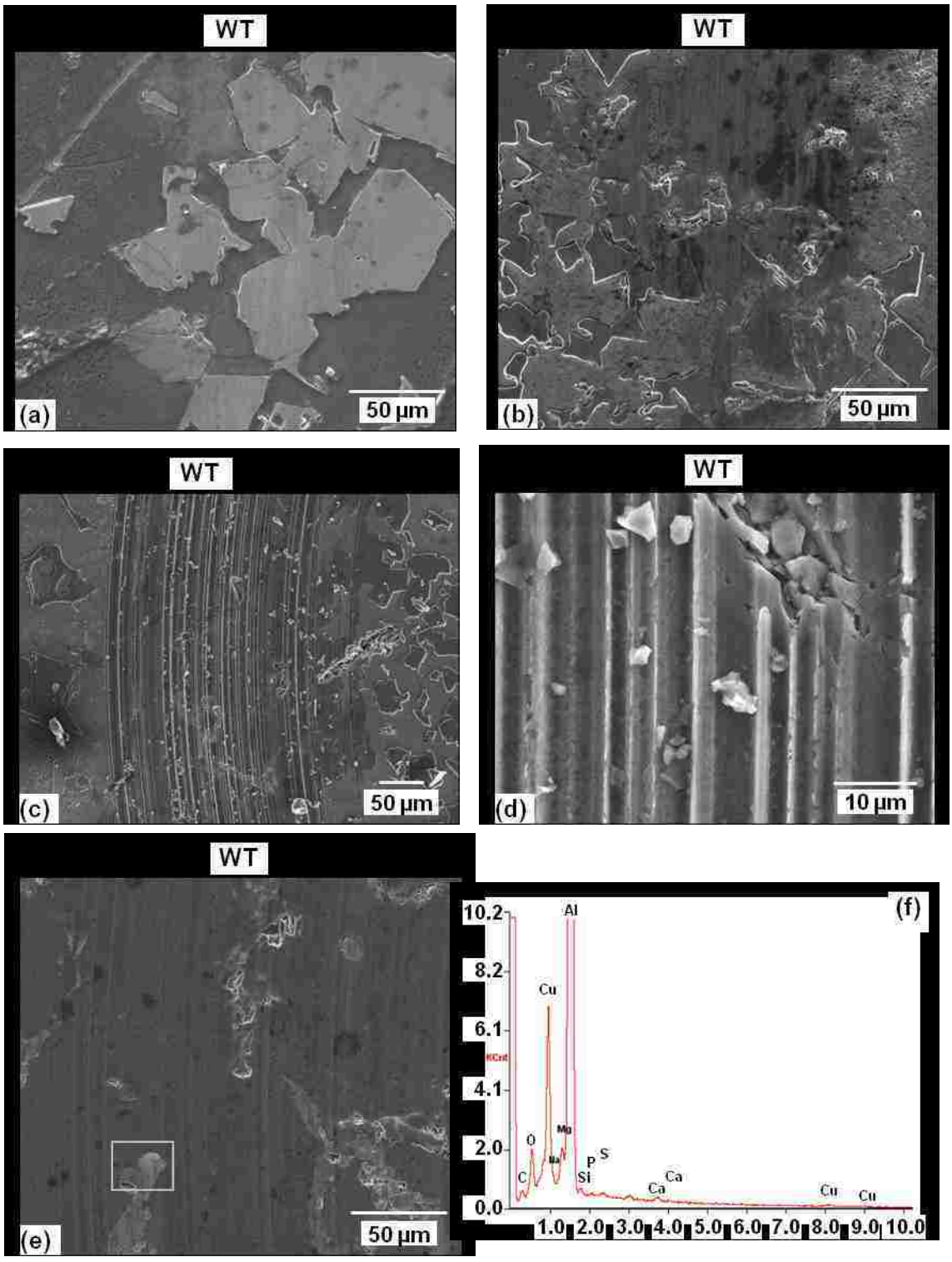

Figure 4. 5: SEM images showing the wear surface after (a) 10^3 (UMW); (b) 10^5 (at the onset of MW) (c) 6×10^5 (MW); (d) magnified image of wear track after 6×10^5 cycles from (c); (e) 2×10^6 (stabilized MW) sliding cycles. The arrow line indicates the location of the wear track. The EDS spectrum in (f) was taken from the inset shown in (e).

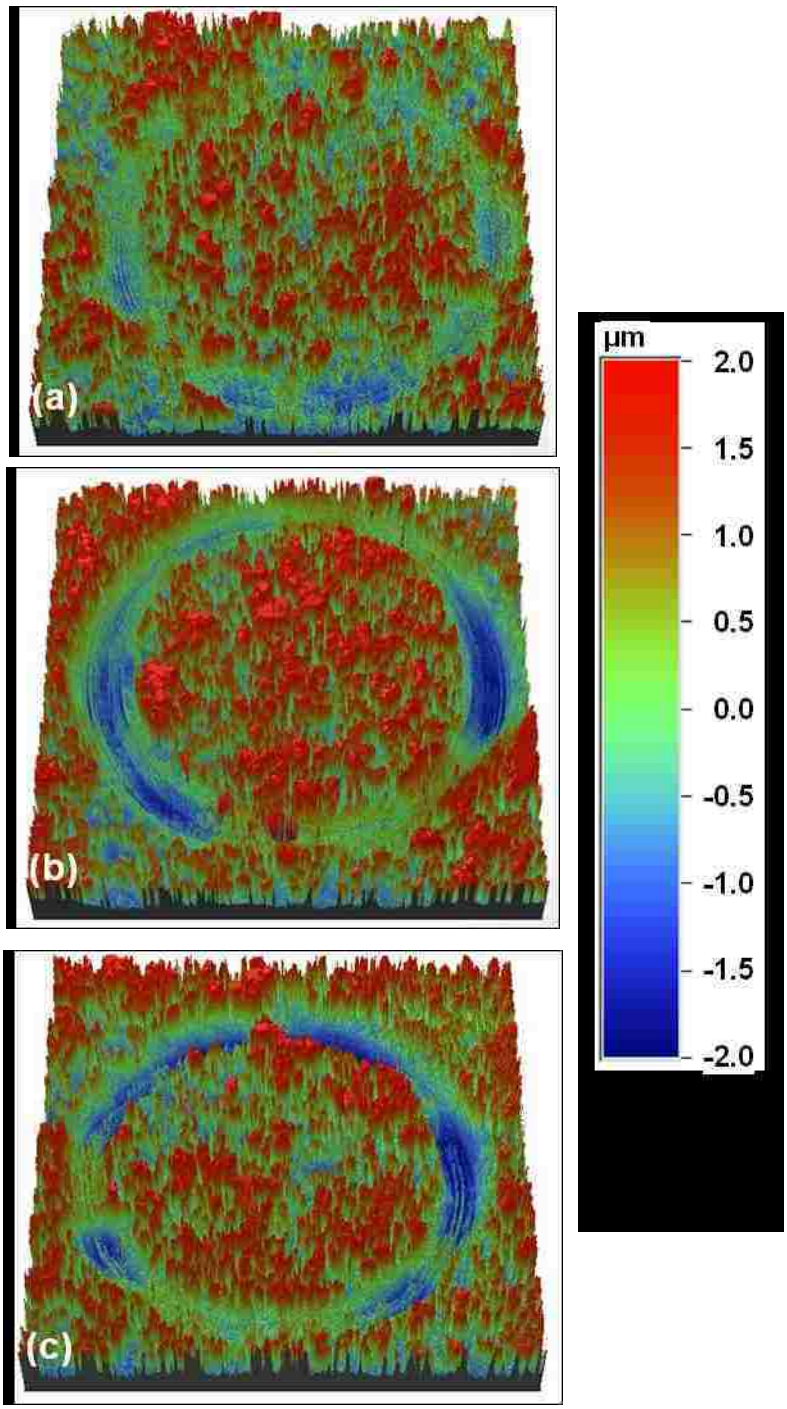

Figure 4. 6: 3D optical interferometer images of complete wear track after (a) 3×10^5, (b) 6×10^5 and 2×10^6 sliding cycles corresponding to MW. The scale bar shows the elevation of the surface, and matrix damage is visible within the wear track.

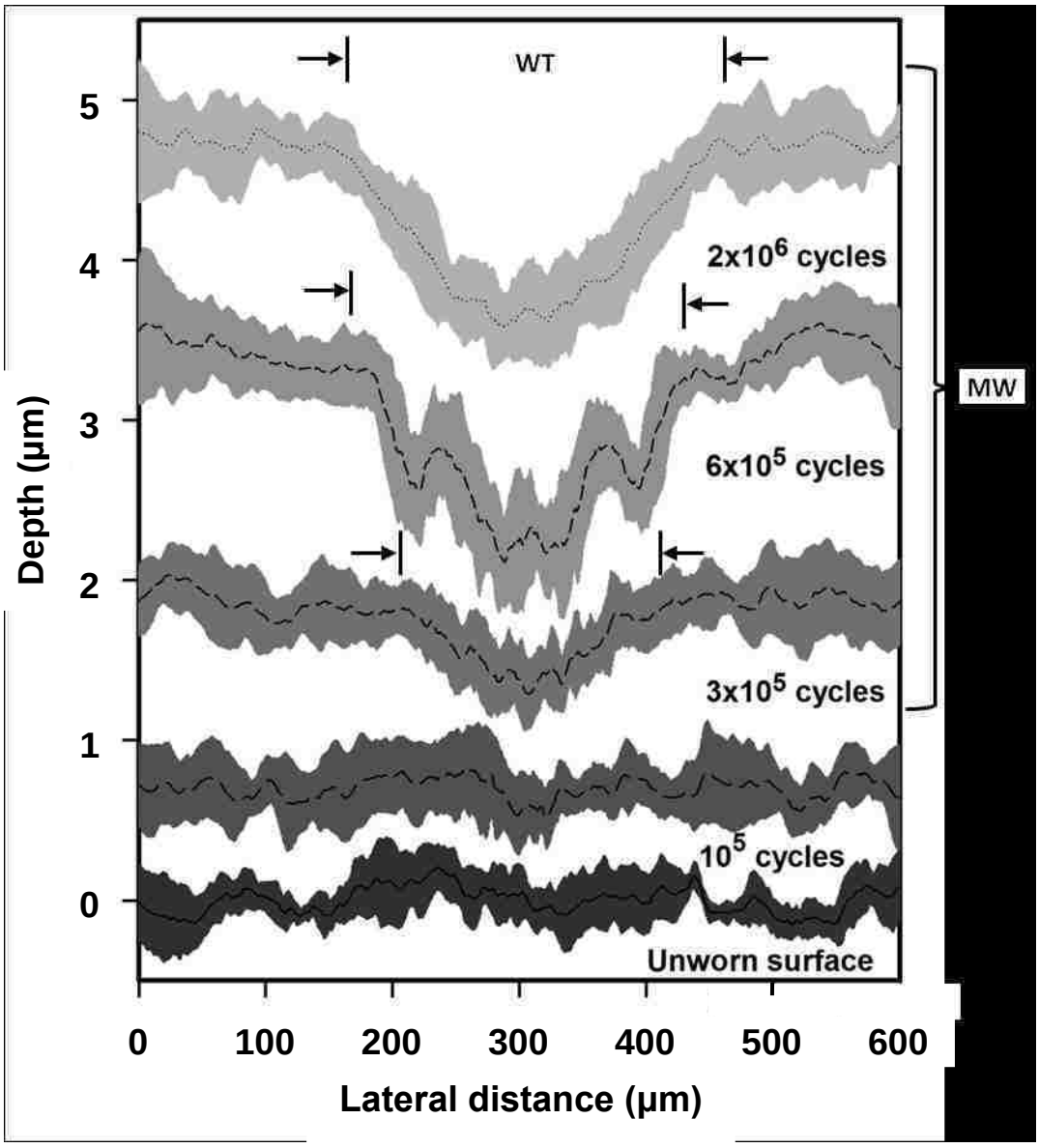

Figure 4. 7: Average surface profiles of the (a) unworn surface and wear surfaces after (b) 10^5, (c) 3×10^5, (d) 6×10^5 and (e) 2×10^6 cycles. The width of each curve represents the standard deviation of the profiles taken from eight different regions in different areas of the wear track. The arrow indicates the location of the wear track.

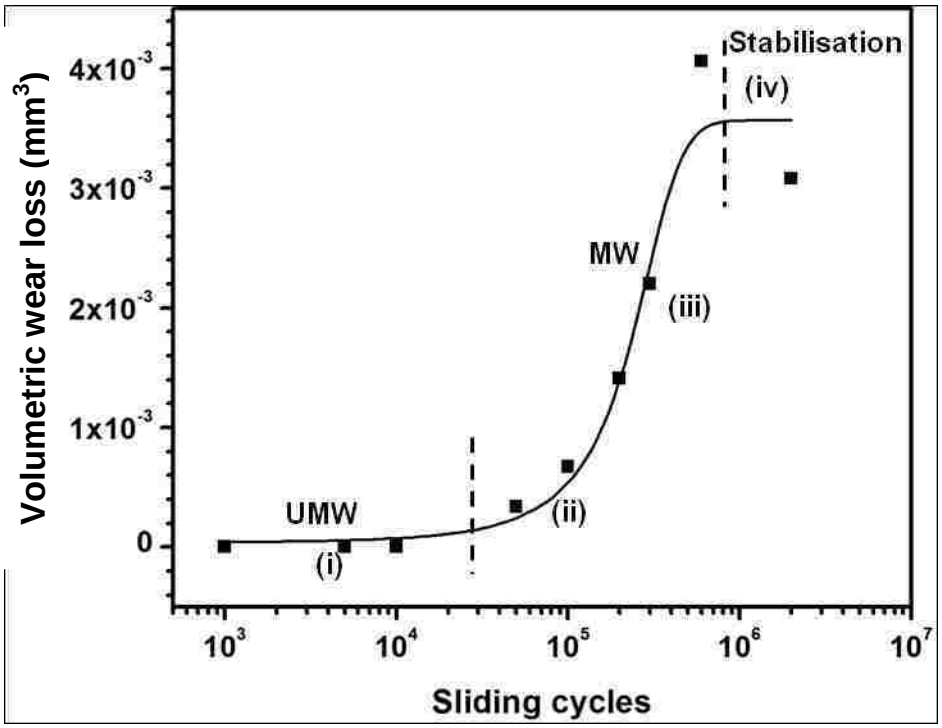

Figure 4. 8: Volumetric wear loss of Al-18.5% Si alloy at 5.0 N load. The wear loss was measurable only after 5×10^4 sliding cycles. The roman numerals indicate the stages of damage process as explained in Section 4.2.3

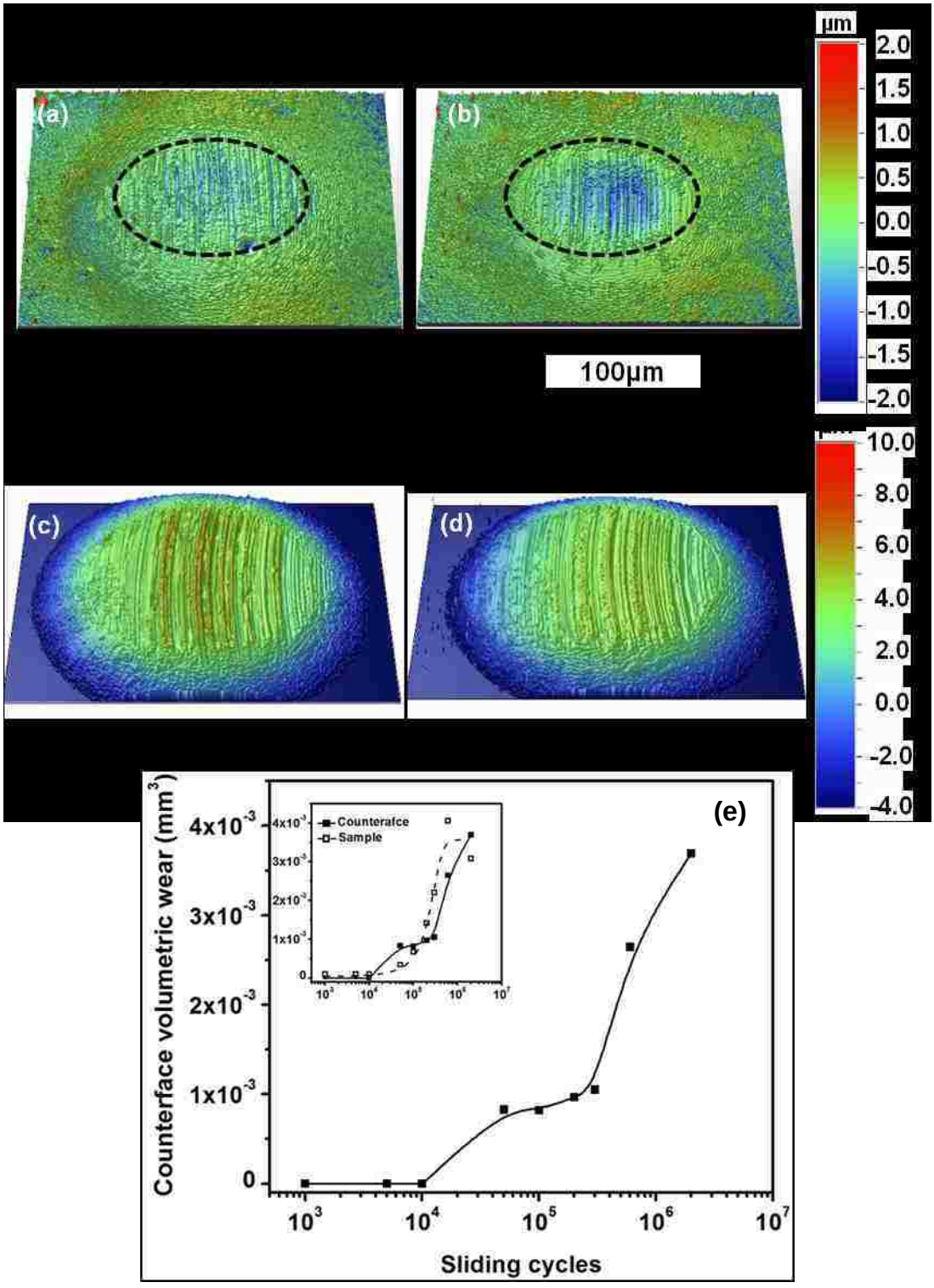

Figure 4. 9: 3D optical interferometer images of the AISI 52100 steel counterfaces against 18.5% Si alloy after (a) 5×10^3 (b) 5×10^3 (c) 6×10^5 and (d) after 2×10^6 sliding cycles. The scale bar shows the elevation of the surface; (e) volumetric wear of the counterfaces as a function of sliding cycles; (f) Change in average surface roughness of the counterface with sliding cycles. The inset in (e) shows the wear of alloy sample for comparison with that of counterface

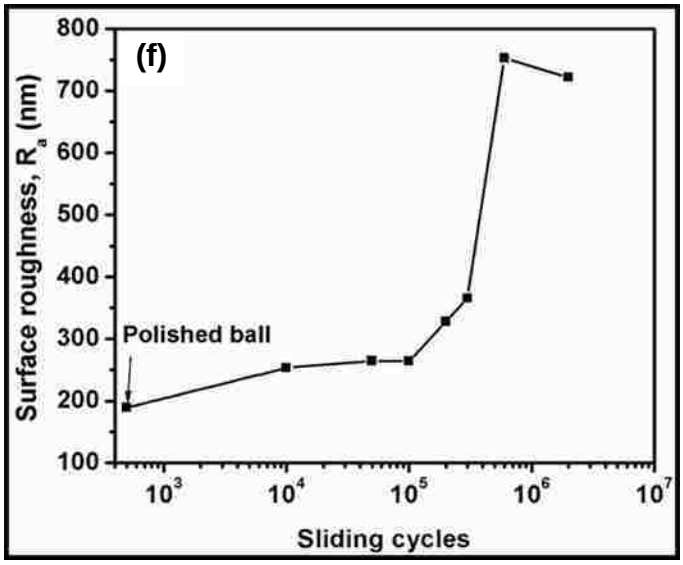

Figure 4. 9: Continued

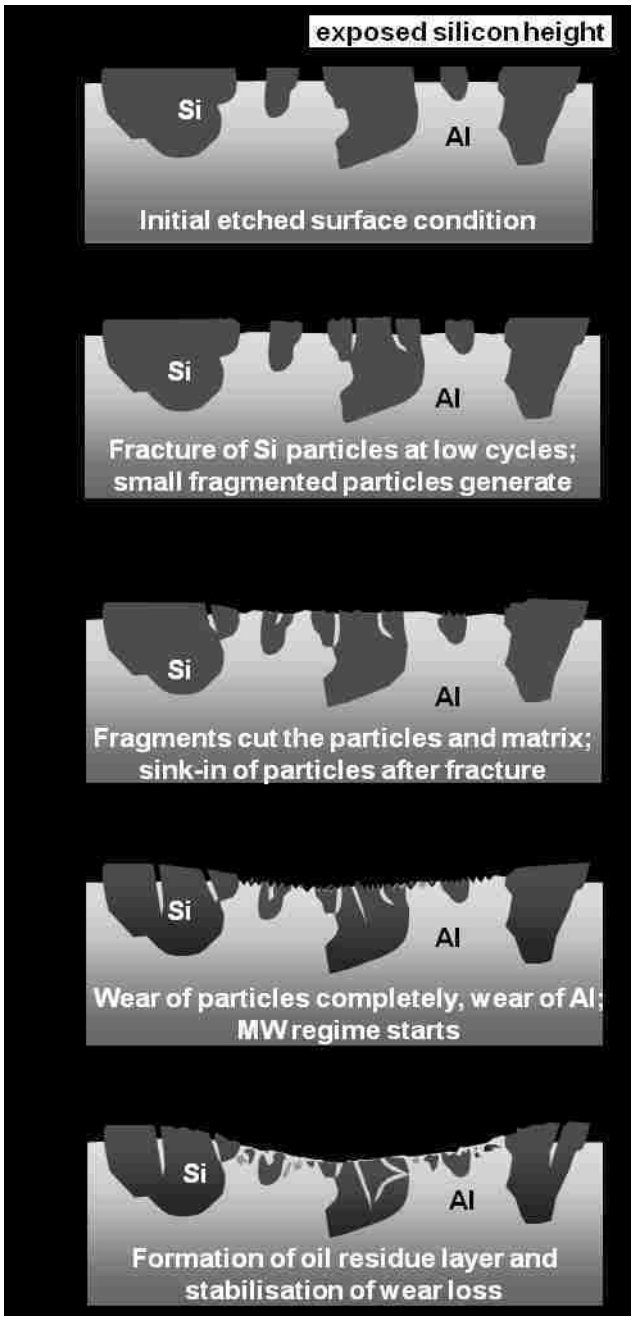

Figure 4. 10: Schematic explaining the wear mechanisms in Al-18.5% Si alloys at 5.0 N load. See text for details. The roman numbers indicate the stages of wear as show in Figure IV. VIII. The cracks within the silicon particles were arrested at Al-Si interface or at other cracks at a different section than depicted in the schematic. Accordingly, the figure does not indicate that cracks were arrested within the particles.

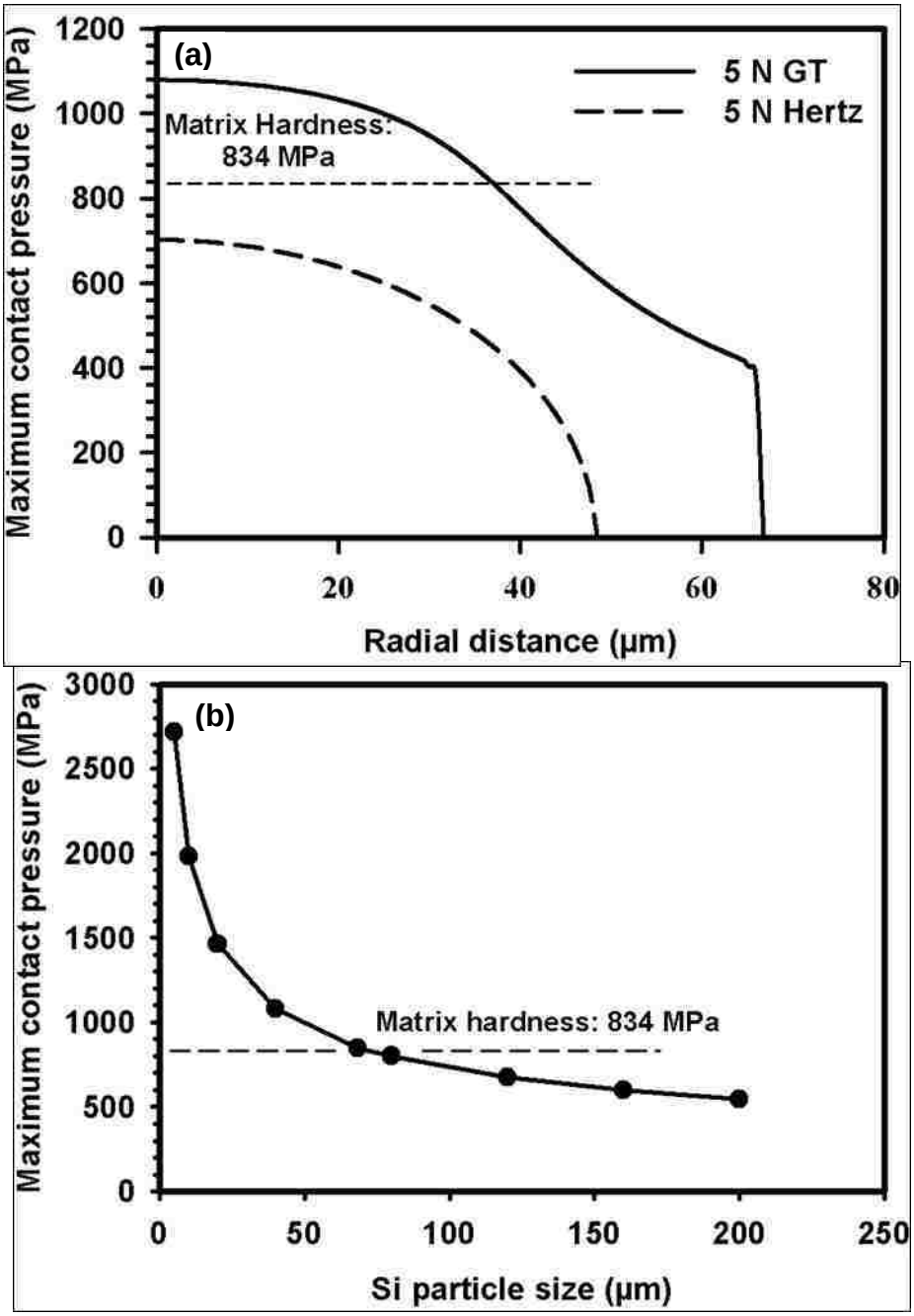

Figure 4. 11: The distribution of maximum contact pressure (both Hertz and Greenwood–Tripp (GT) model) as a function of radial distance from the centre of the contact; (b) change in maximum real contact pressure at the centre of the contact as per GT model as a function of particle size [93]. (c) The Hertz contact pressure distribution after 6×10^6 slicing cycles. Pressure distribution at the beginning of the sliding was also plotted.

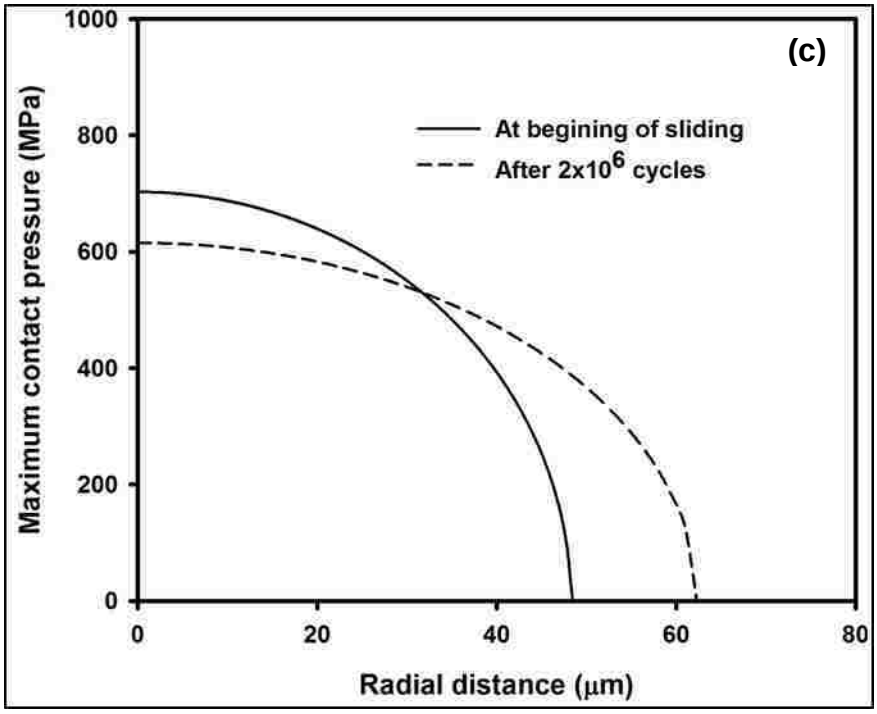

Figure 4.11: Continued

5. CHAPTER 5 – ELEVATED TEMPERATURE UMW OF Al-12.6% Si ALLOY

5.1 Introduction

In the previous chapter, the realm of UMW in a hypereutectic alloy (Al-18.5% Si), the most commonly used alloy in linerless automobile engines at 25 °C, was presented. It was shown that the increase in contact pressure resulted in UMW to last for 10^4 sliding cycles. Then it was required to understand the UMW mechanisms in a eutectic alloy to be used in linerless automotive engines. As suggested by Spikes in his literature review article, the decomposition of ZDDP, an additive in SAE 5W30 engine oil, to zinc phosphates [**85**] is facilitated by the increase in temperature. At 100 °C, which is roughly the engine surface temperature when the lubricating oil comes into contact with the bore surface, it was expected that the formation of tribofilm would happen early in the sliding process and may influence the UMW behaviour. The objective of the lubricated sliding experiments was not to reproduce the identical engine running conditions, but rather to simulate the engine running conditions to understand the wear mechanisms operative in the engine. Accordingly in this chapter, the elevated temperature wear behaviour of Al-12.6% Si alloy at 100 °C and a comparison of the elevated temperature wear behaviour with that at 25 °C will be presented. Understanding the wear mechanisms in laboratory studies and corroborating them with dynamometer studies may facilitate the reduction of expensive dynamometer trials. The choice of the sliding speed and applied normal load were made based on previous laboratory UMW studies at 25 °C conducted on different Al-Si (11%, 12%, 18.5%, and 25%) alloys [**92-94**].

The microscopic evidence of surface damage and measurement of aluminum matrix wear rates showed that there were three stages of UMW at 100 °C, and the micromechanisms were different in the different stages. In the following sections the surface damage parameters, such as silicon particle height change, aluminum pile-up height, and aluminum wear loss in different stages of UMW at 100 °C and 25 °C, will be quantified. The characteristic features of the worn surfaces observed using SEM and the chemistry of two different types of tribolayer analyzed using EDX, XANES, XPS, and TEM will also be presented.

5.2 UMW-I and UMW-II stages

5.2.1 Change in exposure height of silicon particles

Figure 5. 1 shows the decrease in the height of silicon particles at the contact surface as a function of sliding cycles at 25 °C and at 100 °C. After 10^3 sliding cycles, the exposure height of silicon particles reduced from 1.66±0.05 µm to 1.42±0.21 µm in 100 °C tested samples. This reduction in height was primarily due to sinking-in of both fragmented and original particles in the aluminum matrix. Between 10^3 and 10^5 sliding cycles, silicon particle height reduced to 0.30±0.14 µm, and after 6×10^5 sliding cycles, the average silicon particle height was 0.23±0.12 µm. At 25 °C, silicon particle height reduced to 1.12±0.28 µm after 10^3 sliding cycles. After initial height reduction, the particle height reduction rate was again decreased between 10^3 and 10^5 sliding cycles. But after 3×10^5 sliding cycles, silicon particle height was reduced to zero, that is, silicon particle height and aluminum matrix elevation became the same. In summary, at 100 °C the silicon particles at the surface maintained their exposure height for a longer sliding duration, and consequently were effective in protecting the aluminum matrix from wear. It was noted that the particles maintained their height for a longer duration

compared to 25 °C despite the fact that matrix hardness at 100 °C was lower than the hardness at 25 °C.

5.2.2 Aluminum pile-up formation

Silicon particle sinking-in was accompanied by the plastic deformation of the aluminum matrix surrounding the particles, resulting in aluminum pile-up formation. **Figure 5. 2a** shows aluminum pile-up height as a function of sliding cycle up to 10^5 sliding cycles. The pile-up height at 100 °C was 0.38±0.09 µm after 10^3 sliding cycles and then varied between 0.24±0.05 µm and 0.28±0.04 µm up to 105 sliding cycles. At 25 °C, the pile-up height increased from 0.18±0.05 µm after 10^3 sliding cycles to 0.37±0.04 µm after 5×10^4 cycles.

The ratio (α) of average pile-up height ($h_{pile-up}$) to average silicon particle height (h_{Si}) was calculated from the data shown in **Figure 5. 1** and **Figure 5. 2a**. **Figure 5. 2b** shows the ratio of pile-up height to silicon particle height as a function of sliding cycles. It can be observed from **Figure 5. 2b** that with increasing sliding cycles this ratio approached a value close to 1.0 indicating that the height of silicon particles and aluminum pile-up was the same. In other words, the elevation of silicon particles and piled-up aluminum matrix became equal, and the aluminum was exposed to the counterface. Up to 5×10^4 cycles at 100 °C and up to 10^4 cycles at 25 °C, silicon particles protected the aluminum matrix. This stage, where $\alpha<1$, was referred to as UMW-I. As the value of α increased through a transition period, UMW-II (defined by the maximum wear rate of the matrix and to be shown in **Section 5.3**) was observed. For $\alpha_C \geq 1$ represents the UMW-II stage where aluminum matrix wear took place; although the

5.3 UMW-III – Wear of the aluminum matrix

Because of the counterface contact with aluminum pile-ups, some aluminum wear initiated during the UMW-I to UMW-II transition period. **Figure 5. 3** shows the wear loss from

the alloy surface as a function of sliding cycles at 100 °C and 25 °C. Wear loss after 10^5 sliding cycles at 100 °C was 1.18×10^{-5} mm^3, and after 5×10^4 sliding cycles at 25 °C it was 1.68×10^{-4} mm^3 (see **Figure 5. 4c**). The highest wear rate at 100 °C was 8.23×10^{-8} mm^3/m observed between 3×10^5 and 6×10^5 sliding cycles, whereas at 25 °C the highest wear rate (28.0×10^{-8} mm^3/m) was observed at lower sliding cycles designated as the UMW-II stage for both temperatures. Thus, depending on the wear rate values, three different stages were indentified in **Figure 5. 3**: UMW-I corresponded to zero aluminum wear loss stage; UMW-II, where the maximum wear rate was observed; and UMW-III, where a decreased wear rate was observed. The characteristic features of three stages at two temperatures tested were different, which will be discussed in **Section 5.4**.

5.4 Electron microscopy of worn surfaces – microstructure evolution

Figure 5. 4a-d shows the back scattered electron images of the wear track at 25 °C and 100 °C after 10^3 sliding cycles (UMW-I). There was one distinct feature observed from these two micrographs, which showed characteristic differences in UMW-I of Al-12.6 wt.% Si alloy between 100 °C and 25 °C: At 100 °C a discontinuous island-like tribofilm was formed only on top of the silicon particles. The island-like tribofilm on top of silicon particles was not formed at 25 °C (**Figure 5. 4a**) and was a characteristic feature of UMW-I stage at 100 °C only **(Figure 5. 4d**). A lower amount of particle sinking-in (as shown in **Section 5.2.1**) was observed at 100 °C during UMW. In addition, 39% of particles within the wear track were fractured after 10^3 sliding cycles at 100 °C compared to 54% at 25 °C.

Figure 5. 4b-c and e-f show the back scattered electron micrographs of the wear track after 10^4, 5×10^4 sliding cycles at 25 °C and at 100 °C, respectively. At 100 °C, the island-like tribofilm continued to form on top of silicon particles along with sinking-in of silicon particles

(**Figure 5. 4e**) which resulted in pile-up formation of aluminum matrix surrounding the silicon particles. The contact with the counterface was limited to silicon particles and the aluminum pile-ups near the silicon particles up to 5×10^4 sliding cycles (**Figure 5. 4f**). Therefore no measurable volume loss of aluminum matrix occurred up to 5×10^4 sliding cycles at 100 °C (UMW-I). With continued sliding, the transition to UMW-II took place. At 25 °C, however, the particles were subjected to fracture and fragmentation in addition to sinking-in. **Error! eference source not found.1** shows the percentage of particles fractured within the wear track at 25 °C and 100 °C for 10^3, 5×10^3, and 10^4 sliding cycles. After 10^4 sliding cycles (at the end of UMW-I), 74.3% of the particles were fractured at 25 °C compared to 52.3% at 100 °C. At 25 °C after 10^4 sliding cycles, some aluminum matrix wear was observed (**Figure 5. 4b**). With an increase in sliding cycles, the wear of the aluminum matrix continued (**Figure 5. 4c**), as also shown in **Figure 5. 3** earlier for 25 °C.

Figure 5. 4g and **h** shows the wear surface after 6×10^5 sliding cycles at 25 °C and after 2×10^6 sliding cycles at 100 °C, respectively. The worn surface morphology presented in **Figure 5. 4g** and **h** corresponded to the UMW-III as shown in **Figure 5. 3**. At this point a continuous tribolayer or ORL formation was observed on the alloy surface. The chemical characterization of the ORL will be presented in **Section 5.5.2**.

5.5 Formation of island-like tribofilm and oil-residue layer (ORL)

During UMW-I at 100 °C, an island-like tribofilm was formed (**Figure 5. 4d-f**) only on silicon particles. **Figure 5. 5a** and **b** shows magnified images of island-like tribofilms formed on silicon top surface after 10^4 and 5×10^4 sliding cycles. It was observed that these discontinuous tribofilms were formed only on the top of silicon particles in the direction of sliding cycles and at 100 °C. At 25 °C, formation of these films was not observed. The chemistry of these tribofilms

was determined using EDS and XANES, and nanomechanical properties were measured using nanoindentation with a cube corner indenter. The EDS was carried out both from the surface and within the cross sectional microscopy. The ORL on the other hand was continuous and formed both on top of aluminum and silicon particles. The ORL started to form on aluminum (piled-up and worn out next to silicon particles) in UMW-II stage, and in UMW-II stage the surface was completely covered with ORL at both temperatures.

5.5.1 Island-like tribofilm on silicon particles

To facilitate the investigation of the chemical nature of the island-like tribofilms, they were formed on Al-12.6% Si alloy under similar wear testing conditions as explained in **Section 3.3.2**. However, the wear track width was narrow (less than 200 µm) and could not be observed under most spectrometers. Therefore, to increase the thickness of the wear track to 1.0 mm, concentric wear tracks were generated at 2.0 N load by increasing the diameter of the wear track in steps of 0.25 mm starting from 3 mm. The increase in wear track width was necessary for easy identification of it during data collection in synchrotron beam lines. The sliding test was continued until 10^3 cycles, and each time a new counterface (AISI 52100 steel ball) was used. This particular sample was tested using XANES, however the EDS and cross sectional imaging and analysis of the microstructure were carried out on wear tracks generated on Al-12.6% Si alloy.

5.5.1.1 EDS of island-like tribofilms

Figure 5. 6 shows EDS spectra collected from island-like tribofilm. The EDS of the island-like tribofilm shows the presence of Zn, P, S, Ca, Al, and O. The primary source of Zn, P, S, and Ca is from the additive ZDDP and detergents used within the engine oil. These elements formed primarily two compounds, namely zinc sulphide and short chain zinc pyrophosphate, which

were identified from HRTEM image analysis and XANES spectroscopy as shown in the following sections.

5.5.1.2 Cross section imaging and HRTEM analysis of island-like tribofilms

Figure 5. 7a shows the SEM image of cross-sectional TEM sample of the tribofilm formed on silicon particles in Al-12.6% Si alloy, as shown in **Figure 5. 5a** after 10^3 sliding cycles. **Figure 5. 7b** shows a similar cross-sectional TEM image of samples showing tribofilm formed on silicon and an oil-residue layer on the adjacent piled-up aluminum after 5×10^4 sliding cycles (UMW-I) as shown in **Figure 5. 5b**. A thin and dark layer was observed on top of the silicon. The thickness of the tribofilm was measured from FIB cross sections and TEM images and is shown in **Figure 5.7, Figure 5.9a, Figure 5.14, Figure 5. 16c**. The thickness of the island-like tribofilm varied between 100-150 nm and remained constant through the sliding process. EDS mapping was carried out within this tribofilm in STEM imaging mode. **Figure 5. 8** shows the STEM elemental maps showing the distribution of individual elements within the tribofilm. It was observed from the elemental distribution maps that the tribofilm contained Zn, P, S, Ca, C, and O. It is to be noted that ORL was not formed on the aluminum matrix (**Figure 5. 7a**), which did not come into contact with the counterface.

Figure 5. 9a shows a high magnification cross-sectional TEM image of the island-like tribofilm formed on top of silicon particle after 5×10^4 cycles (UMW-I), and **Figure 5. 9b** shows the HRTEM image of the tribofilm shown in **Figure 5. 9a**. The structure was analyzed by taking Fast Fourier Transformation (FFT) of small regions and crystalline regions corresponding to lattice images of zinc sulphide (ZnS) were identified. The inset in **Figure 5. 9b** shows the FFT image recorded from **Figure 5. 9b.**

5.5.1.3 XANES spectroscopy of island-like tribofilm

Figure 5. 10a shows the P L-edge XANES spectra from the tribofilm formed after 10^3 sliding cycles (UMW-I). The chemistry in the tribofilm appears to be primarily composed of a polyphosphate. The polyphosphate chain length can be estimated from the ratio of peak a/c in P L-edge spectra [**119-121**]. The peak ratio in the zinc metaphosphate ($Zn(PO_3)_2$) was as high as 0.62. The peak ratio of a/c in the tribofilm was 0.34, which indicated that the tribofilm had a short chain length as compared to the long chain length in the metaphosphate. The pre-edge feature (prior to peak ″a″) in the tribofilm spectrum aligned to the main feature in the ZDDP spectrum. This indicated the existence of un-reacted ZDDP in the tribofilm. Another observation of P L-edge XANES was that the tribofilm was very thin and was not a continuous film, which makes the signal very noisy. The feature at approximately 142 eV could show some evidence of calcium phosphate [**122**].

The S L-edge XANES spectrum of the tribofilm is exhibited in **Figure 5. 10b**. The S L-edge features in the tribofilm corresponded to a reduced sulphur form (sulphide or un-reacted ZDDP). Since there was no peak up to 175 eV, it was concluded that no sulphate was present in the film. The sulphur content of tribofilm derived from the oil was low.

Figure 5. 10c shows the Zn L-edge XANES spectra of the tribofilm as compared with different model compounds. Peak ″a″ of the tribofilm was observed at lower energy than that of zinc metaphosphate. The feature of the spectra was observed between zinc polyphosphate (with shorter chain length than that of meta phosphate, $Zn(PO_3)_2$) and zinc sulfide or a polyphosphate with Al or Ca as the counter ions. The poor signal to noise ratio indicated that the tribofilm was thin.

The O K-edge XANES spectrum of the tribofilm as compared with model compound, $Zn(PO_3)_2$, is presented in **Figure 5. 10d**. The features of peak 1, 3, and 4 were attributed to

Al_2O_3 [**123**], and peak 2 was possibly due to the contribution of zinc polyphosphate. The tribofilm (made of zinc polyphosphate and zinc sulphide) was very thin, which resulted in the O K-edge spectra (total electron yield (TEY) and fluorescence yield (FY)) being very close to that of Al_2O_3. The bulk sensitive FY mode XANES had less resolved peak 1, which corresponded to a low concentration Al_2O_3 in the bulk of the alloy.

Therefore, the EDS data showed the elemental composition of the island-like tribofilm on silicon, and HRTEM analysis and XANES spectroscopy showed that the island-like tribofilm consisted of zinc sulphide, short chain length zinc polyphosphate, and unreacted ZDDP.

5.5.1.4 Nanomechanical properties of the tribofilm

The island-like tribofilm properties were measured by forming the film on an Al-18.5%Si alloy after conduction wear tests at 2.0 N load at 100 °C for 10^4 sliding cycles. The particles in this alloy were muc3h larger, and locating the tribofilm on these particles was easier than locating them on needle like particles in Al-12.6% Si alloy. Since the underlying substrate and the conditions under which the tribofilm was formed were similar in both alloys, it can be said that the mechanical properties of the island-like tribofilm formed on Al-12.6%Si or in any Al-Si alloys would be the same as that measured in Al-18.5% Si alloy. Typical load-displacement curves of the nanoindentation experiments on the island-like tribofilm showing their elastic-plastic behaviour are given in **Figure 5. 11a**. The residual nano-indent impressions on selected island-like tribofilm taken using the tip of the indenter (scanning probe microscope (SPM)) are shown in **Figure 5. 11b**. Analyzing the load-displacement data using the Oliver-Pharr method [**124**], the elastic modulus of the tribofilm was measured as 82.66±16.41 GPa, the hardness being 3.34±0.67 GPa. Similar indents on silicon particles without a tribofilm were also carried out, and the nanohardness and the elastic modulus of silicon were measured to be 6.75±0.25 GPa and 123.70±4.48 GPa. **Figure 5. 11c** shows typical load-displacement curves on silicon without

island-like tribofilm. From **Figure 5. 11a and c**, the difference in elastoplastic behaviour of silicon particles with and without tribofilm was evident, which altered the mechanics of the contact at 100 °C compared to 25 °C and is discussed in **Section 5.6.2**.

5.5.2 Oil-residue layer (ORL)

The chemistry of the tribolayer (ORL) that formed on both aluminum and silicon during UMW-II was also analyzed using a host of electron and x-ray based spectroscopic methods, such as EDS and XPS. Cross-sectional imaging and nano-beam diffraction were also carried out in TEM.

5.5.2.1 EDS of ORL

A continuous tribolayer (ORL) covering silicon and aluminum surfaces, the characteristic feature of UMW-III, was formed when contact between the aluminum matrix and the counterface occurred, both at 25 °C and at 100 °C. With progression of sliding at 100 °C, the island-like tribofilm was smeared on top of piled-up aluminum by the counterface and formed a continuous layer on top of the worn surface. ORL at 100 °C consisted of elements like C, Ca, Zn, P, and S. **Figure 5. 12b-f** shows an EDS map of the worn surface (**Figure 5. 12a**) after 3×10^5 sliding cycles at 100 °C. This figure shows that regions along the sliding direction were rich in Zn, S, P, and Ca. Oxygen was present over the entire worn surface. A clear difference between the distribution of these elements within and outside the wear track was noted from **Figure 5. 12b-f**. At 25 °C the ORL was no different than that observed in the earlier UMW studies at 25 °C [**94**]. The ORL at 25 °C consisted of a mixture of amorphous carbon and aluminum oxide determined using electron energy loss spectroscopy (EELS), and Ca, S, and Zn determined using XPS.

5.5.2.2 XPS comparative analysis of ORL at 100 °C and 25 °C

Figure 5. 13 shows a comparative elemental composition analysis of the contact surfaces between 100 °C and 25 °C determined using XPS after 3×10^5 sliding cycles. This figure confirms the finding of EDS and shows that the ORL at 100 °C was richer in Zn, P, S, and Ca compared to that at 25 °C. More detailed XPS characterization (high resolution spectra of selected elements and their analysis to investigate the molecular nature of the ORL) of worn surfaces after very long sliding cycles (6×10^6 revolutions) were also carried out to investigate the durability of ORL in maintaining UMW. These results will be presented in the next chapter when showing the characterization of ORL formed after 6×10^6 sliding cycles.

5.5.2.3 Cross-sectional images and STEM characterization of ORL

Figure 5. 14a shows a high magnification SEM image of the subsurface of the piled-up and worn out aluminum matrix and **Figure 5. 14b** shows the bright field TEM image of the ORL formed on piled-up aluminum next to the silicon particle as shown in **Figure 5. 7b**. **Figure 5. 14a** and **b** shows the formation of ultra-fine grains due to sliding induced deformation in the subsurface of the piled-up aluminum and formation of ORL on top of piled-up aluminum. STEM elemental maps were recorded from this region and **Figure 5. 15** shows the distribution of Zn, P, S, Ca, O, Al, and C in the surface and subsurface region. The distribution of these elements showed the presence of aluminum at some locations within the ORL. These maps corroborated well with EDS maps taken from the surface in SEM after 3×10^5 sliding cycles. It was also observed that the surface had approximately 50 nm thick ORL. It appeared that the island-like tribofilm was mixed with subsurface aluminum to form the ORL. **Figure 5. 16a** and **b** shows the cross section of the wear track in the direction of sliding after 3×10^5 and 6×10^5 cycles showing the formation of ORL on top of silicon and aluminum matrix, respectively, and **Figure 5. 16c** shows the variation of ORL thickness at two different temperatures measured from FIB cross

sections and TEM images. The thickness of island-like tribofilm on silicon particles is also shown. At this stage the surface had a continuous and approximately 200 nm thick ORL which consisted of the island-like tribofilm mixed with sliding induced ultra-fine grain aluminum (**Figure 5. 16b**). From **Figure 5. 16a** and **b**, it may be inferred that the ORL is either supported by the silicon particle and/or the ultra-fine grain aluminum.

5.5.2.4 Nanomechanical properties of the ORL

The indentation hardness and the Young's modulus of the ORL formed on aluminum matrix were measured using a multi-cycle indentation experiment with a Berkovich indenter. **Figure 5. 17a** and **b** shows the hardness and Young's modulus of the ORL formed on the sample, respectively, after 6×10^5 sliding cycles at 100 °C and 25 °C. It can be observed that within the first 50 nm the hardness is approximately 2.5 GPa at both temperatures. These measurements showed that the ORL was harder than the aluminum matrix and was able to withstand the normal load (2.0 N) during sliding. However, the hardness and elastic modulus of the ORL was lower compared to the island-like tribofilm formed on silicon. The lowering of the hardness and Young's modulus was probably due to the mechanical mixing of the island-like tribofilm with aluminum matrix in the evolution of ORL from island-like tribofilm during the sliding process. Accurate quantification of the amount of aluminum in the ORL is difficult, but it is conceivable, according to the rule of mixture, that adding of aluminum with a lower Young's modulus can cause a reduction in the Young's modulus of ORL.

5.6 UMW mechanics and mechanisms of Al-12.6% Si alloy

5.6.1 Formation of island-like tribofilm and ORL

Thermal decomposition of ZDDPs in the absence of hydroperoxide and peroxy-radicals to zinc phosphate was reported many years earlier [**125-128**]. The temperature of this

decomposition is dependent on the alkyl group present in ZDDP. Two types of film in the presence of ZDDP are formed: thermal film and a tribofilm. The former is observed on metallic surfaces when submersed in ZDDP-containing solution at temperatures above 100 °C [**129,130**]. However, the tribofilm formation was observed at temperatures as low as 50 °C [**131**] and was only observed on surfaces sliding past each other [**132**]. The rate of thermal film and tribofilm formation increased with increase in temperature. However, chemically they were found to be of a similar nature consisting of a glassy phosphate with a thin outer layer of zinc phosphate [**133,134**].

In the present studies, a similar film on top of silicon particles (island-like tribofilm) to those of the tribofilm formed on steel surfaces was observed at 100 °C only, but not at 25 °C. The mechanical properties of the island-like tribofilm on silicon ($H = 3.34$ GPa ;$E^* = 82.66$ GPa) was found to be very similar to those observed on steel surfaces ($H = 3.5$ GPa ;$E^* = 90$ GPa) [**135**]. On the other hand, the mechanical properties of the thermal film were much lower ($H = 1.5$ GPa; $E^* = 35$ GPa) [**136**]. Thus, based on the mechanical properties it can be said that the formation of island-like tribofilm on silicon particles is the result of tribological action between the contacting asperities of the steel and silicon particles in the presence of ZDDP in the engine oil. The thickness of the tribofilm remained almost constant with sliding cycles (**Figure 5. 16c**). Thus it was inferred that there must be equilibrium in the kinetics of tribofilm formation and the wear of it by the counterface. At 25 °C, lack of thermal activation did not produce this tribofilm on silicon particles. Thus two conditions under which the island-like tribofilm formed in the presence of ZDDP at the contact surface were the thermal activation due to increase in temperature to 100 °C and the contact pressure between the contacting bodies.

The layer formation did not initiate until there was a contact between the piled-up matrix and the counterface (**Figure 5. 7b**) in UMW-II. At higher number of sliding cycles (UMW-

III), the island-like tribofilm is smeared on the surrounding aluminum matrix thus transformed into a continuous tribolayer, ORL, on the worn surface (**Figure 5. 16a and b**). No thermal film formation was observed on the aluminum surface. Thus the contact between the counterface and the piled-up matrix was a precursor of ORL formation. This was true even at 25 °C. However, the difference in ORL at these two temperatures was in their composition: at 100 °C, the ORL consisted of zinc sulphide and zinc phosphates from the smeared island-like tribofilm along with the carbon mixed with aluminum matrix (**Figure 5. 16b**), whereas at 25 °C, it consisted of a mixture of amorphous carbon, aluminum oxide, Ca, S, and Zn [**94**]. The thickness of the ORL also did not change at 100 °C; however at 25 °C, the thickness of the ORL increased gradually. This is because at 25 °C the ORL is formed strictly due to the mechanical mixing during the sliding process which is time dependent.

In the literature, three different mechanisms were proposed by which ZDDP acted as an antiwear agent: (i) formation of a protective film mechanically protecting the substrate [**103**]; (ii) removal of corrosive peroxides or peroxy-radicals [**137,138**]; and (iii) digestion of hard abrasive iron oxide particles [**134,139**]. It was also suggested that when ZDDP acts as a peroxide-decomposing additive, the reaction by-products did not form zincphosphate antiwear films [**140,141**]. There was no direct evidence of iron oxide particle digestion mechanisms proposed by Martin [**139**]. In addition, there are hardly any iron oxide particles in the present Al-Si alloy system (except a few possibly from the counterface material). In the present study, because there was formation of zinc phosphates, it may be inferred that the ZDDP did not act as a peroxide-decomposing additive. Thus the most probable antiwear mechanism is the mechanical protection of the surface from the tribolayers (island-like tribofilm and ORL) in which the direct contact between the steel counterface and the alloy is prevented, and the tribolayer is

considered to be carrying the applied pressure. The hardness of the ORL being harder than the aluminum matrix beneath it prevented the damage by the counterface.

5.6.2 Effect of island-like tribofilm

The island-like tribofilm formation on silicon particles at 100 °C influences the UMW behaviour of Al-Si alloys in two different ways. It altered the composite modulus between the contacting bodies which directly influence the applied real contact pressure. It also acted as an energy absorbing layer and improved the load bearing capacity of particles.

5.6.2.1 Change in composite contact modulus and reduction in particle fracture

The formation of tribofilm altered the mechanics of the contact between the steel counterface and the particles. At 25 °C, the contact during sliding in UMW-I was between silicon particles and the counterface, whereas the contact at 100 °C was between the island-like tribofilm and the counterface. Accordingly, the composite elastic modulus of the contact at 25 °C ($E^*_{25°C}$) and 100 °C ($E^*_{100°C}$) can be calculated by the following equation:

$$\left.\begin{aligned}\frac{1}{E^*_{25°C}} &= \left[\frac{1-(\nu_{Si})^2}{E_{Si}} + \frac{1-(\nu_{Steel})^2}{E_{Steel}}\right] \\ \frac{1}{E^*_{100°C}} &= \left[\frac{1-(\nu_{TF})^2}{E_{TF}} + \frac{1-(\nu_{Steel})^2}{E_{Steel}}\right]\end{aligned}\right\} \quad (5.1)$$

By taking the elastic modulus of silicon (E_{Si}), steel (E_{Steel}), and island-like tribofilm (E_{TF}) as 120 GPa, 210 GPa, and 82.66 GPa, respectively, and the Poisson's ratio of silicon (ν_{Si}), steel (ν_{Steel}), and island-like tribofilm (ν_{TF}) as 0.26, 0.30, and 0.30, respectively, the calculated composite elastic modulus at two temperatures was $E^*_{25°C} = 77.24\ GPa$ and $E^*_{100°C} = 64.58\ GPa$. Thus having a tribofilm on top of silicon particles resulted in a reduction composite modulus by 16%.

The maximum contact pressure (P_r) at the centre of the contact between the contacting bodies by adapting multi-asperity Greenwood-Tripp model can be calculated by the equation below [**100,117**]:

$$P_r = \frac{dP}{dr} = \left(\frac{4}{3\pi}\right) E^* \left(\frac{\sigma}{R_p}\right)^{1/2} \frac{F_{3/2}(h)}{F_1(h)}\Big|_{r=0} \quad (5.2)$$

where E^* is the reduced elastic modulus, R_p is the particle length, σ is the standard deviation of the particle height, and $F_{3/2}(h)$ and $F_1(h)$ are the parabolic cylinder functions; the general solution for such functions for Gaussian distribution can be given as:

$$F_m(h) = \frac{1}{\sqrt{2\pi}} \int_h^\infty (s-h)^m exp\left(-\frac{s^2}{2}\right) \quad (5.3)$$

From **equation 5.2,** it can be seen that the real contact pressure depends on E^*, R_p, σ, $F_{3/2}(h)$, and $F_1(h)$. All these parameters at 25 °C and 100 °C did not change except the $E^*_{25°C}$ and $E^*_{100°C}$. Thus reduction in elastic modulus of particles with tribofilms resulted in 16% reduction in a lower contact pressure according to **equation 5.2**. Consequently, it is conceivable that a lesser amount of particle sinking-in and fracture would occur in the presence of island-like tribofilm on silicon particles.

5.6.2.2 Energy absorbing entity

The total energy dissipated during indentation (W_T) is composed of elastic (W_E) and plastic (W_P) component with W_E and W_P calculated as the area under the unloading curve and the area enclosed by the loading-unloading curve, respectively, W_T being the sum of both W_E and W_P. Thus an average energy dissipation coefficient (η_P) can be defined by taking the ratio of W_P to W_T which signifies the fraction of total energy spent to deform the materials plastically. The values of plastic and total work during the indentation on silicon particles with and without tribofilm are given in **Table 5.2**. The energy dissipation coefficient was 13% higher for indentations in the presence of island-like tribofilm than those without the tribofilm.

Accordingly, it can be said that in the presence of the tribofilm, more energy during indentation would be spent towards deformation of the tribofilm rather than towards deformation of silicon. Thus the island-like tribofilm acts as an energy absorbing layer which deforms during the contact loading and increases the load carrying capacity of the silicon particles without fracturing them.

5.6.3 Summary of micromechanisms of Al-12.6% Si alloy

The ultra-mild wear mechanisms of Al-12.6 wt.% Si alloy were different at 25 °C and at 100 °C. The lower wear loss at 100 °C in UMW-II stage compared to 25 °C can be explained using mechanical analysis of the contact and formation of ORL. The main difference in characteristic features of UMW-I at these two temperatures was the formation of island-like tribofilm at 100 °C and lower amount of silicon particle sinking-in and fracture during sliding.

According to **equation 5.2,** it follows that the maximum exerted contact pressure on silicon particles depends on the composite modulus of the contacting bodies and particle sizes. The smaller the particle size, the higher the maximum contact pressure. It was shown earlier in **Chapter 4** that when the matrix hardness was higher, particle fracture preceded the sinking-in. Once fractured, increased applied contact pressure on smaller particles caused the subsequent sinking-in. However, the particle size was the same for tests at both temperatures in the present study. The matrix hardness of Al-12.6 wt.% Si alloy was reduced from 1.65±0.05 GPa at 25 °C to 1.55±0.10 GPa at 100 °C, but lower contact pressure at 100 °C due to layer formation could be seen as a factor that increased effectiveness of load bearing capacity of the particles. Once the particle fractured and the applied contact pressure increased according to **equation 5.2**, more sinking-in took place, and the amount of pile-up was increased. At long sliding distances once the ORL was established (UMW-III), the wear rates were similar at both temperatures. The ORL, being harder than the softer aluminum matrix and supported by the ultra-fine grain aluminum,

was able to protect the matrix. Thus, the particle sinking-in in UMW-I stage and wear of the piled-up aluminum in UMW-II stage are the precursors for ORL formation. The particles fracture and generation of small fragments cause abrasive action on the worn surface and remove the ORL.

The UMW mechanisms in Al-12.6 wt.% Si alloys at 100 °C and at 25 °C can be summarized with a schematic diagram as shown in **Figure 5. 18**. At 25 °C during UMW-I (**Figure 5. 18b**), the UMW damage occurred as a result of fracture of silicon particles as well as their sinking-in. Aluminum wear after 10^4 sliding cycles at 25 °C initiated from the aluminum pile-ups and the ratio (α) of pile-up height to silicon particle height remained less than 1.0. Sinking-in continued until the height of the silicon particles became equal to the aluminum surface elevation where high matrix wear started to occur (UMW-II). At the same time ORL started to form (**Figure 5. 18c**). Once a continuous ORL was formed supported by sliding induced fine aluminum microstructure, a reduction in wear rate was observed and the UMW-III was achieved (**Figure 5. 18d**).

At 100 °C the formation of island-like tribofilm during UMW-I (**Figure 5. 18e**) occurred. Less particle sinking-in and less particle fracture was observed. With increasing sliding, the UMW-II (**Figure 5. 18f**) transition took place, and an increased wear rate was observed in UMW-II. The island-like tribofilm was transformed into a continuous ORL during UMW-II. At the end of UMW-II, an ORL was formed on the worn surface and caused stabilization in wear rates in UMW-III (**Figure 5. 18g**). But early formation of island-like tribofilm and less particle fracture improved the wear behaviour of Al-12.6 wt.% Si alloy at 100 °C compared to that at 25 °C in UMW-I and delayed the start of UMW-II stage. However at both temperatures, once UMW-III was achieved, the wear rates were reduced.

TABLES – CHAPTER 5

Table 5. 1: Percentages of silicon particles fractured within the wear track at two different temperatures.

Sliding cycles	25 °C	100 °C
10^3	54.0	38.7
5×10^3	59.2	40.6
10^4	74.3	52.3

Table 5. 2: Plastic and total work during indentation (Figure 5. 11a and c) on silicon particles with tribofilm and without tribofilm

	Plastic work (W_T), pJ	Total work (W_T), pJ	energy dissipation coefficient (η_P)
With tribofilm	**0.21**	**0.25**	**0.86**
No tribofilm	**0.13**	**0.17**	**0.76**

FIGURES – CHAPTER 5

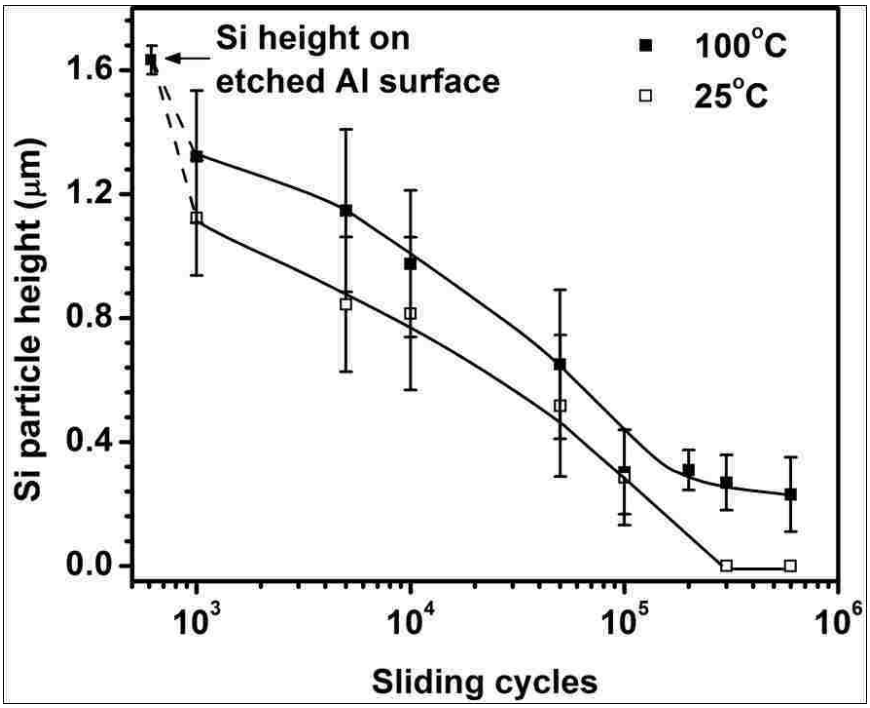

Figure 5. 1: Silicon particle height decrease in Al-12.6 wt.% Si alloy at two different temperatures. The first data point represents silicon particle height on etched aluminum surface (before sliding).

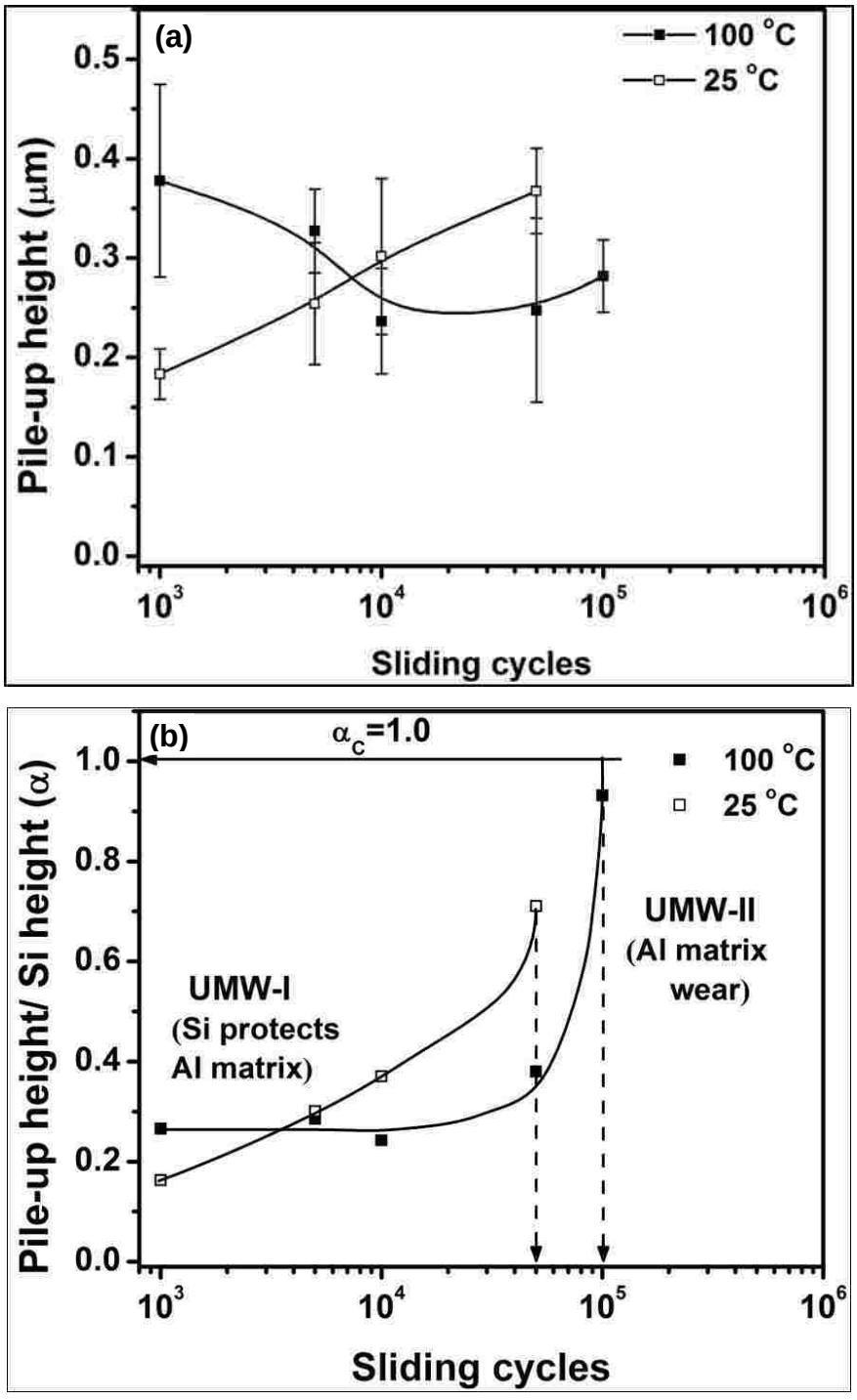

Figure 5. 2: (a) Change in aluminum pile-up height at two different temperatures. The error bar represents the standard deviation of measurements from eight different images similar to Figure 3. 7a,c,e; (b) change in ratio of pile-up height to silicon height with sliding cycles representing a damage criterion for UMW-II stage. The first data point with a value of zero pile-up height (at both temperatures) corresponding to zero sliding cycles is omitted. The vertical arrow indicates the sliding cycles at which the transition to UMW-II stage took place at both temperatures.

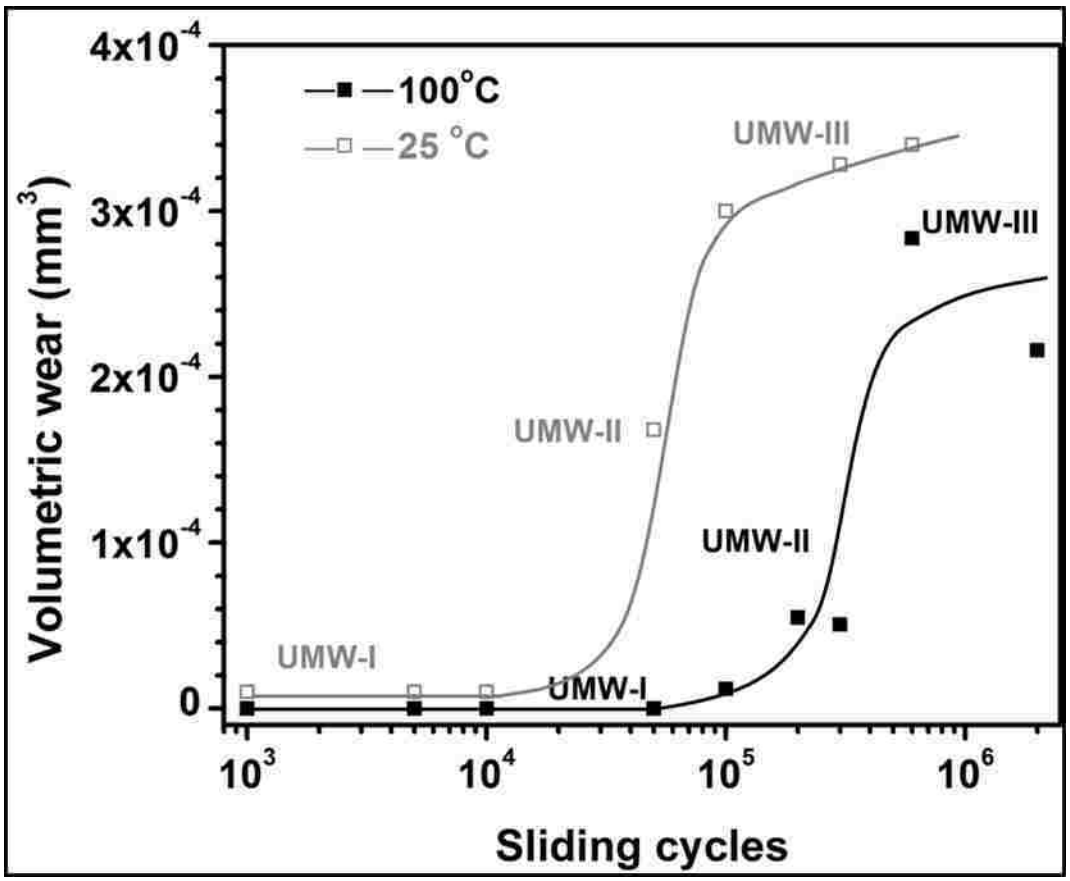

Figure 5. 3: Volumetric wear loss of aluminum against sliding cycles at two different temperatures. Three different stages (UMW-I, UMW-II, and UMW-III) at both temperatures were identified based on the wear rate and the characteristic features of the worn surface.

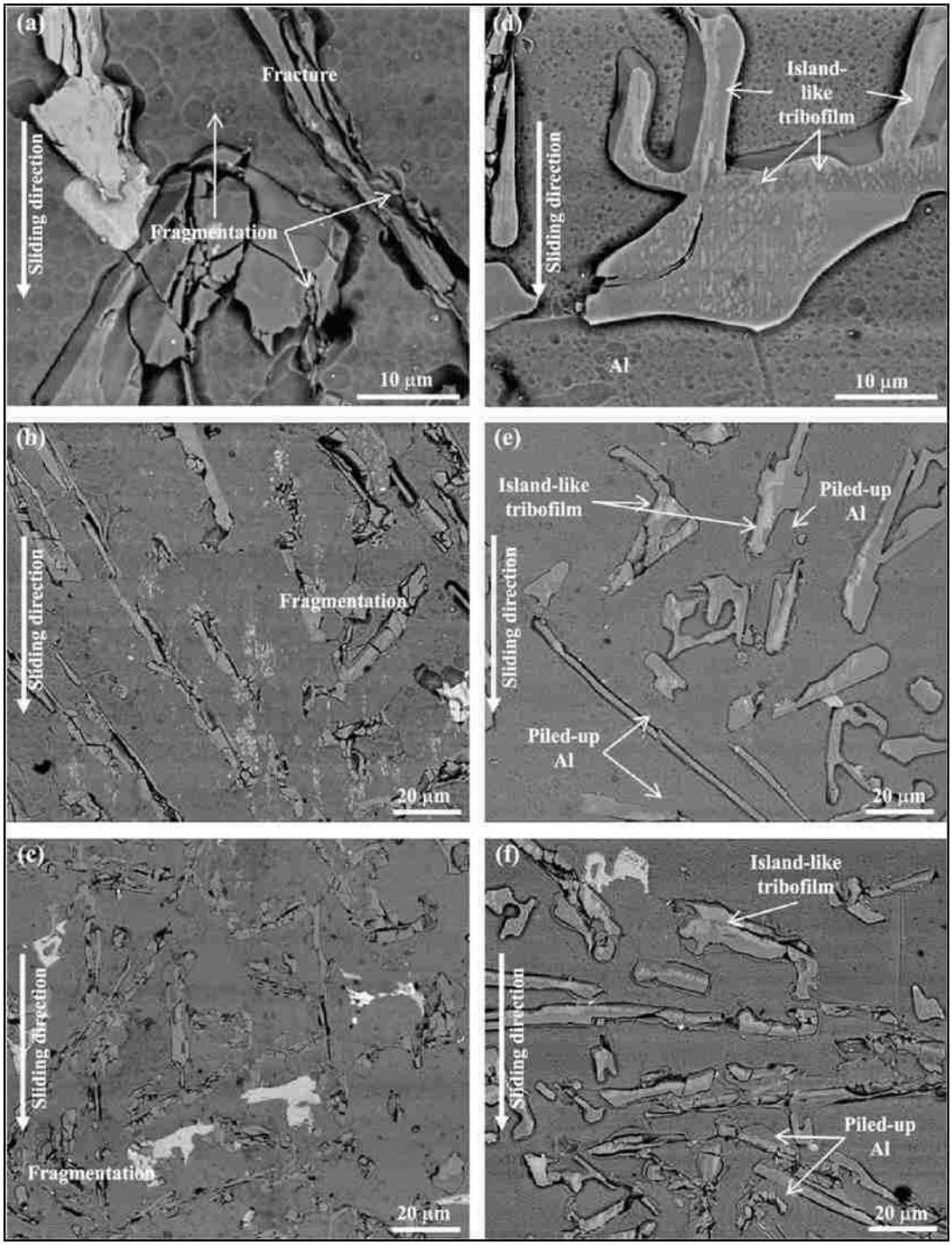

Figure 5. 4: Back scattered electron (BSE) images of the wear tack at 25 °C after (a) 10^3 (b) 10^4 (c) 5×10^4 sliding cycles showing fracture and fragmentation of particles; and at 100 °C after (d) 10^3 (e) 10^4 (f) 5×10^4 sliding cycles showing formation of pad structure and fracture of particles. Secondary electron (SE) images of the wear track after (g) 6×10^5 cycles at 25 °C and (h) 2×10^6 cycles at 100 °C.

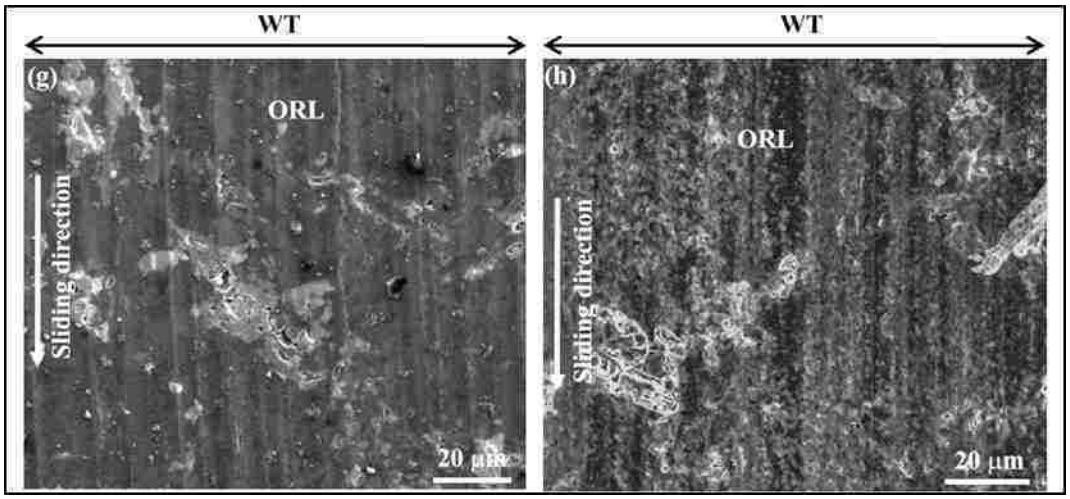

Figure 5. : Continued

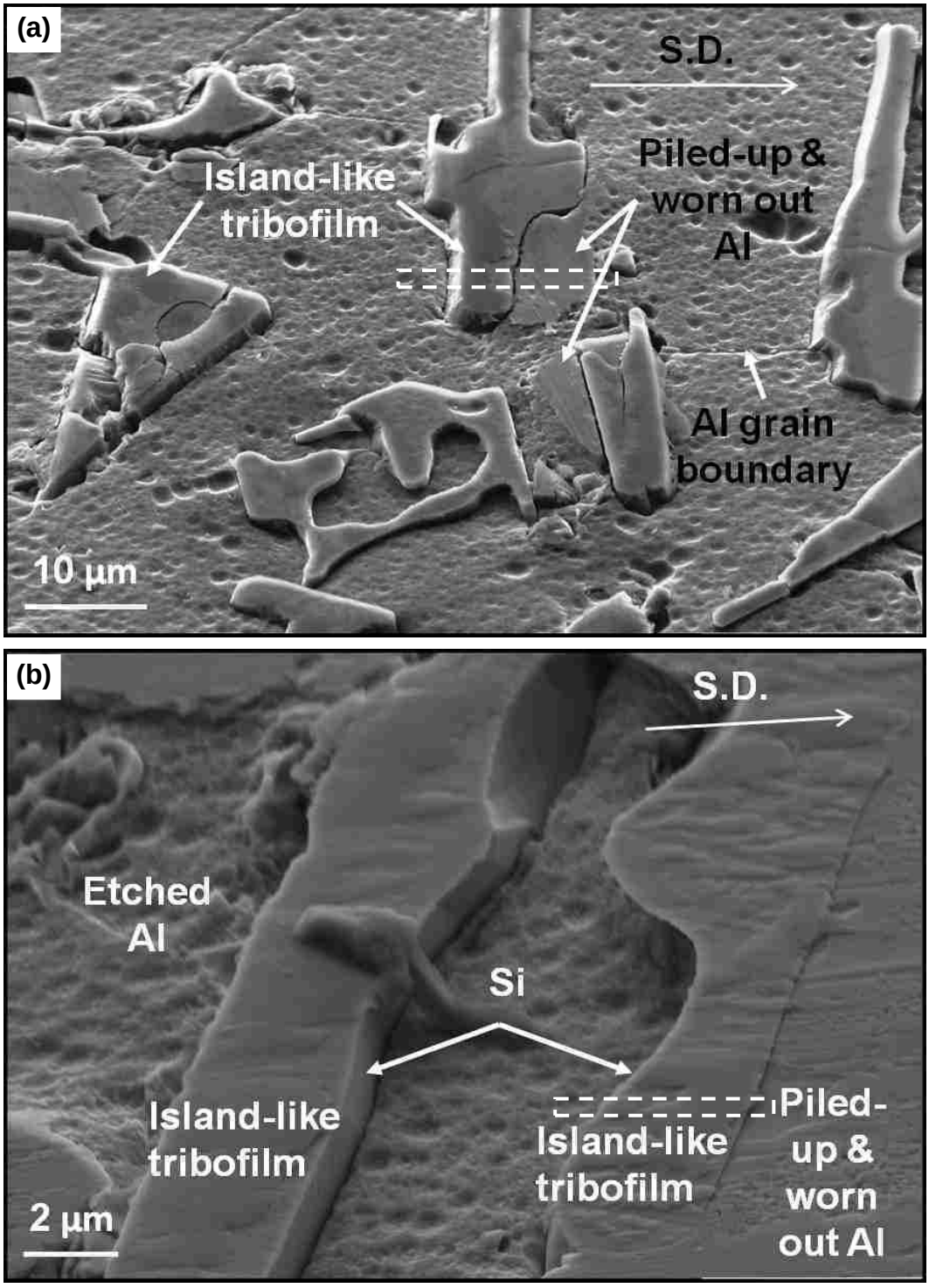

Figure 5. 5: High magnification image of the wear track showing the morphology of island-like tribofilm formed on top of silicon particles in Al-12.6% Si alloy at 100 °C after (a) 10^4 and (b) 5×10^4 sliding cycles. The dotted rectangles represent the location of the TEM sample prepared using FIB-lift-out method.

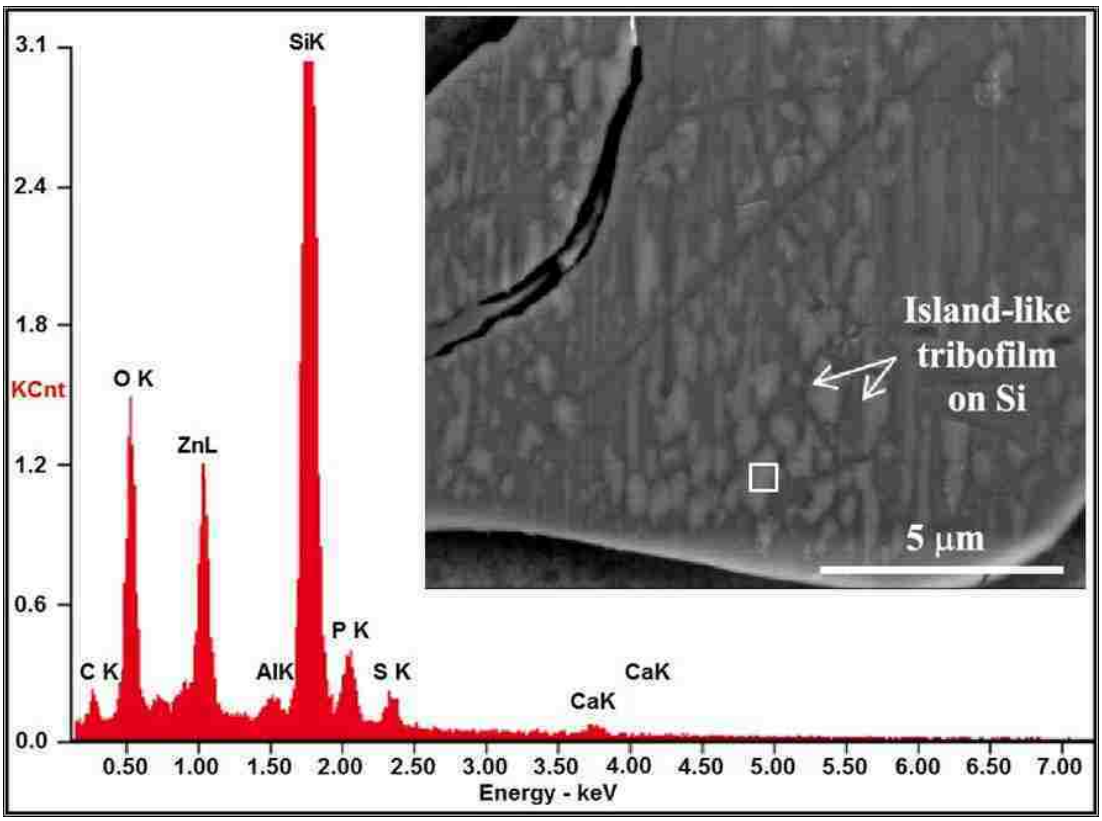

Figure 5. 6: EDS spectra (at 7.0 KV at a working distance of 9.9 mm) of island-like tribofilm formed on top of silicon particles. The inset shows the magnified image of the tribofilm from Figure 5. d. The EDS spectra location is indicated by the square.

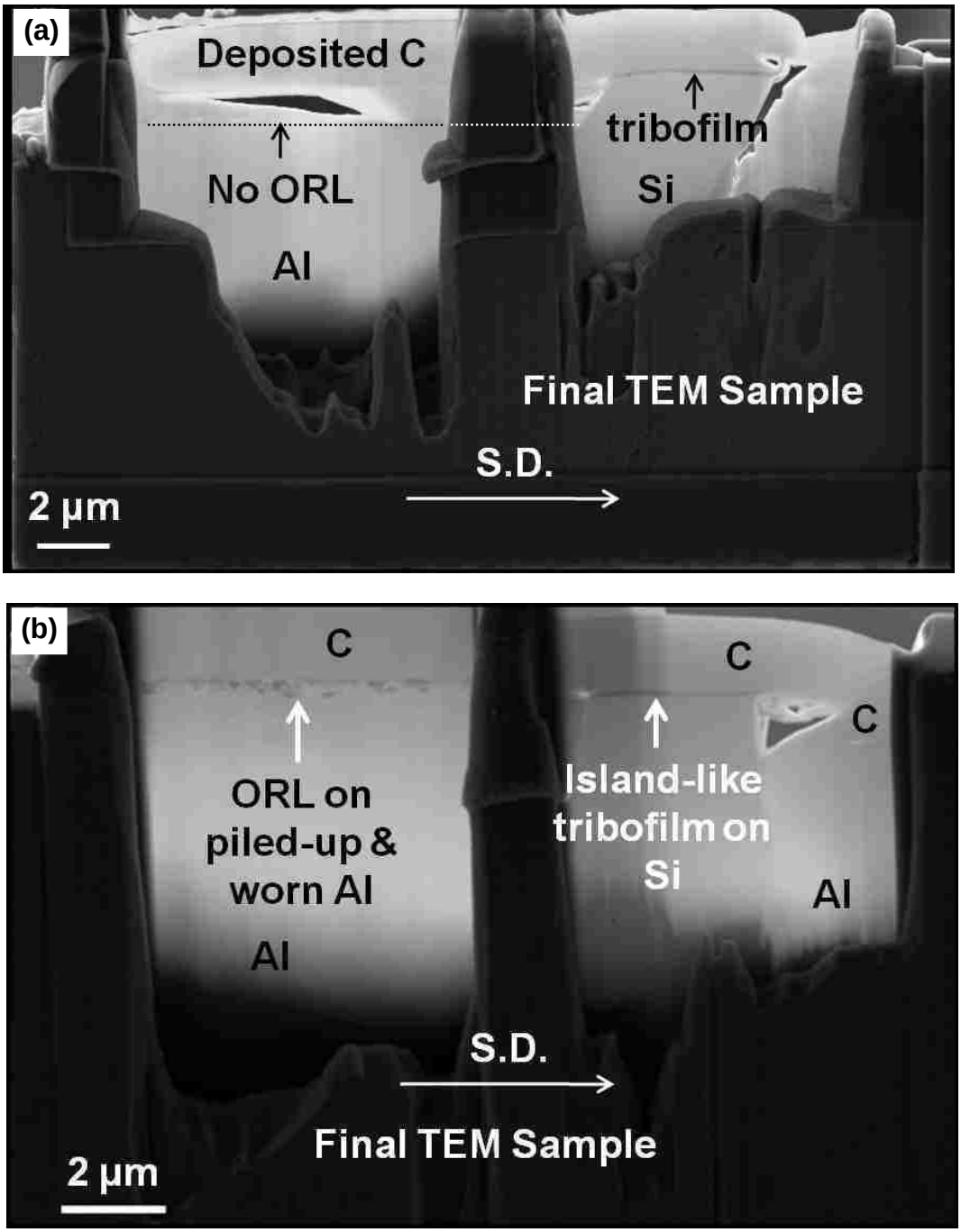

Figure 5. 7: (a) Formation of island-like tribofilm on top of silicon particles after 10^4 sliding cycles (the dotted line represents the approximate boundary between the aluminum surface and the deposited C) and (b) an island-like tribofilm on silicon and an ORL on piled-up and worn out aluminum after 5×10^4 sliding cycles. The square box in b indicates the location of STEM elemental map as shown in Figure 5. 8. See Figure 5. 5b for the location from where the samples were prepared. The deposited C is from TEM sample preparation.

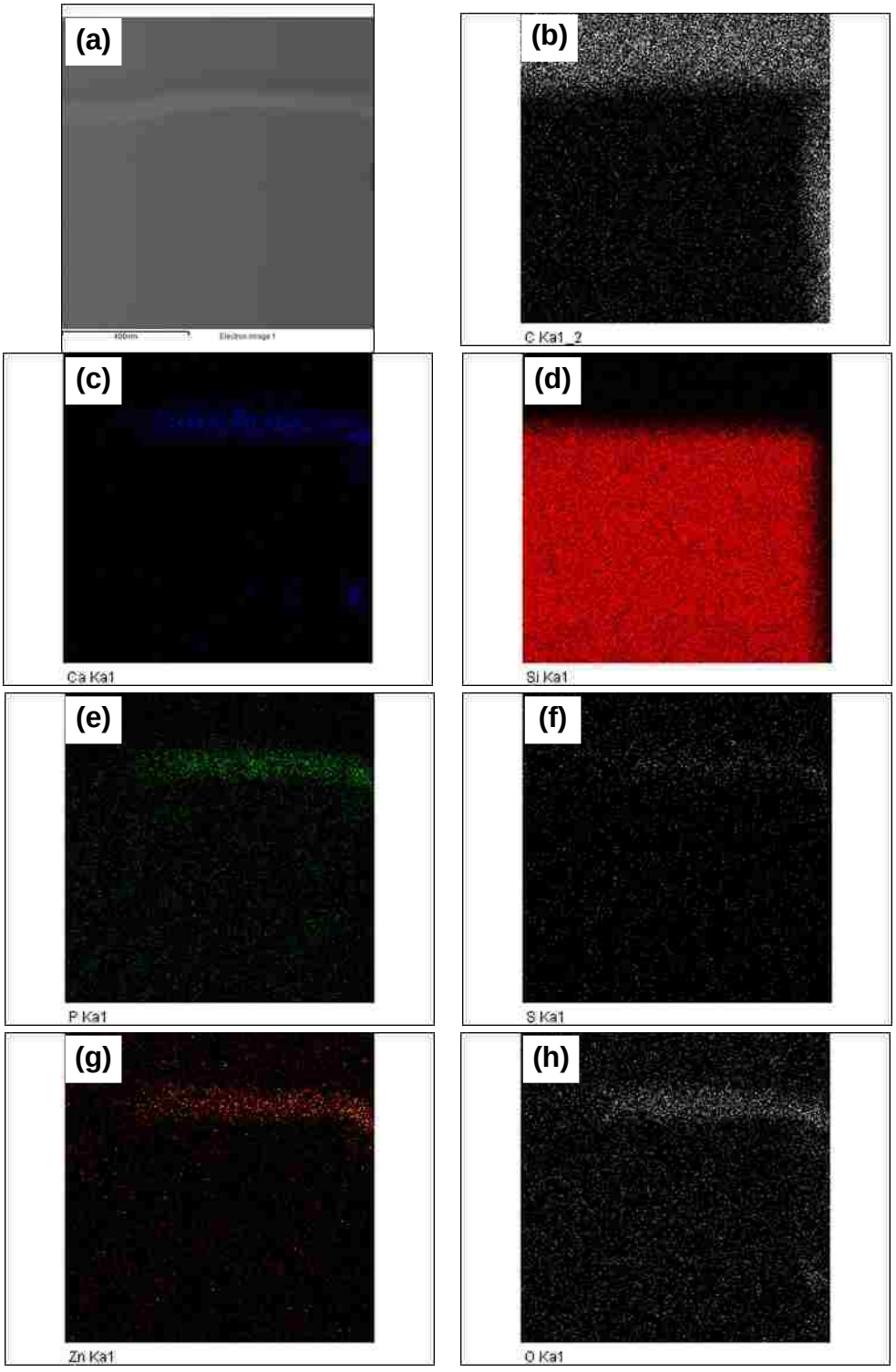

Figure 5. 8: STEM elemental maps of the tribofilm formed on Si after 5×10^4 sliding cycles: (a) electron image, (b) C, (c) Ca, (d) Si, (e) P, (f) S, (g) Zn, and (h) O.

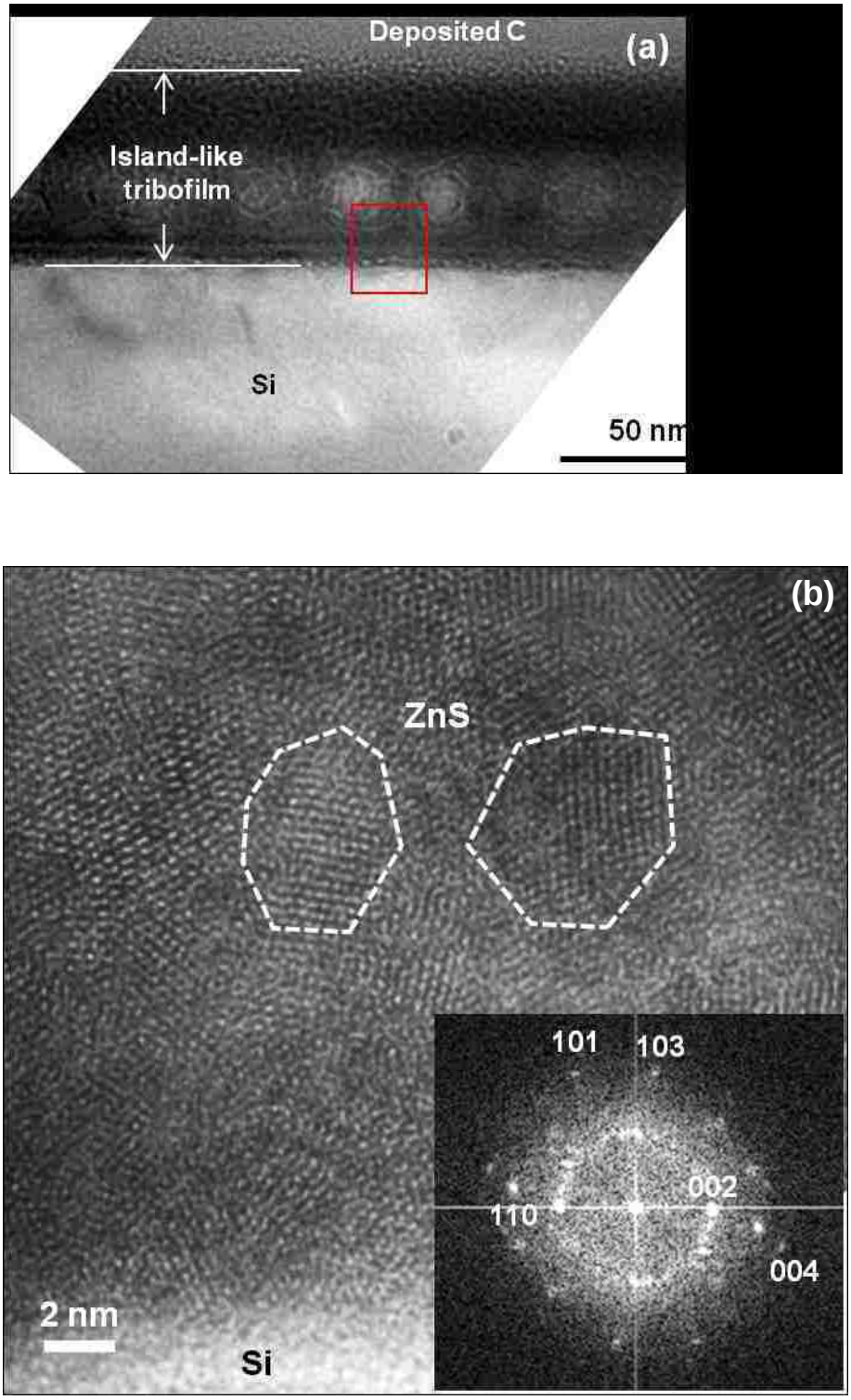

Figure 5. 9: Cross-sectional TEM micrograph showing the island-like tribofilm on Si after 5×10^4 sliding cycles at 100 °C; (b) HRTEM image of the island-like tribofilm as shown in (a) showing crystalline structure of the film. The inset shows the FFT image identifying different planes corresponding to ZnS structure.

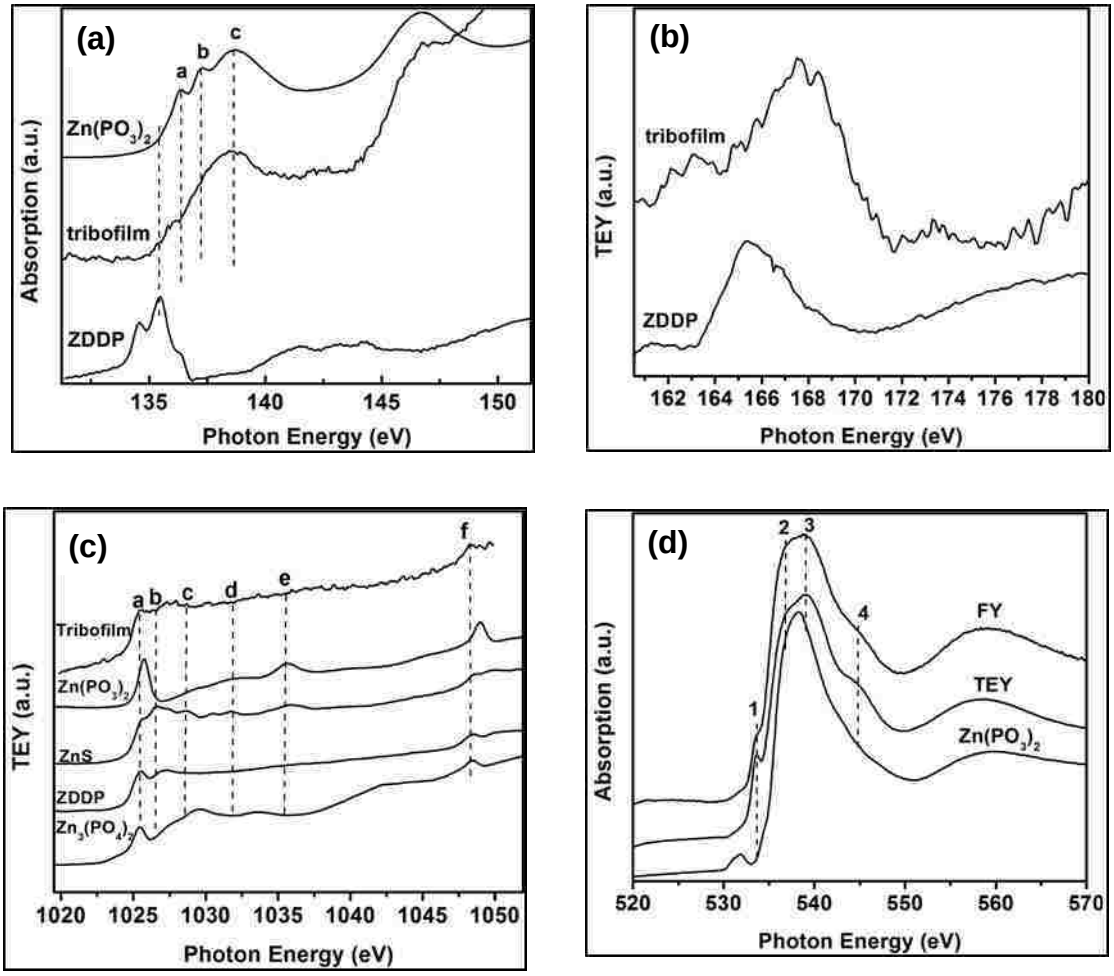

Figure 5. 10: XANES of tribofilm produced by a fully formulated engine oil and reference compounds recorded in TEY mode – (a) P L-edge; (b) S L-edge; (c) Zn L-edge; and (d) O K-edge XANES recorded in TEY and FY mode of island-like tribofilm with a reference compound.

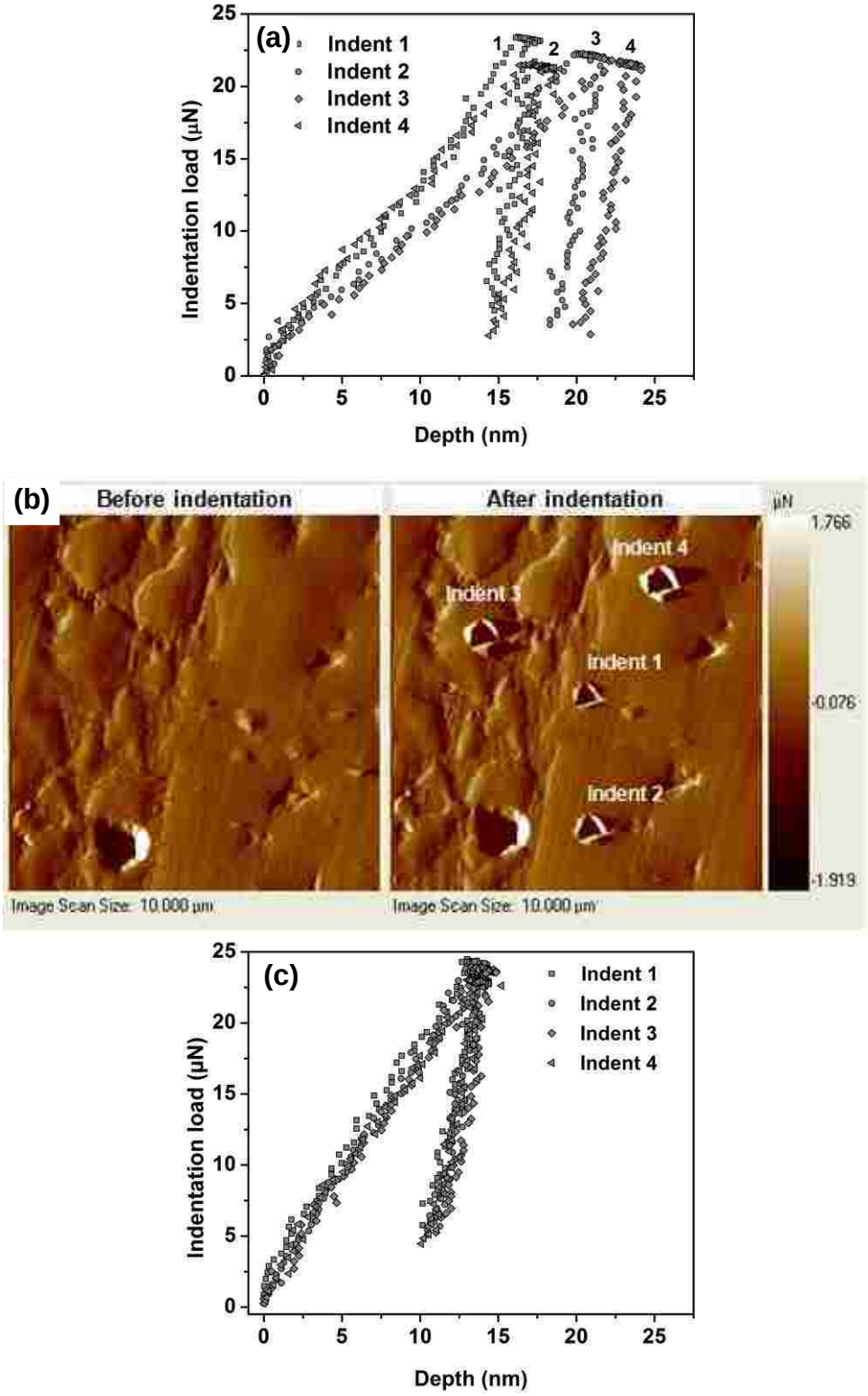

Figure 5. 11: Typical load-displacement curves obtained from nanoindentation experiments performed using a cube corner indenter on (a) island-like tribofilm on silicon; (b) SPM images recorded by the same indenter before and after indentation; and (c) load-displacement curves on silicon without tribofilm.

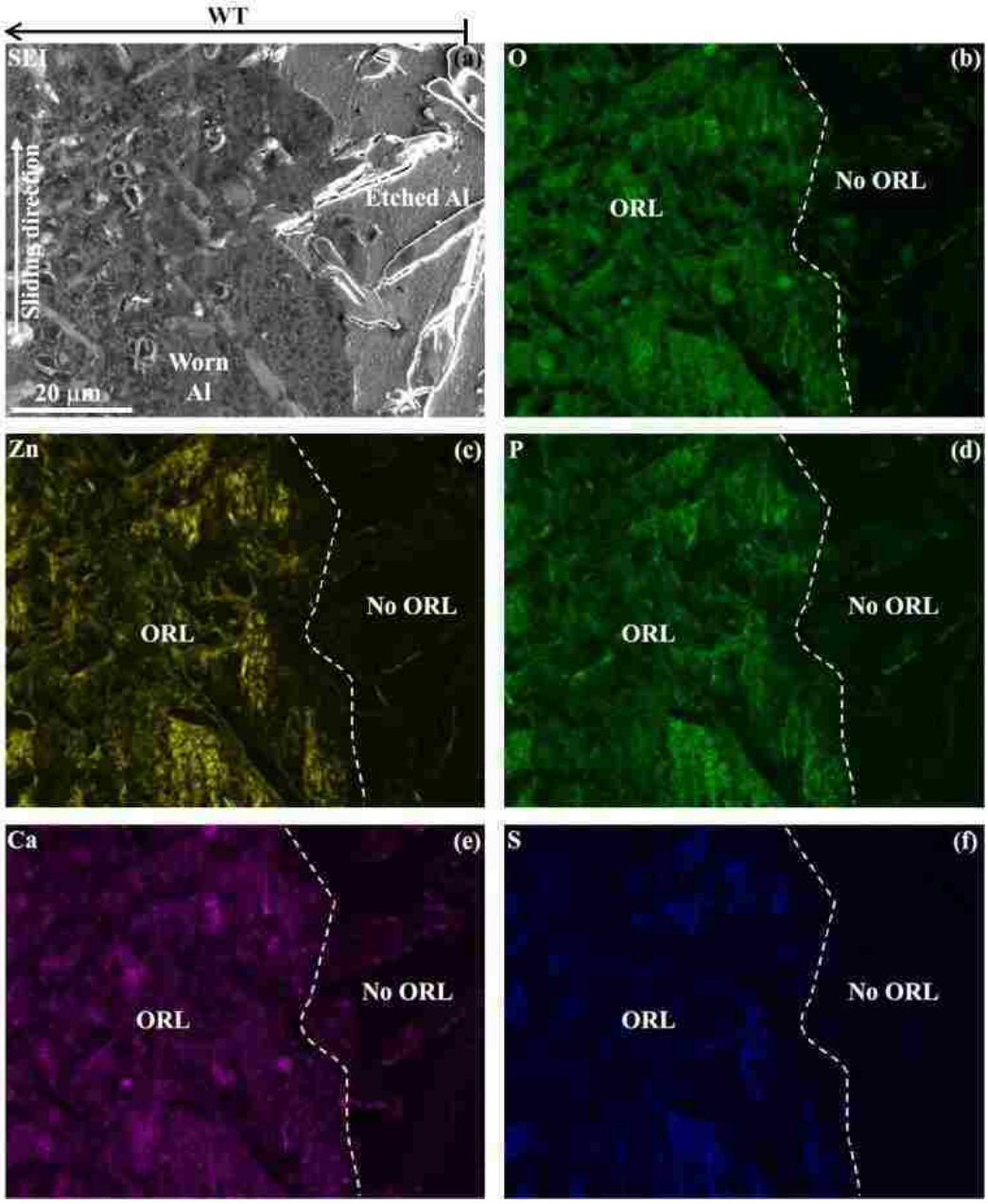

Figure 5. 12: EDS map of wear track at RT after 3×10^5 sliding cycles at 100 °C showing the distribution of various elements: (a) secondary electron image; (b) oxygen; (c) zinc; (d) phosphorus; (e) calcium; and (f) sulphur. The scale bar is the same in all images as in the SEI. WT is the wear track (at the outside edge of WT an island-like tribofilm was formed on Si but no co aluminum wear occurred).

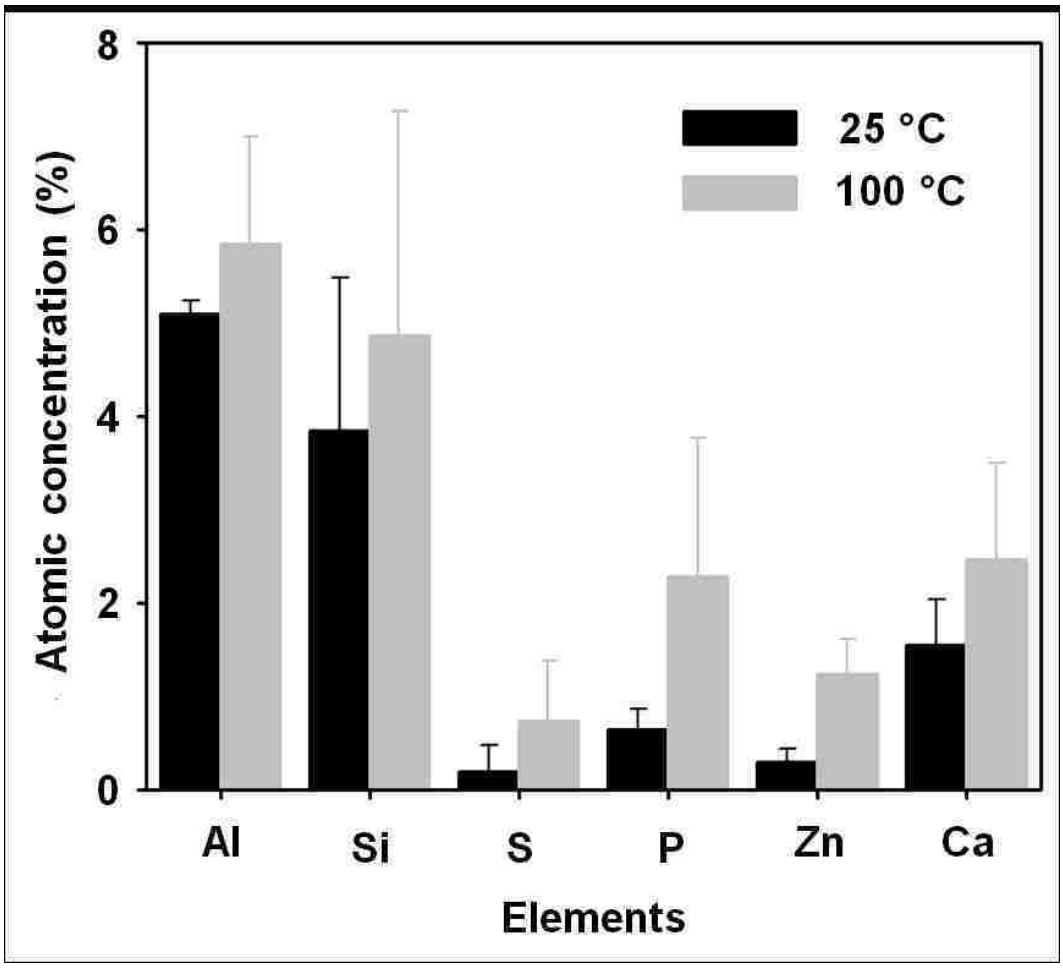

Figure 5. 13: Comparison of semiquantitative analysis of the wear track using XPS at two different temperatures illustrating the difference in composition of oil-residue layer formed during sliding after 3×10^5 sliding cycles. The XPS beam diameter was 200 µm and the data was collected from the top 5-10 nm of the worn surface. The error bar represents the variation in data from two to three locations.

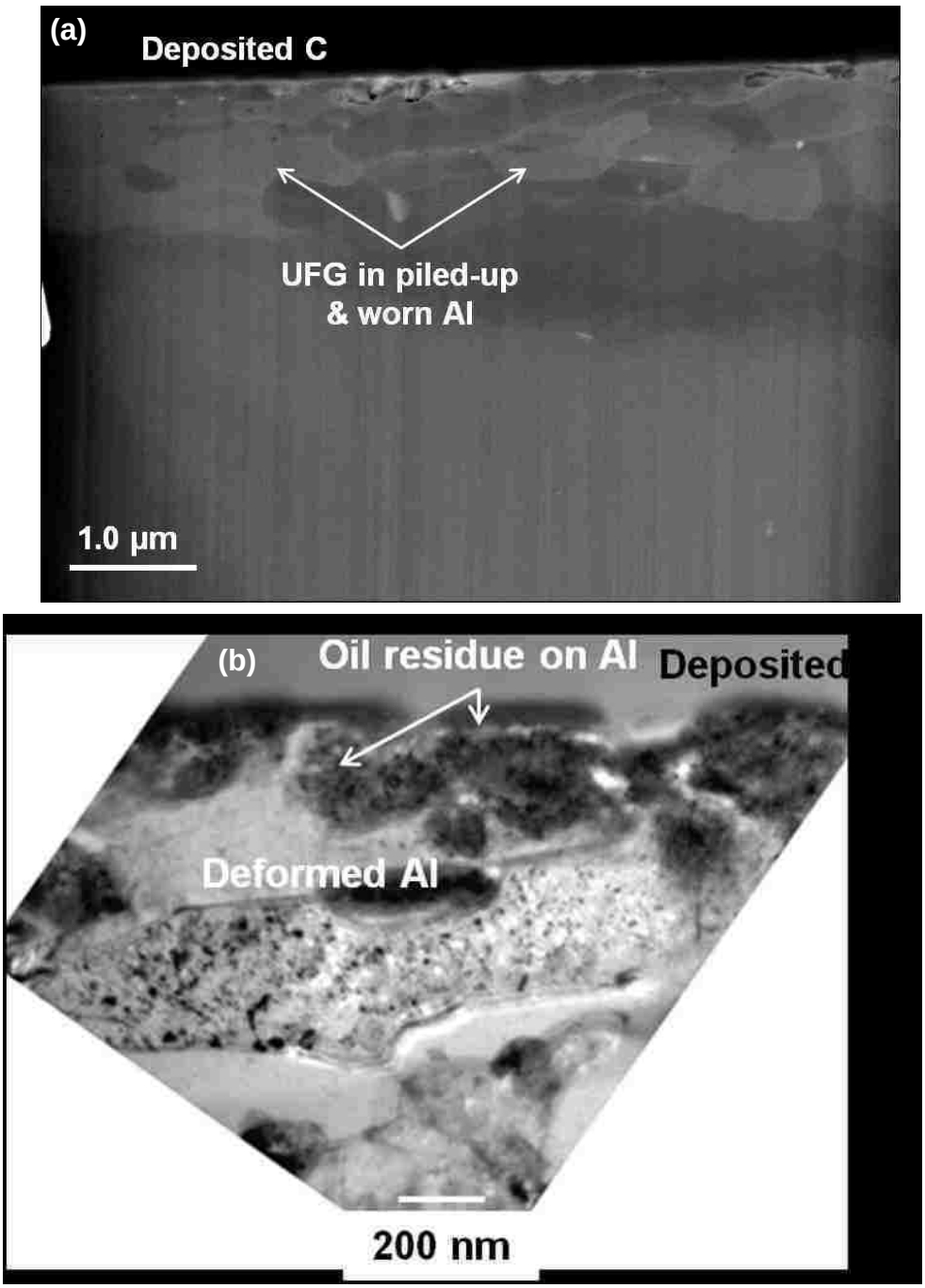

Figure 5. 14: (a) High magnification SEM image and (b) TEM bright field image of the ORL formed on piled-up aluminum after 5×10^4 sliding cycles at 100 °C (from inset in (a)). It was observed that at this stage ORL was formed only on top of piled-up and worn aluminum.

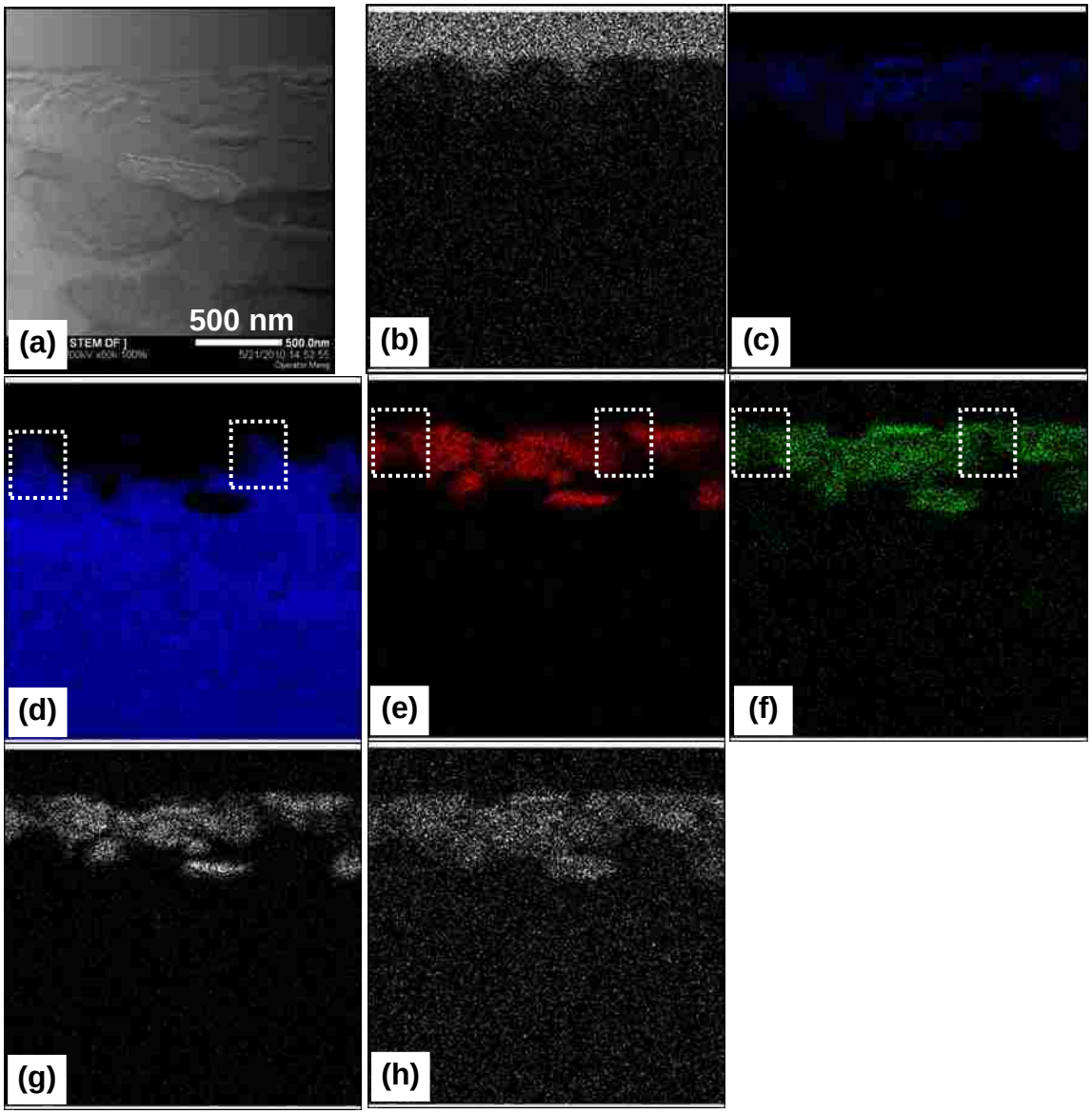

Figure 5. 15: STEM elemental maps of the ORL on piled-up aluminum after 5×10^4 sliding cycles: (a) STEM dark field image, (b) C, (c) Ca, (d) Al, (e) Zn, (f) P, (g) S, and (h) O. The dotted squares in d-f indicate the presence of aluminum within the ORL.

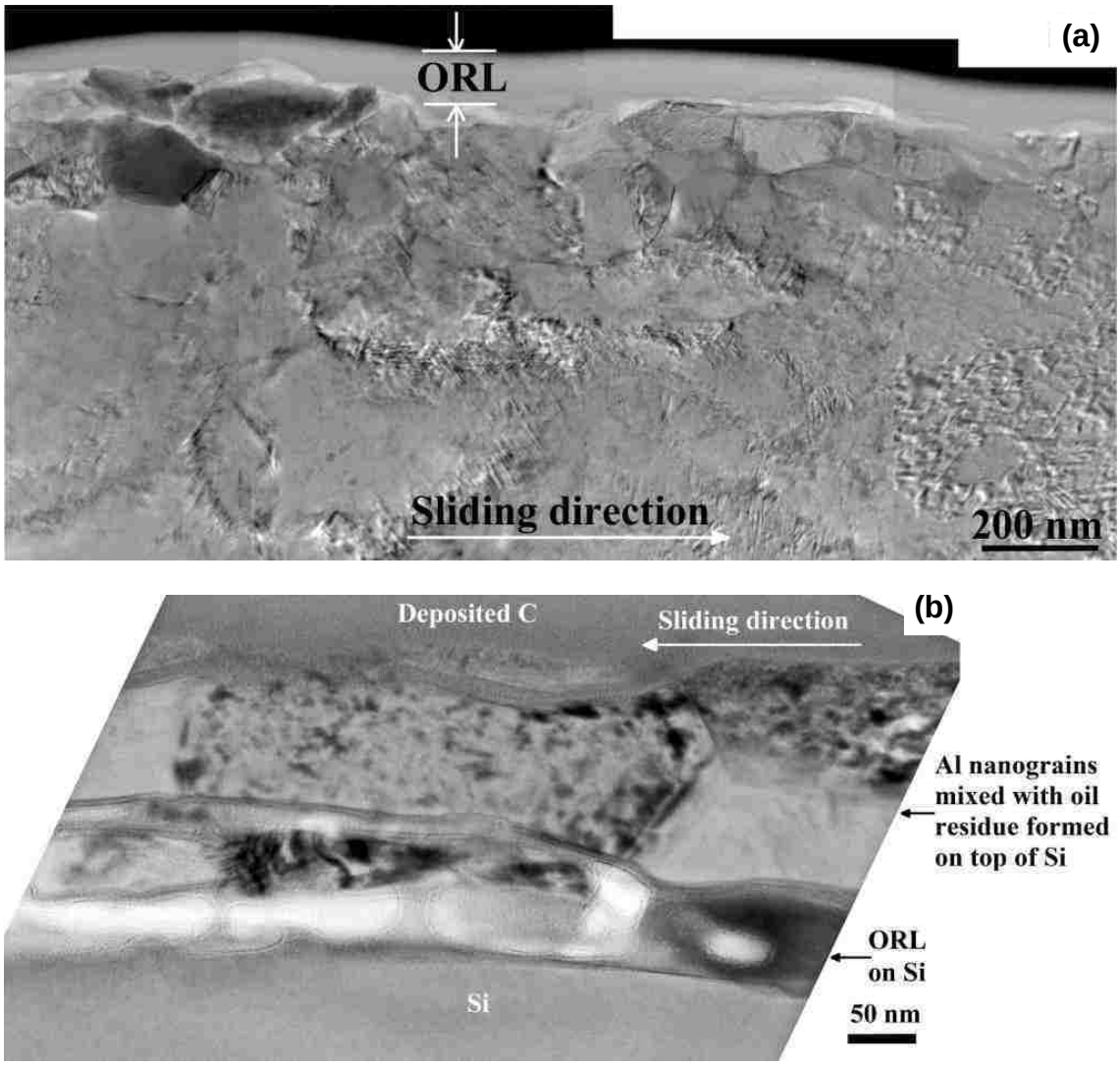

Figure 5. 16: Cross-sectional image of the wear track after (a) 3×10^5 and (b) 6×10^5 sliding cycles at 100 °C showing a continuous ORL on aluminum and silicon, respectively; (c) change in thickness of the island-like tribofilm and ORL with sliding cycles. In (b) mechanical mixing of the ORL with aluminum was observed.

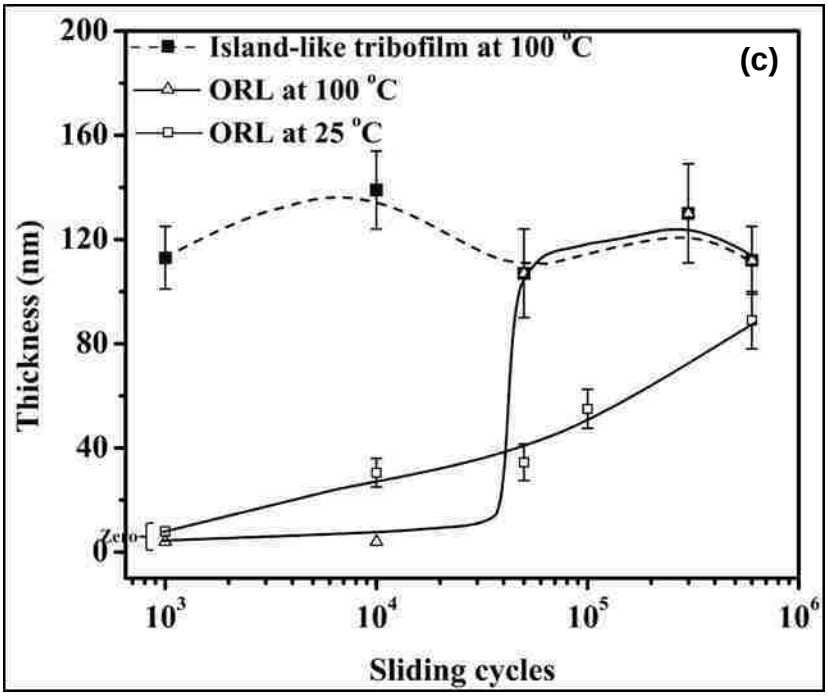

Figure 5. 16: Continued

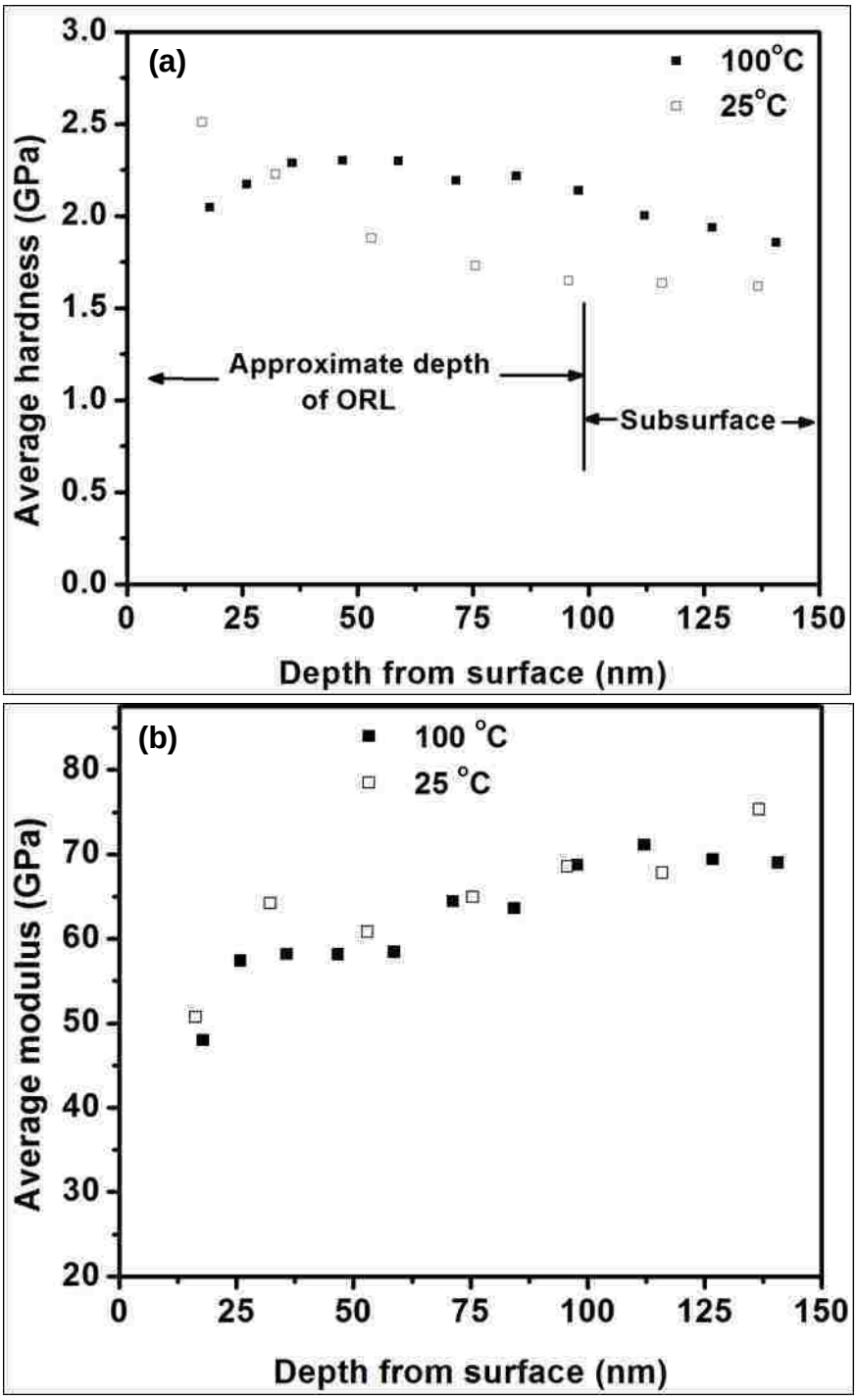

Figure 5. 17: (a) Average hardness and (b) average Young`s modulus of the ORL measured on samples wear tested at two different temperatures using nanoindentation. The measurements were carried out using a Berkovich tip with a progressive multi-cycle indentation. The data represents the average value from six different indents measured on the sample after 6×10^5 sliding cycles. The standard deviation of the data shown in the graph varies between 10% and 30%.

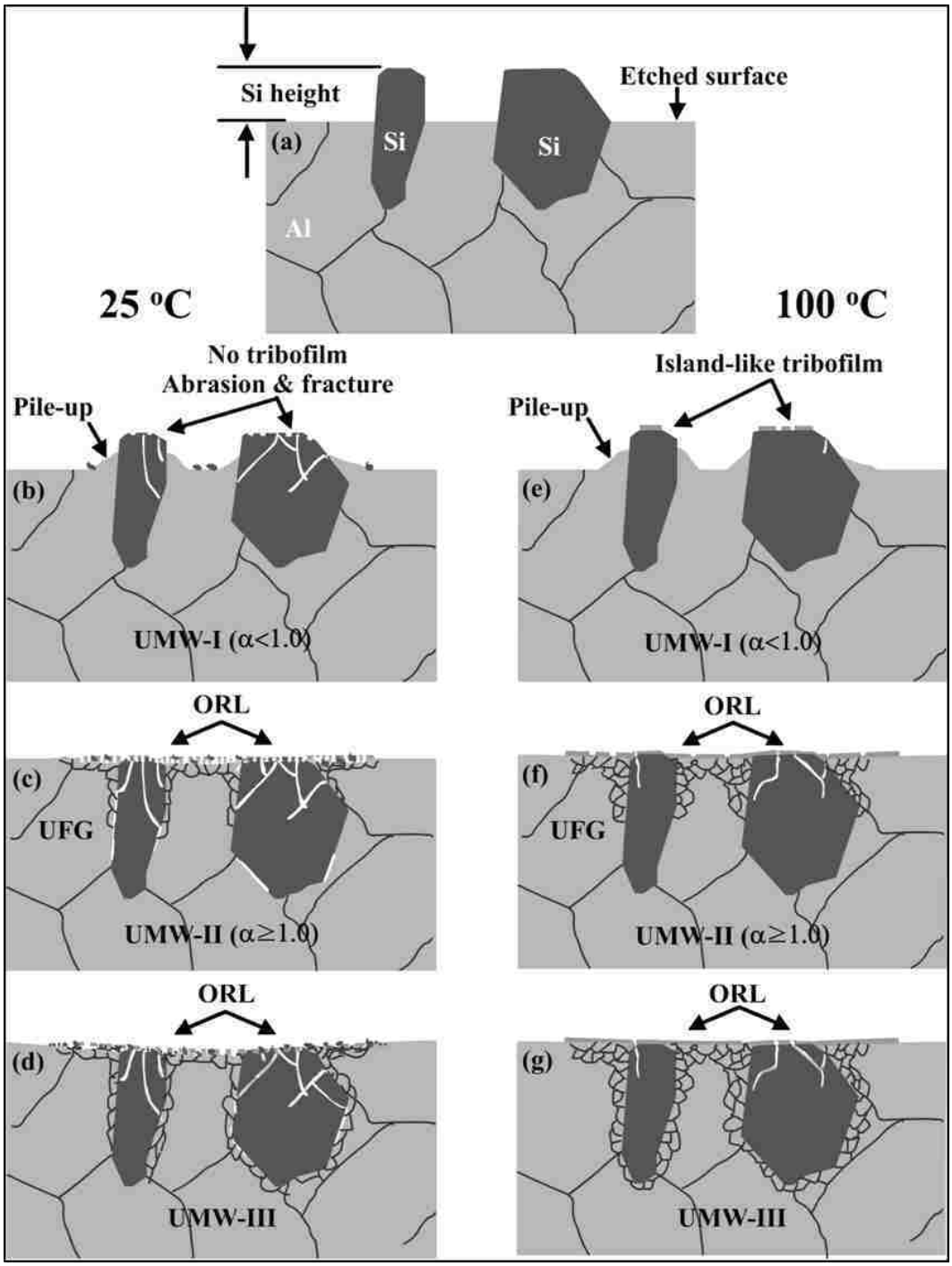

Figure 5. 18: Schematic diagram showing the sequence of events in UMW mechanisms in Al-12.6 wt.% Si alloys at RT and at 100 °C: (a) etched surface; (b)-(d) UMW-I, UMW-II, and UMW-III at RT, respectively; and (e)-(g) UMW-I, UMW-II, and UMW-III at 100 °C, respectively. At 100 °C island-like tribofilm formed on silicon in UMW-I stage leading to less fracture and abrasion of particles compared to that at 25 °C. Island-like tribofilm also delayed the start of UMW-II stage at 100 °C. Once the ORL formed, similar wear rates were observed at both temperatures.

6. CHAPTER 6 – EFFECT OF TEMPERATURE ON UMW AND LONG TERM DURABILITY OF ORL

6.1 Introduction

The laboratory studies conducted in the UMW region to understand the wear mechanisms so far have not studied the durability of Al-Si alloys in the UMW region. Durability means the ability of the alloy to maintain UMW for an extended period of time. It was shown in the previous chapter (**Chapter 5**) that in UMW-III, a stable or reduced wear rate was observed. But it was not known how long the UMW-III can be maintained. The Al-Si alloys derived their wear resistance from the ORL formed during sliding in UMW-III. It was also shown in a previous study [**94**] that once an ORL supported by ultra-fine grain aluminum formed on the worn surface during sliding, the silicon content of the alloy had no effect on wear resistance in the UMW-III region (up to 6×10^5 sliding cycles). But the long term durability of the ORL, that is, whether the ORL was able to sustain the UMW during an extended period of sliding (up to 6×10^6 sliding cycles, an order of magnitude higher), was not studied. Thus, detailed investigation was needed to understand the durability of ORL. Simulation of long term durability using laboratory studies is perhaps a challenge due to a variety of external influences in normal internal combustion engine running, for example, speed, duration, pressure at the cylinder wall. Also during the course of normal running, the engine oil temperature may vary from anywhere between subzero temperatures to approximately 160 °C depending on the weather conditions and the variation in temperatures along the cylinder wall. However, it will be shown in this chapter that the POD studies conducted under boundary lubrication at different temperatures between 25 °C and 160 °C for 3×10^5 sliding cycles and at 100 °C for 6×10^6 sliding cycles provides a strong

indication that the ORL formed in UMW-II and UMW-III stages can sustain UMW in Al-Si alloys and that this ORL makes the replacement of traditional cast iron material with the lightweight Al-Si alloy possible in monolithic (linerless) engine blocks. Thus, it will also be shown that a eutectic Al-Si alloy, which is inexpensive to manufacture, provides an alternative to the expensive high silicon content hypereutectic alloys and can be used in linerless engines of smaller or even entry segment passenger vehicles.

To simulate a variety of the engine running conditions (different temperatures and sliding duration), boundary lubricated POD tests on Al-12.6% Si alloy were conducted at varying temperatures (25–160 °C) at 2.0 N load for 3×10^5 sliding cycles, and four tests were conducted at 100 °C at 2.0 N load for 6×10^6 sliding cycles for four different Al-Si alloys with different silicon contents and heat treatment conditions. The aim of the studies conducted at varying temperatures was to study the formation of ORL against different temperatures, a condition imposed by different oil temperatures, whereas the objective of the later experiments for 6×10^6 sliding cycles was to investigate the long term durability of the ORL.

6.2 Effect of different temperatures

The effect of different temperatures on the formation of ORL and the wear behaviour of Al-12.6% Si alloy were investigated. Detailed experiments at 25 °C and 100 °C for different sliding durations showed that the UMW-III started to occur at 3×10^5 sliding cycles at a normal load of 2.0 N. Accordingly, to study the effect of different temperatures on UMW behaviour of Al-Si alloys, boundary lubricated sliding wear experiments were conducted using POD configuration at a constant normal load of 2.0 N and for constant sliding cycles of 3×10^5 sliding cycles in the presence of SAE 5W30 synthetic grade engine oil. Tests were conducted at five different temperatures: 25, 80, 100, 140, and 160 °C.

6.2.1 Coefficient of friction

The COF during the sliding experiments were recorded and **Figure 6. 1** shows the variation in COF with sliding cycles at five different temperatures between 25 and 160 °C. The inset in **Figure 6. 1** shows the variation of the COF during the initial sliding periods. It was noted that above 80 °C, there was a drop in the friction from an initial high value and then a rise again to the steady state causing a valley in the COF plots. However, at 25 and 80 °C such valley was not observed; from an initial high COF value, the steady state COF was gradually reached. The average COF in all four tests are listed in **Table 6. 1**. The average COF, measured over the complete period of sliding, was the highest (0.15±0.01) at 100 °C and the lowest (0.12±0.01) at 160 °C. However the average COF at the beginning of sliding up to 10^4 sliding cycles (UMW-I) was higher than the steady state average between 10^4 and 3×10^5 sliding cycles, as listed in **Table 6. 1**. During this period the highest average COF was observed at 25 °C and the lowest was observed after 160 °C. The higher COF at 25 °C was due to the absence of an island-like tribofilm during the initial sliding period corresponding to UMW-I; also the lower shear strength of aluminum may have had some influence in lowering the COF at high temperature.

6.2.2 Surface profile of the worn surfaces

The worn surfaces were observed using optical interferometer. **Figure 6. 2a-e** shows the optical profilometer images of worn surface tested at 25, 80, 100, 140, and 160 °C, respectively. The silicon particles within the wear track were observed to have sunk-in completely. Accordingly, the silicon particle height was zero at this stage. Thus it can be said that the alloy entered into UMW-II stage. The width of the WT, observed from eight different locations, varied with the temperature. At 80 °C the width of the WT was the highest, and at 160 °C the width was the lowest. At lower temperatures (25 and 80 °C) the worn surface had multiple grooves

running parallel to the sliding direction. With an increase in temperature the formation of multiple grooves was minimized, and at 160 °C the worn surface was covered with a layer with no grooves. It was also observed that the roughness of the worn surfaces varied with different temperatures. **Figure 6. 3** shows the variation in average surface roughness of the WT with temperature. The surface roughness at the extreme temperatures of 25 °C and 160 °C were the lowest, and at an intermediate temperature of 80 °C, the surface roughness was the highest. The high surface roughness was probably due to abrasion by fractured of particle and the counterface (see **Figure 6. 2b** and **Figure 6. 11b**)

6.2.3 Morphology and surface chemistry of the worn surface

6.2.3.1 Alloy sample surfaces

The worn surface morphology was observed in SEM and analyzed using EDS. **Figure 6. 4** shows the SEM images of the worn surfaces in Al-12.6% Si alloy at 25, 80, 100, 140, and 160 °C, respectively. From the SEM images, the formation of ORL was observed within the worn surfaces. With the increase in temperature and under the contact pressure, the decomposition of the oil additive ZDDP to phosphates was easier [**63**], and at temperatures higher than 100 °C, the WT was covered by such decomposition products of ZDDP probably much earlier than the WT at lower temperatures, 25 °C and 80 °C. Also at the centre of the WT, silicon particles were completely sunk-in in the matrix at all temperatures. The distribution of various elements of ORL within the worn surface was mapped using EDS. **Figure 6. 5b-e** and **Figure 6. 6b-e** show the EDS elemental map of the distribution of Zn, P, S, Ca, and O within the worn surfaces at 140 and 160 °C, respectively. The EDS data confirmed the presence of Zn, P, S, and Ca, which were disintegrated from the engine oil additive to form the ORL. There was also C within the ORL. Based on the characterization of the ORL in **Chapter 5** and in **Section 6.3.3**, it is plausible to say

that the ORL, formed at 100 °C and above up to 160 °C, had zinc sulphide and zinc polyphosphate.

To confirm the findings of EDS, XPS survey scans were performed. The spot size of the beam was 100 µm, and the pass energy was 280 eV with a 0.5 eV step size. **Figure 6. 7a-c** shows the XPS survey scan of the worn surface in samples tested at 25, 100, and 160 °C, and **Figure 6. 7d** shows the survey spectra outside the WT on 100 °C tested sample. The XPS survey spectra showed that all samples had the elements originated from the decomposition of additive packages from the oil, and their concentration was higher at higher temperatures. **Figure 6. 8** shows the atomic concentration of Zn, P, S, Ca, C, O and some other elements measured from the survey scan data. It was observed that atomic concentration of calcium, which originated from the Ca-based detergents used as a sludge removal additive in the oil, increased with temperature. The atomic concentration of Zn, P, and S, which originated from ZDDP in the engine oil, also increased with increasing temperature.

6.2.3.2 Counterface surfaces

The counterface surface was also observed using SEM, and the surface chemistry was probed using EDS. **Figure 6. 9a-c** shows the SEM images of the counterfaces, and **Figure 6. 9d-f** shows the corresponding EDS spectra within the worn surfaces at 80, 140, and 160 °C, respectively. There was no aluminum adhesion observed in the counterfaces at any tested temperatures. However at 140 °C, there was an accumulation of ORL at the trailing edge of the contact. The EDS spectra confirmed the presence of elements from decomposed engine oil additives on the counterface. It was possible that an ORL also formed on the counterface, as it was reported in the literature that in the presence of ZDDP, tribofilm formed on AISI 52100 steel surfaces [**119-121**]. There were many other extensive studies [**132-136,139**] carried out on ZDDP

tribofilm formation on steel under sliding contact. However, the ORL formation on steel counterfaces was not characterized extensively within the scope of this dissertation.

6.2.4 Volumetric wear loss

6.2.4.1 Wear loss of the matrix

The volumetric wear loss of the matrix was calculated from eight different areas of the wear track similar to the interferometer images shown earlier in **Figure 6. 2**. **Figure 6. 10** shows the volumetric wear at different temperatures in Al-12.6% Si alloy after 3×10^5 sliding cycles. The wear loss variation with temperature was non-linear. The highest amount of wear was observed at an intermediate temperature of 80 °C, and the lowest amount of wear was observed at 160 °C. Because increases in temperature under the application of contact pressure aid in decomposition of additives and the formation of ORL, it is plausible to say that at higher temperatures the WT was covered by the ORL much earlier in the sliding process, and the contact between the counterface and the ORL also initiated earlier; thus the reduction in wear loss of the matrix was observed at higher temperatures above 100 °C.

6.2.4.2 Wear loss of the counterface

The counterface was also observed using the optical interferometer after the wear tests, and **Figure 6. 11a-e** shows the interferometer images of the counterface at different temperatures investigated. The counterface surface profile was similar to that of the worn surface of the alloys. The average roughness of the counterfaces was also calculated and is shown in **Table 6. 2**. The counterface roughness was highest at 100 °C and lowest at the extreme temperatures of 25 °C and 160 °C. The area of the worn surfaces on the counterfaces at different temperatures was almost same. But within the worn area the surface had many groves formed in the direction of sliding. The wear loss of the counterface was also calculated, and

Figure 6. 11f and **g** shows the surface roughness and volumetric wear loss of the counterfaces at different temperatures, respectively. The highest amount of wear was observed in the counterface used at 100 °C, and the lowest amount of wear was observed in the counterface used at 25 °C.

6.2.5 Discussion and summary

Result of elevated temperature wear in Al-12.6% Si T7 alloy at different temperatures showed that thermal activation of the lubricating engine oil containing ZDDP was beneficial in providing wear resistance of the alloy at elevated temperatures. Thermal degradation of ZDDP, the main antiwear additives found in 5W30 engine oil, is a well studied research topic [**85**] and suggests that the thermal degradation happens faster with increases in temperature. Upon heating, the ZDDP when in oil, decomposes to produce volatile compounds such as olefin, alkyl disulfide, alkyl mercaptan, and a precipitate of low sulphur containing zinc pyrophosphate [**60,85,90**]. The rate of film formation was found to be directly proportional to the temperature on steel surfaces, and the tribofilm thickness reached a maximum thickness [**149**]. Thereafter, equilibrium existed between formation and removal of the tribofilm, the rate of formation being more dependent on temperature than on the rate of removal. With increasing temperature from 100 to 160 °C, the wear resistance of the eutectic alloy was better than the lower temperatures after 3×10^5 sliding cycles. This was due to the formation of ORL which consisted of the ZDDP decomposition products (zinc phosphates and zinc sulphides) mixed with the aluminum matrix at the contacting surface at temperatures above 100 °C preventing contact between the counterface and the aluminum matrix. Previous study [**150**] also had shown that the Al-12.6% Si alloy had higher scuffing resistance compared to Al-18.5% Si alloy and Al-25.0% Si alloy against iron surfaces and the hot scuffing in presence of 5W30 engine oil did not initiate until the temperature was 200 °C. This alloy had finer particles embedded in the matrix

which had a matrix hardness of 69.1±1.0 HV_{10}. Thus it was expected that the particle sinking-in in this alloy would be faster than in the Al-12.6% Si alloy with large silicon particles which was studied in **Chapter 5**. Based on the microstructural evidence, it can be said that at 3×10^5 sliding cycles the UMW-III was reached at all temperatures in this alloy. The optical interferometer images (**Figure 6. 2**) and SEM images (**Figure 6. 4**) of the WT provided evidence for this. Accordingly, at lower temperature when the tribofilm did not form on silicon particles, the early particle sinking-in (as this was shown in the previous chapter, **Figure 5.1**) resulted in a higher matrix wear. Thus the higher matrix wear at 25 and 80 °C compared to that at temperatures above 100 °C. However, at temperatures above 100 °C, due to early formation of the ORL on the worn surface, the matrix was exposed to the counterface for a shorter duration; thus the ORL caused a reduction in wear at temperatures above 100 °C.

6.3 Long-term durability of ORL

The four different Al-Si alloys used in this study were Al-12.6% Si T7, Al-12.6% Si T6, Al-18.5% Si, and Al-25% Si. The tests were conducted at boundary lubrication condition at a constant normal load of 2.0 N and for constant sliding cycles of 6×10^6 revolutions at 100 °C. SAE 5W30 synthetic oil was used as lubricating oil.

6.3.1 Coefficient of friction

The variation COF during the sliding for four different alloys is shown in **Figure 6. 12**. It was observed that COFs in the four alloys were different during the UMW-I and UMW-II stages. However, constant COF was achieved during the UMW-II stage between 2×10^6 and 6×10^6 cycles. The inset in the **Figure 6. 12** shows the variation of COF during early sliding cycles in the UMW-I region. The variation of COF was typical at 100 °C as shown by the valley in the COF plot also observed earlier in **Figure 6. 1**. The average COF for the complete duration of sliding was

calculated and reported in **Table 6. 3**. The average COF varied between 0.109 and 0.132 among the different alloys with the maximum COF obtained in the Al-12.6% Si T6 sample and minimum COF obtained in Al-25.6% Si alloy. From the COF plot shown in **Figure 6. 12**, it can be said that the four tests were conducted in similar conditions, and the influence of COF on the results of durability studies can be disregarded, that is, any variation or similarity in wear behaviour in the four alloys was not due to COF. It was also noted that the change in silicon content, particle size and morphology, and the heat treatment of the alloy had very little influence on the COF in the UMW-III region.

6.3.2 Morphology of the worn surfaces and the counterfaces

In this section the results of wear surface morphology observed using the optical profilometer and SEM will be presented to show some characteristic features of the worn surfaces in the four alloys studied.

Figure 6. 13a-d shows the optical interferometer images of typical areas from the worn surfaces of the Al-12.6% Si T7, Al-12.6%Si T6, Al-18.5% Si, and Al-25.0% Si alloys, respectively. The worn surfaces of Al-12.6%Si T6 and Al-25.0% Si alloys had multiple grooves formed in the direction of sliding, and the width and the depth of these grooves were smaller in Al-25.0% Si. The appearance of the worn surfaces in Al-12.6% Si T7 and Al-18.5% Si alloys were comparatively smoother. The average surface roughness of the worn surfaces and the corresponding counterfaces are plotted in **Figure 6. 13e**. It may be observed that the roughness of the WT and the counterface in Al-12.6% Si and Al-25.0% Si alloys were higher than the other two alloys, corroborating the typical observations from **Figure 6. 13a-d**. The higher surface roughness in the Al-12.6% Si T6 sample was due to the formation of multiple grooves within the WT. In T6 heat treat condition the hardness of the matrix is higher than in T7 heat treat condition. Therefore, at lower sliding cycles (during UMW-I), particle fracture took place and the

fragmented particles acted as abrasive particles causing formation of multiple grooves. In Al-25.0% Si alloy the higher surface roughness was also due to the formation of multiple grooves. Another observation was the change in surface roughness compared to the initial roughness. The initial (after etching) surface roughness in Al-12.6% Si T7, Al-12.6%Si T6, Al-18.5% Si, and Al-25.0% Si alloys was 0.41±0.01 µm, 0.42±0.02 µm, 0.70±0.09 µm, and 0.71±0.004 µm, respectively. The initial high surface roughness in the hypereutectic alloys was due to higher silicon content. After wear tests, the average surface roughness dropped in all samples except in the Al-12.6% Si T6 sample. The roughness in this sample increased from 0.42±0.02 µm to 0.46±0.11 µm due to the grooves within the WT. Also note the change in standard deviation from 0.02 to 0.11 µm. Changes in surface roughness were also observed in the corresponding counterfaces, and the surface roughness increased in all cases. However, the counterface roughness after the wear tests was always higher compared to the worn surfaces because of the abrasion of the smoother counterfaces by the silicon particles. Thus it may be observed that any change in the alloy surface was also reflected on the counterface. For example, between the two hypereutectic alloys, Al-18.5% Si alloy had a comparatively smoother surface and so did the counterface. Similar observation was also made between the two eutectic alloys and their corresponding counterfaces.

The worn surfaces were also observed using the SEM, and **Figure 6. 14a-d** shows the SEM micrographs of the typical worn surfaces of the Al-12.6% Si T7, Al-12.6%Si T6, Al-18.5% Si, and Al-25.0% Si alloys, respectively. It was observed from the SEM micrographs that all four alloys had very similar surface morphology, and the WT surfaces had a continuous ORL. The surface chemistry was analyzed with EDS and XPS, and the results will be presented in **Section 6.3.3**. In Al-25.0% Si, it was also observed that the silicon particles had the island-like tribofilm.

6.3.3 Surface chemistry of the ORL at 6×10^6 sliding cycles

After the wear tests, the worn surfaces were analyzed using EDS and the XPS to confirm the chemistry of the ORL. Within the worn surfaces, EDS investigation was conducted by collecting spectra to identify the elements, and then the distribution of those elements were mapped. **Figure 6. 15a-d** depicts the EDS spectrum of the worn surfaces in Al-12.6% Si T7, Al-12.6%Si T6, Al-18.5% Si, and Al-25.0% Si alloys shown in **Figure 6. 14a-d**, respectively. It was observed that S, P, Zn, Ca, and O were present within the worn surfaces whose primary source was from the additives in the oil, and the presence of those elements confirmed the formation and existence of ORL even after the extended period of continuous sliding. **Figure 6. 16** shows an EDS map within the worn surface in Al-12.6% Si T7 alloy to illustrate the distribution of ORL elements and the presence of ORL even after 6×10^6 sliding cycles. From the EDS maps it was evident that the continuous ORL was present over the worn surface in all four alloys.

Survey and high resolution spectra were recorded from the worn surfaces using XPS. In the survey spectra C, Zn, P, S, and O signals were detected apart from the elements from the alloy. **Figure 6. 17a** shows a typical survey spectrum from the worn surface of an Al-12.6%Si T7 sample. Subsequently, high resolution spectra of C1s, O1s, S2p, and P2p were recorded. **Figure 6. 17b-e** shows the high resolution spectra of C1s, O1s, S2p, and P2p, obtained from the worn surface of the Al-12.6% Si T7 sample. The high resolution spectra of C1s, O1s, S2p, and P2p are shown in **Figure 6. 18a-d** for Al-12.6%Si T6, **Figure 6. 18e-h** for Al-18.5% Si, and **Figure 6. i-l** for Al-25.0% Si alloy, respectively. The high resolution spectra of P2p and S2p orbital always exhibit doublets, that is, two peaks $2p_{3/2}$ and $2p_{1/2}$, due to the spin-orbit splitting. In the case of sulphur, the spectra in the high resolution scan were too noisy. Two different peaks, each consisting of $2p_{3/2}$ and $2p_{1/2}$ spin-orbit splitting peaks, were observed. Among these two peaks, the low energy peak located around 162.1 eV was due to contribution from sulphide, and the

high energy peak located at 168.57 eV (in Al-12.6% Si T6) or 166.96 eV (in Al-12.6%Si T7) was due to the contribution from sulphate [**142**] or sulphite [**142-143**], respectively. However, the signals for sulphate or sulphite were not always very strong, for example in the case of Al-18.5% Si and Al-25.0% Si alloys, and therefore the data fitting for sulphate or sulphite were not carried out in those two alloys. The Zn peak doublets are always far apart and can be easily identified from the survey scan; therefore Zn2p spectra were not recorded in the high resolution scan.

The oxide signals were fitted with three different peaks. The peak at the lower binding energy of 531.0±0.4 eV was assigned to zinc oxide [**143-146**] and aluminum oxide [**147-148**]. The central peak at 531.9±0.4 eV was observed due to the contribution from NBO in polyphosphates and sulphates (if present). The higher energy peak observed at 532.8±0.4 eV was assigned to the BO, which keeps phosphates group in polyphosphate chains connected. The ratio of BO to NBO was calculated after fitting the O1s peak. This ratio indicates the chain length of the polyphosphate. A ratio less than 0.166 indicates the presence of ortho- and pyrophosphates, whereas a ratio greater than 0.5 indicates cross-linked polyphosphates [**119-121**]. The ratio in the four alloy sample is shown in **Table 6. 4**. The high resolution XPS analysis of the worn surfaces showed that the ORL in the eutectic Al-12.6% Si T7 and T6 alloys after 6×10^6 sliding cycles consisted of zinc sulphide, cross-linked zinc polyphosphates, carbon, and aluminum. Some evidence of sulphite in Al-12.6% Si T7 alloy and sulphate in Al-12.6% Si T7 alloy was observed. The ORL in hypereutectic Al-Si alloys consisted of zinc sulphide, ortho- and pyrophosphates, carbon, and aluminum.

6.3.4 Volumetric wear loss

The volumetric wear loss in the aluminum matrix was calculated from the optical interferometer images as shown in **Figure 6. 13a-d**. Again, eight different such areas were used to calculate the volume loss. **Figure 6. 19** shows the volumetric wear loss in the four alloys after

6×10^5 sliding cycles. It can be observed that the volume loss in all four samples were of the same order of magnitude. The lowest volume loss was observed in Al-25.0% Si alloy, and the highest was observed in Al-12.6% Si T7 alloy. However, the difference in wear loss between the Al-18.5% Si and Al-25.0% Si was almost negligible.

6.3.5 Discussion and summary

Experimental evidence presented in **Sections 6.3.1 to 6.3.4** showed the durability of ORL for long sliding durations. It was observed that ORL formed in all four Al-Si alloys with different silicon content and two different heat treatments. Based on the high resolution spectra shown in **Figure 6. 17b-e** and **Figure 6. 18a-l**, and the data from **Table 6. 4**, the following characteristic on the ORL layer composition in Al-Si alloys after 6×10^6 sliding cycles can be made:

1) The peak at around 162.1 eV S2p spectra indicated that the ORL in all four samples contained zinc sulphide.
2) The absence or presence of an S2p peak at 168.57 eV or 166.96 eV indicated the formation of sulphates or sulphites. Based on this information, it was concluded that the ORL in Al-12.6% Si T6 alloy contained sulphate, and the ORL in Al-12.6% Si T7 alloy contained sulphites.

Based on the BO/NBO ratio and the elemental composition, it was concluded that the ORL in Al-12.6% Si T6 and T7 alloys consisted of cross-linked polyphosphates, whereas that in Al-18.5% Si and Al-25.0% Si had a mixture of ortho- and pyrophosphates. The ORL, once formed on the surface, was protected from further damage by the counterface. The volumetric wear loss in Al-12.6% Si T7 alloy (3.0×10^{-4} mm^3) after 6×10^6 sliding cycles was of the same order of magnitude as that after 2×10^6 sliding cycles (2.2×10^{-4} mm^3) shown earlier in **Chapter 5**. Thus it indicated that after 2×10^6 sliding cycles, equilibrium condition was reached between the kinetics of ORL formation and removal of the same; the formation of ORL and removal of it are a

continuous process in the presence of the engine oil within the contact region. Thus wear was stabilized in the UMW-III stage. The wear in the alloy with T6 heat treated condition and with higher matrix hardness was higher than with T7 heat treated alloy. Thus it can be said that the eutectic Al-Si alloys with over-aged heat treatment condition perform better in long term sliding under boundary lubricated conditions. Previous studies [**92**] indicated that the alloy with higher hardness particle sinking-in is preceded by particle fracture. The results presented here provide direct evidence that the particle sinking-in UMW-I and UMW-II stages is the impeccable condition for long term durability of ORL, and that the hardness of the matrix must be optimized to facilitate particle sinking-in rather than fracturing them. If small fragments are generated due to particles fracture during sliding, they result in formation of multiple grooves but still maintain UMW (see **Figure 6. 13b**) at lower load (2.0 N). But if the load is higher, say 5.0 N, the fragmented particles may cause severe abrasive actions, and the presence of ORL cannot maintain UMW, as this was observed in Al-18.5% Si alloy (see **Figure 4. 5d** and **Figure 4. 6b-c**). Thus the key conditions required to maintain UMW and provide durability in Al-Si alloys for extended period of sliding are: particle sinking-in in a matrix of optimum hardness without generating fragmented particles in UMW-I and UMW-II stages and formation of an ORL in UMW-III. These conditions were achieved by reducing the particle size and providing more uniform distribution of particles in a eutectic alloy under T7 heat treatment conditions. Thus the eutectic alloys performed equally better to those of Al-18.5% Si and Al-25.0% Si under boundary lubricated UMW regime in the presence of SAE 5W30 engine oil.

TABLES – CHAPTER 6

Table 6. 1: Variation in average COF, average COF in UMW-I stage, and steady state COF with temperatures.

Temperature (°C)	Average COF	Average COF in UMW-I	Steady state COF
25	0.14±0.01	0.16±0.01	0.14±0.01
80	0.14±0.01	0.15±0.01	0.14±0.01
100	0.15±0.01	0.14±0.01	0.15±0.01
140	0.13±0.01	0.13±0.01	0.13±0.01
160	0.12±0.01	0.14±0.01	0.12±0.01

Table 6. 2: Average surface roughness of the AISI 52100 steel counterfaces tested against Al-12.6% Si T7 alloys at five different temperatures.

Temperature (°C)	Surface roughness (R_a, nm)
25	229.6
80	530.3
100	416.8
140	517.4
160	274.9

Table 6. 3: Average COF of four different Al-Si alloy samples tested at 100 °C and at 2.0N normal load for 6×10^6 sliding cycles to investigate the durability of ORL.

Alloy	Average COF
Al-12.6% Si T7	0.12±0.01
Al-12.6% Si T6	0.13±0.0
Al-18.5% Si	0.12±0.0
Al-25.0% Si	0.11±0.0

Table 6. 4: C 1s, P 2p, S 2p, O 1s, BO, and NBO peak positions observed from the high resolution spectra in XPS collected with the worn surface of four different Al-Si alloys. The ratio of BO to NBO is also shown.

	Al-12.6% Si T6	Al-12.6% Si T6	Al-18.5% Si	Al-25.0% Si
C 1s	284.84	283.90	284.81	284.91
	-	290.13	-	289.63
P $2p_{3/2}$	133.09	132.31	133.35	133.12
P $2p_{1/2}$	133.94	133.16	134.12	133.97
S $2p_{3/2}$ (sulphide)	161.73	162.99	162.11	161.60
S $2p_{1/2}$ (sulphide)	162.98	164.24	163.36	162.85
S $2p_{3/2}$ (sulphate/sulphite)	168.57	166.96	-	-
S $2p_{1/2}$ (sulphate/sulphite)	169.82	168.21	-	-
Oxide	531.07	530.40	531.33	531.16
NBO	531.92	531.30	532.18	532.04
BO	532.77	532.26	533.03	532.98
BO/NBO	0.53	0.63	0.11	0.24

FIGURES – CHAPTER 6

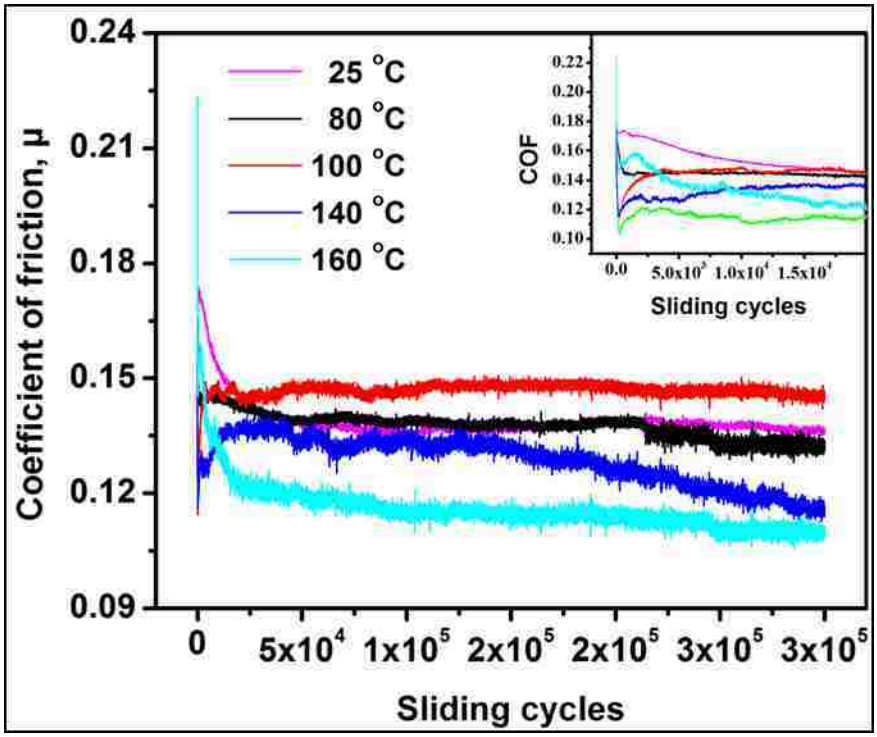

Figure 6. 1: Variation of COF with sliding cycles up to 3×10^5 sliding cycles in Al-12.6% Si alloy at five different temperatures. The average COF values are shown in Table 6.1.

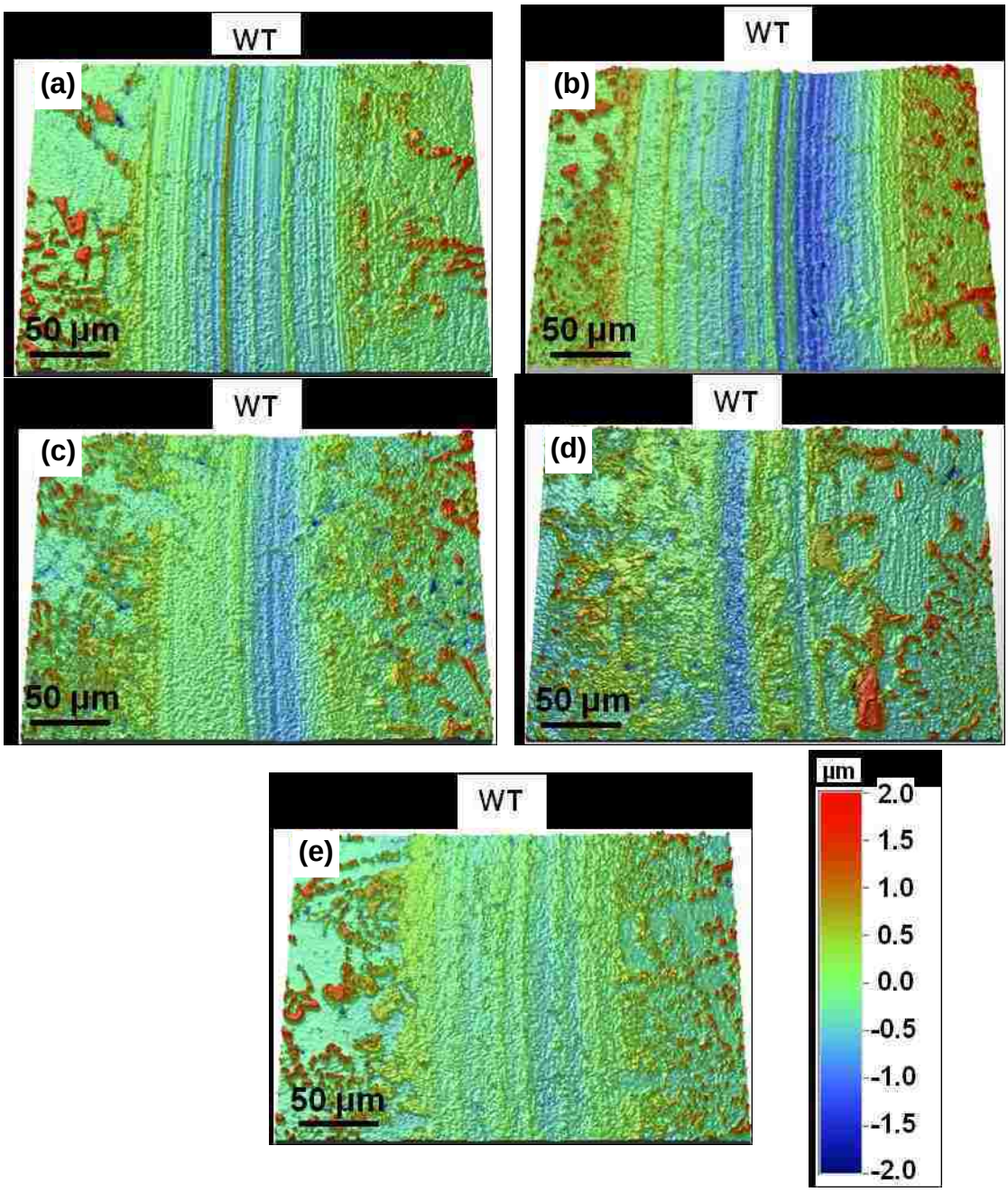

Figure 6. 2: Optical interferometer images of typical worn surface marked by WT after 3×10^5 sliding cycles at (a) 25 °C, (b) 80 °C, (c) 100 °C, (d) 140 °C and (e) 160 °C. The sliding direction is vertically downwards. Note the glazy appearances and fewer grooves within worn surfaces above 100 °C.

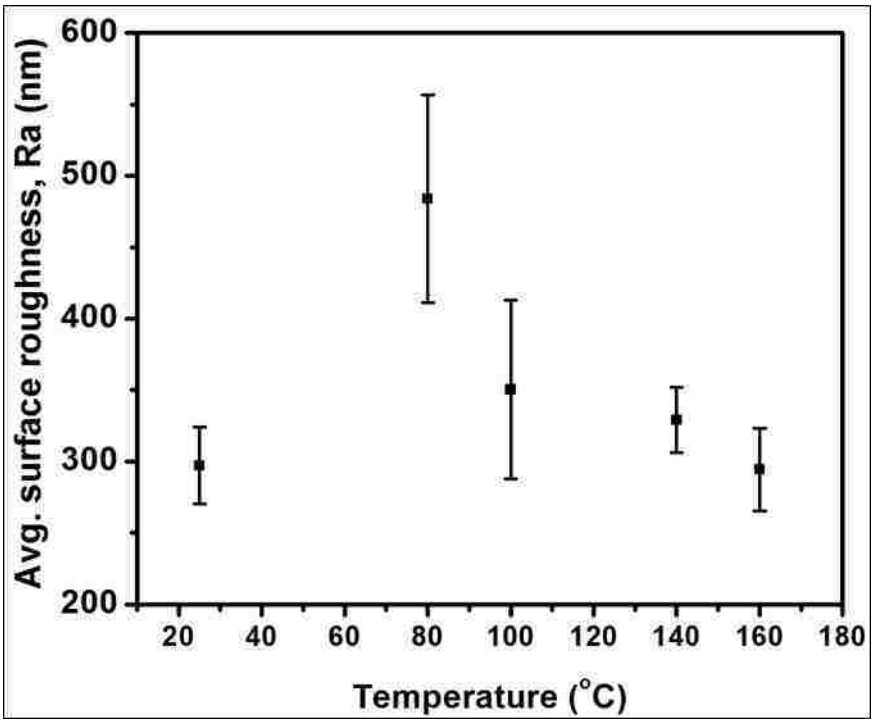

Figure 6. 3: Change in surface roughness (R_a) within the worn alloy surface as marked by WT in Figure 6.2a-e at different temperatures. The standard deviation represents measurements from eight locations within the WT.

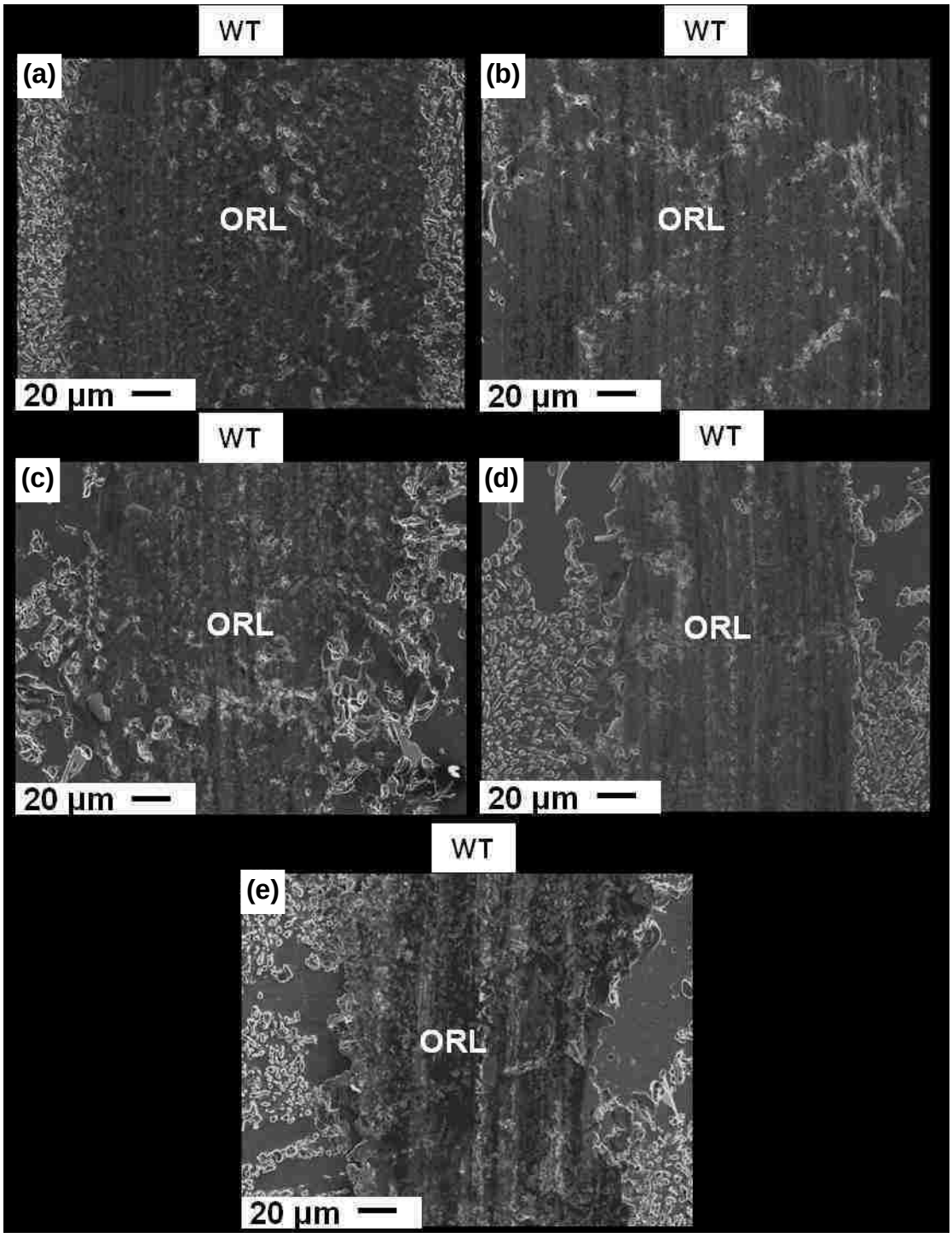

Figure 6. 4: Secondary electron images of the WT after 3×10^5 sliding cycles at (a) 25 °C, (b) 80 °C, (c) 100 °C, (d) 140 °C and (e) 160 °C. The sliding direction is vertically downwards.

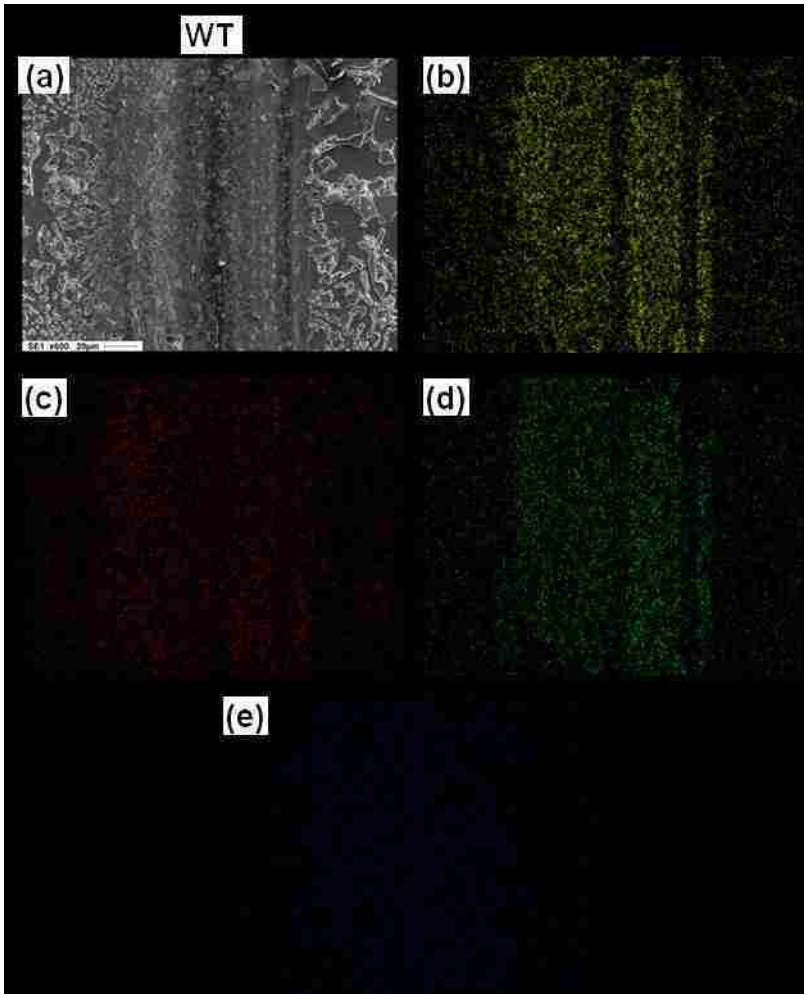

Figure 6. 5: EDS elemental map showing distribution of selected elements – (a) SEI image (b) Zn, (c) P, (d) S, and (e) Ca originated from disintegrated engine oil at 140 °C.

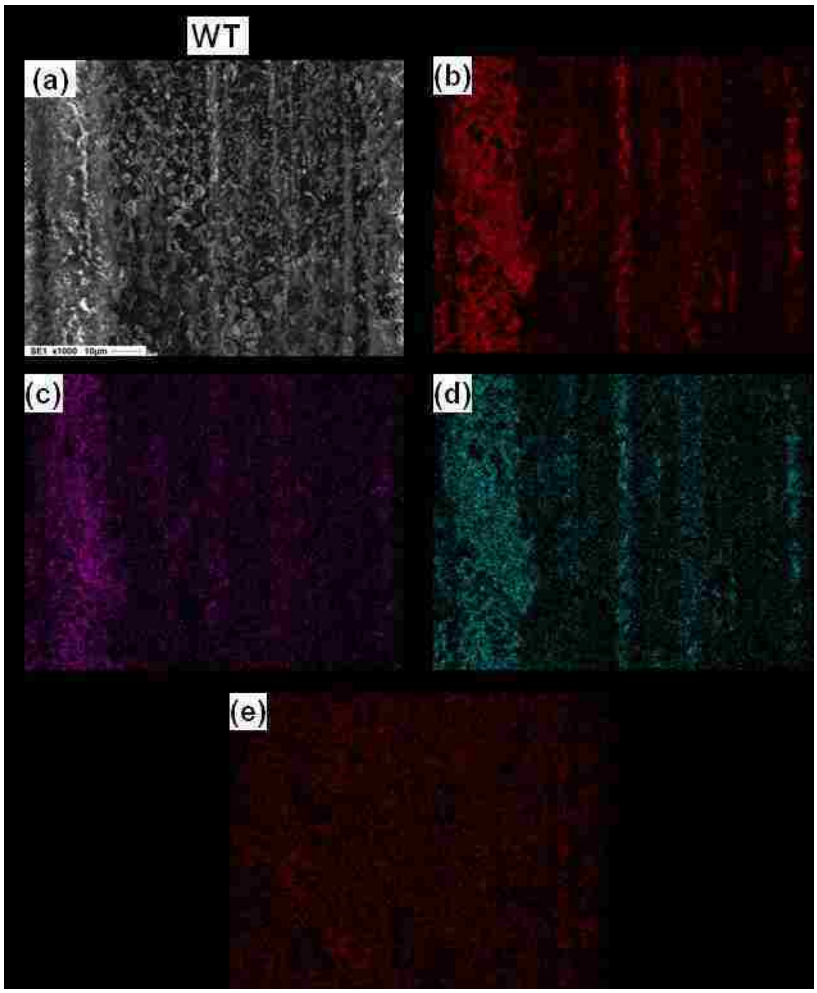

Figure 6. 6: EDS elemental map showing distribution of selected elements – (a) SEI image (b) Zn, (c) P, (d) S, and (e) Ca originated from disintegrated engine oil at 160 °C.

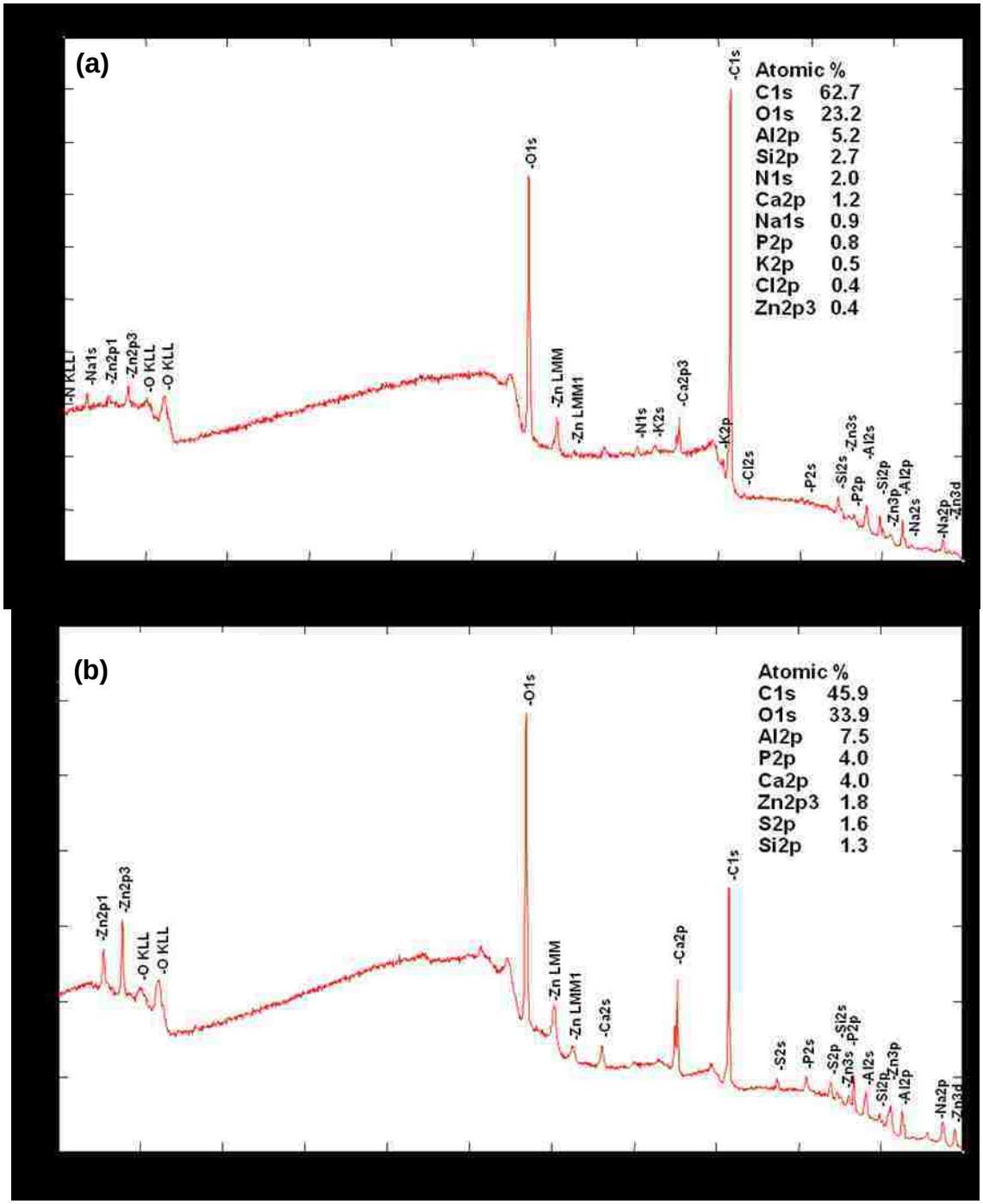

Figure 6. 7: XPS survey scan within the WT at (a) 25 °C, (b) 100 °C, (c) 160 °C and (d) outside the WT at 100 °C tested sample.

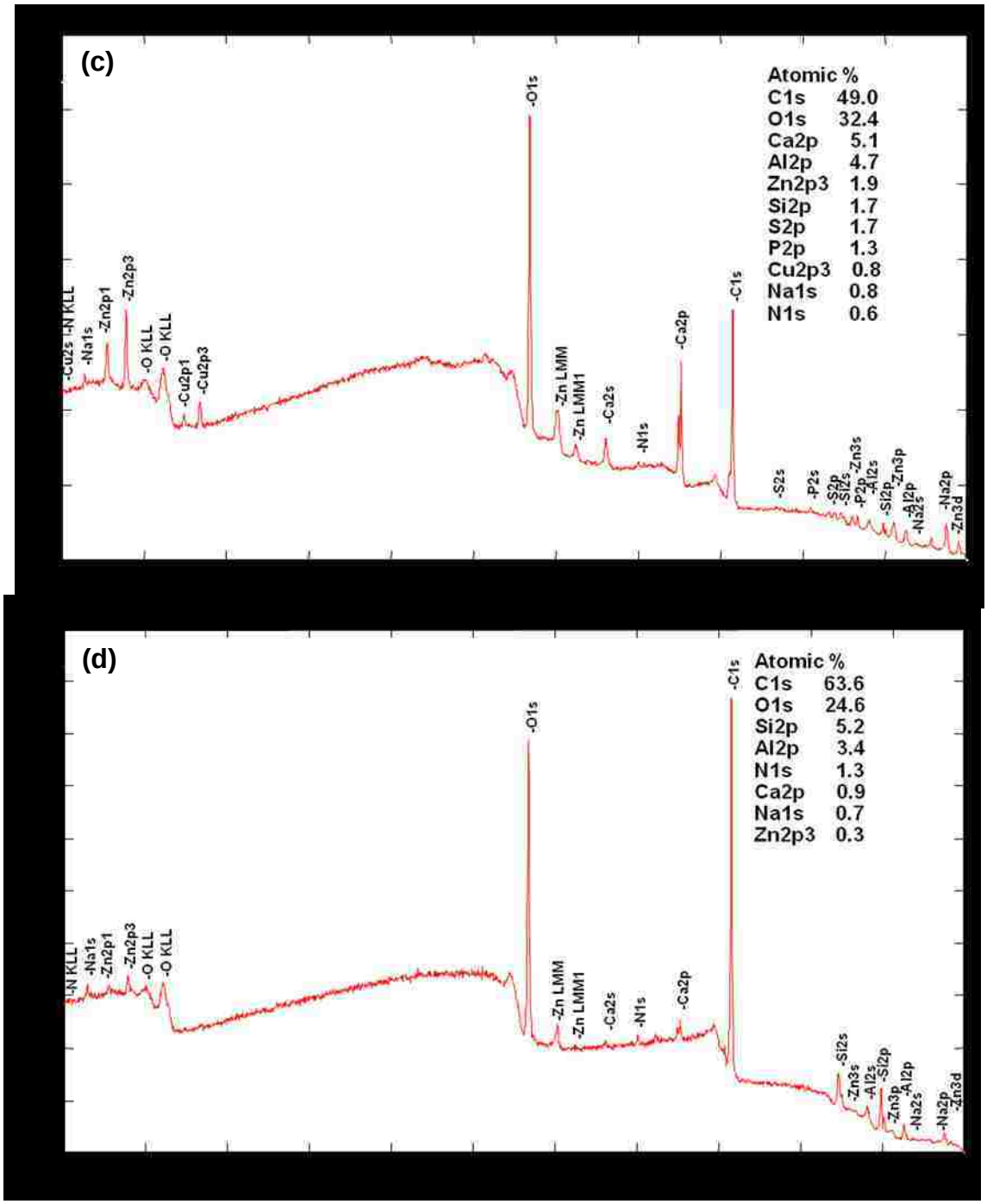

Figure 6. 7: Continued

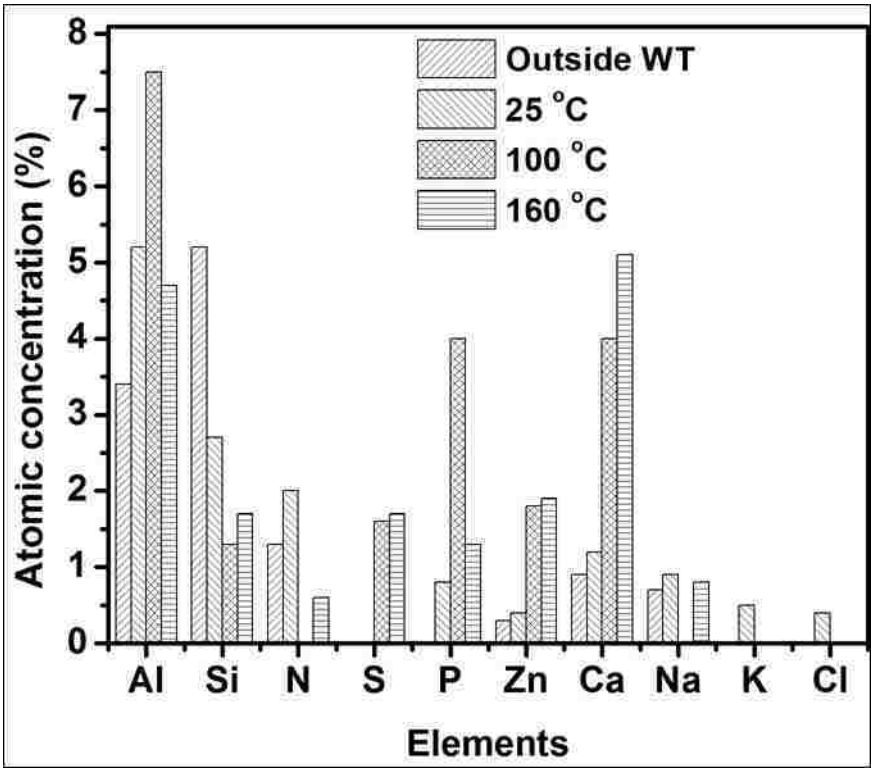

Figure 6. 8: Comparison of XPS semiquantitative analysis of atomic concentration data from Figure 6.7 on few selected elements at three different temperatures within the WT region. Data recorded outside the WT on 100 °C tested sample is also shown.

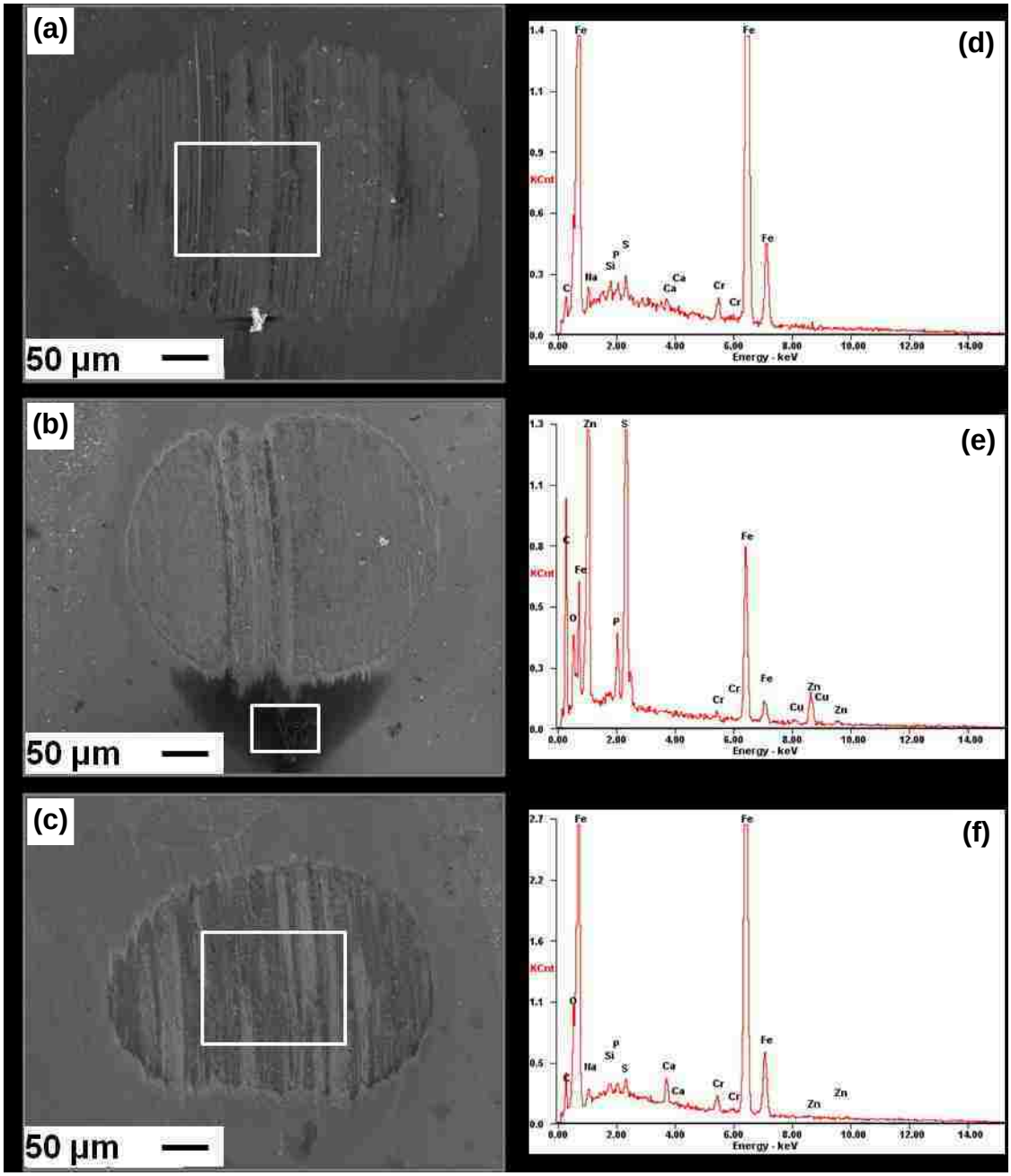

Figure 6. 9: SEI of counterfaces used for wear testing at (a) 80 °C, (b) 140 °C and (c)160 °C, and the corresponding EDS spectra is shown in (d)-(f) taken from the insert indicated with white rectangles. The sliding direction is vertically downwards.

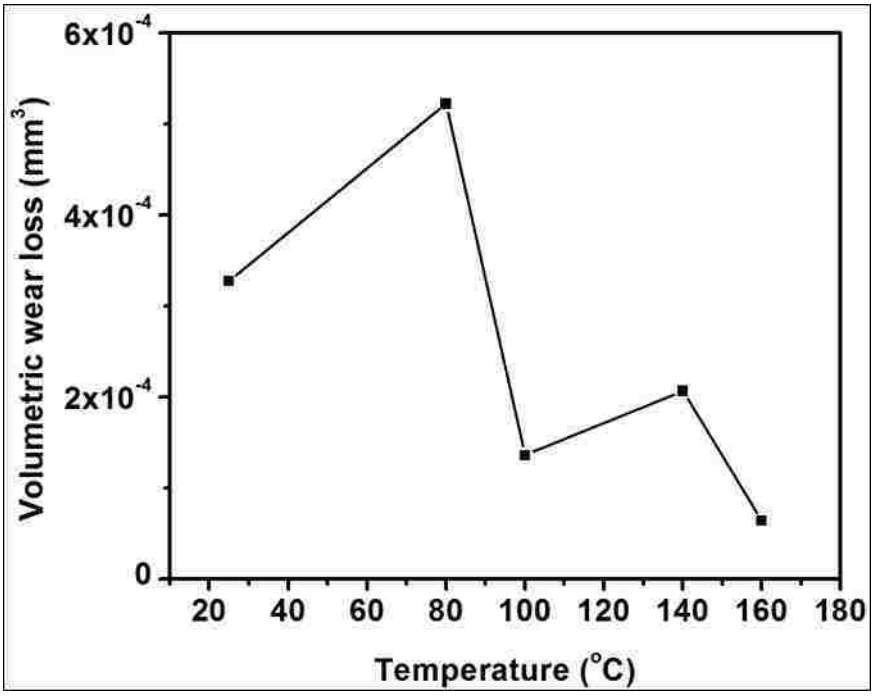

Figure 6. 10: Volumetric wear loss of aluminum matrix in Al-12.6% Si alloys at 2.0 N load and after 3×10^5 sliding cycles at different temperatures.

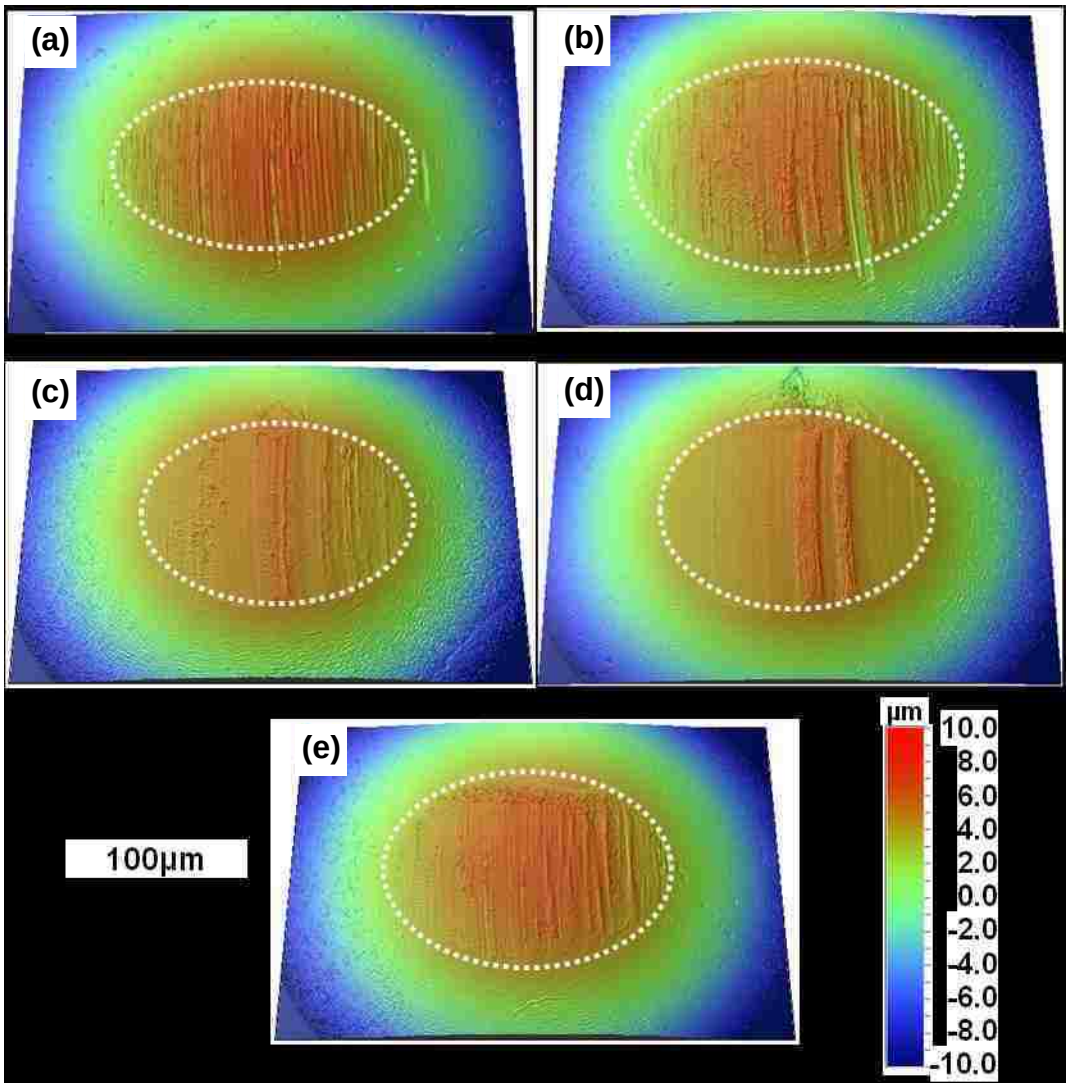

Figure 6. 11: Optical interferometer images of counterface at (a) 25 °C, (b) 80 °C, (c) 100 °C, (d) 140 °C, and (e) 160 °C. Surface roughness (R_a) and volumetric wear loss of the counterface with different temperature are shown in (f) and (g) respectively.

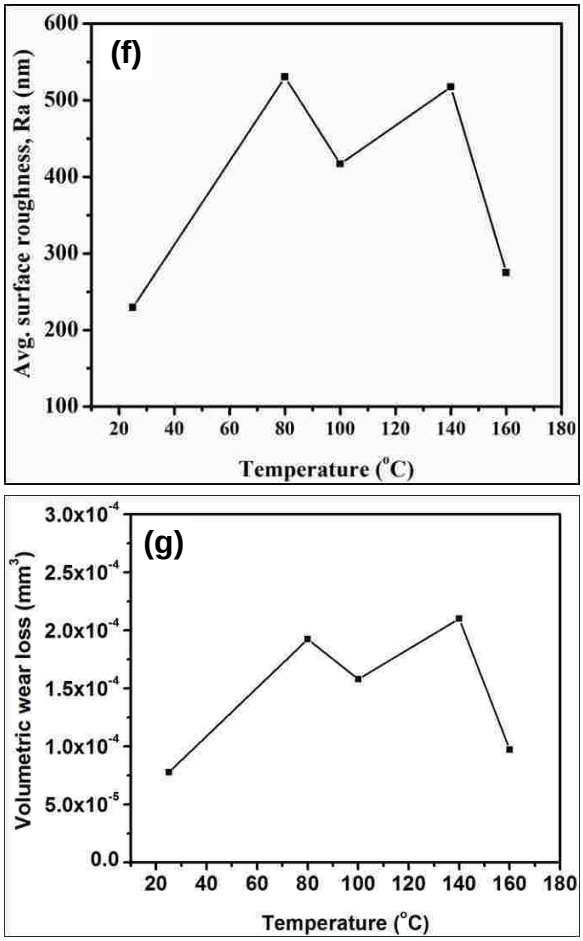

Figure 6.11 Continued

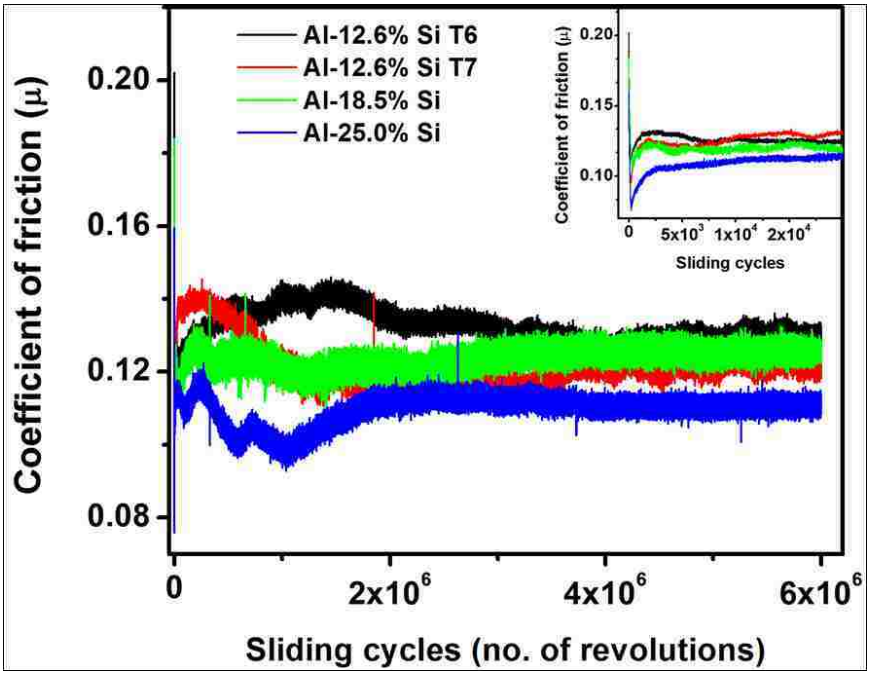

Figure 6. 12: Variation of COF with sliding cycles up to 6×10^6 sliding cycles in four different Al-Si alloys. The average COF values are shown in Table 6. 2.

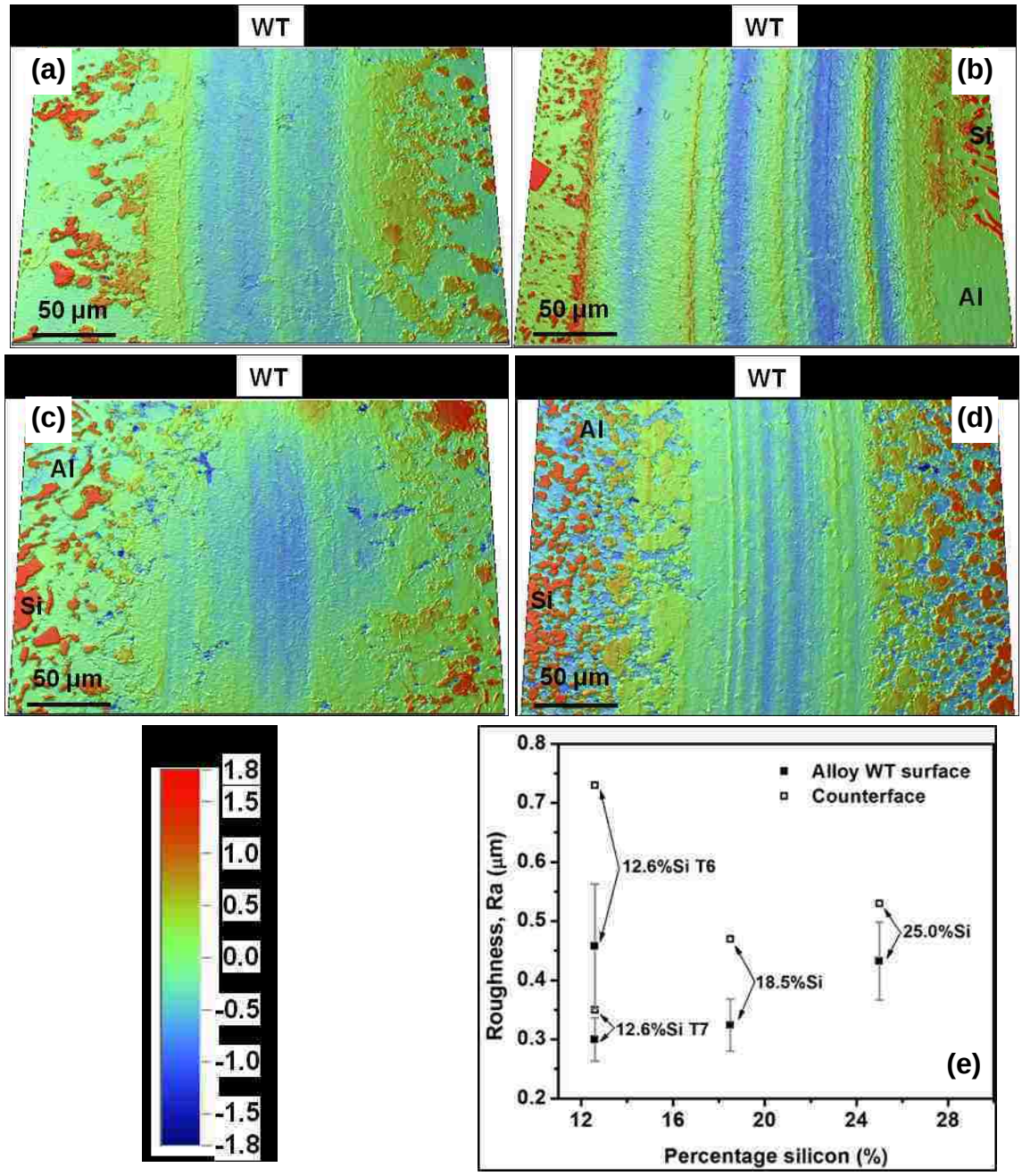

Figure 6. 13: Optical interferometer images showing typical worn surface of (a) Al-12.6%Si T7, (b) Al-12.6%Si T6, (c) Al-18.5%Si and (d)AL-25.0%Si alloy after 6×10^6 sliding cycles; (e) The surface roughness of the WT surface of the alloy and the counterface. The standard deviation in (e) is from eight different areas of the WT in the respective sample.

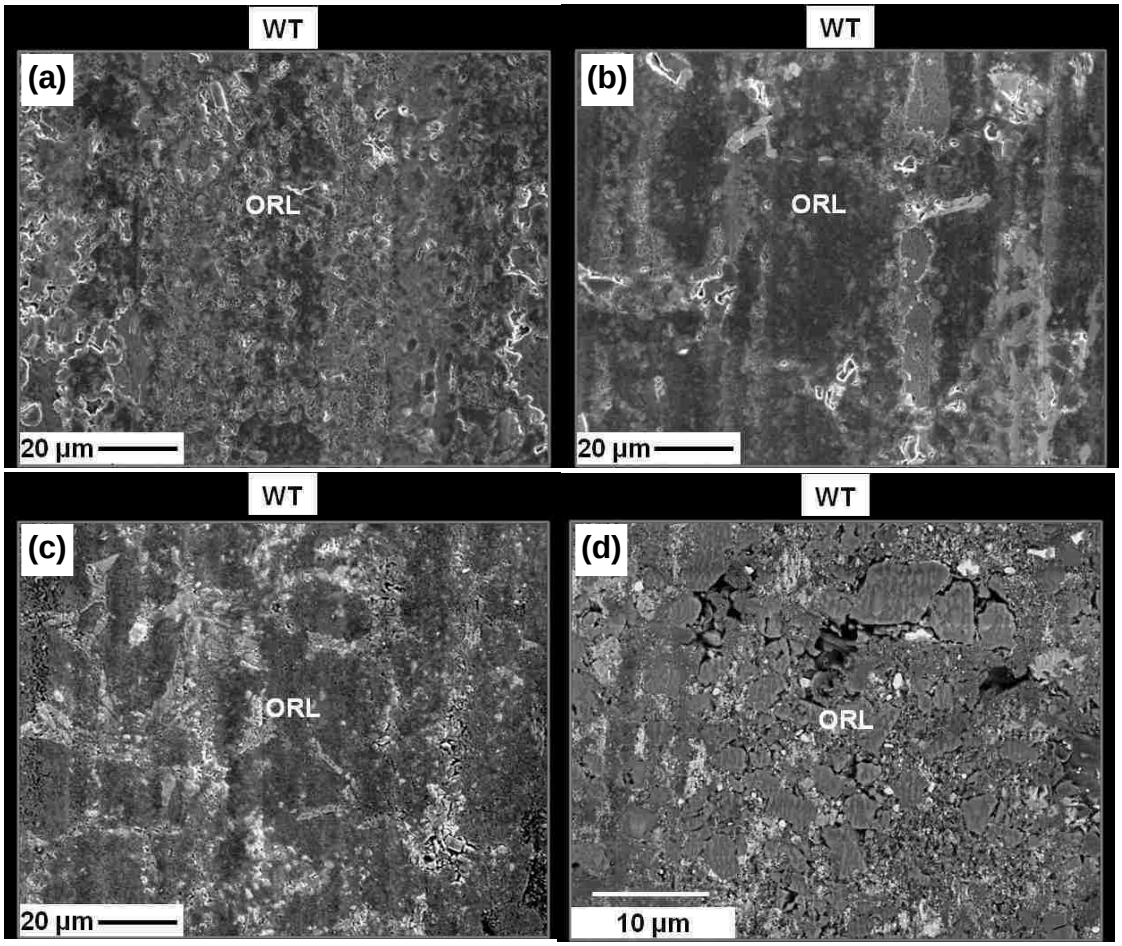

Figure 6. 14: SEM image of typical worn surface of (a) Al-12.6% Si T7, (b) Al-12.6%Si T6, (c) Al-18.5% Si and (d) Al-25.0% Si alloy tested at 2.0N load at 100 °C for 6×10^6 sliding cycles. The EDS spectra from the worn surfaces a-d are shown in Figure 6. 15.

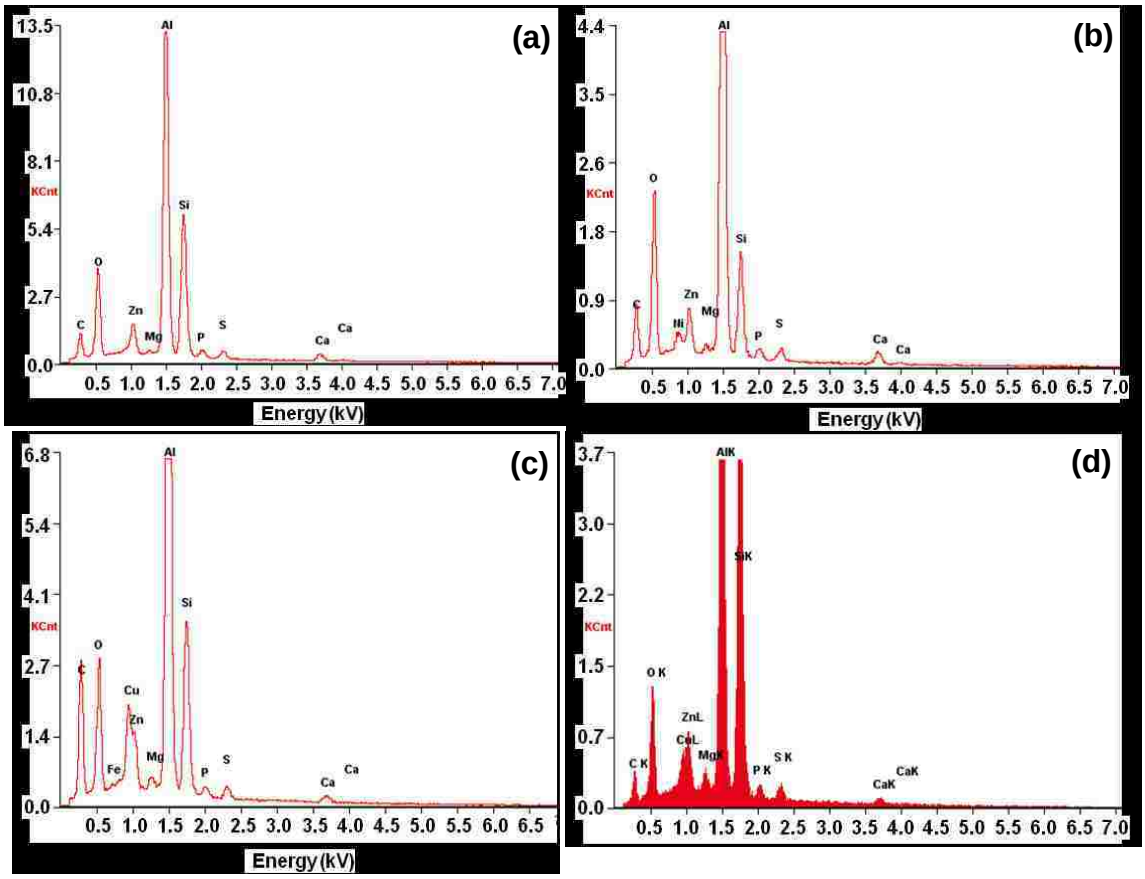

Figure 6. 15: EDS spectra from the worn surfaces as shown in Figure 6. 14 – (a) Al-12.6% Si T7, (b) Al-12.6% Si T6, (c) Al-18.5% Si and (d) Al-25.0% Si alloy showing presence of Zn, P, S, Ca and O, the primary elements of ORL.

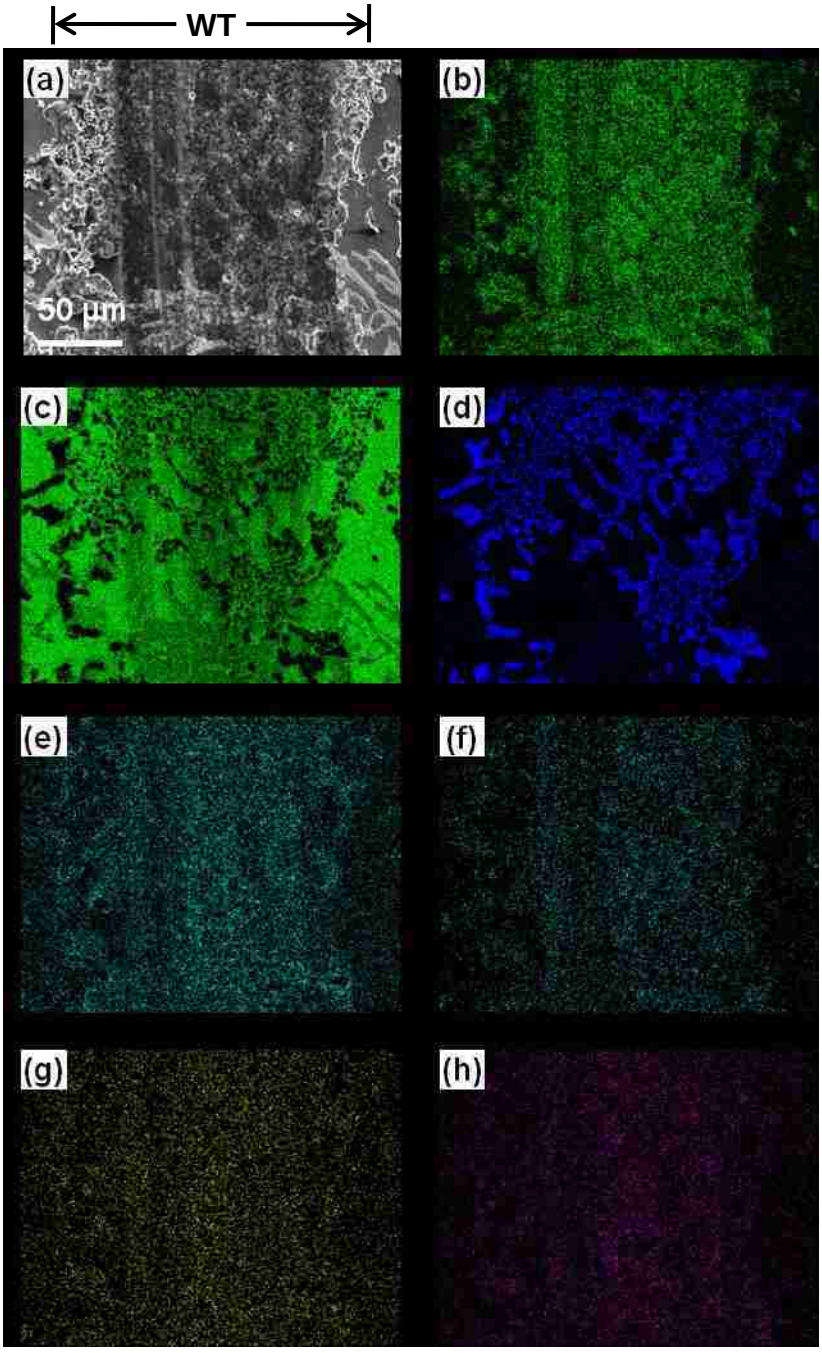

Figure 6. 16: SEM image (a) of the WT and EDS map showing distribution of (b) O, (c) Al, (d) Si, (e) Zn, (f) Ca, (g) P and (h) S in Al-12.6% Si T7 alloy after 6×10^6 sliding cycles.

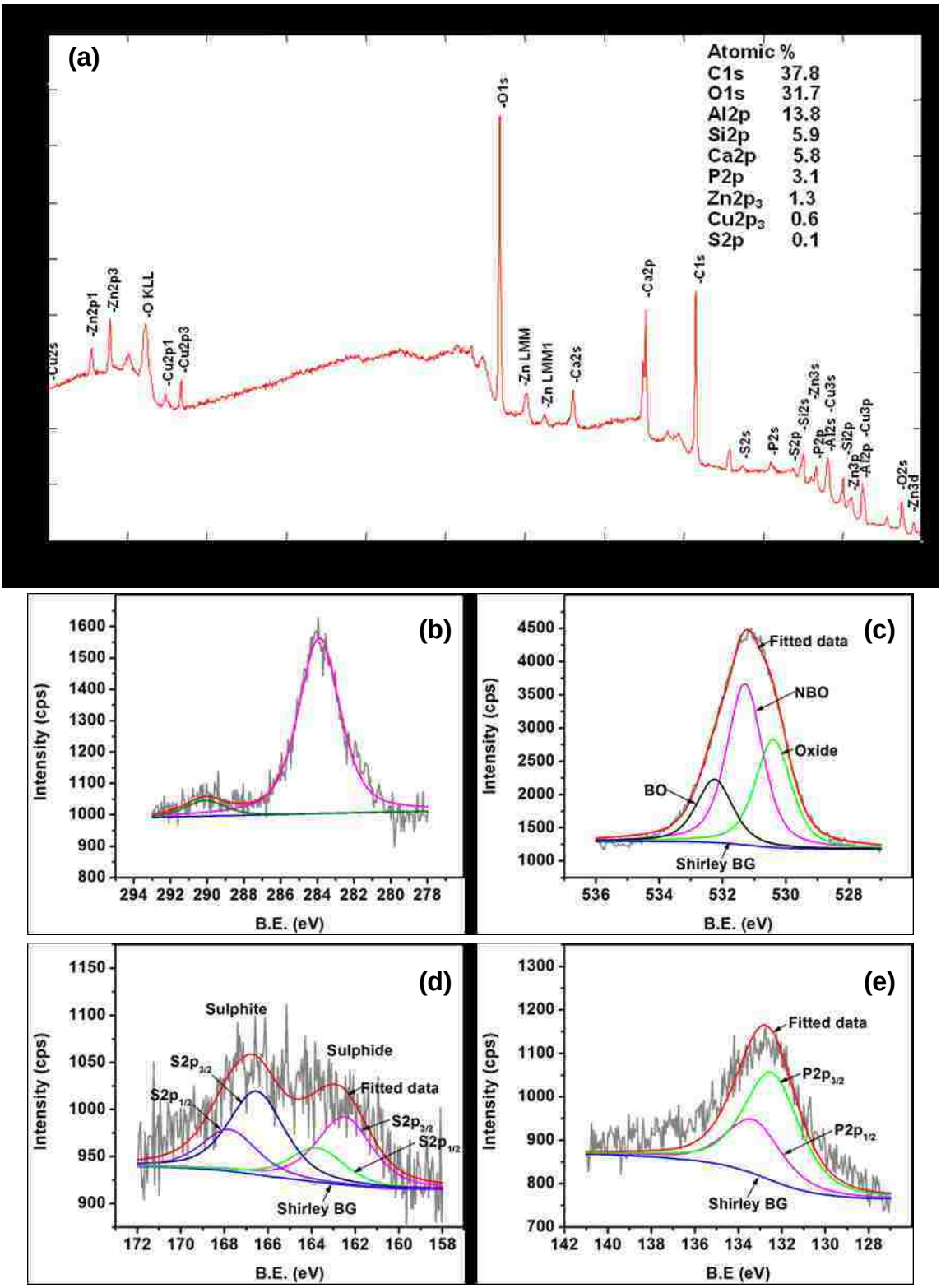

Figure 6. 17: (a) XPS survey spectra of the WT from al-12.6% Si T7 alloy and high resolution spectra (b) C 1s, (c) O 1s, (d) S 2p and (e) P 2p. In O 1s spectra contributions from NBO and BO were observed.

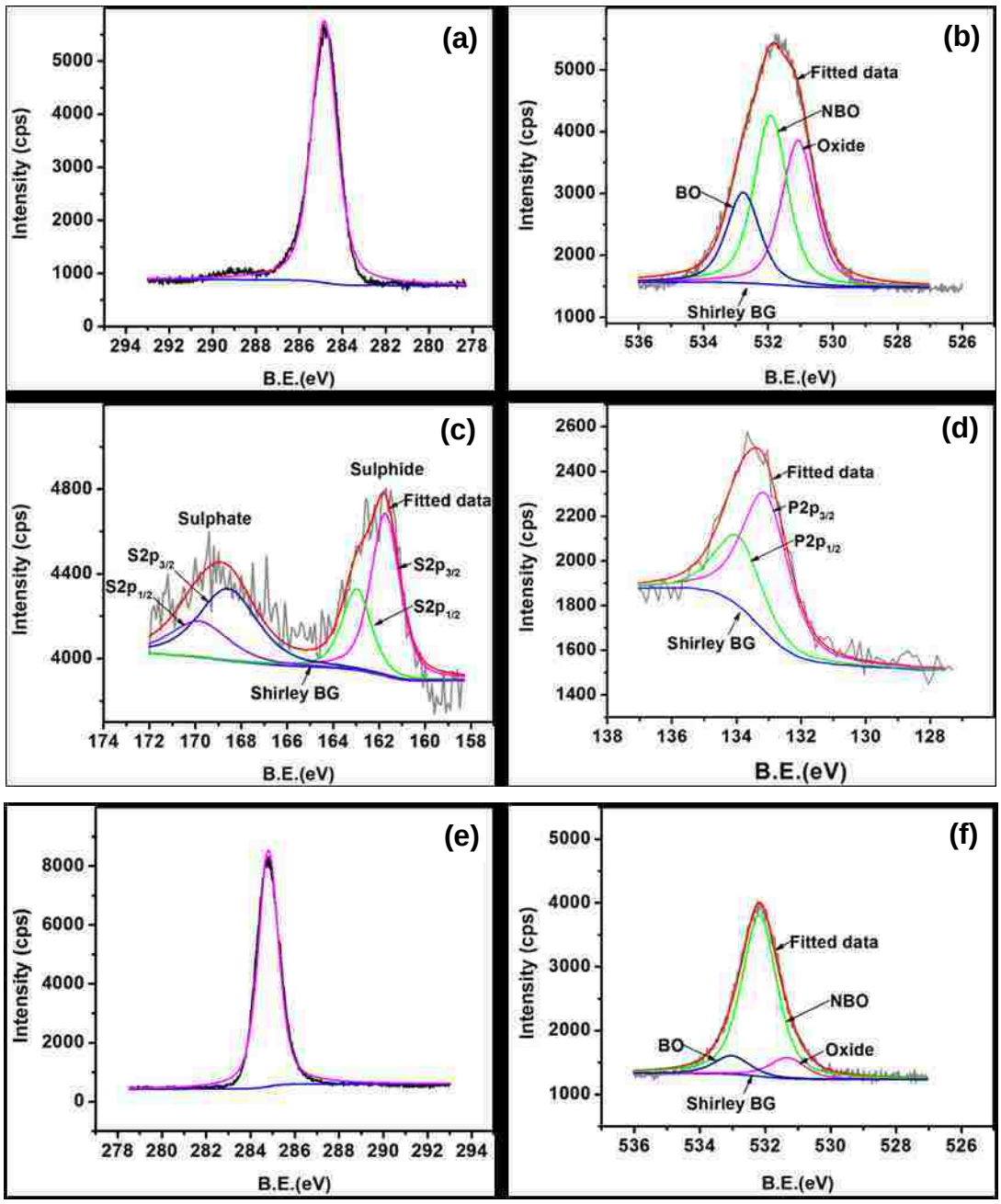

Figure 6. 18: XPS high resolution spectra (a) C 1s, (b) O 1s, (c) S 2p and (d) P 2p for Al-12.6%Si T6; (e) C 1s, (f) O 1s, (g) S 2p and (h) P 2p for Al-18.5% Si and (i) C 1s, (j) O 1s, (k) S 2p and (l) P 2p for Al-25.0% Si alloy.

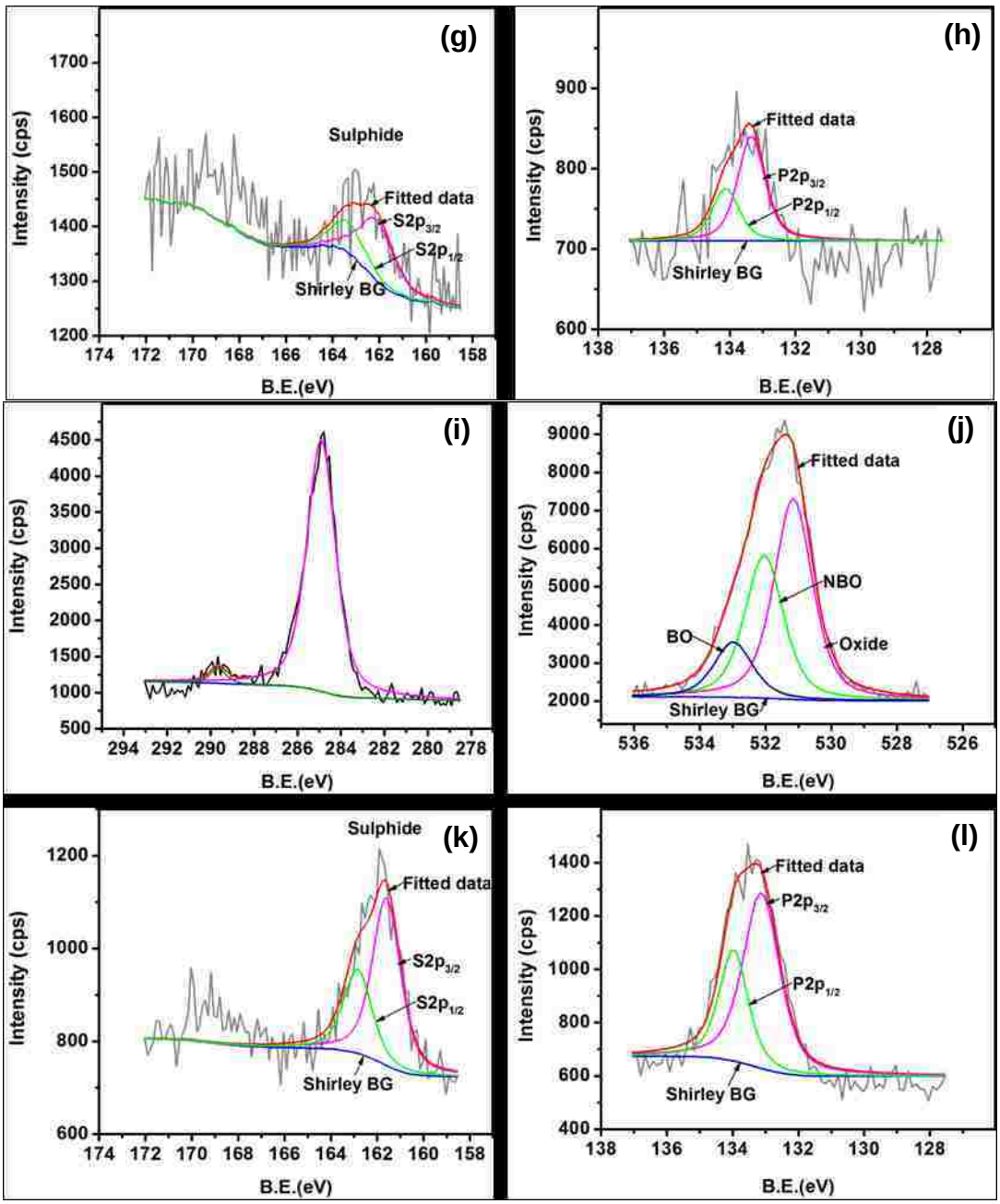

Figure 6. 18: Continued

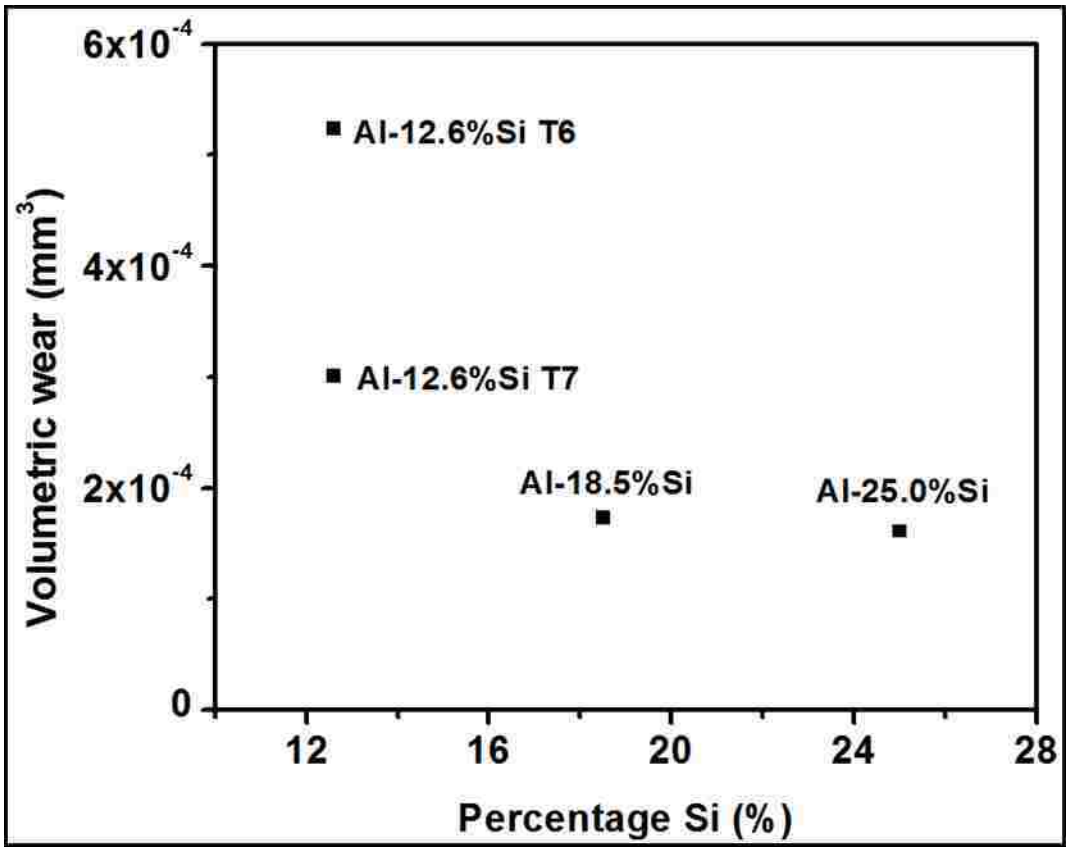

Figure 6. 19: Volumetric wear loss in four different Al-Si alloys at 2.0N load and at 100 °C after 6×10^6 sliding cycles. The graph shows that with ORL formation, the wear resistance of Al-12.6% Si alloy was very similar to the expensive hypereutectic Al-Si alloys.

7. CHAPTER 7 – SIMULATIONS OF UMW MECHANISMS IN UMW-I AND -II STAGES

7.1 Introduction

The studies on ultra-mild wear mechanisms shown in **Chapter 5** and **Chapter 6** have shown that Al-12.6% Si alloy could be a cost effective alternative to Al-25.0% Si or Al-18.5% Si alloys for the linerless engine block application. The physical mechanisms of wear in UMW-I and UMW-II stages were identified as silicon *sinking-in* and consequently the aluminum *pile-up*. **Figure 7. 1a** shows an optical image of the wear track in Al-12.6% Si alloys at 2.0 N load after 10^3 cycles. It was observed that the silicon particle height within the wear track was reduced (**Figure 5. 1**); however there was no wear in the aluminum matrix (**Figure 5. 3**). Through a brief period of zero aluminum wear (UMW-I stage), the second stage of UMW, UMW-II, was observed where the piled-up aluminum started to wear by the counterface. In UMW-II stage an oil-residue from the lubricating oil and aluminum formed on the worn surface which was harder than the matrix and thereby reduced the wear rate. At 100 °C, however, the lubricating oil formed a discontinuous island-like tribofilm on top of silicon particles in the UMW-I stage. **Figure 7. 1b** shows the formation of an island-like tribofilm on top of silicon particles and pile-up formation surrounding the particle in Al-25.0% Si alloy at 2.0 N load. The presence of the tribofilm caused a reduction in the contact pressure applied on the silicon particles (**Section 5.6.1.1**) and a reduction in particle fracture at 100 °C. Therefore a prolonged UMW-I stage existed at 100 °C, which was not observed at 25 °C.

The objective of finite element modeling was to simulate the mechanisms of UMW-I and UMW-II stages (particle sinking-in and aluminum pile-up) to understand the role of mechanical properties of the matrix in UMW. Accordingly, a three-dimension model was developed (**Section 7.2**) using a single particle embedded into the aluminum matrix to study the deformation of the aluminum matrix surrounding the particle. The model represented a microstructure with ideal and axy-symmetrical particle geometry. The particle was exposed by 1.6 µm (silicon particle height on etched aluminum), and a displacement was prescribed to the particle so that the particle was completely embedded in the matrix, while the deformation surrounding the particle, that is, pile-up height, was measured. Previous UMW studies on Al-Si alloys had shown that changing aluminum matrix hardness altered the wear behaviour of these alloys in the UMW region; particle fracture preceded the particle sinking-in. Accordingly, to understand the effect of different matrix yield strength, strain hardening exponent, and formation of tribofilm on top of silicon particles on the pile-up formation of the aluminum matrix, the parametric study was conducted.

A three-dimensional multi-particle model (see **Section 7.3**) was also developed from an actual microstructure of Al-12.6% Si alloy to investigate the effect of geometrical constraint due to the presence of multiple particles on pile-up formation during sinking-in. Then the parametric study was extended to investigate the effect of the mechanical properties of the matrix in the pile-up formation in a multi particle environment. Since the Young's modulus of silicon was 2 times higher than the aluminum matrix, in both single-particle and multi-particle models, the particles were considered as an elastic entity.

7.2 Single particle model

7.2.1 Particle sinking-in

7.2.1.1 Stress-strain analysis

Figure 7. 2a-d shows the contours of von Mises stresses in the matrix of Al-12 wt.% Si alloy at four different stages of particle sinking-in processes. It was observed from the contours of von Mises and effective plastic strain that within a localized region of 1.0 µm wide along the vertical interface between the matrix and the particle, the maximum stress and the plastic strain were experienced. This was due to shearing of the elements belonging to the matrix with the particle sinking-in. Within the matrix, directly below the particle, the von Mises stress was lower compared to that at the localized region next to the vertical interface. During the unloading cycle, when the silicon particle was left free to move in the positive z-direction after complete particle sinking-in (1.6 µm), the maximum value of stresses remained unchanged with a reduction in the size of the zone of maximum von Mises stresses as exhibited in **Figure 7. 2d**. This was due to an elastic recovery in the matrix, which also resulted in the particle movement by 0.057 µm. The variation of normalized von Mises stress (defined as the ratio of von Mises stress to the yield strength) as a function of the normalized depth below the particle (starting from the contact interface) for different stages of Si sinking-in is shown in **Figure 7. 3**. The maximum stress at any stage of Si sinking-in occurred at a normalized depth of 0.47, and then the stress dropped with increases in depth. The normalized depth at which the normalized stress of 1.0 (that is, von Mises stress was equal to the yield strength) was observed was considered as the plastic zone size. The plastic zone size directly below the particle was measured as a function of silicon particle displacement. The plastic zone size was approximately hemispherical, and the plastic zone size increased with the increase in particle displacement.

See **Section 7.2.2.1** for the variation of plastic zone size with silicon particle displacement for different matrix properties. The contours of effective plastic strain at different stages of loading and unloading processes are illustrated in **Figure 7. 4a-d**. The contours of effective plastic strain after silicon particle displacement of 0.1 μm was almost negligible as seen in **Figure 7. 4a**. The maximum value of effective plastic strain within a distance of 0.5 μm from the Al-Si interface varied from 57% to 200% after the silicon particle sinking-in of 1.6 μm (**Figure 7. 4c**), the highest strain observed at the interface. Once the particle was freed to move after maximum sinking-in, no significant change was observed in the zone of maximum plastic strain. The variation in maximum plastic strains increased to 59% to 203% after the unloading and remained constant. The maximum von Mises stress in the plastic zone below the silicon particle was 38% lower than the Vickers hardness of the matrix in Al-12% Si alloy (667 MPa).

7.2.1.2 Pile-up height

As a result of the silicon particle sinking-in into the matrix, displacement of the top surface nodes in the aluminum matrix occurred in both upward and downward directions. The matrix within close proximity of the interface were displaced in the downward direction along with silicon particle displacement, whereas the matrix further away from the interface were displaced in the upward direction resulting in the formation of material pile-up. To measure the maximum pile-up height in the aluminum matrix, the vertical displacement of the nodes on the top surface along the AA′ (**Figure 3.11**) was plotted as a function of distance from the Al-Si interface. **Figure 7. 5a** shows such a plot for three different amounts of silicon sinking-in (0.2, 0.8, and 1.6 μm), and after the unloading when the particle is pushed in an upwards direction due to the elastic recovery of the matrix far below the particle. An increase in pile-up height by 0.015 μm was noted after the unloading to accommodate the elastic recovery within the matrix far below the particle. The pile-up height was considered to be the maximum positive

displacement of any node on the top surface. **Figure 7. 5b** shows the change in maximum pile-up height as a function of particle sinking-in into the matrix. It can be observed that as the silicon height decreased or silicon sinking-in increased, pile-up height increased.

7.2.1.3 Failure of the interface

The separation at the Al-Si interface was considered as failure and the interface failure occurred with silicon sinking-in. **Figure 7.6a-d** shows the separation of the interface in single particle model at four different stages of silicon sinking-in. Initially up to silicon sinking-in of 0.2 µm, the nodes along the interface slide against each other, but the first separation at the interface was observed at silicon sinking-in of 0.2 µm. The separation distance was of the order of few hundredth of a micron (0.02-0.06 µm). With increasing silicon sinking-in the separation of the interface at different location continued to occur and the maximum separation distance did not change. This separation distance was rather smaller compared to the experimentally found value which varied between 0.16 µm and 0.18 µm. However, in multi-particle model the interface separation distance was of the order of the experimentally found value and will be discussed in **Section 7.3.2**.

7.2.2 Pile-up formation – A parametric study

In order to gain an insight on the piling up of the aluminum matrix, the effect of matrix yield strength and strain hardening behaviour were investigated. To study the effect of yield strength of the aluminum matrix on the pile-up formation at the top surface while maintaining a constant strain hardening exponent, numerical studies were conducted with two hypothetical aluminum matrices. The yield strength of the aluminum matrices in compression was considered to be 86.3 MPa ($0.5\sigma_y$, σ_y being the yield strength of the alloy) and 258.9 MPa ($1.5\sigma_y$), respectively. The hypothetical true stress versus true plastic strain curves for those two

materials were generated by shifting the experimentally determined stress-strain data for Al-12wt.% Si alloy.

An investigation to study the influence of the strain hardening exponent (*n*) of the aluminum matrix, with constant yield strength, on the pile-up formation at the top surface was completed. The value of strain hardening exponent for the Al-12 wt.% Si alloy was calculated as 0.17. Two different stress-strain responses in compression were considered with different *n* values ($n_1 = 0.11$ and $n_2 = 0.21$).

7.2.2.1 Stress distribution and plastic zone size

The normalized stress distribution beneath the particle for different matrix yield stress and strain hardening exponent is shown in **Figure 7. 7a** and **b**. With increasing yield strength at the maximum silicon sinking-in of 1.6 µm, the maximum stress within the matrix below the particle as well as the plastic zone size decreased. Similar behaviour was noted at the end of unloading but with a significant decrease in plastic zone size – the plastic zone size was decreased by 79% for the matrix yield strength of 258.9 MPa. A plateau of almost constant stress was observed in all cases just below the interface. The stress distribution was very similar with a different strain hardening exponent but with some differences. The plastic zone sizes for three different strain hardening exponents were almost the same at maximum silicon displacement and after unloading. The plateau region below the contact interface became larger with a lower strain hardening exponent, although the stress at that region was lower compared to those for matrices with a higher strain hardening exponent.

7.2.2.2 Effect of yield strength of the aluminum matrix

Figure 7. 8a illustrates the pile-up height at the top surface of the aluminum matrix with decreasing silicon particle height (or increasing silicon sinking-in) for different yield strength of

the aluminum matrix. **Figure 7. 8b** shows the change in maximum pile-up height with three different yield strengths of the matrix at two different amounts of silicon sinking-in, 0.8 and 1.6 µm. The pile-up height varied inversely to the yield strength of the aluminum matrix. The maximum pile-up height at maximum particle sinking-in (zero particle height) was noted as 0.10 µm and 0.07 µm for matrices having 0.5 times ($0.5\sigma_y$) and 1.5 times ($1.5\sigma_y$) the yield strength of Al-12 wt.% Si alloy, respectively. Another difference was that the location of maximum pile-up height with different matrix yield strengths was not the same. With an increase in the yield strength of the matrix, the pile-up formation was more localized towards the Al-Si interface, that is, the location of maximum pile-up height was closer to the interface for a higher yield strength.

The experimental studies using lubricated POD tests on Al-12.6% Si alloys showed that the ratio of pile-up height to silicon height (**Figure 5. 2b**) was an important damage parameter in ultra-mild wear (UMW) and that it could be used to identify the transition from ultra-mild wear stage-I (UMW-I) to UMW-II. It was shown that when the ratio became equal to 1.0, the aluminum surface elevation became the same as silicon particle height, and the transition from UMW-I to UMW-II stage initiated. In terms of micromechanisms controlling the UMW, this transition translates the transformation of a zero aluminum wear regime to the initiation of a high wear regime. From the numerical studies, the same damage parameter was calculated and plotted in **Figure 7. 8c**. It can be observed from this figure that the UMW-I to UMW-II transition is dependent on the matrix yield strength. Higher matrix strength results in a slower transition from UMW-I to UMW-II due to less pile-up for the same amount of silicon sinking-in. The experimental data from PD tests on Al-12.6% Si alloys at 25 °C (**Figure 5. 2b**) are also plotted in the same figure. The general trend from the simulated data matched quite well with the experimental data. The large variation was due to the fact that in simulated studies only one silicon particle was considered, and perhaps this was a drawback of the single-particle model.

The experimental data represented the statistical measure of pile-up height from many particles of the order of a few hundred to a few thousand, which were at different elevations from the beginning. However, it can be said that the numerical studies using an idealized microstructure were able to predict the general trend of the damage parameter observed during ultra-mild wear tests.

7.2.2.3 Effect of strain hardening exponent of the aluminum matrix

Figure 7. 9a and **b** shows the change in the pile-up height with silicon height and pile-up height to particle height ratio with silicon particle height for three different values of strain hardening exponents (n), respectively. The highest amount of pile-up formation was observed for the aluminum matrix with the lowest strain hardening exponent of 0.11. The maximum pile-up height surrounding the silicon particle was observed to vary inversely with the strain hardening exponent of the aluminum matrix. Accordingly, the UMW damage parameter in the matrix with a lower strain hardening exponent ($n_1 = 0.11$) approached the critical value ($\alpha_C = 1.0$) earlier as shown in **Figure 7. 9b**. In other words, a higher strain hardening exponent results in delayed transition from UMW-I to UMW-II.

7.2.3 Effect of island-like tribofilm on top of silicon particles

Lubricated wear studies at elevated temperature have shown the formation of a tribofilm on top of silicon particles which was formed from the lubricating oil. The tribofilm helped in the reduction of contact pressure applied on silicon particles and thereby reduced the amount of particle fracture within the wear track (**Section 5.6.1.1**). A numerical study was performed to study the effect of the tribofilm on pile-up height formation. The island-like tribofilm was modeled using a plastic kinematic material model, and the interface between the tribofilm and silicon particle was modeled using a tied surface-to-surface contact. Particle

sinking-in was achieved by prescribing motion to the top surface nodes of the tribofilm. The thickness of the tribofilm was considered to be 250 nm. The mechanical properties measured using nanoindentation technique as shown in **Chapter 5** was used in the model to simulate the mechanical response of the material. The Poisson's ratio yield strength and the Young's modulus were considered to be 0.28, 1.11 GPa, and 82.66 GPa, respectively. Thus this model simulated conditions similar to those that existed at 100 °C.

Figure 7. 10a shows the ratio of pile-up height to silicon particle height with the presence of tribofilm on top of silicon particle. The pile-up height without the tribofilm is also shown in the figure. It can be observed that in the presence of the tribofilm, the damage parameter for UMW-I to UMW-II transition approaches the critical value of unity ($\alpha_C = 1.0$) more slowly than in the system with no tribofilm. This finding is in agreement with the experimental data shown in the same plot. It should be noted that the decrease in silicon particle height in the experimental studies was measured against increasing sliding cycles which varied logarithmically. Hence, a small decrease in silicon particle height beyond 0.4 µm corresponds to a few hundred thousand sliding cycles, which emphasize the delay in the transition.

Another important difference is the irreversible work done to displace the silicon particle in the matrix. **Figure 7. 10b** shows the force-displacement data from the simulation for silicon sinking-in with and without tribofilm. The energy dissipated, including any elastic response of the tribofilm, is determined as the area bound by the force/displacement response and was calculated per unit area of the silicon particles. The amount of total energy dissipation was determined to be 2.6 kJ/m^2 and 2.65 kJ/m^2 for particle sinking-in with and without tribofilm on top of the silicon particle, respectively, that is, an increase in 19%. Thus with tribofilm, more

plastic work was needed for the same amount of silicon sinking-in. In other words, for the same amount of work done, less particle sinking-in should be observed with the presence of tribofilm.

7.3 Multi-particle model

From the numerical results obtained from the multi-particle model, similar data analysis to that of the single-particle model was carried out. Maximum pile-up height was calculated by measuring the maximum displacement of any node belonging to the top surface of the aluminum matrix. The parametric study to explore the effect of matrix mechanical properties, such as the yield strength and strain hardening exponent on the aluminum deformation, was conducted. However, simulating the sinking-in phenomena by the counterface did bring up some additional details which were more consistent with experimental observations. The results of the UMW mechanism simulation using the multi-particle model will be shown in **Section 7.3.1-Section 7.3.3**.

7.3.1 Pile-up formation – A parametric study

In the multi-particle model due to the asymmetrical nature of the particles, the aluminum top surface displacement was inhomogeneous unlike the single-particle model where the displacement surrounding the particle was uniform and homogeneous surrounding the particle. Thus to measure the pile-up height, displacement of 5630 top surface nodes (**Figure 3.13f**) of the aluminum matrix were measured, and the maximum displacement of any particular node out of those 5630 nodes was considered as the maximum pile-up height. **Figure 7. 11** shows a scatter diagram of displacement of all the nodes of the top aluminum surface in z-direction for the matrix with a yield strength of 172.6 MPa. Clearly there were two distinct sets of nodes – one set in which the nodes were very close (within 0.5 nm) to the interface and were displaced in the negative z-direction (similar to the negative displacement of the nodes in **Figure**

7. 5a) and another set in which the nodes were displaced in the positive z-direction causing aluminum pile-up. **Figure 7. 12a-e** shows the fringe plot of the displacement within the aluminum matrix at different stages of silicon sinking-in. It was evident from this figure that the aluminum pile-up was not symmetrical surrounding the particles.

7.3.1.1 Effect of yield strength of the aluminum matrix

The pile-up height formation for three different yield strengths of the matrix was measured from the displacement of the nodes on the top of aluminum surfaces. The maximum pile-up height in the single-particle model was observed at the end of load removal when the elastic recovery in the matrix from far below the top surface caused a further displacement of the plastically deforming matrix closer to the particle and the free surface in the positive z-direction. A similar observation was made in the case of the multi-particle model as well. However, in the case of the multi-particle model, the maximum pile-up height was measured at the particle sinking-in of 1.34 μm or at the particle height of 0.335 μm. This was due to the fact that sinking-in was simulated by bringing the counterface into contact with silicon particles and then prescribing the displacement to it, so that after sinking-in of 1.34 μm, the piled-up aluminum came into contact with the counterface. Thereafter, the counterface also displaced the aluminum matrix along with silicon particles in the negative-z direction and caused lowering of the pile-up height. Thus, this method was able to simulate the physical phenomena of the UMW mechanisms more closely, considering the wear of the aluminum matrix by the counterface.

Figure 7. 13a and b shows the variation of maximum pile-up height with different amounts of particle sinking-in (or silicon height) and the maximum pile-up height in the aluminum matrix at three different stages of silicon sinking-in (0.67, 1.34, and 1.675 μm), respectively, for three different yield strengths of the matrix. It was observed that the general

trend of the pile-up formation within the matrix was very similar to that observed in the single-particle model. Decreasing the yield strength by half caused a reduction of 9.8% in pile-up height within the matrix. However, the amount of maximum pile-up height was higher in the multi-particle model than that observed in the single-particle model. However, the amount of pile-up height observed using the multi-particle model represented the experimental findings more closely. For example, the maximum pile-up height with matrix yield strength of 172.6 MPa for single- and multi-particle models was 0.077 µm and 0.378 µm, respectively; experimentally the maximum pile-up height in Al-12.6% Si alloy during lubricated sliding at 2.0 N load was 0.37±0.04 µm (**Figure 5.2a**)

Figure 7. 14 shows the UMW damage parameter (ratio of pile-up height to silicon particle height) for the multi-particle model for three different yield strengths of the matrices. It was noted that in the multi-particle model, the critical value of the damage criteria ($\alpha_c = 1.0$) was reached at particle height of 0.42, 0.38, and 0.34 µm for the matrices with yield strength of 86.3, 172.6, and 258.9 MPa, respectively. Thus it was observed that the higher the yield strength of the matrix, the lower the silicon particle height at which the critical value of the UMW damage criteria was reached, and the slower the transition from UMW-I to UMW-II.

7.3.1.2 Effect of strain hardening exponent of the aluminum matrix

Figure 7. 15a and b shows the change in maximum pile-up height with silicon particle height and variation in maximum pile-up height at three different stages of silicon sinking-in for matrices with three different strain hardening exponents (n= 0.11, 0.17, and 0.21), respectively. **Figure 7. 16** shows the UMW damage parameter for matrices with three different strain hardening exponents. The maximum pile-up height for all three strain hardening exponent was observed at the particle sinking-in of 1.34 µm. The maximum pile-up height was lowered after the silicon sinking-in of 1.34 µm because of the contact between the counterface and the piled-

up matrix. The critical value of the UMW damage parameter ($\alpha_c = 1.0$) was observed at the particle height of 0.415, 0.38, and 0.335 µm. Thus, it was shown that a higher strain hardening exponent of the matrix would result in a slower transition from UMW-I to UMW-II.

7.3.2 Al-Si interface failure

The interface failure was measured in multi-particle model too in similar way it was carried out in single-particle model. The maximum separation distance at the interface was measured for all the particles and it was observed that the separation distance was maximum for the Si_3 particle, as identified in **Figure 3.13d**, which was smaller compared to other particles and was almost spherical in three dimensions. **Figure 7. 18a-d** shows the interface failure of the Si_3 particle at the end of unloading and the maximum separation distance for this particle at the end of unloading was 0.74 µm which was higher compared to the experimental findings ranging from 0.16 µm to 0.18 µm as shown in **Figure 7. 18e** and **f**. However, one must note that during sliding experiments the particles are loaded and unloaded for multiple times; due to this cycling nature of loading and unloading of silicon particles and also because of the sliding, the interface separation measured from the cross sectional micrographs may be underestimated. The decohesion of the Al-Si interface for small particles like particle 3 may have detrimental effect on the UMW wear behaviour and will be discussed in **Chapter 8**.

7.3.3 Effect of tribofilm: estimation of silicon particle fracture

The effect of formation of island like tribofilm was also investigated suing the multi-particle model. The model was set up using similar to the single-particle model. The thickness of the tribofilm was considered to be 250 nm, but the tribofilm was discretised using four noded tetrahedral elements. After the simulation the maximum pile-up was measured by measuring the maximum nodal displacement of any node from the top surface of the aluminum surface.

Figure 7. 19 shows the variation of UMW damage criterion, the ratio of aluminum pile-up height to the silicon particle height with silicon height. It can be observed again that with the tribofilm on top of silicon particles the UMW-I to UMW-II transition is delayed. The experimental data is also included in the **Figure 7. 19**. Thus once again it was shows that presence of tribofilm would improve the wear behaviour of Al-Si alloys.

The von Mises stress within silicon particles in multi-particle model was observed closely to get an estimation of possible initiation of particle fracture. The assumption was that initiation of particle fracture would take place if the stress within the particle exceeded the fracture strength of silicon (4.1-7.2 GPa). **Figure 7. 20a-b** shows the von Mises stress distribution in the silicon particles in the multi-particle model with no tribofilm and with tribofilm for matrix with yield strength of 172.6 MPa. It can be observed that in presence of tribofilm the von Mises stress in silicon particles is lower than that in the particles with no tribofilm: in some location the stress exceeded the yield strength of silicon where the fracture would initiate. However in both these situations, the yield strength of the matrix was the same. In other words for the matrix yield strength of 172.6 MPa, the volume of silicon particle where von Mises stress exceeded the silicon particles' yield strength was lower in presence of tribofilm. With increase in temperature the matrix yield strength reduces. **Figure 7. 20c** shows the von Mises stress distribution within the particles for matrix yield strength of 86.3 MPa and it may be observed that there was further reduction in stress within the particles. Thus a combination of tribofilm formation and reduction in matrix yield strength reduces the probability of particle fracture due to lowering of stress concentration within the particles. Therefore, the multi-particle simulation with lower matrix yield strength of 86.3 MPa and with a tribofilm on top of silicon particles simulated the condition that existed during sliding at elevated temperatures (**Chapter 5** and **6**) and provided evidence for lower particle fracture.

7.4 Discussion on numerical findings

From the numerical investigation on UMW damage mechanisms conducted using single- and multi-particle models, it was shown that higher yield strength and higher strain hardening exponent of the matrix resulted in a lower amount of pile-up in the aluminum matrix and a slower transition to UMW-II. Thus altering these mechanical properties of the matrix, the UMW behaviour can be further improved. It must be noted that the numerical model did not consider particle fracture, which was associated with higher matrix yield strength (or hardness) as found in the previous UMW studies [**92**] and also shown in **Chapter 5**. But the estimation of particle fracture was possible from the von Mises stress generated within the particles for different yield strength of the matrices. Increasing the matrix yield strength makes the particle sinking-in difficult which results in increasing the stress within silicon particle.

The difference in findings between single-particle and multi-particle models can be rationalized using slip-line theory used in plasticity studies. The particle sinking-in in the aluminum matrix is very similar to the indentation of a thick block with a narrow punch. For the later problem, it was shown [**151**] that due to the presence of a rigid wall next to the plastically deforming materials, a geometric constraint was developed which resulted in an increase in indentation pressure to three times the stress that was required for yielding in uniaxial compression. During the numerical modeling, the failure of the interface happened very early in the sinking-in process (approximately after 12.5% of the total sinking-in), and once the interface failure occurred, the sinking-in problem became similar to the indentation of the thick block by a punch. In the case of particle sinking-in in the single-particle model, the geometric constraint was provided by the boundary conditions alone, so that the material could deform plastically, and the flow of the material at the free surface was the minimum. However, in the case of the multi-particle model, the presence of other silicon particles (elastic) provided the additional

geometric constraint resulting in flow of the material at the free surface causing pile-up of material. In the POD experiments, similar constraint was developed in the presence of multiple particles allowing the flow of matrix material at the top free surface causing pile-up. Thus the multi-particle model was able to simulate the particle sinking-in and pile-up phenomena more closely with the real situation, and the findings thereof matched with the experimental results. **Figure 7. 17** plots the pile-up height to silicon particle ratio for the single- and multi-particle models; the experimental results for Al-12.6% Si alloy are also shown for comparison. Although the maximum pile-up height was the same, there was a difference of almost 0.13-0.15 between the ratio of pile-up height to silicon height obtained from the experimental and the simulated multi-particle models; the difference was observed due to the difference in particle height at which the maximum pile-up height was observed.

Thus, it is the geometric constraint provided by the silicon particles within the matrix which results in the formation of pile-up. It was shown for the Al-18.5% Si alloy (**Chapter 4**) that even though the contact pressure was higher than the matrix hardness, sinking-in did not take place immediately. Because the interparticle distance in this alloy was larger, the geometric constraint did not develop until the particles fractured, but once fractured, part of the particles provided the constraint for the plastic deformation of the aluminum matrix causing the flow to occur at the free surface, and the pile-up formation was observed. However in Al-12.6% Si and Al-25.0% Si alloy, due to the lower interparticle distance compared to Al-18.5% Si alloy, the plastic constraint was developed right from the beginning of particle sinking-in causing pile-up formation.

7.5 Summary

The findings of the numerical study showed the effect of the matrix properties on plastic deformation of the aluminum matrix below the silicon particles and the formation of pile-up. Both models with single- and multi-particles were able to predict the general trend from the experimental observations. The multi-particle model predicted the UMW damage criterion more closely to that of experimental findings. The higher the matrices yield strength and strain hardening exponent, the lower the aluminum pile-up. Thus the transition from UMW-I to UMW-II can be delayed by altering these mechanical properties of the matrix. The effect of the presence of a tribofilm was also studied using the single-particle model, and it was observed that in the presence of the tribofilm, 19% more energy could be dissipated during particle sinking-in. Also the transition to UMW-II occurred more slowly than what was observed without a tribofilm. Thus, the presence of the tribofilm was beneficial in prolonging the UMW-I stage where zero matrix loss is observed.

FIGURES – CHAPTER 7

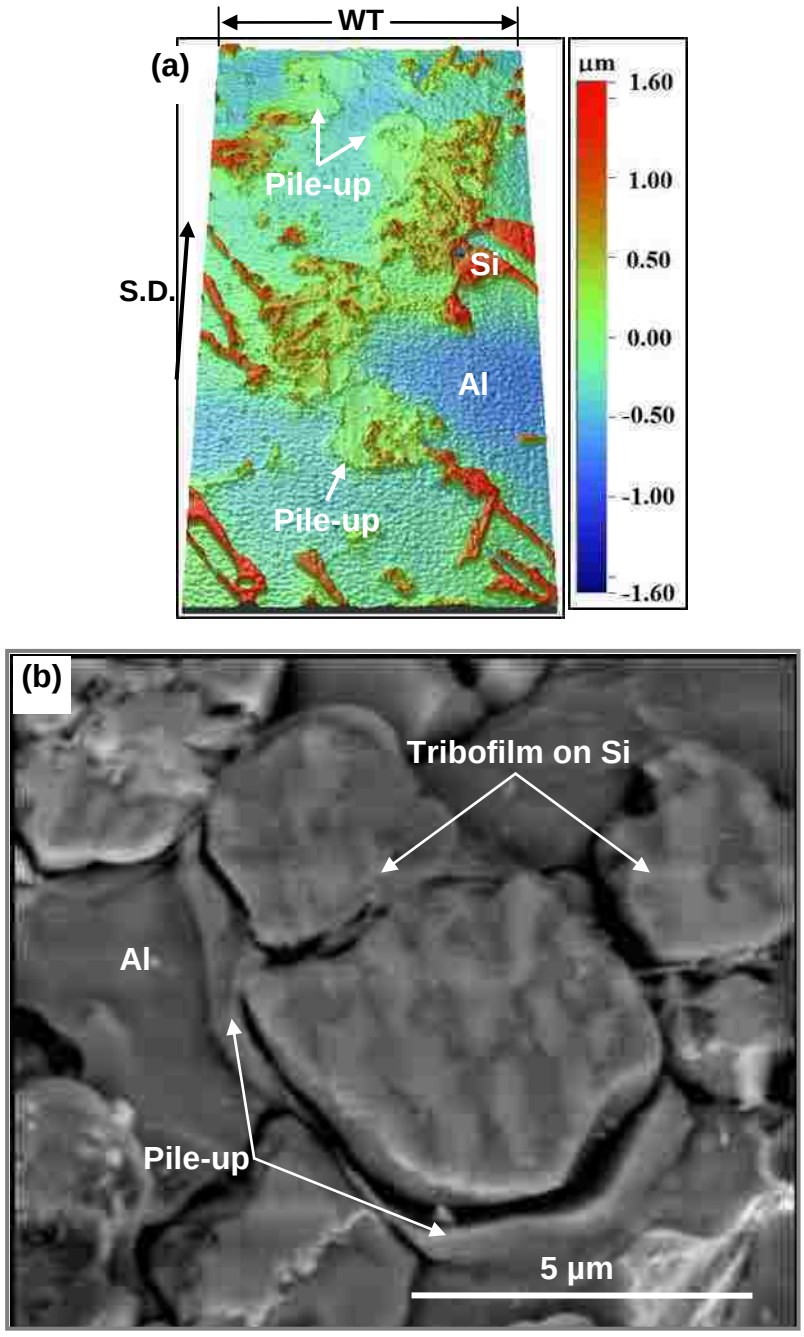

Figure 7. 1: (a) Optical profilometer image of an Al-12.6% Si alloy tested for lubricated sliding up to 10^5 cycles at 2.0 N load; (b) Formation of island-like tribofilm on top of silicon particles and aluminum pile-up in Al-25% Si alloy after 5×10^4 sliding cycles.

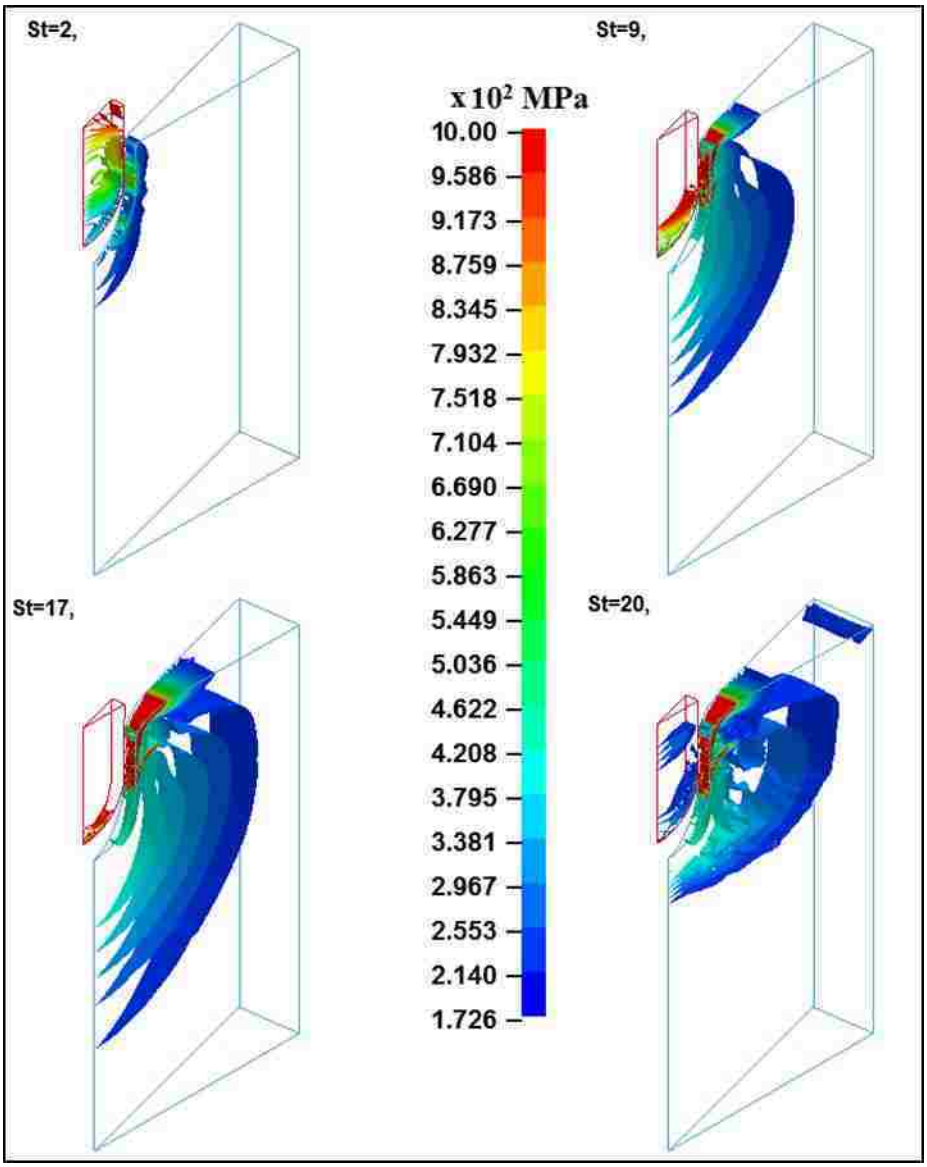

Figure 7. 2: von-Mises' stress distribution in the aluminum matrix after silicon particle sink-in in the matrix by (a) 0.1 µm and (b) 0.8 µm (c) 1.6 µm; and (d) after unloading (at the end of the simulation).

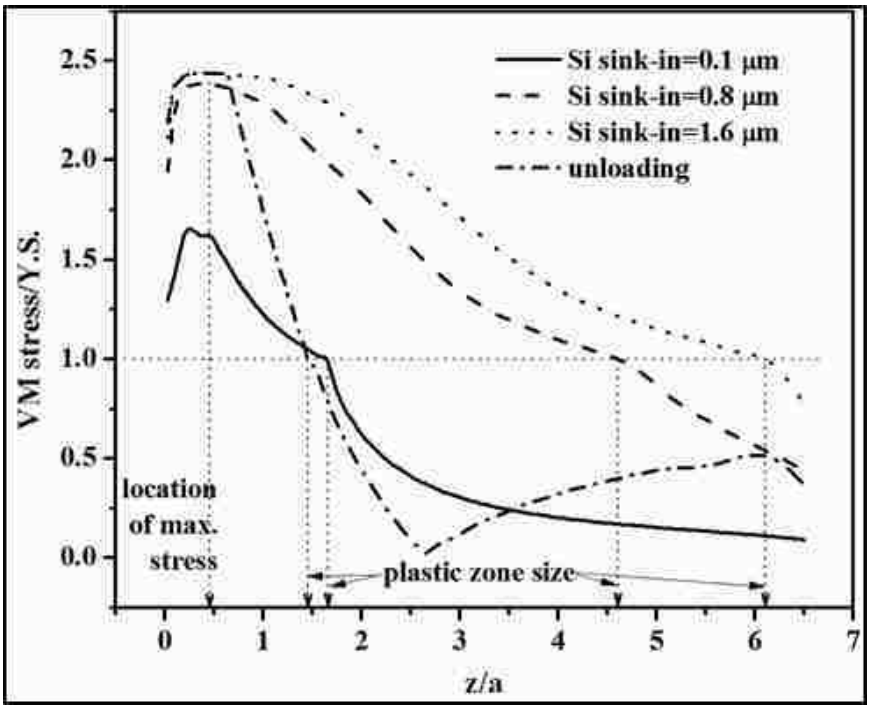

Figure 7. 3: Normalised von-Mises' stress distribution in the aluminum matrix below the particle after silicon particle sink-in in the matrix by (a) 0.1 μm and (b) 0.8 μm (c) 1.6 μm; and (d) after unloading (at the end of the simulation). The von-Mises' stress and the depth below particle was normalised by the yield strength of the matrix and the radius of the buried end of the particle (3.0 μm), respectively.

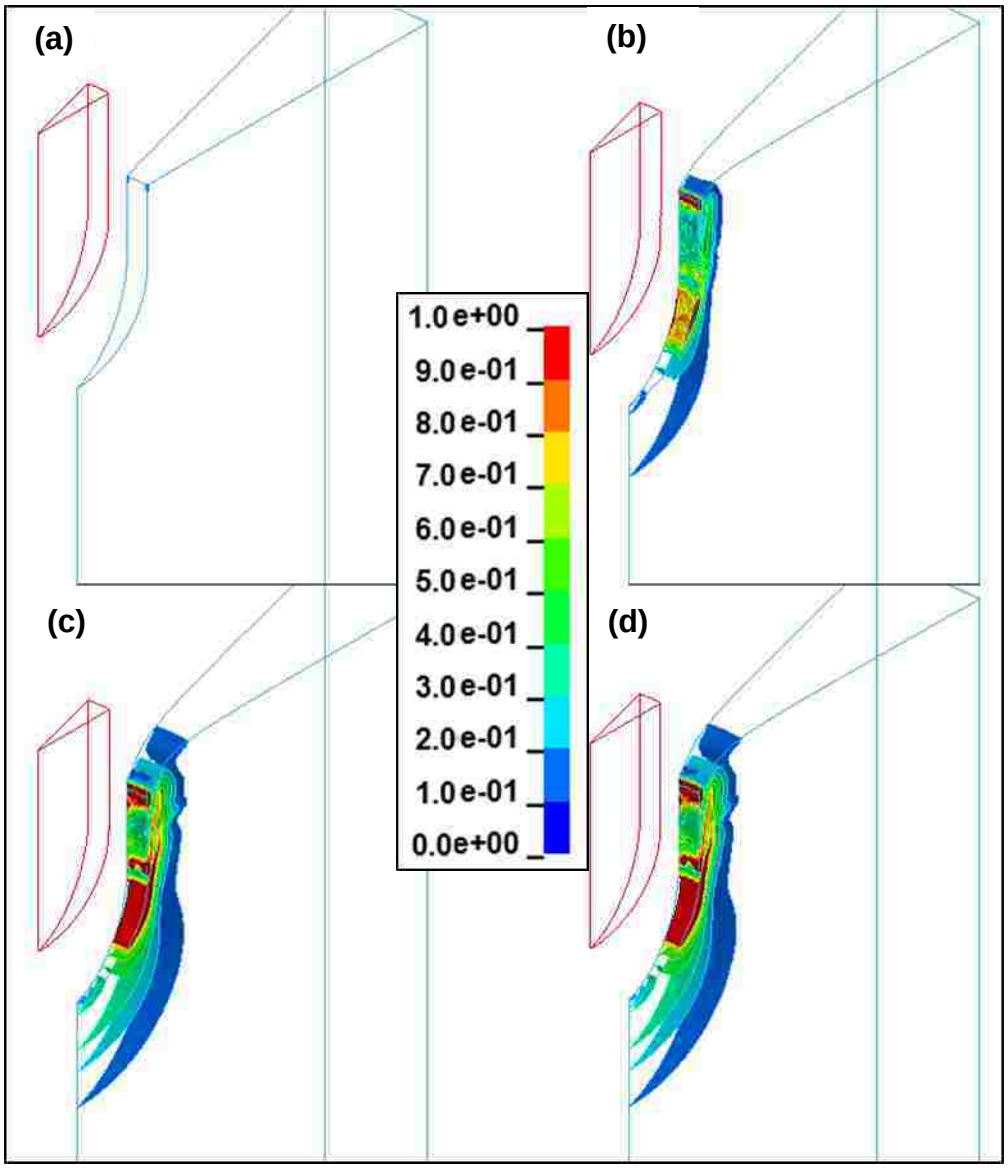

Figure 7. 4: Effective plastic strain distribution in aluminum matrix after silicon particle sink-in in the matrix by (a) 0.1 µm and (b) 0.8 µm (c) 1.6 µm; and (d) after unloading (at the end of the simulation).

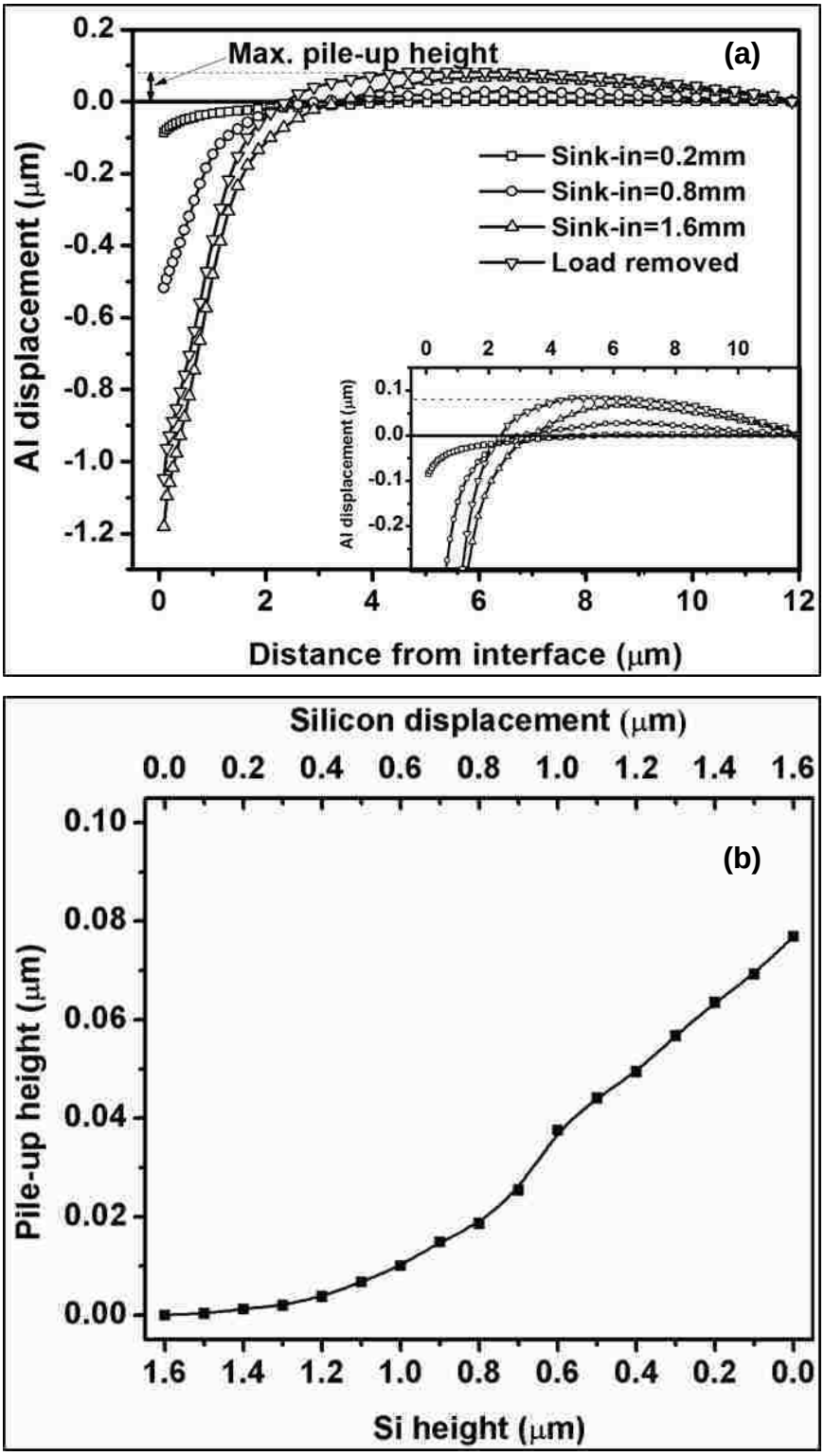

Figure 7. 5: (a) Surface elevation of aluminum matrix at four different stages of particles sinking-in; (b) variation of maximum pile-up height as a function of silicon height after unloading.

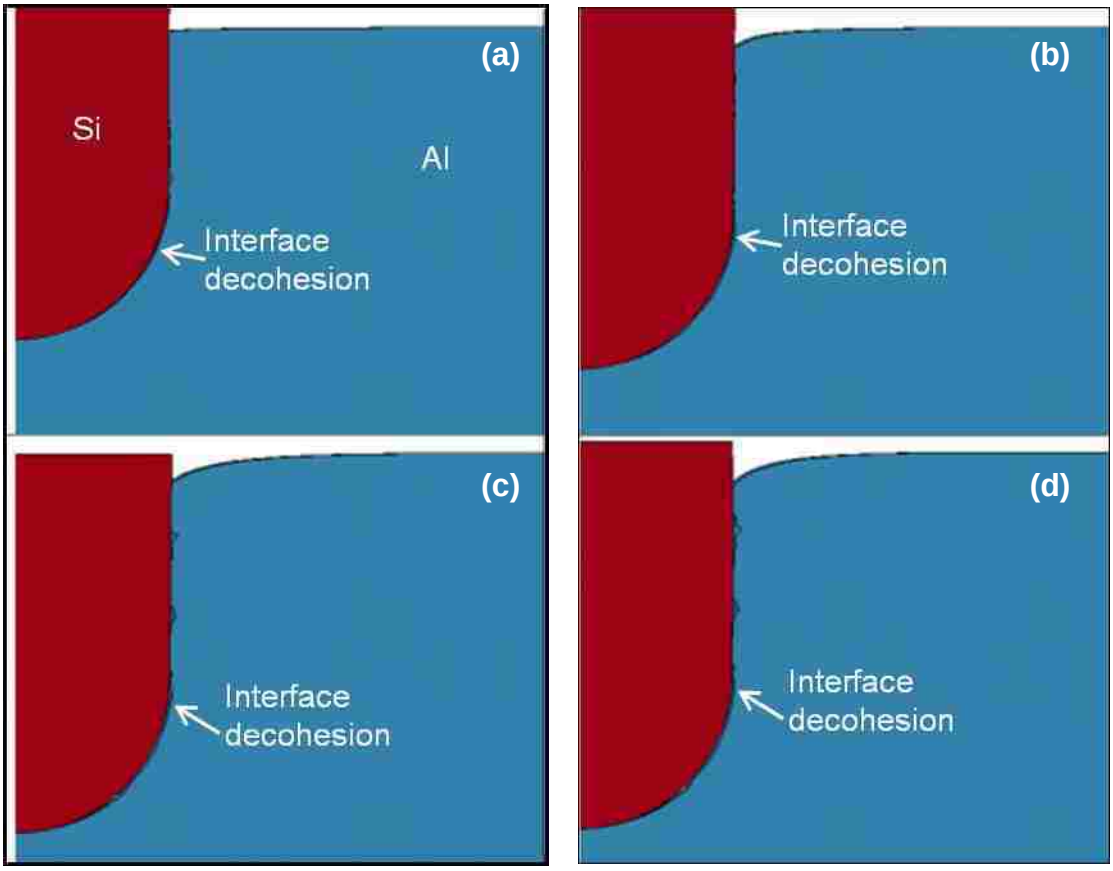

Figure 7. 6: The Al-Si interface separation after silicon sinking-in of (a) 0.2 µm; (b) 0.8 µm (c) 1.6 µm and (d) after unloading in single particle model. The displacements in x-axis was magnified by three times to show the separation clearly.

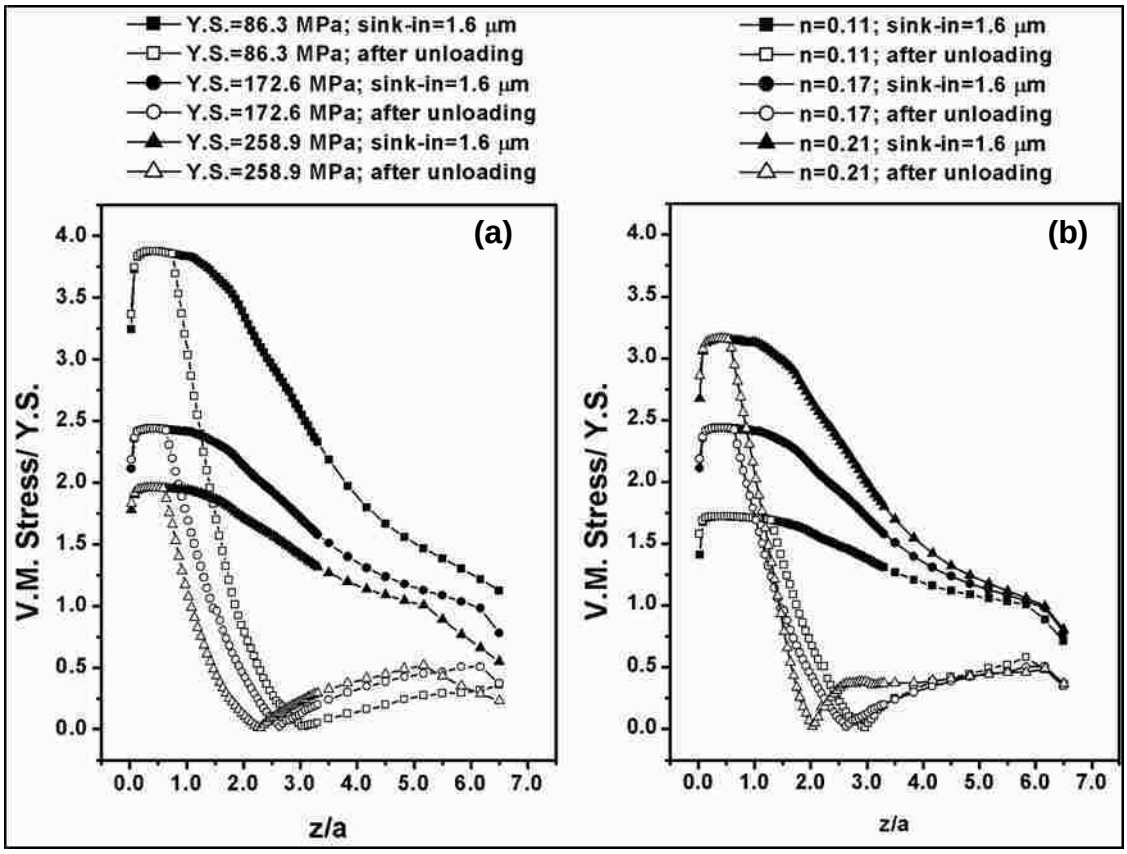

Figure 7. 7: Normalised stress distribution in matrix below the particle for (a) different yield strengths and (b) strain hardening exponents at maximum silicon sinking-in and after unloading.

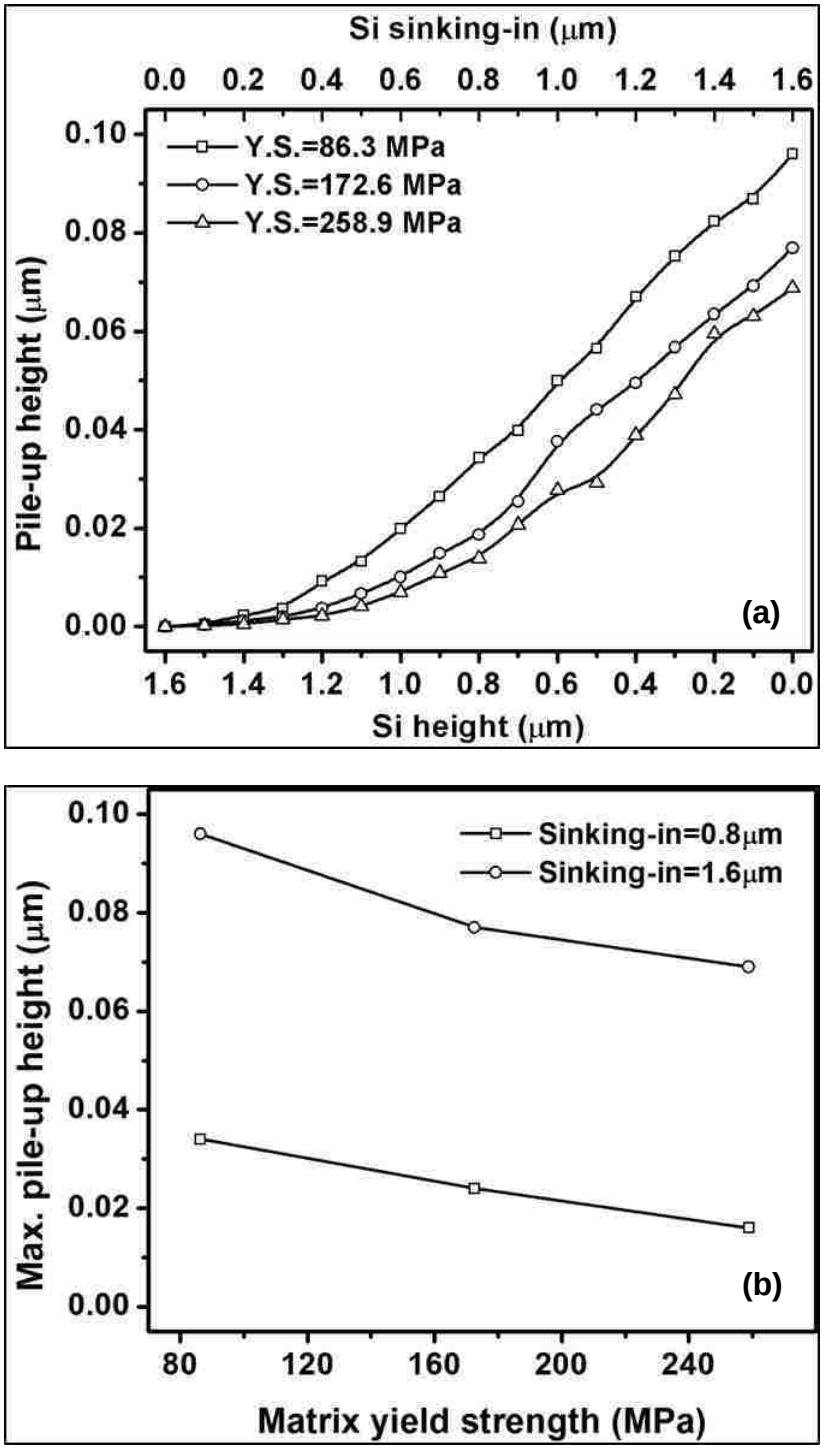

Figure 7. 8: (a) Change in pile-up height with silicon particle height for three different yield strength of aluminum matrices and (b) variation of maximum pile-up height with matrix yield strength at two different particle sinking-in amount. (c) Evolution of the UMW damage parameter (ratio of pile-up height to silicon height) with silicon height for different matrix yield strengths showing the transition from UMW-I to UMW-II stage. Experimental data from lubricated test at 25 °C is also shown in (c).

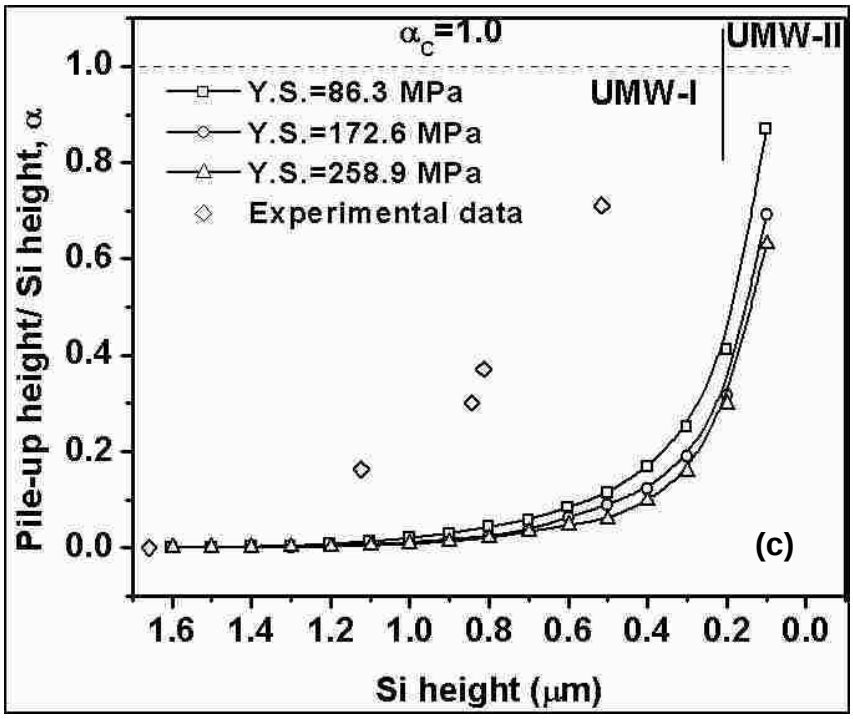

Figure 7. 8: Continued

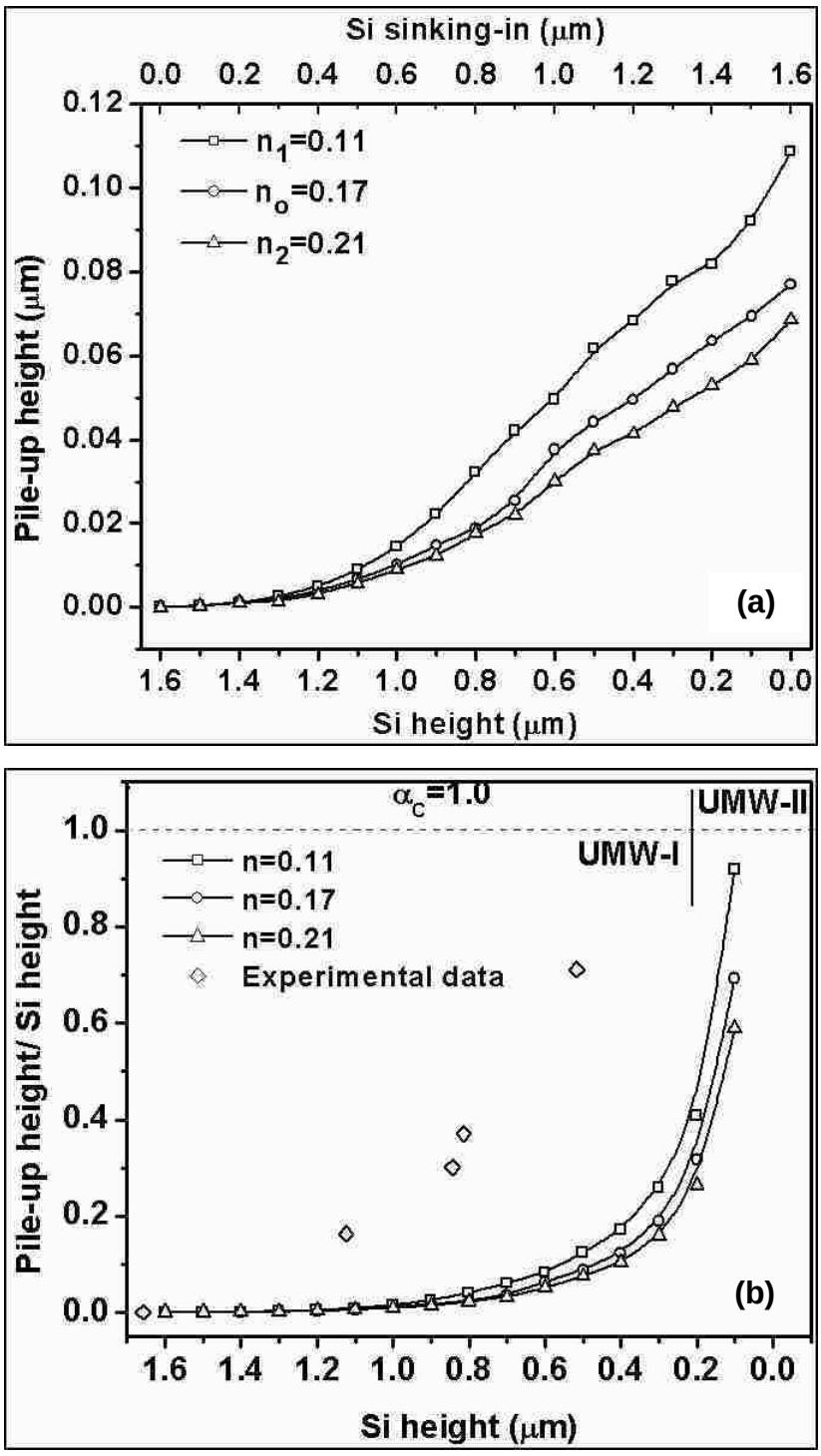

Figure 7. 9: (a) Change in pile-up height with silicon particle height and (b) evolution of the UMW damage parameter (ratio of pile-up height to silicon height) with silicon height for aluminum matrix with three different strain hardening exponents showing the transition from UMW-I to UMW-II stage. Experimental data from lubricated test at 25 °C is also shown in (b).

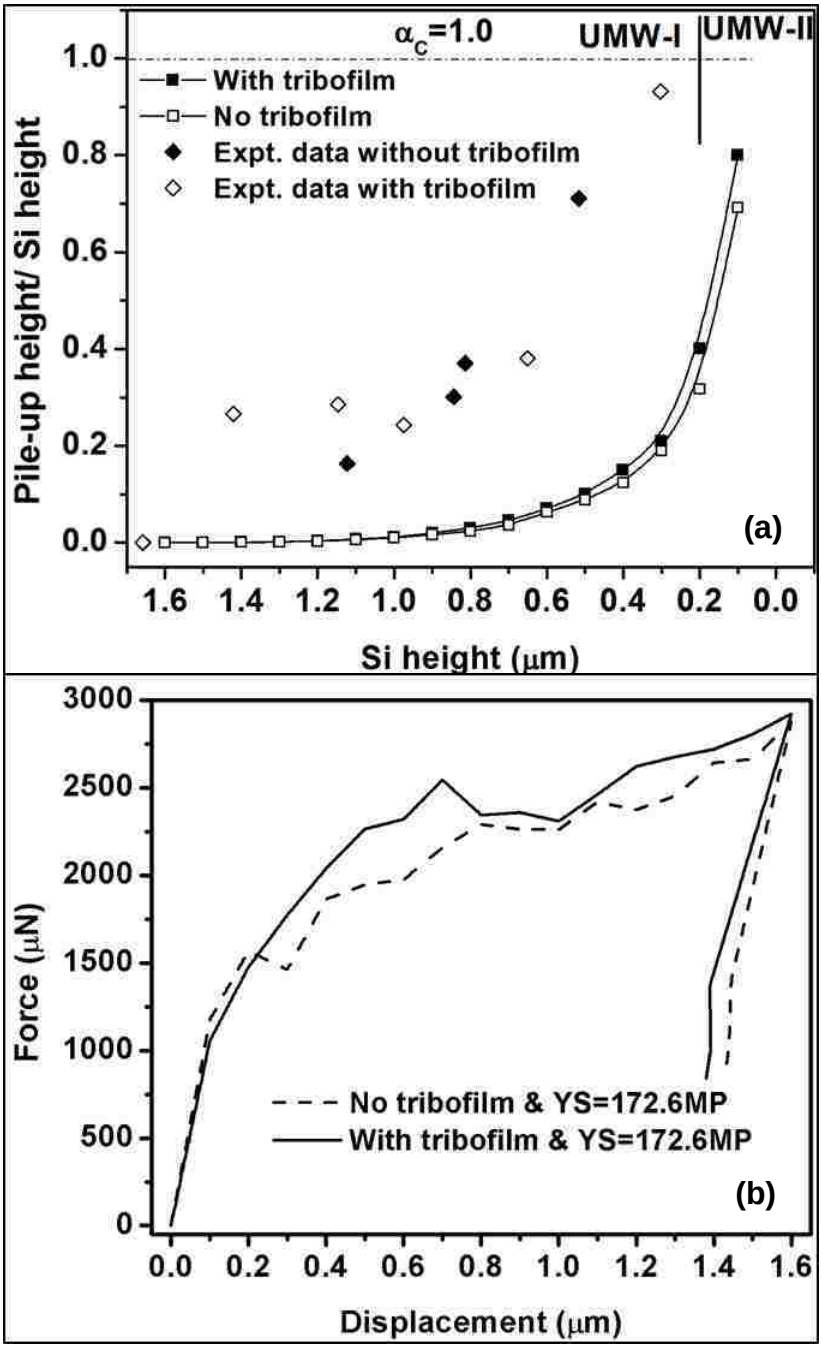

Figure 7. 10: (a) Evolution of the UMW damage parameter (ratio of pile-up height to silicon height) with silicon height is shown to illustrate the effect of formation of tribofilm. With tribofilm the transition from UMW-I to UMW-II is delayed thereby improving the wear behaviour of Al-Si alloys. The experimental data from lubricated test at 25 °C (no tribofilm) and 100 °C (with tribofilm) is also shown in the plot; (b) Force-displacement plot during particle sinking-in with and without tribofilm.

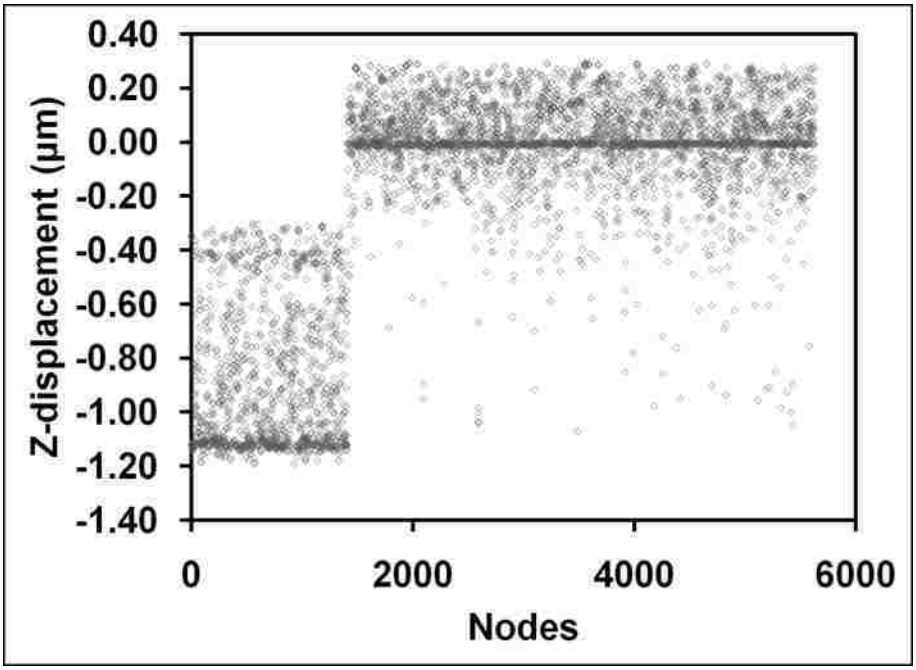

Figure 7. 11: Z-displacement of 5630 nodes belonging to the top aluminum surface of the multi-particle model. The maximum displacement of any nodes was considered as the maximum pile-up height.

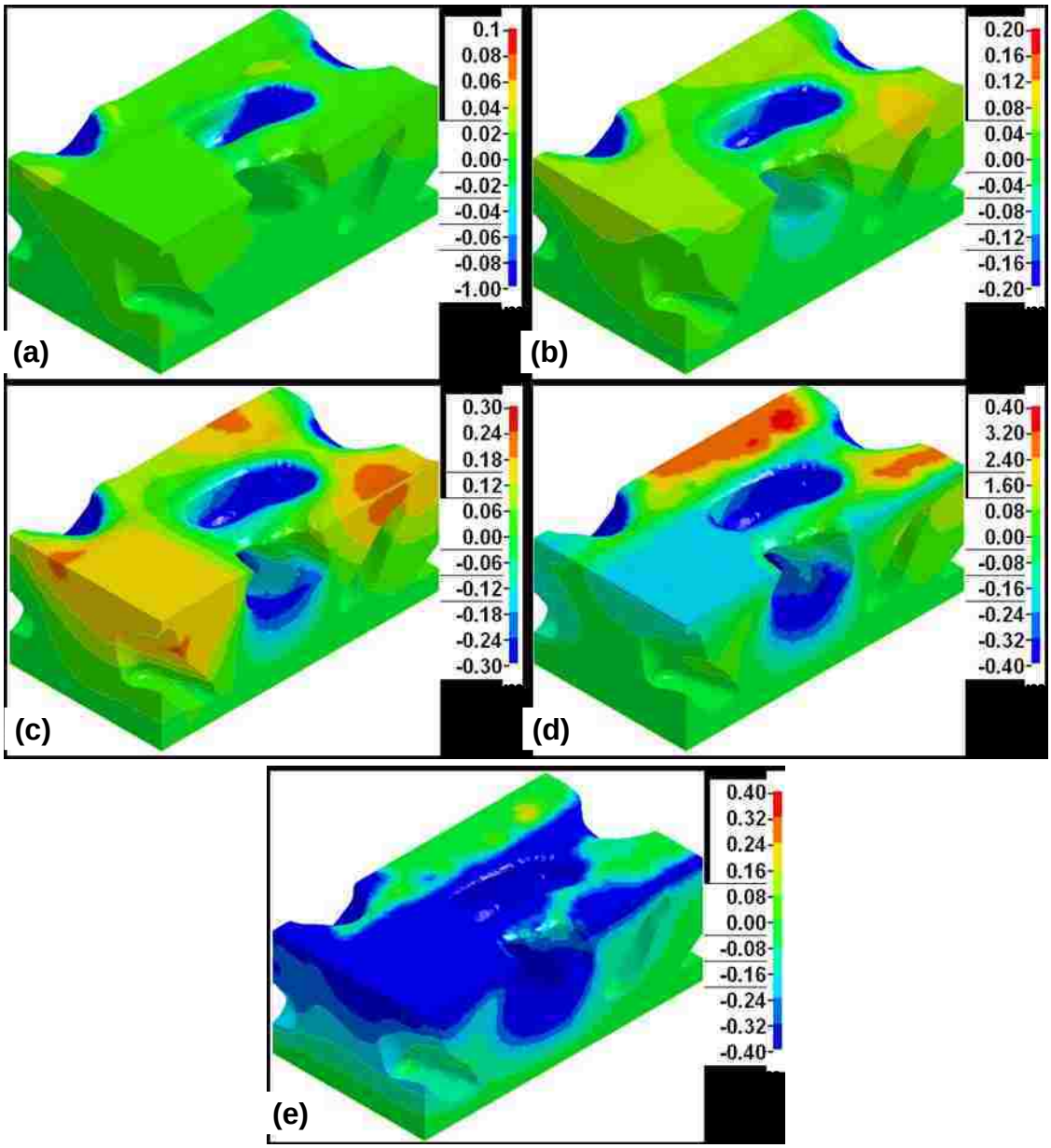

Figure 7. 12: Fringe plot showing the pile-up in the aluminum matrix at different amounts of silicon particles sinking-in (or particle height) – after (a) 0.34 µm (1.34 µm), (b) 0.67 µm (1.00 µm), (c) 1.00 µm (0.67 µm), (d) 1.34 µm (0.34 µm) and (e) 1.68 µm (0.00 µm). Maximum displacement was observed after silicon sinking-in of 1.34 µm in (d). Note the changes in scale bar in each plot.

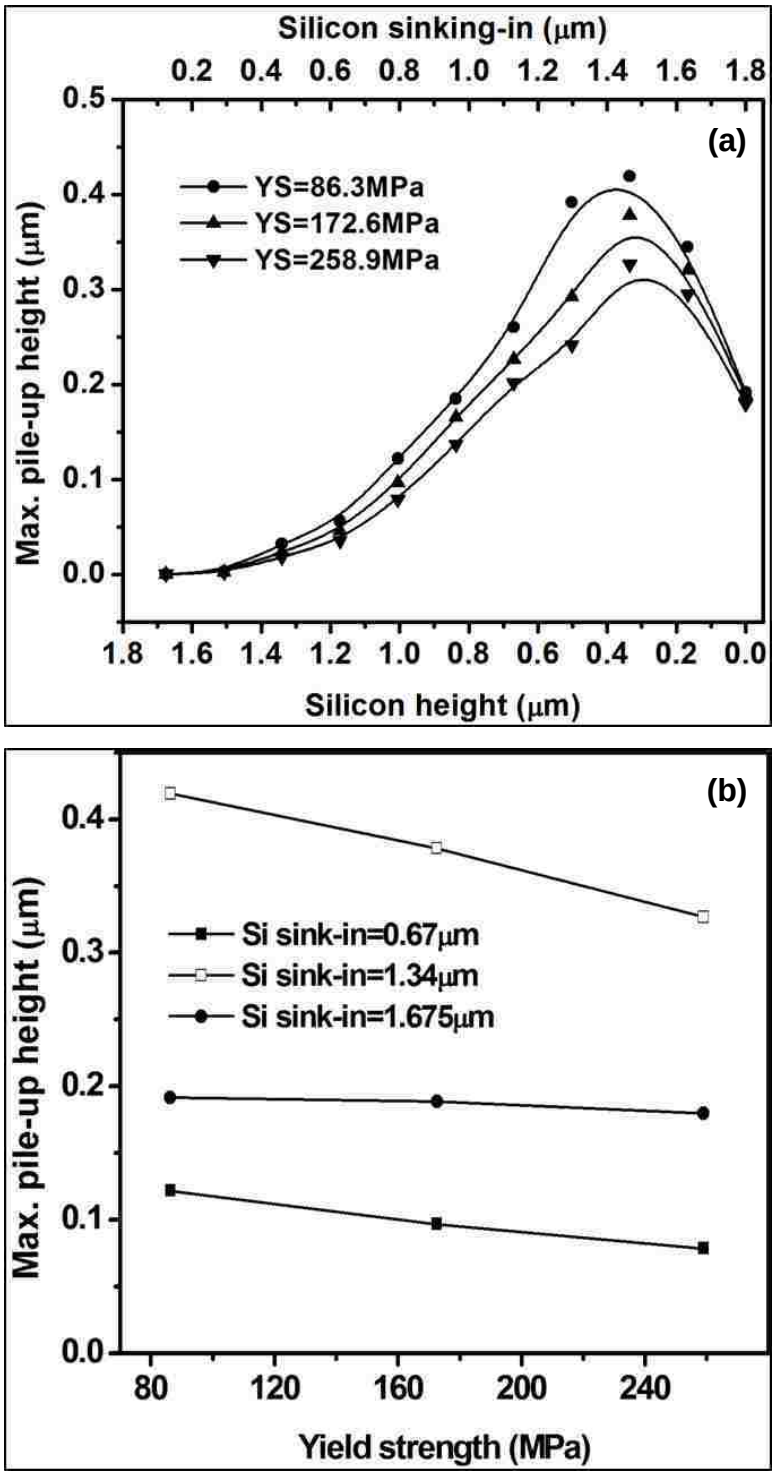

Figure 7. 13: (a) Maximum pile-up height changes with different amount of particle height and (b) maximum pile-up height at three different stages of silicon sinking-in for three different yield strength of the aluminum matrix in the multi-particle model.

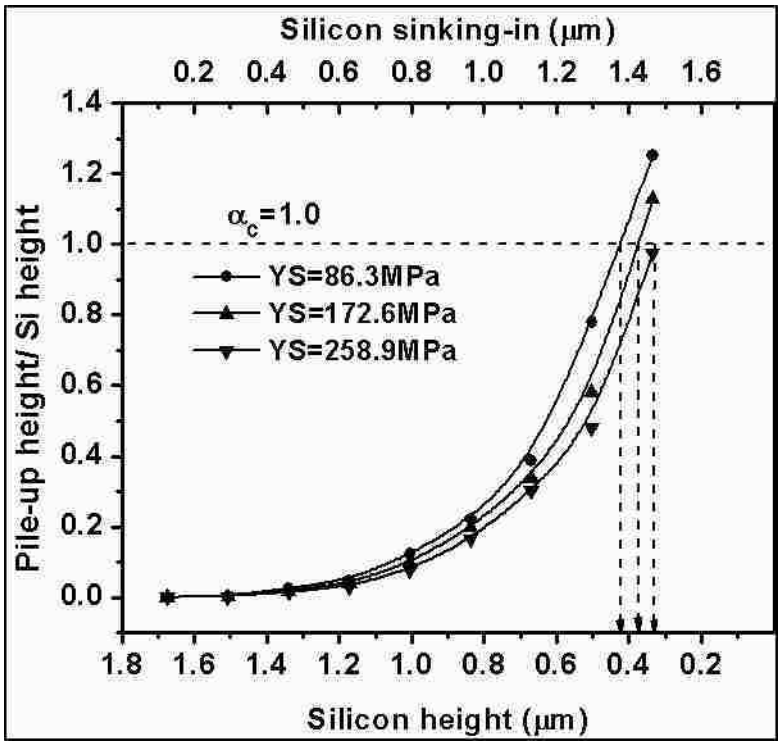

Figure 7. 14: Change in pile-up height to silicon height (α) with silicon height (or, silicon sinking-in) for three different yield strength of the aluminum matrix in the multi-particle model.

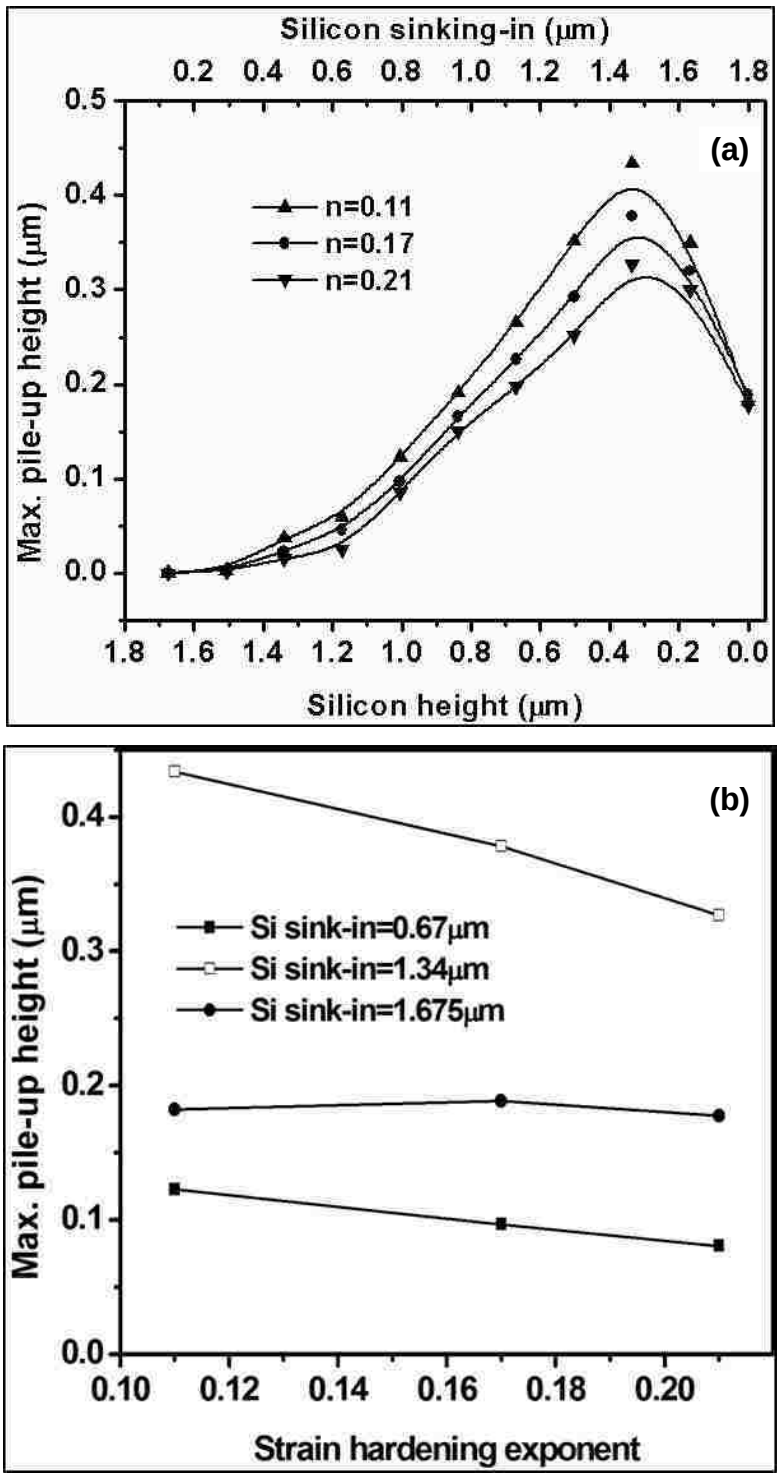

Figure 7. 15: (a) Maximum pile-up height changes with different amount of particle height and (b) maximum pile-up height at three different stages of silicon sinking-in for three different strain hardening exponent of the aluminum matrix in the multi-particle model.

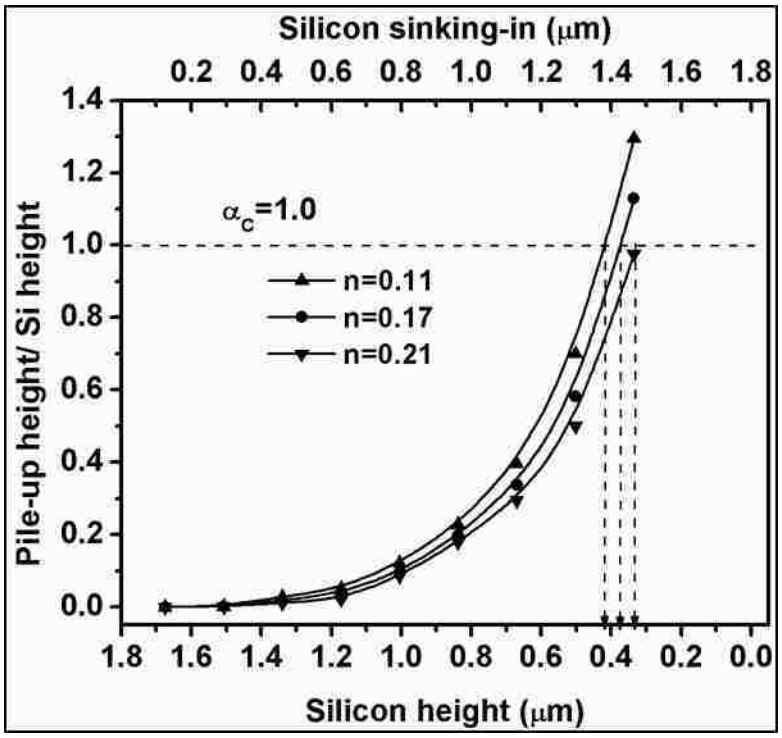

Figure 7. 16: Change in pile-up height to silicon height (α) with silicon height (or, silicon sinking-in) for three different strain hardening exponent of the aluminum matrix in the multi-particle model.

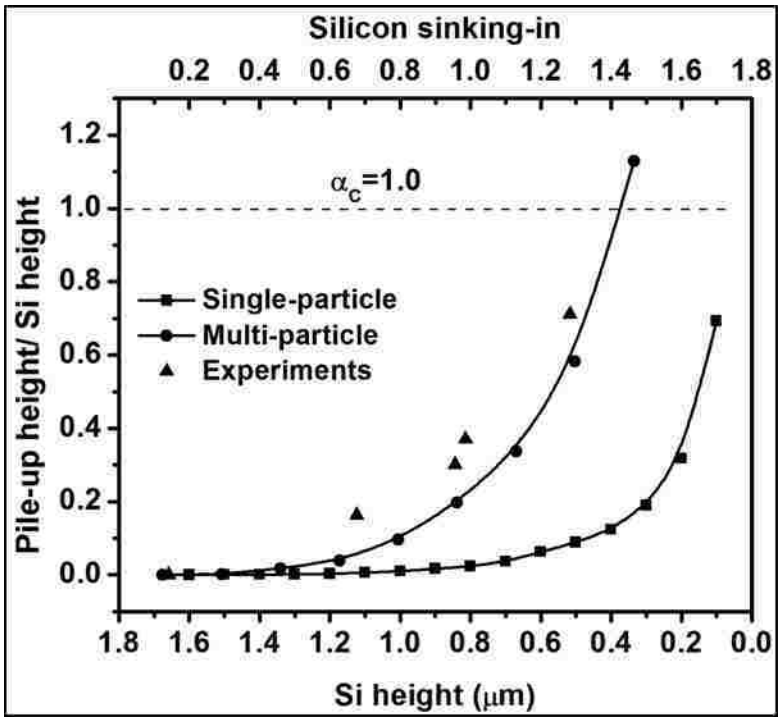

Figure 7. 17: Comparison of the ratio of pile-up height to silicon height from numerical simulation using single- and multi-particle model with the experimental observations at 25 °C as shown in Chapter V. A difference of 0.13-0.15 was observed in the ratio between multi-particle model and the experimental observations.

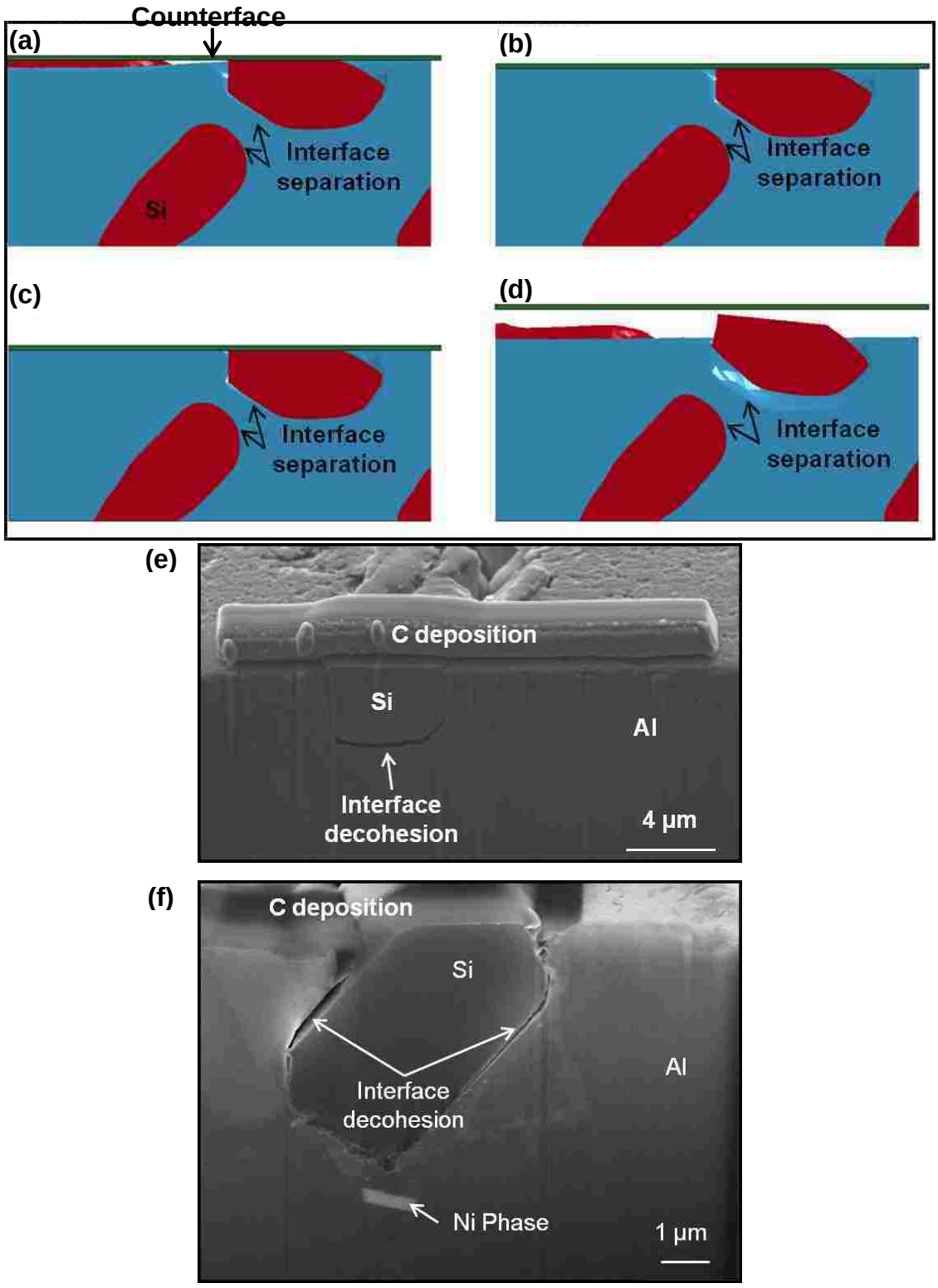

Figure 7. 18: Interface decohesion after (a) 1.00 µm, (b) 1.34 µm, (c) 1.68 µm and (d) after unloading in multi-particle model. (e) and (f) shows decohesion at the Al-Si interface in the Al-12.6% Si alloy wear tested for 5×10^4 and 6×10^5 sliding cycles at 2.0 N load, respectively.

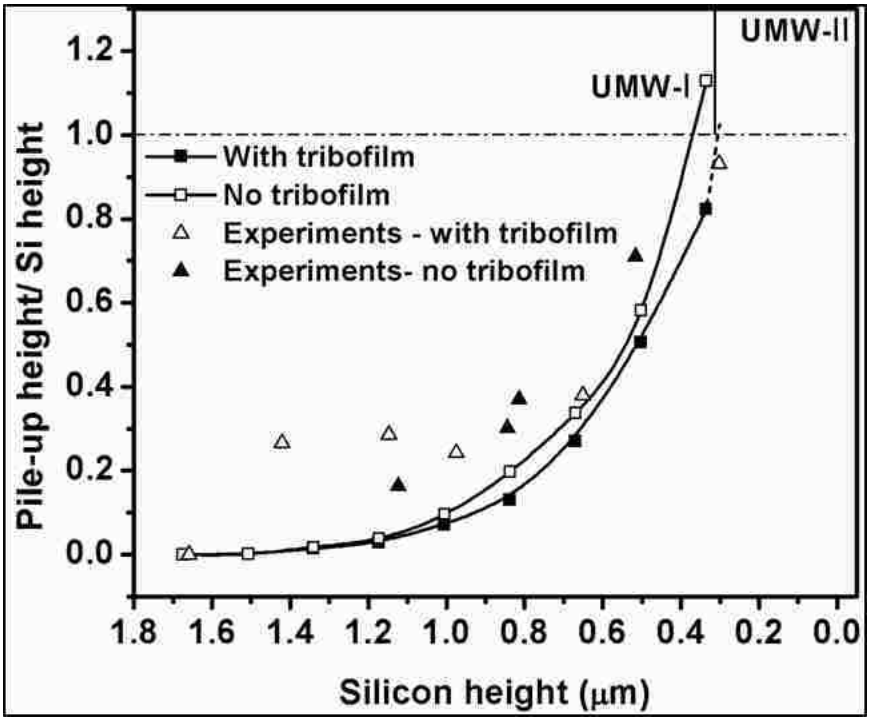

Figure 7. 19: Evolution of the UMW damage parameter (ratio of pile-up height to silicon height) with silicon height is shown to illustrate the effect of formation of tribofilm in multi-particle model. With tribofilm the transition from UMW-I to UMW-II is delayed thereby improving the wear behaviour of Al-Si alloys. The experimental data from lubricated test at 25 °C (no tribofilm) and 100 °C (with tribofilm) is also shown in the plot.

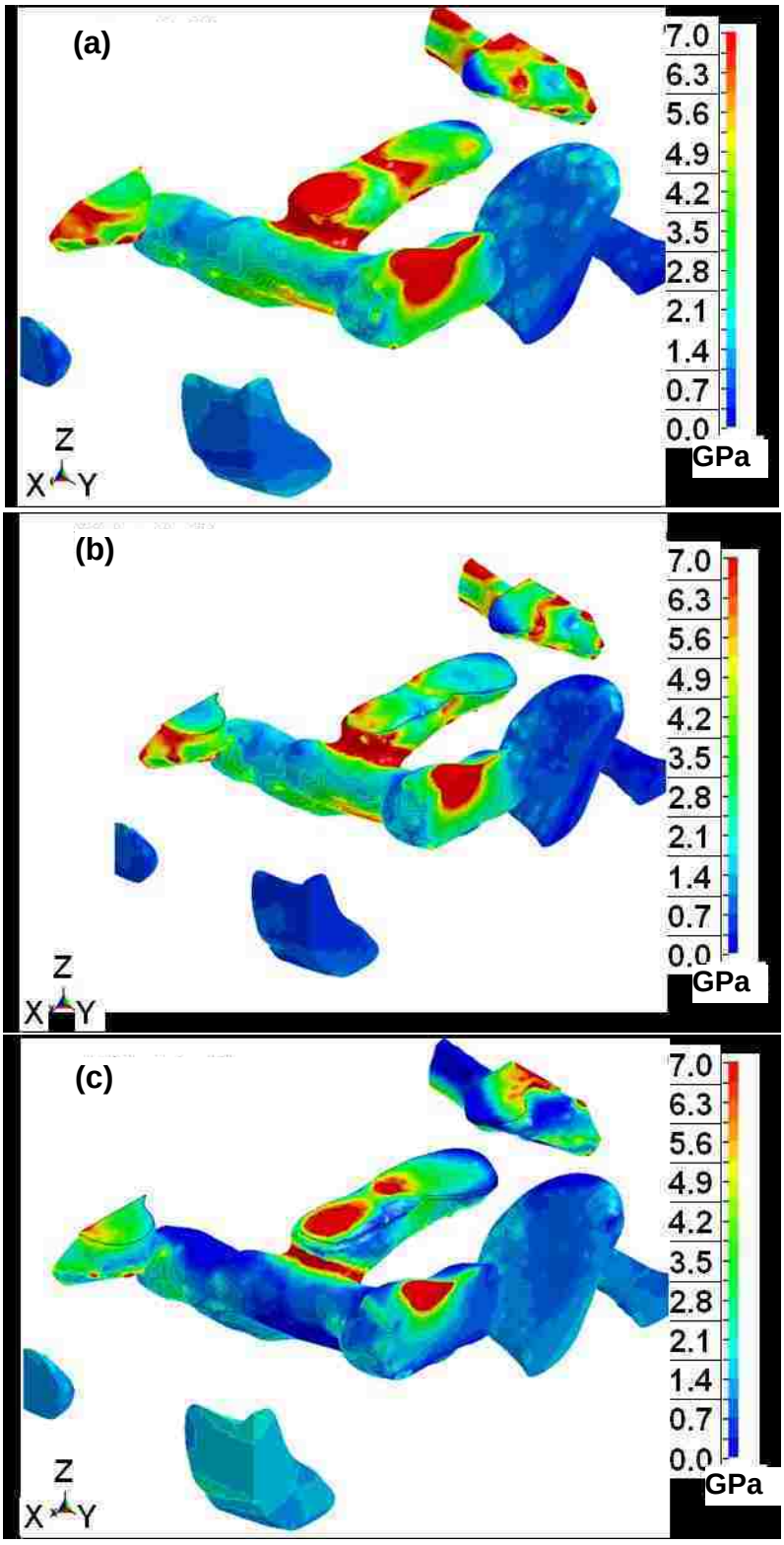

Figure 7. 20: von Mises stress distribution within particles at zero silicon height: (a) no tribofilm, (b) with tribofilm for matrix yield strength of 172.6 MPa; and (c) with tribofilm for matrix yield strength of 86.3 MPa. The maximum value of the scalebar represents the yield strength of silicon

8. CHAPTER 8 – GENERAL DISCUSSION

8.1 Effect of heat treatment

The effect of heat treatment was investigated by conducting lubricated UMW tests in Al-12.6% Si alloys in two different heat treatment conditions such as T6 and T7. The Vicker's hardness of the aluminum matrix in these two conditions was 69.1±1.0 HV_{10} and 115.2±20.9 HV_{10}. As it was observed in **Figure 6.19**, the volumetric wear loss in T6 heat treat condition was higher than the volumetric wear loss in T7 heat treat condition. The effect of matrix hardness in maintaining the UMW for Al-Si alloys was studied earlier in [**92**]. Increasing the matrix hardness from 40.0±8.3 HV_{10} in Al-12.0% Si alloy to 68.0±12.5 HV_{10} at 0.5 N load caused particles fracture. The study with Al-11.0% Si alloy [**92**] was conducted for10^5 sliding cycles and the matrix damage was not initiated, i.e. the study corresponded to UMW-II stage. In case of Al-12.0% Si alloy, due to lower matrix hardness the matrix damage was inflicted earlier compared to the alloy with higher matrix hardness.

The general understanding of UMW in Al-Si alloys had been that the silicon particles carry the applied load and protect the matrix from further damage. This may be true for Al-18.5% Si alloys because of the presence of large block-like primary particles. With increase in particles size and lowering aspect ratio (such as in Al-18.5% Si alloys), the contact pressure applied in these particles are lowered; if the contact pressure is lower than the matrix hardness then the hypothesis of 'particles carrying the load' become a fact and no matrix damage is experienced. This was observed in a previous study by Chen and Alpas [**93**]. However, if the contact pressure is increased beyond the matrix hardness, as observed during the POD tests

conducted at 5.0 N load (**Figure 4.11**), the argument of particles carrying the load falls apart and the matrix hardness starts altering the UMW behaviour. Particles fracture becomes a controlling parameter in maintain UMW irrespective of the particles size and morphology. The evidence of particles fracture and how that affected the UMW-MW transition was shown in **Chapter 4** for Al-18.5% Si alloy. Once the particles start to fracture, a lot of other factors come in to play, such as contact pressure, temperature and lubrication condition. Thus the role of matrix hardness, particle morphology and particle fracture are inter related and altering one often requires careful control of other parameters.

However, all the previous studies in UMW region were conducted until the beginning of UMW-III stage; durability of Al-Si alloys in presence of ORL formation was not studied. **Chapter 6** showed the durability of ORL in maintaining UMW-III stage. Increasing the hardness from 69.1±1.0 HV_{10} in T7 condition to 115.2±20.9 HV_{10} in T6 condition had a very similar effect as it was observed earlier in [**92**]. Based on the results presented in [**92**] it may be postulated that in T6 condition with higher matrix hardness the particles were fractured but in T7 heat treat condition the particles were sunk-in. However, the load (2.0 N) used in these experiments was intermediated between the two extreme conditions studied earlier [**92,93**] and in **Chapter 4**. Therefore the response of the Al-12.6% Si alloy in maintaining UMW due to particle fracture was also somewhat in between, i.e. the fractured particles inflicted damage to the Al matrix by forming individual trenches in the direction of sliding as observed in **Figure 6.13b**, but because of the lower load the damage was not as severe as it was observed in Al-18.5% Si alloy at 5.0 N load (**Figure 4.6**). Therefore a direct comparison between the **Figure 2.15** [**92**] and **Figure 6.19** raise the apparent contradiction on the effect of matrix hardness in maintaining UMW. However, the studies in [**92**] were conducted only up to UMW-I and UMW-II stages, whereas, the data presented in **Figure 6.19** correspond to UMW-II stage.

8.2 Simulation of UMW mechanisms

8.2.1 Effect of particle distribution

The FE model showed the distinct effect of multiple particles surrounding a sinking-in silicon particle. The particle sinking-in problem is analogous to a flat punch deforming plastic material which is constrained to flow in one direction only. The solution of this problem was solved using slip line field theory and was discussed in [**151**]. Using the solution from slip line field theory it may be suggested that the yield pressure for the indentation of aluminum matrix with a silicon particle can be nearly three times the stress required for the yielding of the matrix which is the approximately the Vicker's hardness of the matrix. In the FE model the macroscopic material behaviour is used with to simulate the microscopic phenomena of particle sinking-in and matrix pile-up. In the single particle model the matrix surrounding the particle was only constrained by the boundary conditions of the matrix. Therefore, the plastic constraint was not developed during particle sinking-in for the materials to flow unidirectionally in the upward direction to form pile-up. The stress induced in the matrix by particle sinking-in deformed the matrix plastically in the close proximity of the particle and elastically away from the particles. In the multi-particle model, all the other silicon particles surrounding the sinking particle were not deforming plastically and thus the aluminum matrix was surrounded by the rigid material providing the constraint for plastic flow. In such situation the matrix could only flow in the upward direction casing pile-up formation surrounding the particles.

The direct evidence of the under developed plastic constraint was observed in Al-18.5% Si alloy. In this alloy due to the presence of large primary silicon the interparticle distance was significantly higher compared to the eutectic Al-12.6% Si alloys (**Chapter 5**) or Al-25.0% Si alloy [**94**]. Thus the matrix pile-up could not be observed in this particular alloy until the contact

pressure applied on the particles fractured them. After the fracture, fractured particle could sink-in and the remaining of the fractured particle provided plastic constraint such that the pile-up was observed (**Figure 4.3d**).

8.2.2 Fracture of silicon particles and decohesion of Al-Si interface

In the FE model silicon particles fracture was not simulated. However the stress within the silicon particles can be used as an indication of fracture of particles. For single crystal silicon the yield strength is 7.0 GPa [**152**]. The von Mises stress within silicon particle(s) from FE model was compared with the yield strength and it was found that in some locations within the particles the stress exceeded 7.0 GPa. Another important observation was that the increase in von Mises stress with increasing yield strength of the matrix. This evidence suggested that reduction of contact pressure applied on silicon particles through the formation of island-like tribofilm is beneficial in reducing particles fracture. This was also found experimentally at 100 °C, where the formation of tribofilm reduced the particles fracture in UMW-I stage and ultimately resulted in improved wear resistance at 100 °C compared to 25 °C.

Particle fracture and decohesion of the Al-Si interface has some implications on the UMW behaviour of Al-Si alloys. Fracture of particles often generates small fragments of silicon particle which may result in abrasion and reduction in the effectiveness of ORL in preventing the matrix damage. This phenomenon was observed in Al-12.6% Si alloy in T6 heat treatment condition and was discussed in **Section 8.1**. The effect of interface decohesion is twofold and is more detrimental for small spherical silicon particles. Because the small spherical particles are then easier to be removed from the surface and such particles may act as source of abrasion. Secondly, once the particles are removed from the surface due to complete interfacial decohesion (**Figure 7. 18**), the resulting crater may act as porosity and or reservoir of the lubricating oil. The effect of whether those craters acts as porosity or reservoir of the lubricating

oil on the wear resistance are competitive. In dry sliding, the wear resistance of Al-Si alloys depend on the relative size of the pores and the contacting asperity. If the contacting asperity is larger or of the same size as the crater, the crater becomes less effective in generating the wear particles [**153**] and the wear occurs by delamination. However, delamination was not observed in the UMW region because in the presence of lubrication, the length scale over which the damage happened was of the order of 1-2 μm from the surface. Hence, the strain was large enough to refine the grain size within the subsurface region of 1-2 μm from the surface, but it did not initiate crack or void formation in the subsurface region – necessary microstructural changes for initiation of delamination. However, if the crater size is smaller than the asperity size then wear occurs by covering of the craters with deformed aluminum layer and break-up of such layer during the subsequent passes. In UMW, such deformed layer is mixed with lubricant and the degraded products of lubricant additive to form oil-residue layer which because of its higher hardness is beneficial in protecting the softer matrix beneath it.

8.2.3 Energy dissipation mechanism

From the experimental observations it may be said that the total work done on the system during particle sinking-in is dissipated primarily in three ways, internal energy, which is the expended towards elastic and inelastic deformation within the material, sliding interface energy due to the sliding of contact interfaces and the energy due to fracture of particles. In the numerical study, it was possible to estimate the energy spent during deformation of the materials and sliding of various interfaces; however, the particles were considered as elastic and fracture of particles was not simulated. Thus it was not possible to estimate the energy spent in fracturing the particles. In addition, the kinetic energy due to silicon sinking-in was negligible compared to the other energies. In the multi-particle model without tribofilm there were two sliding surfaces; one was between the counterface and the silicon and the other was between

aluminum and silicon once the interface failure occurred. In the model with tribofilm there was an additional sliding interface between the tribofilm and the silicon. The internal energy constituted more than 92.00% of the total energy and the balance energy was comprised of the sliding interface energy and the friction energy. In presence of the tribofilm on top of silicon particles 92.56% of the total energy was expended as the internal energy at the maximum silicon displacement and the rest 7.44% was expended as sliding interface energy; out of that 5.73% was towards the sliding between the counterface and the tribofilm and the aluminum matrix and 1.71% towards the sliding at the Al-Si interface after the decohesion. However in the absence of tribofilm, 92.24% of the total energy was expended as internal energy and the rest 7.76% was towards the sliding interface energy. Thus the model showed that in presence of tribofilm 0.32% more energy was spent as internal energy and 0.72% more energy was spent towards the sliding between the counterface and the tribofilm; in other words the tribofilm acted as an energy absorbing entity. When the yield strength of the matrix was reduced by half, 92.82% of the total energy was internal energy and the rest 7.18% was expended towards the sliding, that is, further increase in energy absorption was observed. Thus at elevated temperature localised drop in yield strength would cause further increase in energy absorption in presence of tribofilm.

9. CHAPTER 9 – SUMMARY & CONCLUSIONS

The research work within the scope of this dissertation was to investigate the UMW mechanisms at an elevated temperature of 100 °C, characterise the ORL layer and develop a finite element model to study the UMW mechanism in UMW-I and UMW-II stages. Accordingly, boundary lubricated POD tests were conducted in a eutectic Al-12.6% Si alloy and two hypereutectic, Al-18.5% Si and Al-25.0% Si alloys to facilitate microstructure-based design of liner less automotive engines made out of the eutectic Al-12.6% Si alloy.

The realm of UMW was investigated in one of the most used hypereutectic alloy (Al-18.5% Si alloy) and then the UMW mechanisms were studied in the eutectic alloy Al-12.6% Si alloy at 25 °C and 100 °C. The effect of temperature on the formation of ORL in the Al-12.6% Si alloys were investigated at the beginning of UMW-II stage and then the durability of ORL in maintaining UMW for extended period of sliding was studied by conducting boundary lubricated POD tests in the eutectic alloy and two hypereutectic alloys. A single particle and multi-particle finite element models were developed to simulate the UMW mechanisms (particle sinking-in and aluminum pile-up) and to understand the effect of matrix properties on the UMW mechanisms by conducting a parametric study.

Findings on characteristic features of UMW in eutectic Al-Si alloys:

- Three distinct stages of UMW were observed at 25 °C and 100 °C, namely UMW-I, UMW-II and UMW-III stage.
- The characteristic features of UMW-I was zero matrix wear and damage to silicon particles in terms of particle sinking in and fracture depending on particles size and matrix hardness.

- A damage criterion in terms of the ratio (α) of aluminum pile-up height to particle height was derived to quantify the UMW damage. The critical value of the UMW damage criterion equal to 1.0 indicated the transition to UMW-I to UMW-II.
- UMW-II stage was characterised by an accelerated wear rate and acted as a precursor to UMW-III stage. A tribolayer, named as oil-residue layer (ORL) due to tribochemical reactions and mechanical mixing of the engine oil additives and the Al-Si alloys, started to form in this stage on the piled-up matrix.
- The UMW-III, however, was a stabilised wear or decelerated wear rate stage featuring the formation of a continuous ORL on the worn surface. The ORL, supported either by hard silicon particles or a sliding induced ultra-fine grain aluminum matrix protected the matrix from further wear and thus the stabilised wear was achieved in this stage, irrespective of the initial microstructure.
- Key factors in maintaining the UMW are to minimise silicon particles fracture to avoid abrasive action which could be achieved either by large block-like primary silicon particles at lower contact pressures, e.g., in Al-18.5% Si alloy or by a uniform distribution of the silicon particles, e.g., in Al-12.6% Si alloys or Al-25.0% Si alloys. The particles fracture could also be minimised by increasing the temperature of engine oil to form a tribofilm on the silicon particles.

The conclusions from the study to investigate the effect of matrix properties on UMW mechanisms using a single particle and multi-particle finite element model were:

1. A Single particle model and a multi-particle FEM model were developed to study particle sinking-in and aluminum pile-up. By conducting a parametric study, both models showed that higher yield strength and strain hardening exponent resulted in lower amount of pile-

up. However, the multi-particle model was able to simulate the UMW mechanisms more closely with experimental observations.

2. Using the damage criterion it was shown that the UMW-to UMW-II stage transition could be delayed by increasing the matrix yield strength (or hardness) and strain hardening exponent. Thus an alloy with higher yield strength and strain hardening exponent would provide better wear resistance.
3. It was shown that the presence of tribofilm on top of silicon particles resulted in reduction in stress within the particles which may lead to the reduction in fracture; therefore the effectiveness of silicon particles was increased by the tribofilm.

The following conclusions were derived on UMW mechanisms of Al-Si alloys at 25 °C:

1. The UMW in Al-18.5% Si at 5.0 N load and at 25 °C lasted only up to 10^4 sliding cycles. During the UMW, abrasive actions occurred on contact surface of the exposed silicon particles and fracture of larger particles. At 5.0 N load the fracture of the particles within the WT occurred early in the sliding process and controlled the UMW mechanisms.
2. The particle sinking-in, which is the dominant UMW mechanism observed in eutectic alloys with relatively lower matrix hardness in UMW-I stage, was observed only after the particles were fractured making them easier to sink-in due to increase in contact pressure.
3. In Al 12.6% Si, three different stages of UMW were identified. However in UMW-I stage the particles fracture and sinking-in were observed. UMW-I stage lasted up to 10^4 sliding cycles followed by an accelerated wear stage, UMW-II. UMW-III was observed after 10^5 sliding cycles where the formation of ORL stabilised the wear.

The following conclusions were made on UMW mechanisms of Al-Si alloys at elevated temperatures:

1. The UMW in Al-12.6% Si alloys at 100 °C was also consisted of three stages similar to those observed at 25 °C. However there was an important difference in characteristic features in UMW-I stage. Two different types of tribolayer were formed at 100 °C. A discontinuous tribofilm named as island-like tribofilm (due to its morphology) formed on top of silicon particles at 100 °C and a continuous type ORL on top of the worn surface originated from the island-like tribofilm and mechanically mixed with the aluminum matrix.
2. The island-like tribofilm formed on top of silicon particles at 100 °C which acted like an energy absorbing layer thus minimising particles fracture and prolonging the UMW-I stage to 5×10^4 sliding cycles compared to 10^4 cycles at 25 °C.
3. The island-like tribofilm had hardness of 3.34±0.67 GPa and Young's modulus of 82.66±16.41 GPa measured by nanoindentation technique at a penetration depth of 15-25 nm. This composition of the tribofilm consisted of zinc sulphide and short chain zinc polyphosphate analysed by HRTEM and XANES spectroscopy. Some unreacted ZDDP was also found in the tribofilm.
4. The initiation of ORL started by smearing of tribofilm on top of piled-up aluminum and then slowly covering the worn surface, thereby, forming a continuous ORL which resulted in lower wear in UMW-II and UMW-III stage compared to that in UMW-II and UMW-III stage at 25 °C.
5. The hardness and Young's modulus of the ORL was 2.5 GPa and 50-60 GPa at both temperatures measured by nanoindentation technique at a penetration depth of 50 nm. The composition of the ORL in UMW-III stage consisted of zinc sulphide, and zinc polyphosphate with varying chain length mixed with aluminum from the matrix confirmed by the XPS.

6. Increasing the temperature beyond 100 °C facilitated the formation of ORL on the worn surface resulting lower amount of wear at elevated temperatures (100-160 °C) compared to the lower temperatures (25-80 °C). However, further investigation was needed to confirm the durability of the ORL at continuous sliding at temperatures above 100 °C.
7. The durability study at 100 °C, however, showed that the ORL formed at this temperature was effective in maintaining the UMW-II stage up to 6×10^6 sliding cycles. The volumetric wear in the eutectic alloy was almost same as that in the hypereutectic alloys. Thus, it was concluded that the eutectic alloy could be used as a cost effective replacement for the expensive hypereutectic alloys for the linerless automotive engine.

9.1 Significance of the research findings

The findings of this research work suggest that the cast eutectic Al-Si alloy can be used as a cost effective alternative to hypereutectic Al-Si alloys to manufacture linerless automotive engines. The potential savings from replacing the hypereutectic Al-Si alloys can be realised through cost savings from machining as in the eutectic alloys does not have primary silicon particles which result in high tool wear during machining. Replacing the Al-Si alloy engine block with cast iron liners with a monolithic design made of eutectic Al-Si alloys can save weight of the engine block by approximately a pound per bore by replacing the cast iron liner; it also eliminates the distortion in the engine bore arising from thermal mismatch between the Al-Si alloys and the cast iron, therefore, improving the life of the engine. Thus, the use of eutectic Al-Si alloys may prove beneficial in lower displacement engines where the cost savings from weight reduction alone cannot justify the total cost of manufacturing and the costs involved over the lifecycle of the engine.

It was also found that the tribological performance of Al-Si alloys improved at elevated temperature in presence of engine oil. Thus, it may be beneficial to use external heating to heat the engine oil before start of the engine during the cold weathers to avoid damage to the bore surface from scarcity of lubrication.

9.2 Suggestions for future work

The following suggestions for the future work are made:

1. Conduct lubricated UMW studies on DLC coated Al-Si alloys to study the effect of a hard coating on UMW mechanisms and how the DLC coating can be used to avoid cold scuffing in the absence of lubrication.
2. Develop a finite element model to incorporate the fracture of silicon particles and use microscopic material behaviour determined using nanoindentation; subsequently, carry out a design optimisation to find out the optimum matrix hardness required for a given particle size and distribution.
3. Develop Mg-based composite to replace Al-Si alloys as a further weight reduction measurement for the engine block.

REFERENCES

[1]. WD Menzie, JJ Barry, DI Bleiwas, EL Bray, TG Goonan, G Matos, The global flow of aluminum from 2006 through 2025, U.S. Geological Survey. Open-File Report 2010–1256 (2010) 1-73, available at http://pubs.usgs.gov/of/2010/1256/.

[2]. The Aluminum Association, Aluminium: The Corrosion Resistant Automotive Material, AT7 (May 2001) 1-25.

[3]. J Clarke, AD Sarkar. Wear characteristics of as-cast binary aluminium-silicon alloys, Wear. 54 (1979) 7-16.

[4]. R Antoniou, DW Borland. Mild wear of Al-Si binary alloys during unlubricated sliding, Materials Science and Engineering. 93 (1987) 57-72.

[5]. J Zhang, AT Alpas. Delamination wear in ductile materials containing second phase particles, Materials Science and Engineering A. 160 (1993) 25-35.

[6]. H Torabian, JP Pathak, SN Tiwari. Wear characteristics of Al-Si alloys, Wear. 172 (1994) 49-58.

[7]. AS Reddy, BN Pramila Bai, KSS Murthy, SK Biswas. Wear and seizure of binary Al-Si alloys, Wear. 171 (1994) 115-127.

[8]. AR Riahi, AT Alpas. The role of tribo-layers on the sliding wear behavior of graphitic aluminum matrix composites, Wear. 250-251 (2001) 1396-1407.

[9]. L Lasa, JM Rodriguez-Ibabe. Wear behaviour of eutectic and hypereutectic Al-Si-Cu-Mg casting alloys tested against a composite brake pad, Materials Science and Engineering A. 363 (2003) 193-202.

[10]. M Elmadagli, AT Alpas. Progression of wear in the mild wear regime of an Al-18.5% Si (A390) alloy, Wear. 261 (2006) 367-381.

[11]. J Li, M Elmadagli, VY Gertsman, J Lo, AT Alpas. FIB and TEM characterization of subsurfaces of an Al-Si alloy (A390) subjected to sliding wear, Materials Science and Engineering A. 421 (2006) 317-327.

[12]. M Elmadagli, T Perry, AT Alpas. A parametric study of the relationship between microstructure and wear resistance of Al-Si alloys, Wear. 262 (2007) 79-92.

[13]. KC Ludema. A review of scuffing and running-in of lubricated surfaces, with asperities and oxides in perspective, Wear. 100 (1984) 315-331.

[14]. BS Shabel, DA Granger, WG Truckner, Friction and wear of aluminum-silicon alloys, in: Blau PJ (Ed.), ASM Handbook, Volume 18 - Friction, Lubrication, and Wear Technology, ASM International, Materials Park, OH, USA, 1992, pp. 785-794.

[15]. M Chen, Mechanics and mechanisms of surface damage in Al-Si alloys under ultra-mild wear conditions, Ph.D. Dissertation, University of Windsor. (2008) 270.

[16]. A Kaye, A Street, Die casting metallurgy, Butterworths Scientific, London, 1982.

[17]. JL Jorstad. The hypereutectic aluminum-silicon alloy used to cast the Vega engine block, Modern Casting. 60 (1971) 59-64.

[18]. JL Jorstad. The progress of 390 alloy: From inception until now, AFS Transactions. (2009) 241-249.

[19]. KU Kainer, Metal matrix composites: custom-made materials for automotive and aerospace engineering, Wiley-VCH, Weinheim, 2006, pp. 314.

[20]. E Erginer, The strengthening of aluminum due to its cast microstructure modified by silicon, Ph.D. Dissertation, Brown University. (1969) 206.

[21]. F Kiyota, T Fujita, T Hirano, S Horie, Heat-resistant, wear-resistant, and high-strengthaluminumalloypowder and body shaped therefrom, United States Patent and Trademark Office Granted Patent. 259402 (3 July, 1990).
[22]. R Perrot, J Mazodier, Method of producinghollowbodies in aluminum-siliconalloys by powder-extrusion, United States Patent and Trademark Office Granted Patent. 774424 (11 July, 1978).
[23]. F Ruckert, P Stocker, R Rieger, Cylinder liner of a hypereutectic aluminum/silicon alloy for casting into a crankcase of a reciprocating piston engine and process for producing such a cylinder liner, United States Patent and Trademark Office Granted Patent. 790939 (6 April, 1999).
[24]. A Leatham. Spray forming: Alloys, products and markets, Metal Powder Report. 54 (1999).
[25]. A Kearney, EL Rooy, Aluminum foundry products, in: ASM International Handbook Committee (Ed.), ASM Handbook, Volume 02 - Properties and Selection: Nonferrous Alloys and Special-Purpose Materials, ASM International, 1990, pp. 123-151.
[26]. JG Kaufman, EL Rooy, Aluminum alloy castings - Properties, processes and applications, ASM International, Materials Park, Ohio, USA, 2004.
[27]. JL Murray, AJ McAlister. The Al-Si (Aluminum-Silicon) system, Bulletin of Alloy Phase Diagrams. 5 (1984) 74-84.
[28]. BK Prasad, K Venkateswarlu, OP Modi, AK Jha, S Das, R Dasgupta, et al. Sliding wear behavior of some Al-Si alloys: Role of shape and size of si particles and test conditions, Metallurgical and Materials Transactions A: Physical Metallurgy and Materials Science. 29 (1998) 2747-2752.
[29]. M Elmadagli, AT Alpas. Sliding wear of an Al-18.5 wt.% Si alloy tested in an argon atmosphere and against DLC coated counterfaces, Wear. 261 (2006) 823-834.
[30]. MA Moustafa, FH Samuel, HW Doty, S Valtierra. Effect of Mg and Cu additions on the microstructural characteristics and tensile properties of Sr-modified Al-Si eutectic alloys, The International Journal of Cast Metals Research. 14 (2002) 235-253.
[31]. Y-H Cho, Y-R Im, S-W Kwon, H-C Lee, The effect of alloying elements on the microstructure and mechanical properties of Al-12Si cast alloys, Materials Science Forum. 426-432 (2003) 339-344.
[32]. AL Dons, G Heiberg, J Voje, JS Mæland, JO Løland, A Prestmo. On the effect of additions of Cu and Mg on the ductility of Al-Si foundry alloys cast with a cooling rate of approximately 3 K/s, Materials Science and Engineering A. 413-414 (2005) 561-566.
[33]. J Barresi, MJ Kerr, H Wang, MJ Couper. Effect of magnesium, iron and cooling rate on mechanical properties of Al-7Si-Mg foundry alloys, AFS Transactions. 117 (2000) 563-570.
[34]. M Dash, M Makhlouf. Effect of key alloying elements on the feeding characteristics of aluminum-silicon casting alloys, Journal of Light Metals. 1 (2001) 251-265.
[35]. G Gustafsson, T Thorvaldsson, GL Dunlop. The influence of Fe and Cr on the microstructure of cast Al-Si-Mg alloys, Metallurgical Transactions A: Physical Metallurgy and Materials Science. 17A (1986) 45-52.
[36]. JE Gruzleski, BM Closset, The treatment of liquid aluminum-silicon alloys, American Foundrymen's Society, Inc., Des Plaines, ILL, 1990.
[37]. SG Shabestari, F Shahri. Influence of modification, solidification conditions and heat treatment on the microstructure and mechanical properties of A356 aluminum alloy, Journal of Materials Science. 39 (2004) 2023-2032.
[38]. HR Ammar, C Moreau, AM Samuel, FH Samuel, HW Doty. Influences of alloying elements, solution treatment time and quenching media on quality indices of 413-type Al-Si casting alloys, Materials Science and Engineering A. 489 (2008) 426-438.

[39]. R Antoniou, C Subramanian. Wear mechanism map for aluminium alloys, Scripta Metallurgica. 22 (1988) 809-814.
[40]. SC Lim, MF Ashby. Wear-mechanism maps, Acta Metallurgica. 35 (1987) 1-24.
[41]. Y Liu, R Asthana, P Rohatgi. A map for wear mechanisms in aluminium alloys, Journal of Materials Science. 26 (1991) 99-102.
[42]. NP Suh. An overview of the delamination theory of wear, Wear. 44 (1977) 1-16.
[43]. J Zhang, AT Alpas. Transition between mild and severe wear in aluminium alloys, Acta Materialia. 45 (1997) 513-528.
[44]. S Wilson, AT Alpas. Wear mechanism maps for metal matrix composites, Wear. 212 (1997) 41-49.
[45]. AS Reddy, BN Pramila Bai, KSS Murthy, SK Biswas. Mechanism of seizure of aluminium-silicon alloys dry sliding against steel, Wear. 181-183 (1995) 658-667.
[46]. M Elmadagli, Microstructural studies of wear mechanisms in cast aluminum alloys, Ph.D. Dissertation, University of Windsor. (2005) 280.
[47]. R Shivanath, PK Sengupta, TS Eyre. Wear of aluminum-silicon alloys, British Foundryman. 70 (1977) 349-356.
[48]. AD Sarkar, J Clarke. Wear characteristics, friction and surface topography observed in the dry sliding of as-cast and age hardening Al-Si alloys, Wear. 75 (1982) 71-85.
[49]. JB Andrews, MV Seneviratne, KP Zier, TR Jett, Influence of silicon content on the wear characteristics of hypereutectic Al-Si alloys. Wear of materials: International Conference on Wear of Materials. (1985) 180-185.
[50]. BN Pramila Bai, SK Biswas. Characterization of dry sliding wear of Al-Si alloys, Wear. 120 (1987) 61-74.
[51]. F Wang, H Liu, Y Ma, Y Jin. Effect of Si content on the dry sliding wear properties of spray-deposited Al-Si alloy, Materials and Design. 25 (2004) 163-166.
[52]. D Apelian, S Shivkumar, G Sigworth. Fundamental aspects of heat treatment of cast Al-Si-Mg alloys, AFS Transactions. 97 (1989) 727-742.
[53]. L Lasa, JM Rodriguez-Ibabe. Effect of composition and processing route on the wear behaviour of Al-Si alloys, Scripta Materialia. 46 (2002) 477-481.
[54]. AR Riahi, T Perry, AT Alpas. Scuffing resistances of Al-Si alloys: Effects of etching condition, surface roughness and particle morphology, Materials Science and Engineering A. 343 (2003) 76-81.
[55]. K Razavizadeh, TS Eyre. Oxidative wear of aluminium alloys, Wear. 79 (1982) 325-333.
[56]. K Razavizadeh, TS Eyre. Oxidative wear of aluminium alloys: Part II, Wear. 87 (1983) 261-271.
[57]. P Heilmann, J Don, TC Sun, DA Rigney, WA Glaeser. Sliding wear and transfer, Wear. 91 (1983) 171-190.
[58]. SL Rice, H Nowotny, SF Wayne. Characteristics of metallic subsurface zones in sliding and impact wear, Wear. 74 (1981) 131-142.
[59]. CM Taylor, Lubrication regimes and the internal combustion engine, in: Taylor CM (Ed.), Engine Tribology, 1993, pp. 75-87.
[60]. WD Philips, Ashless phosphorus-containing lubricating oil additives, in: Rudnick LR (Ed.), Lubricant additives : chemistry and applications, 1st ed., Marcel Dekker, New York, 2003, pp. 45-108.
[61]. RC Gunther, Lubrication, Bailey Brothers and Swinfen Ltd., Folkestone, UK, 1971.
[62]. M Priest, CM Taylor. Automobile engine tribology - approaching the surface, Wear. 241 (2000) 193-203.
[63]. Z Pawlak, Tribochemistry of lubricating oils, 1st ed., Elsevier, Amsterdam ;London, 2003.

[64]. RM Mortier, ST Orszulik, Chemistry and technology of lubricants, Blackie Academic & Professional, London, 1997.
[65]. G Timmermans, L Froyen. Tribological performance of hypereutectic P/M Al-Si during sliding in oil, Wear. 231 (1999) 77-88.
[66]. S Das, SK Biswas. Boundary lubricated tribology of an aluminium-silicon alloy sliding against steel, Tribology Letters. 17 (2004) 623-628.
[67]. S Das, T Perry, SK Biswas. Effect of surface etching on the lubricated sliding wear of an eutectic aluminium-silicon alloy, Tribology Letters. 21 (2006) 193-204.
[68]. S Das, K Varalakshmi, V Jayaram, SK Biswas. Ultra mild wear in lubricated tribology of an aluminium alloy, Journal of Tribology. 129 (2007) 942-951.
[69]. M Kawamura, K Fujita. Antiwear property of lubricant additives for high silicon aluminium alloy under boundary lubricating conditions, Wear. 89 (1983) 99-105.
[70]. T Konishi, EE Klaus, JL Duda. Wear characteristics of aluminum-silicon alloy under lubricated sliding conditions, Tribology Transactions. 39 (1996) 811-818.
[71]. Y Wan, L Cao, Q Xue. Friction and wear characteristics of ZDDP in the sliding of steel against aluminum alloy, Tribology International. 30 (1997) 767-772.
[72]. M Fuller, M Kasrai, JS Sheasby, GM Bancroft, K Fyfe, KH Tan. X-ray absorption spectroscopy of antiwear films on aluminum alloys generated from zinc dialkyldithiophosphate, Tribology Letters. 1 (1995) 367-378.
[73]. M Fuller, Z Yin, M Kasrai, GM Bancroft, ES Yamaguchi, PR Ryason, et al. Chemical characterization of tribochemical and thermal films generated from neutral and basic ZDDPs using X-ray absorption spectroscopy, Tribology International. 30 (1997) 305-315.
[74]. A Neville, A Morina, T Haque, M Voong. Compatibility between tribological surfaces and lubricant additives-How friction and wear reduction can be controlled by surface/lube synergies, Tribology International. 40 (2007) 1680-1695.
[75]. L Hu, J Chen, W Liu, Q Xue, C Kajdas. Investigation of tribochemical behavior of Al-Si alloy against itself lubricated by amines, Wear. 243 (2000) 60-67.
[76]. J Qu, JJ Truhan, S Dai, H Luo, PJ Blau. Ionic liquids with ammonium cations as lubricants or additives, Tribology Letters. 22 (2006) 207-214.
[77]. J Qu, PJ Blau, S Dai, H Luo, HM Meyer III, JJ Truhan. Tribological characteristics of aluminum alloys sliding against steel lubricated by ammonium and imidazolium ionic liquids, Wear. 267 (2009) 1226-1231.
[78]. MA Nicholls, PR Norton, GM Bancroft, M Kasrai. X-ray absorption spectroscopy of tribofilms produced from zinc dialkyl dithiophosphates on Al-Si alloys, Wear. 257 (2004) 311-328.
[79]. MA Nicholls, PR Norton, GM Bancroft, M Kasrai, G De Stasio, LM Wiese. Spatially resolved nanoscale chemical and mechanical characterization of ZDDP antiwear films on aluminum-silicon alloys under cylinder/bore wear conditions, Tribology Letters. 18 (2005) 261-278.
[80]. G Pereira, A Lachenwitzer, MA Nicholls, M Kasrai, PR Norton, G De Stasio. Chemical characterization and nanomechanical properties of antiwear films fabricated from ZDDP on a near hypereutectic Al-Si alloy, Tribology Letters. 18 (2005) 411-427.
[81]. G Pereira, A Lachenwitzer, M Kasrai, PR Norton, TW Capehart, TA Perry, et al. A multi-technique characterization of ZDDP antiwear films formed on Al (Si) alloy (A383) under various conditions, Tribology Letters. 26 (2007) 103-117.
[82]. X Xia, A Morina, A Neville, M Priest, R Roshan, CP Warrens, et al. Tribological performance of an Al-Si alloy lubricated in the boundary regime with zinc dialkyldithiophosphate and molybdenum dithiocarbamate additives, Proceedings of the Institution of Mechanical Engineers, Part J: Journal of Engineering Tribology. 222 (2008) 305-314.

[83]. AE Jiménez, A Morina, A Neville, MD Bermúdez. Surface interactions and tribochemistry in boundary lubrication of hypereutectic aluminium-silicon alloys, Proceedings of the Institution of Mechanical Engineers, Part J: Journal of Engineering Tribology. 223 (2009) 593-601.
[84]. A Mahato, A Sachdev, SK Biswas. Lubricated tribology of a eutectic aluminium-silicon alloy in the ultra-mild wear and mild wear regimes for long sliding times, ACS Applied Materials and Interfaces. 2 (2010) 2870-2879.
[85]. H Spikes. The history and mechanisms of ZDDP, Tribology Letters. 17 (2004) 469-489.
[86]. TH Handley, JA Dean. O,O-dialkyl phosphorodithioic acids as extractants for metals, Analytical Chemistry. 34 (1962) 1312-1315.
[87]. GW Kennerly, WL Patterson. Kinetic studies of petroleum antioxidants, Industrial & Engineering Chemistry. 48 (1956) 1917-1924.
[88]. T Colclough, JI Cunneen. Oxidation of organic sulphides. Part XV. The antioxidant action of phenothiazine, zinc isopropylxanthate, zinc di-isopropyldithiophosphate, and zinc dibutyldithiocarbamate, in squalene, Journal of the Chemical Society (Resumed). (1964) 4782-4790.
[89]. S Al-Malaika, M Coker, G Scott. Mechanism of antioxidant action: Nature of transformation products of dithiophosphates-Part 1. Their role as antioxidants in polyolefins, Polymer Degradation and Stability. 22 (1988) 147-159.
[90]. RB Jones, RC Coy. Chemistry of the thermal degradation of zinc dialkyldithiophosphate additives, ASLE Transactions. 24 (1981) 91-97.
[91]. M Chen, AT Alpas, Ultra-mild wear of aluminum alloys: Role of silicon particles, Proceedings of STLE/ASME International Joint Tribology Conference, IJTC 2006. (2006) 1-2.
[92]. M Chen, T Perry, AT Alpas. Ultra-mild wear in eutectic Al-Si alloys, Wear. 263 (2007) 552-61.
[93]. M Chen, AT Alpas. Ultra-mild wear of a hypereutectic Al-18.5 wt.% Si alloy, Wear. 265 (2008) 186-195.
[94]. M Chen, X Meng-Burany, TA Perry, AT Alpas. Micromechanisms and mechanics of ultra-mild wear in Al-Si alloys, Acta Materialia. 56 (2008) 5605-5616.
[95]. M Dienwiebel, K Pöhlmann, M Scherge. Origins of the wear resistance of Al-Si cylinder bore surfaces studies by surface analytical tools, Tribology International. 40 (2007) 1597-1602.
[96]. H Yu, Tribological failure analyses of automotive engine blocks subjected to sliding wear damage, M.A.Sc. Thesis, University of Windsor. (2006) 147.
[97]. BE Slattery, T Perry, A Edrisy. Microstructural evolution of a eutectic Al-Si engine subjected to severe running conditions, Materials Science and Engineering A. 512 (2009) 76-81.
[98]. BE Slattery, A Edrisy, T Perry. Investigation of wear induced surface and subsurface deformation in a linerless Al-Si engine, Wear. 269 (2010) 298-309.
[99]. X Meng-Burany, TA Perry, AK Sachdev, AT Alpas. Subsurface sliding wear damage characterization in Al-Si alloys using focused ion beam and cross-sectional TEM techniques, Wear. 270 (2011) 152-162.
[100]. JA Greenwood, JH Tripp. The elastic contact of rough spheres, ASME Journal of Applied Mechanics. 34 (1967) 153-159.
[101]. M Scherge, K Pohlmann, A Gerve. Wear measurement using radionuclide technique, Wear. 254 (2003) 8001-8817.
[102]. C Tomastik, M Jech, T Wopelka, F Franek. Surface analysis of cylinder liners from tribological model experiments and internal combustion engines, Surface and Interface Analysis. 42 (2010) 1357-1360.

[103]. IM Hutchings, Tribology: friction and wear of engineering materials, CRC Press, Boca Raton, 1992.
[104]. DA Shirley. High-resolution x-ray photoemission spectrum of the valence bands of gold, Physical Review B. 5 (1972) 4709-4714.
[105]. TrueGrid Manual. XYZ Scientific Applications, Inc. 2001; Version 2.1.0.
[106]. Reference Guide, ScanIP, +ScanFE, +ScanCAD, Simpleware Ltd. 2009; Release 3.0.
[107]. LSTC. "LS-Prepost Overview." LS-Prepost Online Documentation. 2011. Livermore Software Technology Corporation. 14 May 2011.
[108]. LS-DYNA, Keyword Users Manual, Volume I, May 2007, Version 971.
[109]. JC Brewer, PA Lagace. Quadratic stress criterion for initiation of delamination, Journal of Composite Materials 22 (1988) 1141-155.
[110]. H Zhang, DY Li. The mechanisms of interfacial failure for lateral force-sensing microindentation test: finite element analysis, Acta Materialia. 56 (2008) 6197-6204.
[111]. A Noreyan, Y Qi, V Stoilov. Critical shear stresses at aluminum-silicon interfaces, Acta Materialia. 56 (2008) 3461-3469.
[112]. DK Ward, WA Curtin, Y Qi. Mechanical behavior of aluminum-silicon nanocomposites: A molecular dynamics study, Acta Materialia. 54 (2006) 4441-4451.
[113]. DK Ward, WA Curtin, Y Qi. Aluminum-silicon interfaces and nanocomposites: A molecular dynamics study, Composites Science and Technology. 66 (2006) 1148-1158.
[114]. ASTM E8 / E8M, 2009, Standard Test Methods for Tension Testing of Metallic Materials, ASTM International, West Conshohocken, PA, 2009, www.astm.org.
[115]. ASTM E9, 2009 Standard Test Methods of Compression Testing of Metallic Materials at Room Temperature, ASTM International, West Conshohocken, PA, 2009, www.astm.org.
[116]. ASTM G99 – 05 (2010) Standard Test Method for Wear Testing with a Pin-on-Disk Apparatus, ASTM International, West Conshohocken, PA, 2010, www.astm.org.
[117]. J.A. Greenwood, J.H. Tripp, Contact of flat surfaces, Proceedings of the Royal Society, London 295A. (1966) 300–319.
[118]. D. Tabor, The Hardness of Metals, Oxford University Press, Oxford, 1951, pp. 46–51.
[119]. G Pereira, A Lachenwitzer, M Kasrai, GM Bancroft, PR Norton, M Abrecht, PUPA Gilbert, T Regier, RIR Blyth and J Thompson. Chemical and mechanical analysis of tribofilms from fully formulated oils Part 1 – Films on 52100 steel, Tribology - Materials, Surfaces & Interfaces. 1.1 (2007) 48-61.
[120]. Z Yin, M Kasrai, GM Bancroft, KH Tan, X Feng. X-ray-absorption spectroscopic studies of sodium polyphosphate glasses, Physical Review B. 51 (1995) 742-750.
[121]. R Heuberger, A Rossi, ND Spencer. XPS study of the influence of temperature on ZnDTP tribofilm composition, Tribology Letters. 25 (2007) 185-196.
[122]. J Kruse, P Leinweber, K-U Eckhardt, F Godlinski, Y Huc, L Zuinc. Phosphorus $L_{2,3}$-edge XANES: overview of reference compounds, Journal of Synchrotron Radiation. 16.2 (2009) 247-259.
[123]. W Hetaba, A Mogilatenko, W Neumann. Electron beam-induced oxygen desorption in γ-$LiAlO_2$, Micron. 41 (2010) 479-483.
[124]. WC Oliver, GM Pharr. Improved technique for determining hardness and elastic modulus using load and displacement sensing indentation experiments, Journal of Materials Research. 7 (1992) 1564-1580.
[125]. WW Hanneman, RS Porter. The thermal decomposition of dialkyl phosphates and O,O-dialkyl dithiophosphates, Journal of Organic Chemistry. 29 (1964) 2996-2998.
[126]. NE Gallopoulos. Thermal Decomposition of Metal Dialkyldithiophosphate Oil Blends, ASLE Transactions. 7 (1964) 55-63.

[127]. JS Ashford, L Bretherick, P Gould. The thermal decomposition of zinc di-(4-methylpentyl-2) dithiophosphate, Journal of Applied Chemistry. 15 (1965) 170-178.
[128]. JJ Dickert Jr., CN Rowe. The thermal decomposition of metal O,O-dialkylphosphorodithioates, Journal of Organic Chemistry. 32 (1967) 647-653.
[129]. RJ Bird, GD Galvin. The application of photoelectron spectroscopy to the study of e. p. films on lubricated surfaces, Wear. 37 (1976) 143-167.
[130]. GM Bancroft, M Kasrai, M Fuller, Z Yin, K Fyfe, KH Tan. Mechanisms of tribochemical film formation: Stability of tribo- and thermally-generated ZDDP films, Tribology Letters. 3 (1997) 47-51.
[131]. H Fujita, RP Glovnea, HA Spikes, (2004).
[132]. H Fujita, HA Spikes. The formation of zinc dithiophosphate antiwear films, Proceedings of the Institution of Mechanical Engineers, Part J: Journal of Engineering Tribology. 218 (2004) 265-277.
[133]. Z Yin, M Kasrai, M Fuller, GM Bancroft, K Fyfe, KH Tan. Application of soft X-ray absorption spectroscopy in chemical characterization of antiwear films generated by ZDDP Part I: The effects of physical parameters, Wear. 202 (1997) 172-191.
[134]. JM Martin, C Grossiord, T Le Mogne, S Bec, A Tonck. The two-layer structure of Zndtp tribofilms, Part I: AES, XPS and XANES analyses, Tribology International. 34 (2001) 523-530.
[135]. S Bec, A Tonck, JM Georges, RC Coy, JC Bell, GW Roper. Relationship between mechanical properties and structures of zinc dithiophosphate anti-wear films, Proceedings of the Royal Society A: Mathematical, Physical and Engineering Sciences. 455 (1999) 4181-4203.
[136]. M Aktary, MT McDermott, GA McAlpine. Morphology and nanomechanical properties of ZDDP antiwear films as a function of tribological contact time, Tribology Letters. 12 (2002) 155-162.
[137]. JJ Habeeb, WH Stover. Role of hydroperoxides in engine wear and the effect of zinc dialkyldithiophosphates. ASLE Transactions. 30 (1987) 419-426.
[138]. F Rounds. Effects of hydroperoxides on wear as measured in four-ball wear tests, STLE Tribology Transactions. 36 (1993) 297-303.
[139]. JM Martin. Antiwear mechanisms of zinc dithiophosphate: A chemical hardness approach, Tribology Letters. 6 (1999) 1-8.
[140]. PA Willermet, LR Mahoney, CM Haas. Effects of antioxidant reactions on the wear behaviour of a zinc dialkyldithiophosphate, ASLE Transactions. 22 (1979) 301-306.
[141]. PA Willermet, LR Mahoney, CM Bishop. Lubricant degradation and wear III. Antioxidant reactions and wear behaviour of a zinc dialkyldithiophosphate in a fully formulated lubricant. ASLE Transactions. 23 (1980) 225-231.
[142]. RV Siriwardane, JM Cook. Interactions of NO and SO_2 with iron deposited on silica, Journal of Colloid and Interface Science. 104 (1985) 250-257.
[143]. RV Siriwardane, JM Cook. Interactions of SO_2 with sodium deposited on CaO, Journal of Colloid and Interface Science. 114 (1986) 525-535.
[144]. DW Langer, CJ Vesely. Electronic core levels of zinc chalcogenides, Physical Review B. 2 (1970) 4885-4892.
[145]. PA Zhdan, AP Shepelin, ZG Osipova, VD Sokolovskii. The extent of charge localization on oxygen ions and catalytic activity on solid state oxides in allylic oxidation of propylene, Journal of Catalysis. 58 (1979) 8-14.
[146]. C Battistoni, JL Dormann, D Fiorani, E Paparazzo, S Viticoli. An XPS and Mössbauer study of the electronic properties of $ZnCr_xGa_{2-x}O_4$ spinel solid solutions, Solid State Communications. 39 (1981) 581-585.

[147]. VI Nefedov. A comparison of results of an ESCA study of nonconducting solids using spectrometers of different constructions, Journal of Electron Spectroscopy and Related Phenomena. 25 (1982) 29-47.
[148]. E Paparazzo. XPS and auger spectroscopy studies on mixtures of the oxides SiO_2, Al_2O_3, Fe_2O_3 and Cr2O3, Journal of Electron Spectroscopy and Related Phenomena. 43 (1987) 97-112.
[149]. L Taylor, A Dratva, HA Spikes. Friction and wear behavior of zinc dialkyldithiophosphate additive, Tribology Transactions. 43 (2000) 469-479.
[150]. Y Wang, C Yao, GC Barber, B Zhou, Q Zou. Scuffing resistance of coated piston skirts run against cylinder bores, Wear. 259 (2005) 1041-1047.
[151]. GE Dieter, Mechanical metallurgy, SI Metric Edition ed., McGraw-Hill, New York, 1976.
[152]. GTA Kovacs. Micromachined Transducers Sourcebook. (1998) 26.
[153]. MA Islam, ZN Farhat. The influence of porosity and hot isostatic pressing treatment on wear characteristics of cast and P/M aluminum alloys, Wear. 271 (2011) 1594-1601.

APPENDICES

Appendix A1 – SEM images to generate multi-particle model

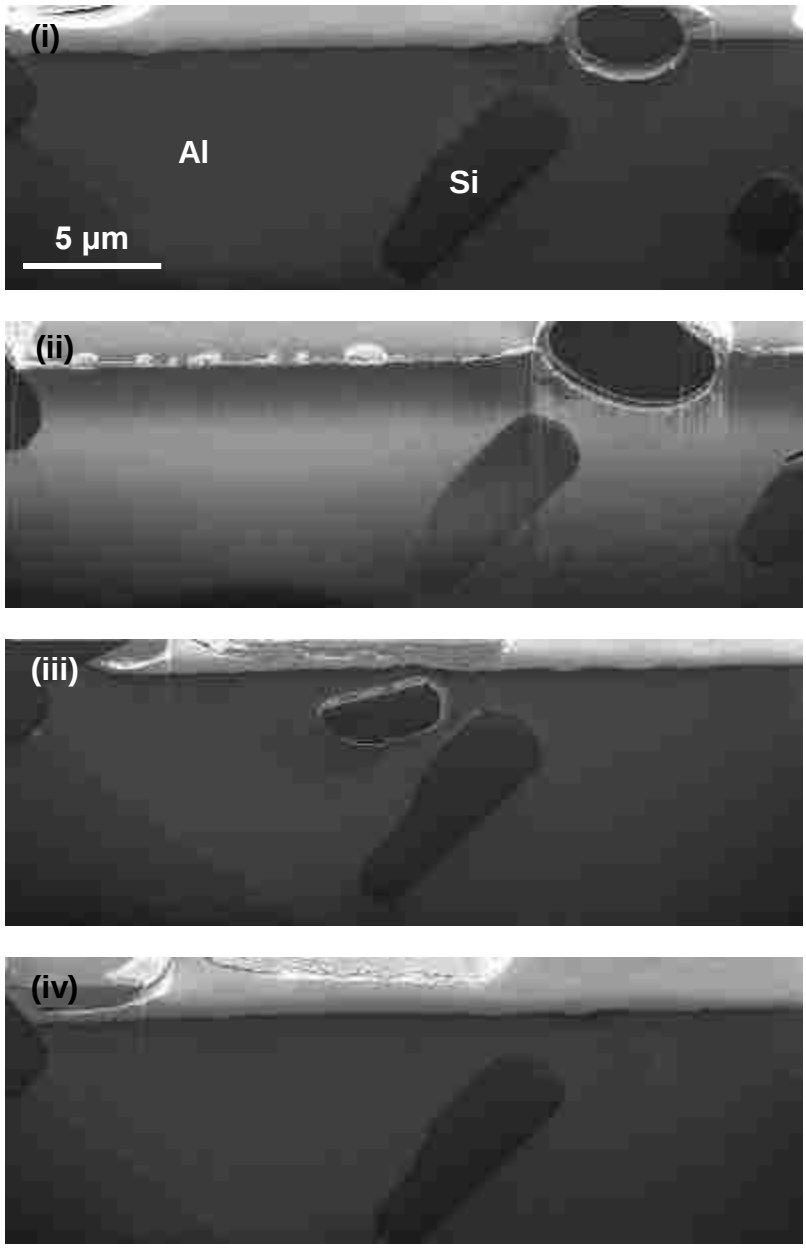

Figure A1. 1: SEM images used to generate the 3D multi-particle model. Dark grey phases are silicon particles and the light grey phase is aluminum. Nine images (i-ix) with spacing of 2.0 µm are shown out of a total of eighty two images. The scalebar is same for all images and is shown in image (i)

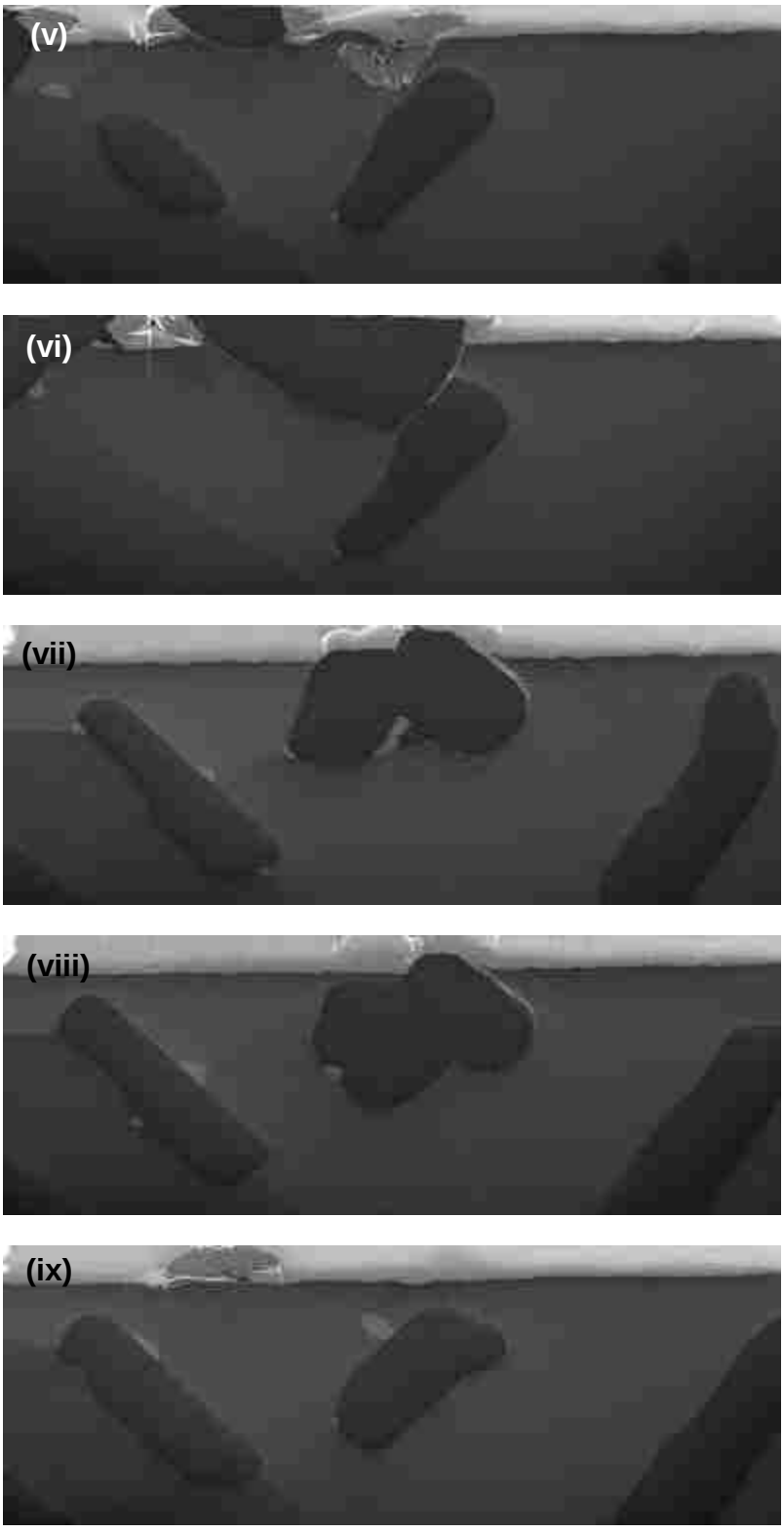

Figure A1. 1: Continued

Appendix A2 – Sample input for single-particle model

```
$# LS-DYNA Keyword file created by LS-PREPOST 2.4(Beta) - 17Jan2009(16:11)
$# Created on Apr-11-2011 (11:43:52)
*KEYWORD
*TITLE
$# title
LS-DYNA keyword deck by LS-Prepost
*CONTROL_IMPLICIT_DYNAMICS
$#   imass     gamma      beta    tdybir    tdydth    tdybur     irate
         0  0.500000  0.250000     0.0001.0000E+281.0000E+28
*CONTROL_IMPLICIT_GENERAL
$#  imflag       dt0    imform      nsbs       igs     cnstn      form    zero_v
         1 5000.0000         2         1         2         0         0         1
*CONTROL_IMPLICIT_SOLUTION
$#  nsolvr    ilimit    maxref     dctol     ectol     rctol     lstol    abstol
         2       100        10  0.005000  0.0300001.0000E+10  0.9000001.0000E-10
$#   dnorm    diverg     istif   nlprint    nlnorm   d3itctl
         2         1         1         2         2
$#  arcctl    arcdir    arclen    arcmth    arcdmp
         0         0     0.000         1         2
*CONTROL_TERMINATION
$#  endtim    endcyc     dtmin    endeng    endmas
 1.9000E+5
*DATABASE_BNDOUT
$#      dt    binary      lcur     ioopt
 10000.000         1
*DATABASE_ELOUT
$#      dt    binary      lcur     ioopt
 10000.000         1
*DATABASE_GLSTAT
$#      dt    binary      lcur     ioopt
 10000.000         1
*DATABASE_MATSUM
$#      dt    binary      lcur     ioopt
 10000.000         1
```

```
*DATABASE_NODOUT
$#      dt    binary      lcur     ioopt      dthf     binhf
 10000.000         1
*DATABASE_RCFORC
$#      dt    binary      lcur     ioopt
 10000.000         1
*DATABASE_SLEOUT
$#      dt    binary      lcur     ioopt
 10000.000         1
*DATABASE_SPCFORC
$#      dt    binary      lcur     ioopt
 10000.000         1
*DATABASE_BINARY_D3PLOT
$#      dt      lcdt      beam     npltc    psetid
 10000.000
$#   ioopt

*DATABASE_BINARY_D3THDT
$#      dt      lcdt      beam     npltc    psetid
 10000.000
*DATABASE_HISTORY_NODE_SET
$#     id1       id2       id3       id4       id5       id6       id7       id8
         7
*BOUNDARY_PRESCRIBED_MOTION_SET
$#    nsid       dof       vad      lcid        sf       vid     death     birth
         6         3         2         1  1.000000         0 1.6010E+5
*BOUNDARY_SPC_SET
$#    nsid       cid      dofx      dofy      dofz     dofrx     dofry     dofrz
         1         0         1         1         1         1         1         1
*SET_NODE_LIST_TITLE
Bottom nodes
$#     sid       da1       da2       da3       da4
         1
$#    nid1      nid2      nid3      nid4      nid5      nid6      nid7      nid8
    223777    223778    223775    223776    223817    223818    223815    223816
…
    238628
```

```
*BOUNDARY_SPC_SET
$#    nsid       cid      dofx      dofy      dofz     dofrx     dofry     dofrz
         2         0         0         1         0         1         0         1
*SET_NODE_LIST_TITLE
Global XZ nodes
$#     sid       da1       da2       da3       da4
         2
$#    nid1      nid2      nid3      nid4      nid5      nid6      nid7      nid8
     89969     90998     89986     91007     90003     91016     90020     91025
…

    163823    164860    165897    166934    167971
*BOUNDARY_SPC_SET
$#    nsid       cid      dofx      dofy      dofz     dofrx     dofry     dofrz
         3         1         0         1         0         1         0         1
*SET_NODE_LIST_TITLE
local xz plane
$#     sid       da1       da2       da3       da4
         3
$#    nid1      nid2      nid3      nid4      nid5      nid6      nid7      nid8
     91006     89985     91015     90002     91024     90019     91033     90036
    227965    227964    233295    230905    230904
*BOUNDARY_SPC_SET
$#    nsid       cid      dofx      dofy      dofz     dofrx     dofry     dofrz
         4         2         1         1         1         1         1         1
*SET_NODE_LIST_TITLE
wedge plane
$#     sid       da1       da2       da3       da4
         4
$#    nid1      nid2      nid3      nid4      nid5      nid6      nid7      nid8
    169070    169131    169192    169253    169314    169375    169436    169497
…

    227836    227835    232647    236067    226134    226133    232077
*BOUNDARY_SPC_SET
$#    nsid       cid      dofx      dofy      dofz     dofrx     dofry     dofrz
         5         0         1         1         0         1         1         1
```

```
*SET_NODE_LIST_TITLE
z nodes
$#     sid       da1       da2       da3       da4
         5
$#    nid1      nid2      nid3      nid4      nid5      nid6      nid7      nid8
    211686    211685    211684    211683    211682    211681    211680    211679
…

    232131    232132    232133    232134    232135    232136    232137
*BOUNDARY_SPC_SET
$#    nsid       cid      dofx      dofy      dofz     dofrx     dofry     dofrz
         8         0         1         1         1         1         1         1
*SET_NODE_LIST_TITLE
z nodes fixed
$#     sid       da1       da2       da3       da4
         8
$#    nid1      nid2      nid3      nid4      nid5      nid6      nid7      nid8
    169009    169010    169011    169012    169013    169014    169015    169016
…

*CONTACT_AUTOMATIC_SURFACE_TO_SURFACE_TIEBREAK_ID
$#     cid                                                                title
         1
$#    ssid      msid     sstyp     mstyp    sboxid    mboxid       spr       mpr
         2         1         0         0         0         0         0         1
$#      fs        fd        dc        vc       vdc    penchk        bt        dt
  0.200000  0.100000 10.000000     0.000     0.000         0     0.0001.0000E+20
$#     sfs       sfm       sst       mst      sfst      sfmt       fsf       vsf
 10.000000 10.000000     0.000     0.000  1.000000  1.000000  1.000000  1.000000
$#  option      nfls      sfls     param
         3 7200.0000 318.00000
$#    soft    sofscl    lcidab    maxpar     sbopt     depth     bsort    frcfrq
         1  0.100000         0  1.025000  2.000000         2         0         1
*SET_SEGMENT_TITLE
Al segment
$#     sid       da1       da2       da3       da4
         2
```

```
$#      n1        n2        n3        n4        a1        a2        a3        a4
    194843    194822    194823    194844
…

    120634    119597    119536    120573
*SET_SEGMENT_TITLE
Si segment
$#     sid       da1       da2       da3       da4
         1
$#      n1        n2        n3        n4        a1        a2        a3        a4
     89761     89774     89775     89762
…

     75735     75766     75767     75736
*PART
$# title
Si
$#     pid     secid       mid     eosid      hgid      grav    adpopt      tmid
         1         1         1
*SECTION_SOLID
$#   secid    elform       aet
         1         2
*MAT_ELASTIC
$#     mid        ro         e        pr        da        db  not used
        12.3290E-12 1.1240E+5  0.280000
*PART
$# title
Al
$#     pid     secid       mid     eosid      hgid      grav    adpopt      tmid
         2         2         2
*SECTION_SOLID
$#   secid    elform       aet
         2         2
*MAT_PLASTICITY_COMPRESSION_TENSION
$#     mid        ro         e        pr         c         p      fail      tdel
        22.7200E-12 70690.000  0.300000     0.000     0.0001.0000E+20
$#   lcidc     lcidt              lcsrc     lcsrt    srflag
```

```
         2         3
$#      pc        pt               pcutc     pcutt     pcutf
 57.534328-57.534328
$#       k


*DEFINE_CURVE_TITLE
Si particle displacement
$#    lcid      sidr       sfa       sfo      offa      offo    dattyp
         1         0 1.0000E+5 -1.000000
$#                a1                  o1

           1.6000000           1.6000000
           1.9000000
*DEFINE_CURVE_TITLE
Compression curve
$#    lcid      sidr       sfa       sfo      offa      offo    dattyp
         2         0  1.000000  1.000000
$#                a1                  o1
               0.000         172.6000061
           0.0014200         187.8222198
…

           0.2419939         416.6188049
*DEFINE_CURVE_TITLE
Tension Curve
$#    lcid      sidr       sfa       sfo      offa      offo    dattyp
         3         0  1.000000  1.000000
$#                a1                  o1
               0.000         172.6000061
      3.4999999e-004         178.1390076
      7.6734001e-004         183.1696625
*SET_NODE_LIST_TITLE
Si top nodes
$#     sid       da1       da2       da3       da4
         6
…
```

```
     89730     89951
*SET_NODE_LIST_TITLE
pile-up nodes
$#     sid       da1       da2       da3       da4
         7
$#    nid1      nid2      nid3      nid4      nid5      nid6      nid7      nid8
    194923    194566    194545    194902    195280    195259    195637    195616
…

   209161    209518    209875    210232    210589    210946    211303    211660
*ELEMENT_SOLID
$#   eid     pid      n1      n2      n3      n4      n5      n6      n7      n8
       1       1      77     102     101      76       2       2       1       1
  215218       2  237827  230026  227092  227091  237828  230028  227096  227095
*NODE
$#   nid               x               y               z      tc      rc
       1           0.000           0.000      10.0000200
…

  238628      15.0000000           0.000     -10.0000000
*END
```

Appendix A3 – Copyright releases from publications

Chapter 4

License Number	2725440167812
License date	Aug 10, 2011
Licensed content publisher	Elsevier
Licensed content publications	Wear
Licensed content title	Micromechanisms of low load wear in as Al-18.5% Si alloy
Licensed content author	S.K. Dey,T.A. Perry,A.T. Alpas
Licensed content date	15 June 2009
Licensed content volume number	267
Licensed content issue number	1-4
Number of pages	10
Start page	515
End page	524
Type of Use	reuse in a thesis/dissertation
Intended publisher of new work	other
Portion	full article
Format	both print and electronic
Are you the author of this Elsevier article	Yes
Will you be translating	No
Order reference number	
Title of your thesis/dissertation	ELEVATED TEMPERATURE LUBRICATED WEAR OF Al-Si ALLOYS
Expected completion date	Sep 2011
Estimated size (number of pages)	260
Elsevier VAT number	GB 494 6272 12
Permissions price	0.00 USD
VAT/Local Sales Tax	0.0 USD / 0.0 GBP
Total	0.0 USD

Chapter 5

License Number	2725430184499
License date	Aug 10, 2011
Licensed content publisher	Elsevier
Licensed content publications	Wear
Licensed content title	Ultra-mild wear mechanisms of Al-12.6wt.% Si alloys at elevated temperature
Licensed content author	S.K. Dey,M.J. Lukitsch,M.P. Balogh,X. Meng-Burany,A.T. Alpas
Licensed content date	29 July 2011
Licensed content volume number	271
Licensed content issue number	9-10
Number of pages	12
Start page	1842
End page	1853
Type of Use	reuse in a thesis/dissertation
Portion	full article
Format	both print and electronic
Are you the author of this Elsevier article	Yes
Will you be translating	No
Order reference number	
Title of your thesis/dissertation	ELEVATED TEMPERATURE LUBRICATED WEAR OF Al-Si ALLOYS
Expected completion date	Sep 2011
Estimated size (number of pages)	260
Elsevier VAT number	GB 494 6272 12
Permissions price	0.00 USD
VAT/Local Sales Tax	0.0 USD / 0.0 GBP
Total	0.0 USD

VITA AUCTORIS

Name	Sanjib K. Dey
Place of Birth	Cuttack, Orissa, India
Year of Birth	1979
Education	Bachelor of Enginering (B.E.), Metallurgical Engineering, National Institute of Technology, Surathkal, Karnataka, India. 1997-2001.
	Master of Applied Science (M.A.Sc.), Engineering Materials, University of Windsor, Windsor, Ontario, Canada. 2005-2007.
	Doctor of Philosophy (Ph.D.), Engineering Materials, University of Windsor, Windsor, Ontario, Canada. 2007-2011.
Work	Senior Planning Engineer, Robert Bosch India, Bangalore 2001-2005.